Advances in Civil Engineering

New Structures and Structural Materials in Engineering

Lead Guest Editor: Wenjie Ge
Guest Editors: Ashraf Ashour, Pu Zhang, and Wei Li

New Structures and Structural Materials in Engineering

Advances in Civil Engineering

New Structures and Structural Materials in Engineering

Lead Guest Editor: Wenjie Ge
Guest Editors: Ashraf Ashour, Pu Zhang, and Wei Li

Contents

Hindawi
Advances in Civil Engineering
Volume 2022, Article ID 2014376, 17 pages
https://doi.org/10.1155/2022/2014376

Research Article

Numerical Analysis of Subgrade Behavior under a Dynamic Maglev Train Load

Wubin Wang,[1,2] **Zhixing Deng**,[2] **Yandong Li**,[2] **Zhichao Huang**,[2] **Yunbin Niu**,[2] **and Kang Xie**[3]

[1]*National Engineering Laboratory for Technology of Geological Disaster Prevention, Land Transportation, Southwest Jiaotong University, Chengdu 611731, China*
[2]*School of Civil Engineering, Southwest Jiaotong University, Chengdu, Sichuan 610031, China*
[3]*Department of Civil Engineering, Central South University, Changsha 410075, China*

Correspondence should be addressed to Kang Xie; xiekang1995@outlook.com

Received 7 July 2021; Revised 7 December 2021; Accepted 22 February 2022; Published 11 May 2022

Academic Editor: Wenjie Ge

Medium-low-speed maglevs are increasingly used in the urban rail transit industry because of their advantages, such as low noise and low energy consumption. In this study, a finite element analysis of the responses of the subgrade that supports a medium-low-speed maglev structure under a dynamic maglev load is presented. First, the finite element analysis considers a low-lying structure with different elastic moduli. Then, the attenuation laws of the dynamic stress and dynamic deformation for different depth ranges of the subgrade under the rail beam are analyzed. In addition, the magnitude of the influence of the dynamic load is clarified. The results lead to a recommendation of a base bed thickness of 1.5 m, graded gravel or group A filler as the surface layer of filler, and gravel soil as the bottom layer. This study provides theoretical support for the construction design of a subgrade structure under the rail beam of a low-lying maglev line.

1. Introduction

A maglev transportation system is a rail transit system that uses electromagnetic force to keep trains and tracks out of contact [1]. As a new type of rail transportation system, maglev transportation has good prospects for application in urban transportation, regional traffic, intercity traffic, and the national backbone network [2]. Medium-low-speed (MLS) maglev traffic refers to a traffic system whose maximum operating speed does not exceed 160 km/h [3].

Since MLS maglev rail transit has advantages of low noise, low vibration, low energy consumption, and strong adaptability to tight curves and steep slopes [4–6], this configuration is increasingly used in the urban rail transit industry [7, 8]. It is important to design a proper superstructure and substructures in rail transport systems. Relevant research has examined the use of ballast-less track systems [9] and metro track systems [10] to improve the reliability of design and reduce the impact of vibration on the environment. However, MLS maglev rail transit systems mostly use the overhead line method, and there are few application examples of low-lying structures where rail beams are placed directly on the subgrade [11]. Past MLS maglev line engineering research has mainly focused on overpasses [12], and further research on low-lying structures between the overhead line and the underground line is needed. Additionally, there is still a lack of relevant research and technical standards for the beds of MLS maglev subgrade structures.

At present, related scholars have conducted many studies on the dynamic response of the low-set roadbed structure of low and medium-speed magnetic levitation: relying on the Zhuzhou test line, China Railway Second Institute Engineering Group Co., Ltd., analyzed and tested the stress of the roadbed under the bearing rail beam through simulation analysis and field running tests, and derived the stress distribution law of the roadbed filler under the train load [13]. Cai and Yang analyzed and studied the

key technologies of track design, track beam stiffness, and dynamic coefficient of the test line by simulation analysis combined with Zhuzhou field running test, respectively [14, 15]; Gao analyzed and tested the stress of track beam and roadbed under the track beam by field test [16]; Li's team from Southwest Jiaotong University cooperated with China Railway Fourth Survey and Design Institute Group Co. Ltd., has carried out an in-depth study on the coupled dynamics of magnetic levitation vehicles and rails, and has conducted a systematic study on the dynamic characteristics of the low-set structure roadbed. The vibration response under the vehicle-low-mounted beam coupling was obtained by the field running test combined with numerical simulation by Li and Wang, respectively [17, 18]. At present, the technical standards for subgrade beds for MLS maglev structures, such as the use of padding and their compaction standards [19], are formulated mainly with reference to the technical standards for subgrade beds for high-speed railways [20]. Therefore, the above-mentioned series of studies were also conducted on this basis. Research on subgrade beds of MLS maglev low-lying structures based on speeds of 120 km/h and 160 km/h is still lacking. However, MLS maglev systems are quite different from high-speed railway systems in their load action mode, load intensity, and transmission method of the system structural force [21]. Fully referring to the high-speed railway design code [22] would cause certain deviations and greater safety reserves. Thus, it is necessary to further study the dynamic behaviors of subgrade beds under different speed standards according to the characteristics of MLS maglev rail transit projects [23].

The main focus of this paper is the MLS maglev subgrade for low-lying structures. The commercial finite element analysis software ABAQUS [24] is used to conduct finite element analysis of low-lying structures with different elastic moduli and to analyze the attenuation of the dynamic stress and deformation of the subgrade. In addition, the analyses of the trends of dynamic stress and dynamic deformation in different depth ranges of the subgrade under the rail beam are also implemented by ABAQUS. Finally, the magnitude of the influence of the dynamic load and theoretical support for the construction design of a subgrade structure under the rail beam of a low-lying maglev line are clarified.

2. Review of Existing MLS Maglev Systems

Typical MLS maglev lines include the Aichi High-Speed Transit Tobu Kyuryo Line in Japan [25], the Incheon Airport Maglev in South Korea [26], and the MLS Test Line (rail holding car) of The German Company Borg [27], as shown in Figure 1.

Since the beginning of the twenty-first century, there have been some relevant studies on MLS maglev technology, and several test lines have been successively built, including the Changsha Test Line of the National University of Defense Technology [29], the Qingchengshan Test Line of Southwest Jiaotong University [30], the Shanghai Lingang Test Line of Tongji University [31], the Tangshan test line [32], and the CRRC Zhuzhou test line [13]. On April 5, 2002, a MLS maglev test line developed and built by the National University of Defense Technology and other institutions was opened to traffic in Changsha [23]. The test line is 204 m in length, including a 100 m radius curve and a gradient of 4‰, with a gauge width of 2 m. The coach is 15 m long and can carry more than 130 passengers. It is designed to travel at a speed of 150 km/h. In 2003, Southwest Jiaotong University established the MLS maglev test line in Qingchengshan, Chengdu, Sichuan [30]. The maglev test track is 420 m long, and the coach is 11.2 m in length, 2.6 m in width, 3.3 m in height, and 18 *t* in weight. By the end of 2006, the Shanghai MLS maglev test line was completed, with a total length of approximately 1.5 km, and vehicle assembly and commissioning were also completed [31]. In November 2008, the Shanghai low-speed maglev line realized 85 km/h trial operation of three connected trains, and in December 2008, the line reached a 101 km/h trial operation speed. In June 2010, the Tangshan MLS maglev test line with a total length of 1547 m was completed [32]. This short test line of only approximately 1,000 m incorporates various features, such as a 70‰ gradient and 100 or 50 m radius space rotation and turning. In addition, the coach is 15 m in length and 3 m in width. The above test lines are shown in Figure 2.

However, these existing test lines did not adopt a low-lying structure in which the rail bearing beam is directly placed on the subgrade. In July 2012, the MLS maglev test line of Zhuzhou Locomotive Corporation, with a total length of 1.7 km, was completed and commissioned. Approximately 800 m of the line was adopted in the form of a rail bearing beam placed directly on the subgrade of a low-lying structure. Since the MLS maglev train suspension clearance, that is, the distance between the train and the track, is approximately 8 mm, the requirements of deformation of the offline structure, i.e., the line foundation system below the track, are more stringent than the traditional railway lines. At that time, worldwide consensus was that maglev rail transit should not adopt a low-lying structure of the subgrade; thus, at the beginning of the design of Zhuzhou test lines, there was a lack of research about the rail bearing beam of low-lying structures. Therefore, a conservative design was adopted: The subgrade was filled with graded gravel, the maximum filling height was approximately 4.0 m, and the subgrade base was reinforced with a composite foundation.

The Zhuzhou test line has been used to conduct research on low-lying structures [13], primarily on the rail bearing beam. The stress of the subgrade under the rail bearing beam has been analyzed and tested through simulation analysis and field driving tests only. The subgrade bed under the rail bearing beam has not been studied systematically. Based on the relevant research results of the Zhuzhou test line, the Changsha Maglev Express Line has optimized the design of the subgrade bed with a low-lying structure. The surface of the subgrade is made of 0.3 m thick graded gravel, and group A filler (the grouping standard of filler refers to the code for railway Earth subgrade design [34]) is used below the surface of the subgrade. The compaction standard adopted the compaction standard of a high-speed railway subgrade bed for reference. The main line section and depot section of the Changsha maglev line feature 6 sections of low-lying structures with a total length of approximately 1.2 km. Solid

(a) (b) (c)

Figure 1: Typical MLS maglev lines: (a) Aichi High-Speed Line; (b) Incheon Airport Maglev; (c) MLS Test Line [12, 28].

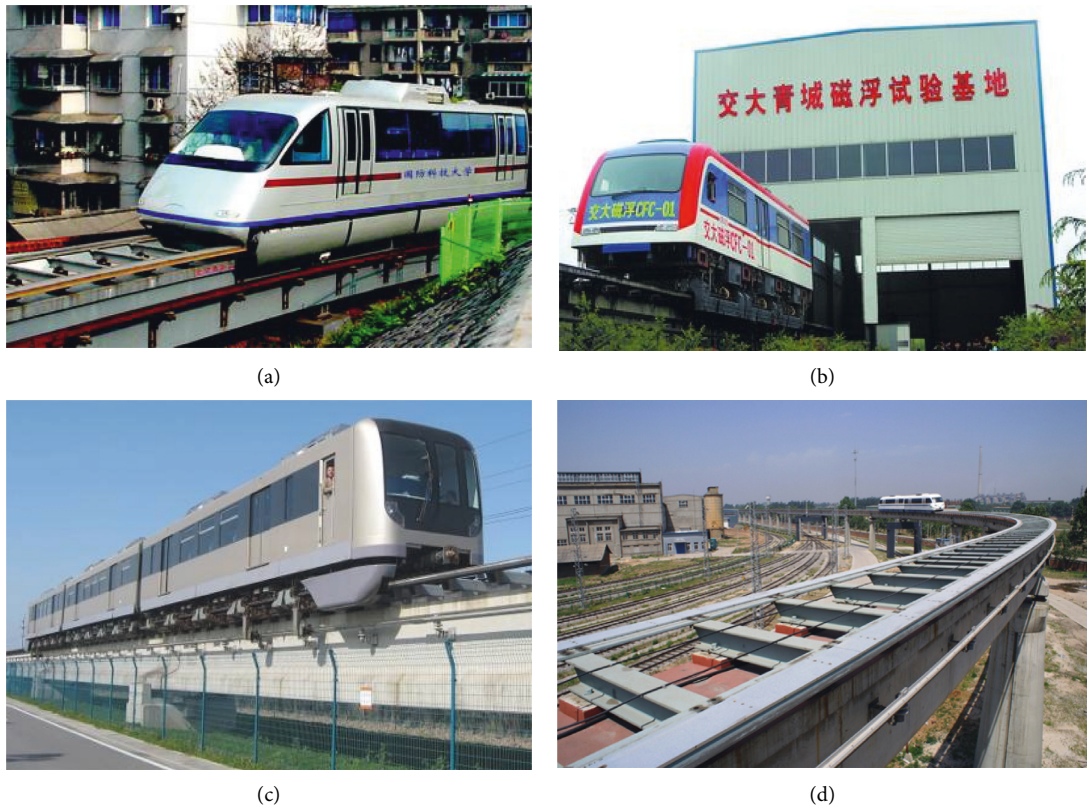

(a) (b)

(c) (d)

Figure 2: Mls maglev test lines: (a) Changsha test line; (b) Qingchengshan test line; (c) Shanghai Lingang test line; (d) Tangshan test line [3, 12, 33].

beams are used in the main line section, and frame column beams are used in the depot section. Two of these 6 sections are filled embankments with a height of approximately 3.5 m. This is the world's first MLS maglev operating line with a low-lying structure in which the rail beam is directly placed on the subgrade, thus breaking the technical restriction—originally maintained by experts worldwide—that maglev rail transit should not use low-lying structure subgrades. This design extends the geological and terrain conditions in which MLS maglev transportation can be applied, reduces engineering costs, and demonstrates leading-edge technology.

Relying on the Changsha Maglev Express Line, a systematic study was conducted on the subgrade bed of a low-lying structure [19]. The dynamic stress and deformation of the subgrade surface, the stiffness of the subgrade, the limit of the deformation of the subgrade, the dynamic strength of the subgrade, the design of the subgrade, and the thickness of the subgrade replacement of the cutting were studied. The related research on the Zhuzhou test line and Changsha Maglev Express Line involves the following main problems:

(1) The research objects are all MLS maglev lines with a design speed of 100 km/h. Research on the subgrade

beds of MLS maglev lines with speeds of 120 km and 160 km is still lacking.

(2) In the theoretical analysis, the dynamic coefficient adopts the calculation formula of the wheel-rail system, and the dynamic stress of the subgrade surface is considered at 30 kPa, while the measured maximum value on the Changsha Maglev Express Line and the Zhuzhou test line is approximately 10 kPa, which is too conservative [35].

(3) The research adopted the compaction standards of high-speed railway filling but failed to conduct a systematic study on subgrade filling and compaction standards.

(4) The influence of the backfill layer and cushion layer on the dynamic stress distribution along the depth of the subgrade was not considered.

(5) The research results are still unable to provide comprehensive support for the technical standards of subgrade beds with low-lying structures. At present, the corresponding design, including filling and compaction standards and calculation of dynamic coefficients, mainly adopts the relevant technical standards of high-speed rail, which provide more safety reserves.

3. Numerical Modeling of a Maglev Train Subgrade Bed

To study the force and deformation of a subgrade bed under a maglev train load, a 3D numerical model is established based on finite element theory using ABAQUS. The upper part is a block-type rail bearing beam structure and track structure, which are further described in Section 3.2. The subgrade has a two-layer structure: the surface layer of the subgrade bed with a thickness of 0.3 m and the bottom layer of the subgrade with a thickness of 1.2 m. Numerical calculations are used to study whether the structure of the subgrade can meet the required deformation and strain control in this case. An overall three-dimensional model diagram is shown in Figure 3. The specific introduction is as follows.

3.1. Development of the Model. The model is established with the aim of simulating the actual situation as much as possible, with some simplification. In the model, the maglev train load is simplified as a uniformly distributed load, and the bolt connection of the fixed track is simplified as a binding contact. The track structure and the soil layer within the vibration range have linear elastic properties [36]. Therefore, in the finite element model (FEM), the track structure, the rail beam, and the surface filling of the subgrade bed are set as linear elastic models, and the other soil layers are set as Mohr-Coulomb elastic-plastic models. The size of the model is sufficiently large [37], and the length of the longitudinal dimension is 3 times the length of a single-section rail beam. The bottom surface of the model is a fixed boundary, and the side of the model restricts horizontal displacement. The data of the two side rail beams are compared with the middle rail beam. In this study, the data of the middle rail beam was extracted and analyzed to reduce the influence of the boundary effect of the model. The grid of the model adopts a C3D8R eight-node linear hexahedral three-dimensional stress element, which reduces integrals and controls hourglass effects. The overall grid division is relatively regular with a total of 123783 nodes and 78172 elements. The base of the rail beam is in hard contact with the surface normal of the bed, the tangent is in contact with a penalty function, and binding constraints are used between other model components. When exploring the influence of dynamic load on the foundation bed, the gravity of the foundation bed and the foundation is not considered, but when analyzing the self-weight stress distribution of the depth of the dynamic load influence, gravity is considered. The dynamic implicit integral algorithm is adopted to simulate the running process from the head of the train entering the middle rail beam model to the end of the train leaving the model.

3.2. Dimensions of the Model. The upper rail beam structure of the model mainly comprises three parts: the top plate, the column and the base. In this model, three rail beams are established. The length of the base of each rail beam is 11.58 m, with a 20 mm expansion joint between each section. The bases are connected by dowel steel (Q235 steel, $\varphi 50 \times 5 \times 700$ mm), and the total length of the rail bearing beam base is 34.78 m. The spacing between the blocks is 1.2 m, and the specific structural dimensions are shown in Figure 4.

The upper part of the supporting rail beam is equipped with a track structure. Above the top plate is an H-shaped rail, which is connected by backing plates and gaskets as shown in Figure 5. In this simulation, the different parts are connected by binding instead of bolts. The F-shaped rail is laid longitudinally at the two ends of the H-shaped rail and is loaded to simulate the load of the actual maglev train.

The subgrade structure is composed mainly of a subgrade surface layer, a subgrade bottom layer, and its underlying filled layers. The total thickness of the embankment is 3 m, the thickness of the lower base model is 2.5 m, and the subgrade structure is modeled with a slope of 1 : 1.5. Considering the influence of the boundary conditions, a sufficient width of the base soil is set to reduce the influence of the boundary on the centerline of the line. There is a 0.1 m thick concrete cushion on the surface of the base bed and a rail bearing beam structure above the cushion. A backfill soil layer is set around the base of the rail bearing beam. The overall length of the model is 36.8 m, and the width is 20.5 m. The schematic diagram is provided in Figure 6.

3.3. Material Properties. The structural properties of the subgrade bed are determined according to the theoretical analysis. The Mohr-Coulomb model is selected to define the elastoplastic behavior of soils. Therefore, the deformation modulus is used as its modulus parameter. The properties are shown in Table 1.

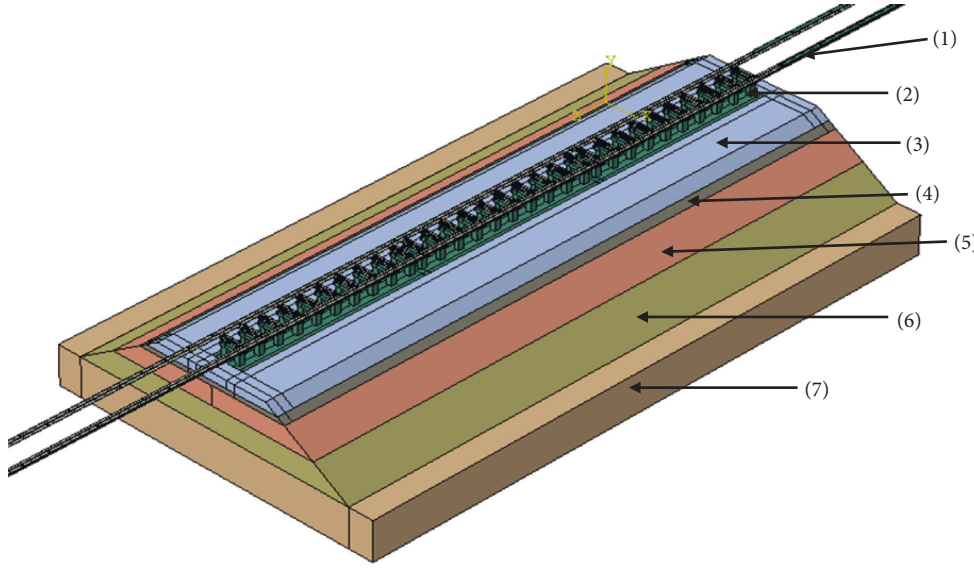

(1) track structure
(2) rail bearing beam
(3) 0.5m backfill layer
(4) 0.3m subgrade surface layer
(5) 1.2m subgrade bottom layer
(6) 1.5m embankment soil
(7) 2.5m foundation soil

Figure 3: Three-dimensional model diagram.

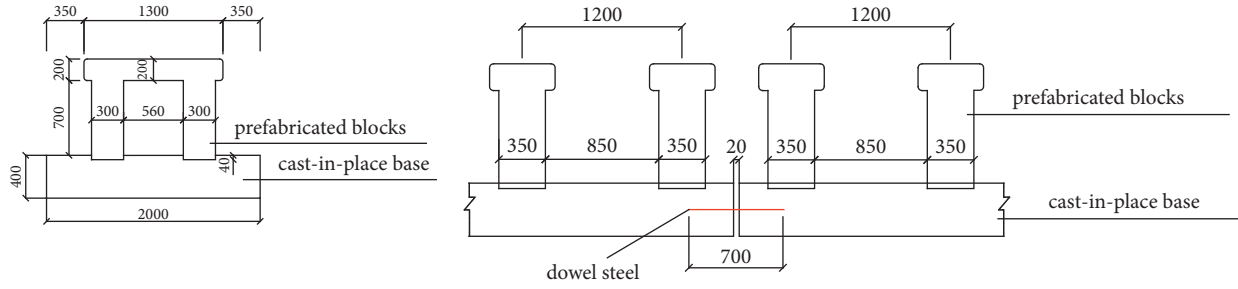

Figure 4: Rail beam specific structural dimensions (unit: mm); (a) cross-sectional diagram; (b) longitudinal diagram.

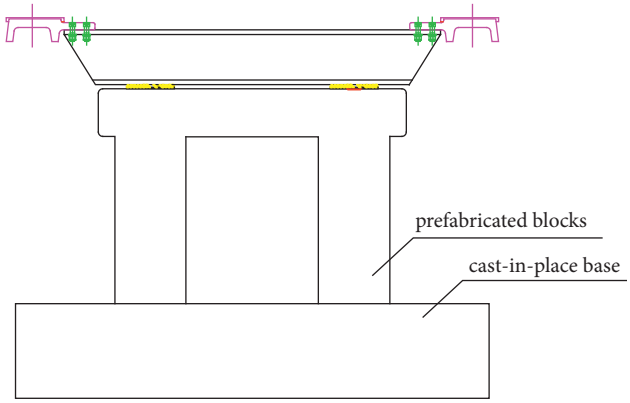

Figure 5: Cross-sectional diagram of the track and rail bearing beam.

3.4. Loading. The load acting on the top surface of the rail beam mainly includes the dead load and the vertical live load of the train. The dead load includes the self-weight of the rail beam structure and the self-weight of the track structure acting on the rail beam. According to the design achievements of Changsha Maglev Express and Qingyuan Maglev, the height of the track structure is 0.292 m (excluding the track platform), and the dead weight of the track structure is shown in Table 2.

The calculation shows that the dead load value is approximately 4.5 kN/m. In this simulation, this dead load is applied by the gravity method of the track structure. According to the "Basic Technical Parameters of Changsha Maglev Vehicles" [38], the load of a single train in suspension is as shown in Figure 5, and the uniform load is 12.9 kN/m. Therefore, the actual simulated load in the model is as shown in Figure 7. There are three trains in total, and the distance between each train is 1.68 m. According to the actual load width of the F-shaped rail subjected to the maglev train, a load with a width of 0.218 m is established in the model, which is converted into an area load of 59.174 kPa, which is taken as 60 kPa.

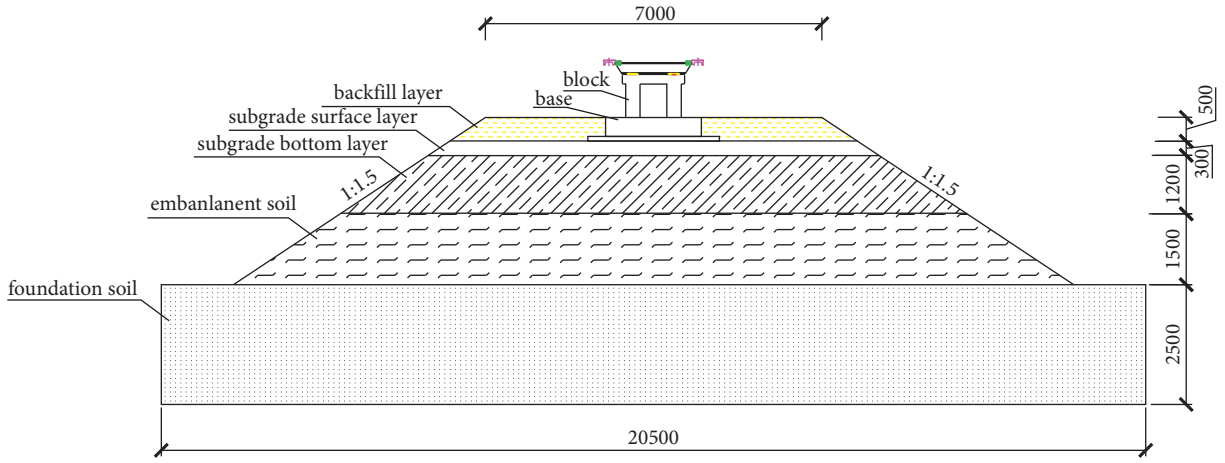

Figure 6: Geometric parameters of the maglev subgrade used in the FEM.

Table 1: Material properties considered in the FEM of the maglev subgrade.

Soil type		Density (kg/m^3)	Modulus of deformation (MPa)	Poisson's ratio	Internal friction angle (°)	Cohesive force (kPa)
Backfill layer		1700	100	0.35	20	15
Base bed surface layer	Graded broken stone	2200	140	0.25	—	—
	Group A filler	2100	140	0.3	—	—
Base bed bottom layer	Gravelly soil	2000	120	0.3	25	20
	Coarse-grained soil	1900	97	0.32	20	25
	Fine-grained soil	1850	63	0.35	20	32
Embankment soil		1850	70	0.35	25	60
Foundation soil		1700	120	0.35	32	20

Table 2: Track load statistics.

Project	Material		Unit weight (kg/m)	
			1.2 m fastener spacing	0.8 m fastener spacing
F-shaped steel	Q235D	126.5 kg/m	253.00	253.00
Senseboard	Aluminum		6.80	6.80
Sleeper	Q235D	95.15 kg/m	115.33	173.00
Fastener	QT450-10, 35VB, etc.	23.16 kg/group	38.60	57.90
Total			413.74	490.7
Average			452.22 kg/m ≈ 4.5 kN/m	

4. Simulation Results

The material in the X-axis direction of the subgrade structure is continuous and homogeneous. When the train arrives at the middle position of the model, the dynamic load of the subgrade is the most unfavorable. The dynamic deformation and dynamic strain of the subgrade under this working condition are studied. At this time, the train load is over the model, and the top surface of the foundation bed is under the greatest stress. At this time, whether the dynamic stress, dynamic deformation, and dynamic strain of the foundation bed structure meet the requirements is determined. The cross section along the X direction of the subgrade with the largest stress distribution is selected to study the stress distribution along the depth direction.

To facilitate analysis, horizontal and vertical coordinate systems are established, as shown in Figure 6, for the horizontal and vertical directions of the subgrade structure. The surface of the subgrade is taken as a plane with a Z-axis coordinate of 0. In addition, the X-axis along the longitudinal direction of the line and the Y-axis along the transverse direction are established. The centerline of the longitudinal line is the X-axis, and the middle position along the longitudinal direction is the 0 point on the Y-axis. The coordinate system is shown in Figure 8.

4.1. Dynamic Stress of the Subgrade Bed. To determine the dynamic stress response of the top surface of the subgrade under the moving load, first, the working conditions of the

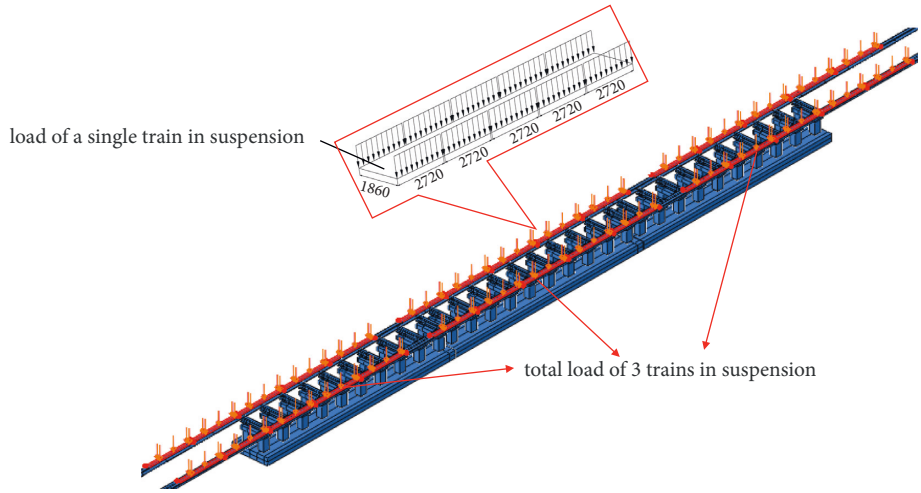

Figure 7: Suspended load diagram.

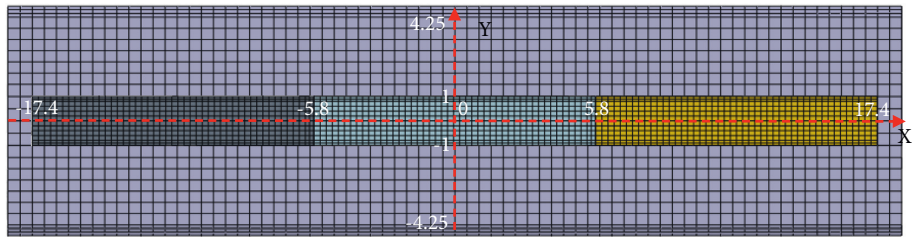

Figure 8: Top view coordinate map of bed structure.

train load statically placed on the model and the moving speeds of 100 km/h, 120 km/h, and 160 km/h are simulated. The maximum value of the vertical dynamic stress on the top surface of the subgrade bed is extracted under different working conditions, and the dynamic load results on the top surface of the subgrade bed are shown in Table 3.

When the design speed is 100~160 km/h, the dynamic load response of the subgrade surface increases with increasing speed, and the dynamic static stress ratio is the largest (1.182) at a speed of 160 km/h. The impact of different speeds on the surface dynamic load is generally small, with an impact difference within 10%. Therefore, the following analysis selects the most unfavorable working condition, with a speed of 160 km/h, to analyze the response of the subgrade bed.

4.1.1. Dynamic Stress on the Top Surface of the Bed. When the dynamic load of the train acts on the middle position of the model, the middle section is as shown in Figure 9. The white dashed frame in the figure is the outer edge of the concrete cushion, and the black dashed frame is the outer edge of the base of the rail beam. The Y coordinates of the outer edge line of the base and the cushion layer are ±1.5 m and ±1 m, respectively. The stress at this time is concentrated mainly on the position where the rail beam acts. In addition, the stress at the three-section base is the largest. The specific numerical analysis is as follows.

Along the longitudinal center axis of line z, the vertical stress distribution on the surface of the foundation bed is extracted. The contour diagram reveals that, along the horizontal line, the stress is not the largest at the central axis position but close to the edge of the base. Therefore, the stress distribution along the X-axis of the two places is as plotted in Figure 10(a), and the stress distribution along the Y-axis is as plotted in Figure 10(b).

The stress distribution along the X-axis direction (longitudinal) corresponds to the distribution position of the rail beam base. At the three-section base position, the stresses at the corresponding base bed positions are all large, and the maximum amplitude is essentially the same. At the expansion joint between the two bases, the stress is reduced. At ±18.4 m, the stress is reduced to 0 due to the boundary effect of the model, and the stress distribution at the two bases adjacent to the boundary is affected to a certain extent. The position where the maximum stress on the surface of the bed is in the longitudinal direction is the middle rail beam at $Y = \pm 0.5$ m (close to the edge of the base), and the maximum stress is approximately 13.61 kPa. At the same time, the vertical stress distribution on the central axis is relatively small, with a maximum stress value of 9.46 kPa. For the distribution of vertical stress along the Y-axis of the bed surface, the position $X = 0$ is chosen. There are two stress peaks at $Y = \pm 0.5$ m. These two positions are close to the edge of the base, and the stress amplitude is 13.61 kPa, while the stress at the central axis is slightly smaller, with a value of 9.46 kPa. The influence range of the stress in the transverse

Table 3: Dynamic load on the top surface of the bed at different speeds.

Design speed (km/h)	0 (static load)	100	120	160
Vertical stress on the surface of the base bed (kPa)	11.51	12.67	13.06	13.61
Static and static stress ratio	1	1.1	1.135	1.182

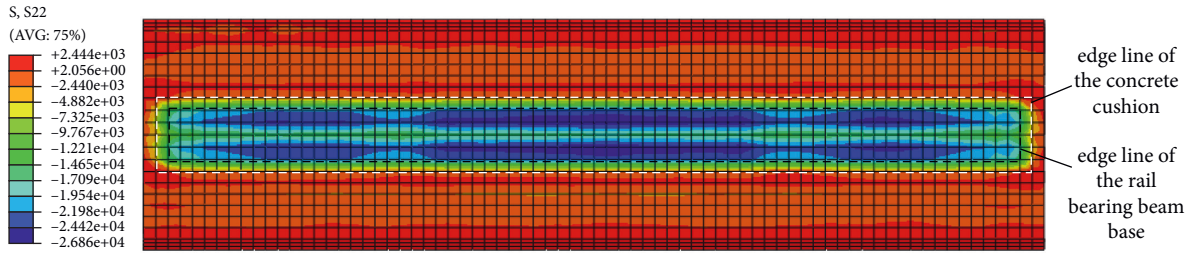

Figure 9: Cloud diagram of vertical stress distribution on the upper surface of the base bed.

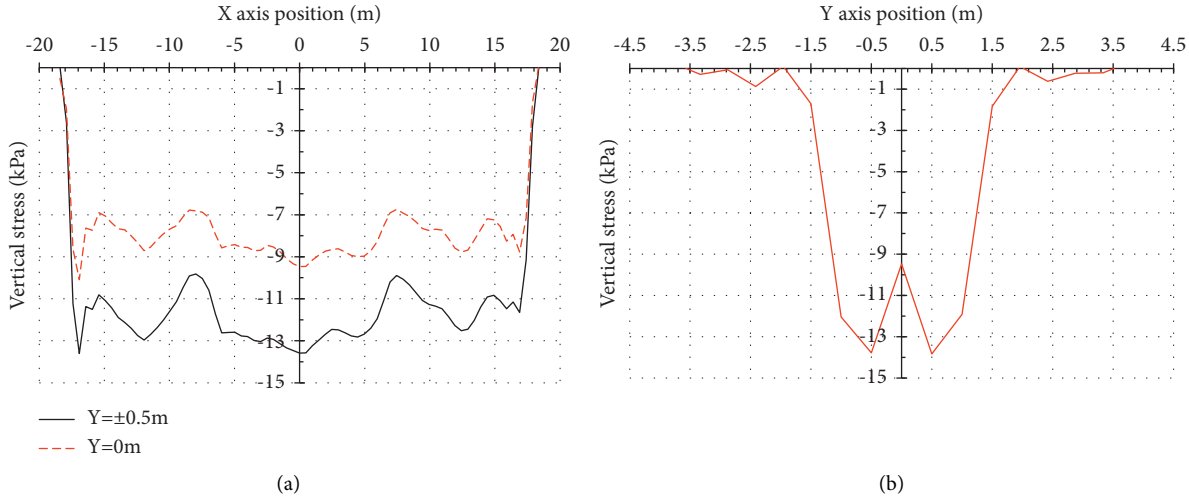

Figure 10: Curve of vertical stress distribution on the upper surface of the bed surface: (a) distributed along the X-axis (longitudinal); (b) distributed along the Y-axis (longitudinal).

direction is approximately 3 m, that is, the width of the concrete cushion. When the position exceeds 3 m, the stress rapidly decreases to less than 1.71 kPa, which is close to zero. The stress near the edge of the base ($Y = \pm 0.5$ m) is approximately 43.87% larger than the stress at the central axis ($Y = 0$). The conclusion can be drawn from the above analysis that, under the full load, the maximum stress on the surface of the subgrade is along $X = 0$ (the middle position along the longitudinal direction) and $Y = \pm 0.5$ m (the base close to the edge), and the maximum stress is approximately 13.61 kPa.

4.1.2. Dynamic Load Influence Depth. The maximum stress ($X = 0$) is chosen to intercept the cross section and study the distribution of stress along the depth direction at this time.

Figure 11 shows the distribution cloud diagram of the vertical additional dynamic stress inside the subgrade. The maximum stress occurs at the edge of the foundation on the surface of the subgrade, and the stress decreases with increasing depth. To determine the reasonable design thickness of the subgrade, the distribution data of the stress of the subgrade under self-weight and the stress along the depth under different subgrade fillings only under dynamic load were extracted. In addition, with reference to the design of the railway subgrade, according to the principle that the ratio of dynamic stress to subgrade self-weight stress is 0.2 produced by the train, Figure 12 can be acquired.

The attenuation curve of the additional dynamic stress along the depth shows that the attenuation is faster within the thickness of the substratum. When this stress reaches the bottom of the substratum (1.5 m), the stress attenuates significantly under different filler combinations. The combined stress attenuation effect of surface graded gravel + bottom gravel soil is the best. When the surface filler is the same, the stress attenuation effect decreases in turn when the bottom filler is gravelly soil, coarse-grained soil, and improved soil. From the figure, the reasonable design thickness of the foundation bed determined under the different foundation bed packing conditions and the attenuation of the stress in the range of the bottom of the foundation bed is as statistically shown in Table 4.

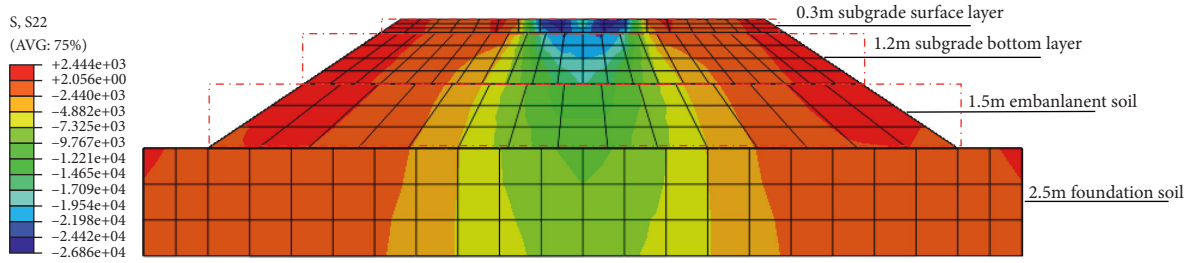

Figure 11: Cloud diagram of the vertical stress distribution of the subgrade bed.

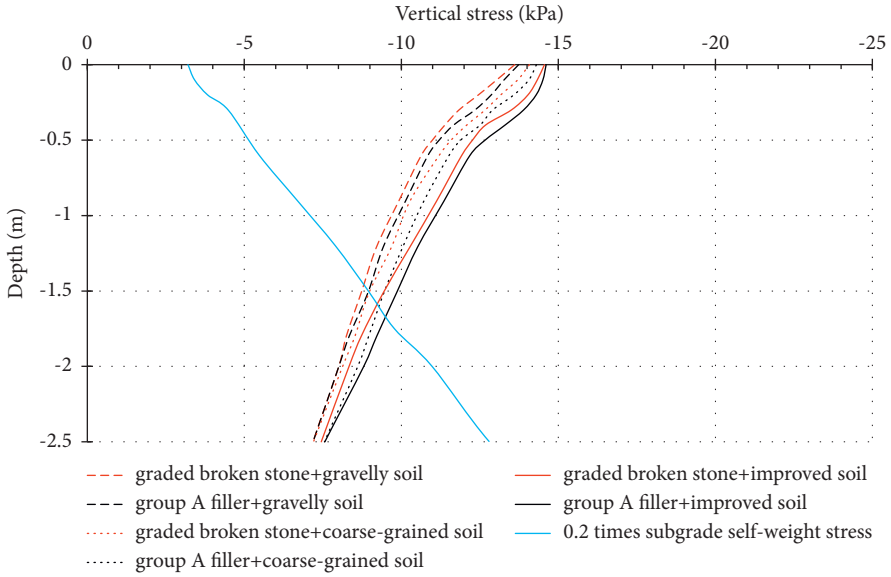

Figure 12: Vertical stress distribution curve of the subgrade bed.

Table 4: Reasonable thickness of different bed fillers.

	Working condition 1	Working condition 2	Working condition 3	Working condition 4	Working condition 5	Working condition 6
Base bed surface filler	Graded broken stone			Group a filler		
Base bed filler	Gravelly soil	Coarse-grained soil	Improved soil	Gravelly soil	Coarse-grained soil	Improved soil
Bed thickness (m)	1.46	1.50	1.59	1.49	1.60	1.70
Stress attenuation (%)	36.63	35.423	35.21	35.71	34.132	32.243

Based on the stress attenuation curve and statistics of the bed thickness table, the order of the stress attenuation effect of different bed fillers is as follows: working condition 1 > working condition 4 > working condition 2 > working condition 3 > working condition 5 > working condition 6. According to the principle that the ratio of dynamic stress to self-weight stress is 0.2, the trend in the substrate thickness is consistent with the trend in the stress attenuation effect. Therefore, the surface layer of the subgrade has the best effect with graded crushed stone + bottom gravelly soil, followed by the use of group A filler + gravelly soil on the surface.

4.2. Dynamic Deformation of the Subgrade Bed. For the deformation of the subgrade bed, the time when the middle section train acts on the middle position of the model is selected, and the deformation distribution cloud diagram of the surface of the foundation bed at this time is extracted as shown in Figure 13 The white and black dashed boxes in the figure are the concrete cushion and edge line of the rail bearing beam base, respectively. The deformation is distributed mainly in the area of the rail beam, and the base of the middle section is the main deformation position. The specific deformation distribution is as follows.

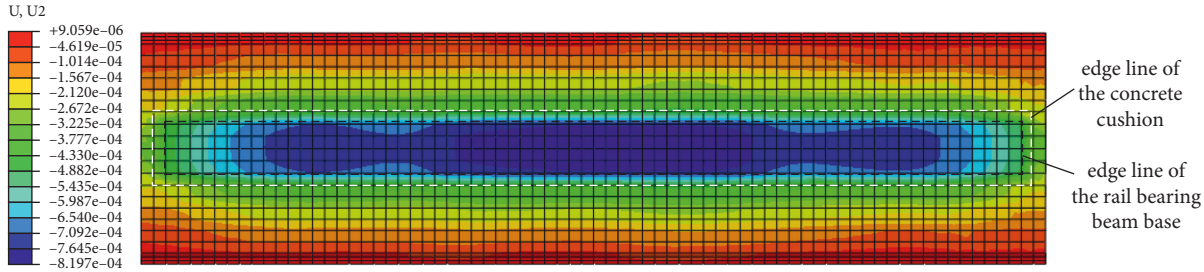

Figure 13: Deformation distribution cloud diagram of the surface of the foundation bed.

In the cloud diagram, the X-axis direction (longitudinal) has the largest surface deformation along the central axis, so this direction is used as a path to extract its deformation distribution value and is drawn on the graph. The X-axis middle position (coordinate 0) has the largest deformation value, so the cross section on this coordinate is chosen, and its deformation distribution curve along the Y-axis is extracted as shown here.

Combined with the cloud image, Figure 14 shows that there are three major deformation peaks along the X-axis, which correspond to the three-section rail beam base. The deformation of the middle section is consistent with the actual deformation, while the deformation of the base at both ends is affected to a certain extent due to the boundary effect of the model so that the deformation at both ends is smaller than that at the middle position. The deformation distribution along the Y-axis can be seen at the position of the coordinate at ±1 m, and the deformation value has a more obvious turning point on the edge of the rail beam base. The distribution within ±1 m is relatively uniform; thus, the deformation is concentrated mainly on the central axis 1 m on each side, that is, within the range of the base of the rail beam.

Statistics of the deformation of the subgrade structure under different filling conditions are shown in Table 4. Combined with the surface deformation distribution curve of the subgrade, it can be seen that the best control effect for the deformation of the subgrade is condition 1 (surface grade gravel + bottom gravel soil), followed by working condition 4 (surface layer group A filler + bottom gravel soil); the rest are working condition 2, working condition 5, working condition 3, and—finally—working condition 6.

As shown in Table 5 under working condition 1, the maximum deformation is 0.322 mm, and the deformation at the position of the expansion joint between the bases is reduced to 0.302 mm. The dynamic deformation of the working condition (condition 3, condition 6) where the bottom layer is improved soil exceeds the allowable limit of 0.4 mm. In summary, the position where the maximum deformation occurs is the X-axis origin position and the Y-axis coordinate ±0.5 m (the edge of the base), with a maximum deformation value of 0.322 mm, which meets the maximum dynamic deformation limit of 0.4 mm in the theoretical analysis.

The location that produces the largest deformation is selected, and the cross-sectional deformation distribution cloud map is shown in Figure 15 showing that the main deformation is concentrated in the range of the bed.

4.3. Dynamic Strain of the Subgrade Bed. Based on the previous analysis, the position on the surface of the foundation bed with the greatest stress and deformation is determined, as well as the distribution of stress and deformation at the cross section at this location. For another control index of the foundation bed structure, the dynamic strain is determined based on the previous theoretical analysis to determine whether the maximum dynamic strain and mean dynamic strain limits are satisfied. For this purpose, the dynamic strain distribution value along the depth is extracted and plotted on a graph as shown in Figure 14.

The attenuation law of strain along the depth direction of the surface layer and the bottom layer of the subgrade is essentially the same. The strain gradually decreases with increasing depth. However, due to the difference between the surface layer and the bottom layer, a sudden change in strain occurs at the interface. The strain of the material with little difference in the modulus of deformation changes gradually, while the strain of the material with a large difference in the modulus of the surface and bottom changes significantly. This is mainly because the dynamic stress at the interface between the surface layer and the bottom layer is continuous, so the difference in value is small. From the stress-strain relationship formula (1), when the stress is continuous, the deformation modulus has a sudden change, so the corresponding strain also produces mutations.

$$\varepsilon = \frac{\sigma}{E}, \tag{1}$$

ε is the strain, σ is the stress (MPa), and E is the deformation modulus (MPa).

The variation law of dynamic strain along the depth direction is strongly dependent on the material of the base bed under a certain load. As shown in Figure 16(a), when the surface layer is graded broken stone and group A filler, the strain values of the surface layer of the base bed are 0.0151% and 0.0173%, respectively. As the depth increases, the strain decreases. In addition, different underfills of subgrades have a certain influence on the attenuation law of surface strain. The effect can be ordered in turn as gravelly soil, grained soil, and improved soil.

The different fillers on the surface of the base bed have little effect on the strain attenuation law of the bottom layer, but when the surface layer is graded crushed stone, the strain attenuation effect is better than the working condition of the group A filler, as shown in Figure 16(b). The main influence

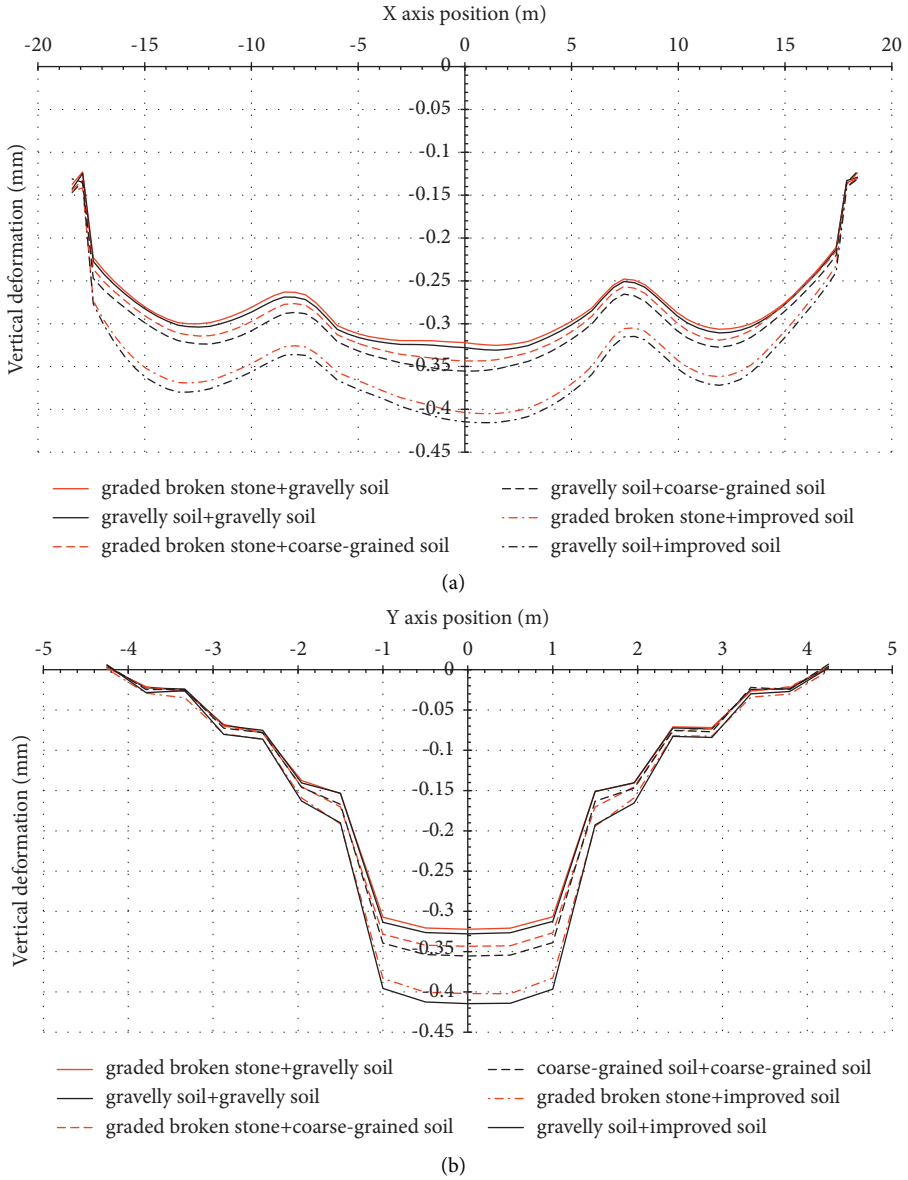

Figure 14: Deformation distribution curve of the surface layer of the subgrade: (a) distributed along the *X*-axis (longitudinal); (b) distributed along the *Y*-axis (horizontal).

Table 5: Reasonable thickness of different bed fillers.

	Working condition 1	Working condition 2	Working condition 3	Working condition 4	Working condition 5	Working condition 6
Base bed surface filler	Graded broken stone			Group A filler		
Base bed filler	Gravelly soil	Coarse-grained soil	Improved soil	Gravelly soil	Coarse-grained soil	Improved soil
Maximum deformation (mm)	0.322	0.343	0.402	0.328	0.355	0.415
Internode deformation (mm)	0.302	0.313	0.357	0.307	0.321	0.366
Dynamic deformation limit (mm)	0.4					

on the bottom layer strain attenuation law is the difference in the bottom layer filler, and the effect is significant. The maximum dynamic strain and average dynamic strain statistics of the bottom layer under different filler conditions are shown in Table 6. The maximum dynamic strain of the bottom layer under different filler conditions all satisfies

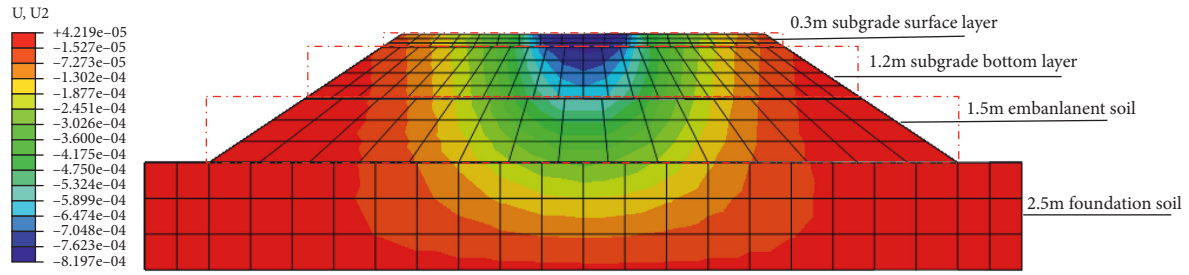

Figure 15: Deformation distribution cloud map of the cross section of the foundation bed.

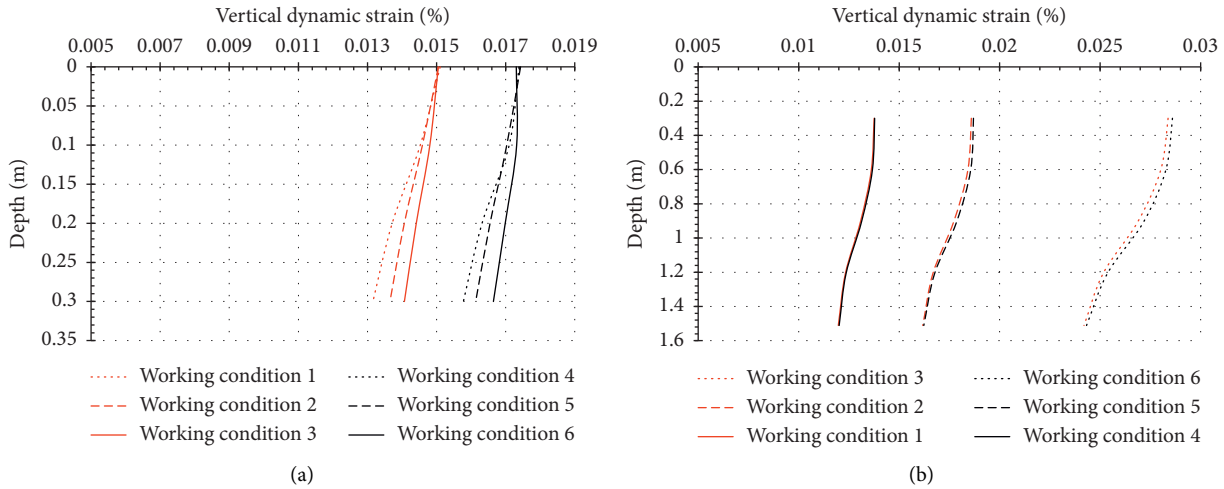

Figure 16: Strain distribution curve of the cross section of the foundation bed: (a) surface layer of the subgrade bed; (b) bottom of the subgrade bed.

the corresponding limits, while the only condition that the average dynamic strain index satisfies is that the bottom filler is gravel soil.

4.4. Influence Analysis of the Bottom Thickness of the Subgrade. In the analysis of the previous section, the feasibility of the 1.5 m thick foundation bed is verified by three indicators: dynamic stress, dynamic deformation, and dynamic strain. According to this analysis, this section mainly analyzes the influence of different base bed thicknesses. In addition, two sets of foundation bed thickness models are established: 1.2 m (0.3 m surface layer + 0.9 m bottom layer) and 1.8 m (0.3 m surface layer + 1.5 m bottom layer). The bottom layer of the foundation bed is analyzed to further reduce the impact on the dynamic response of the foundation bed. Figure 17 shows the dynamic stress, dynamic deformation, and average dynamic strain response diagrams under three bed thicknesses.

Based on the above analysis data:

(1) With increasing thickness of the bottom of the foundation bed, the dynamic stress response value of the foundation bed shows a decreasing trend. However, the reduction in the stress on the upper and lower surfaces of the foundation bed is relatively small, while the stress reduction at the bottom of the foundation bed is relatively large, indicating that the increase in the thickness of the bottom of the subgrade has a strong impact on the stress attenuation inside the bottom of the subgrade and has a certain impact on the surface of the subgrade, but the effect is small.

(2) With increasing thickness of the bottom of the foundation bed, the dynamic deformation response law inside the foundation bed exhibits a similar trend as the stress. The deformation amount of the surface layer and the interface of the foundation bed decreases, but the decreased value is small, and the decrease law of the bottom of the foundation bed is unambiguous. However, the upper and lower surfaces of the base bed have a much smaller reduction than the bottom of the base bed.

(3) For the dynamic strain response of the foundation bed, when the thickness of the foundation bed is 1.2 m, the average dynamic strain is 0.0133%, which exceeds the allowable average strain limit. With increasing thickness of the base bed, the average dynamic strain shows a significant decrease, but the value is relatively small.

(4) Comprehensive analysis shows that, with increasing thickness of the bottom layer of the subgrade, the dynamic deformation and strain response of the

Table 6: Reasonable thickness of different bed fillers.

	Working condition 1	Working condition 2	Working condition 3	Working condition 4	Working condition 5	Working condition 6
Base bed surface filler		Graded broken stone			Group A filler	
Base bed filler	Gravelly soil	Coarse-grained soil	Improved soil	Gravelly soil	Coarse-grained soil	Improved soil
Maximum of bottom (%)	0.01376	0.0186	0.0284	0.01378	0.0187	0.0286
Threshold limit (%)	0.028	0.036	0.048	0.028	0.036	0.048
Average of bottom (%)	0.01295	0.01752	0.02652	0.01299	0.01762	0.02675
Average limit (%)	0.013	0.016	0.026	0.013	0.016	0.026

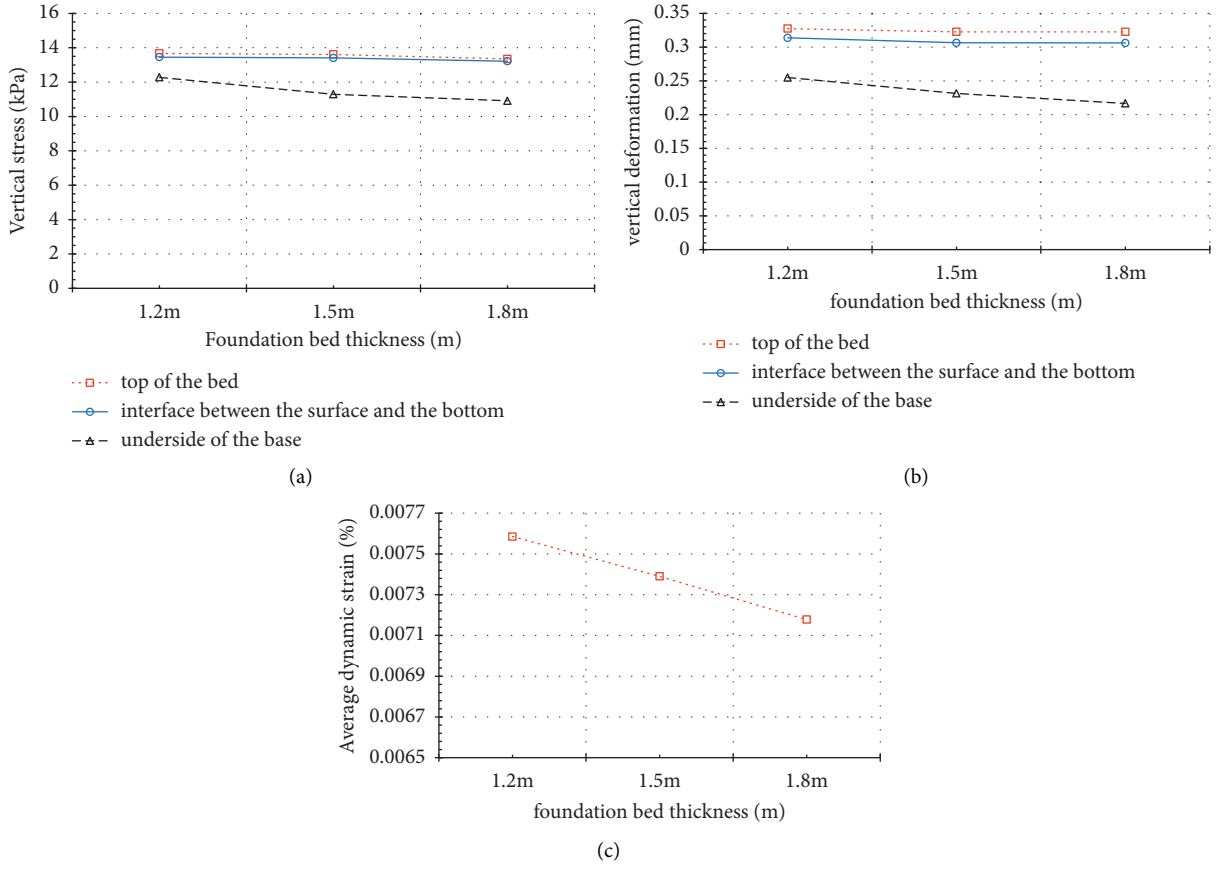

Figure 17: Strain distribution curve of the cross section of the foundation bed: (a) dynamic stress response; (b) deformation response; (c) dynamic strain response.

subgrade is unambiguous, while the dynamic stress response is relatively small.

(5) The increase in the thickness of the bottom layer of the foundation bed affects mainly the dynamic stress and dynamic deformation response within the bottom layer of the foundation bed and has relatively little effect on the surface layer of the foundation bed.

The above charts and analysis establish that, under the working condition of a 1.5 m thick bed, further changes in the bed thickness affect the dynamic response of the bed. Increasing the thickness of the bed improves the strain and stress attenuation effect of the bed; thus, the driving is safer, so no further analysis is performed here. However, reducing the thickness of the bottom layer worsens the dynamic response of the foundation bed. Here, further statistical analysis can be conducted on the indicators under the working condition of the 1.2 m foundation bed thickness. The specific conditions are shown in Table 7.

When the thickness of the bed is 1.2 m, the surface dynamic stress, dynamic deformation, maximum dynamic strain, and average dynamic strain indexes are 13.67 kPa,

Table 7: Dynamic response results of the 1.2 m thick foundation bed.

1.2 m thick foundation bed	Maximum dynamic stress (kPa)	Maximum dynamic deformation (mm)	Maximum dynamic strain (%)	Average dynamic strain (%)
Response value	13.67	0.327	0.0146	0.0133
Limit value	—	0.4	0.028	0.013

Table 8: Comparison of technical standards for an MLS Maglev structure.

Indexes for comparison		High-speed railway design codes [39]	Zhuzhou test line	Changsha maglev express line	This study
Surface layer of subgrade bed	Thickness/m	0.4 (0.7)	—	0.3	0.3
	Filler type	Graded crushed rock	Graded crushed rock	Graded crushed rock	Graded crushed rock/group A filler
Bottom layer of subgrade bed	Thickness/m	2.3	—	—	1.2
	Filler type	Group A, B filler/improved soil	Graded crushed rock	Group A, B filler	Gravelly soil

Note. The thickness of the surface layer is 0.4 m on the track of the high-speed railway without ballasts and 0.7 m on the track of a high-speed railway with ballasts.

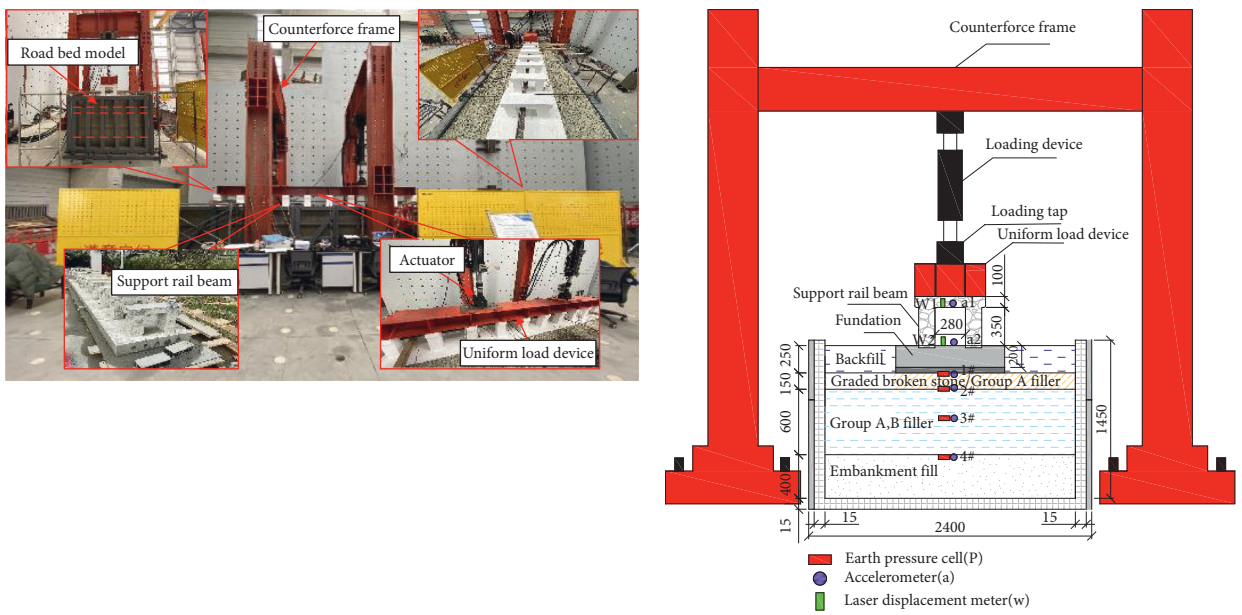

(a) (b)

Figure 18: Continued.

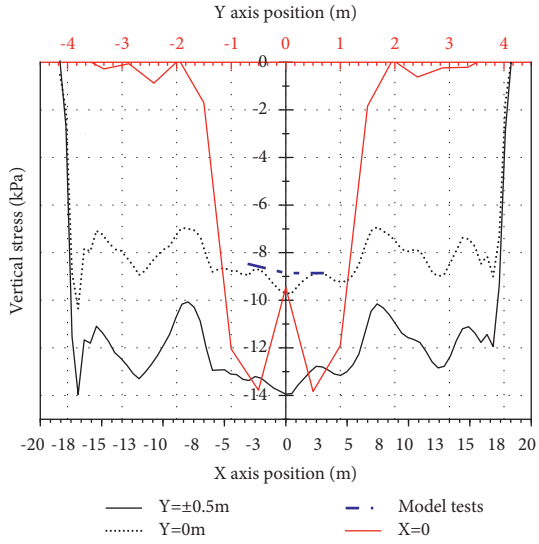

(c)

Figure 18: Comparison of model test and results: (a) Physical picture of model. (b) Schematic diagram of cross section of model test. (c) Comparison curve of vertical stress distribution on the upper surface of bed surface.

0.327 mm, 0.0146%, and 0.0133%, respectively. At this time, the average dynamic strain index is outside the specification limit. Thus, adopting this scheme has certain risks. When the thickness is increased to 1.5 m and 1.8 m, the dynamic deformation and dynamic strain of the foundation bed are improved.

5. Discussion of Results

Based on the research results of this study, the recommended indexes for the selection criteria of the subgrade bed structure thickness and subgrade filler type for the MLS maglev structure are given. The research results of this study are compared with current high-speed railway design codes and the application achievements of the Zhuzhou test line and Changsha Maglev Express Line in Table 8.

This study has reasonably optimized the relevant technical indicators of the MLS maglev subgrade bed structure and made corresponding reductions based on existing construction experience and previously reported application results. Therefore, the results of this study are more economical and reasonable.

In addition, researchers from NEDL of Southwest Jiaotong University are currently conducting research on the MLS magnetic levitation low-mounted structure roadbed bed in conjunction with the current status of research on the low-middle-speed magnetic levitation low-mounted structure roadbed bed, relying on the 2018 Science and Technology Major Project (2018-A01) "Engineering Application Research on the Complete Set of Technology of Low-Middle Speed Magnetic Levitation Transportation System" of China Railway Construction Co. model tests related to this study, as shown in Figures 18(a) and 18(b).

Since the model test related to this research is still underway, and the collection and analysis of related test data are also underway, this study only focuses on the comparison and analysis of the numerical simulation and model test on the dynamic stress of the subgrade bed. The numerical simulation coordinates corresponding to the surface stress of the subgrade bed at the position of the longitudinal center axis of the extracted model test and the position under the loading plate are shown in Figure 18(c). At the position of $X = 0$ m, the numerical simulation result is 9.46 kPa, and the model test result is 8.86 kPa; at the position of $X = \pm 3$ m, the numerical simulation results are 8.99 kPa and 8.66 kPa, and the model test results are 8.85 kPa and 8.48 kPa, which consists with the general law, indicating that the numerical model is reliable.

6. Conclusion

In this study, the numerical model of MLS maglev structure laid on the ground is established using ABAQUS, and the analysis and research are carried out, taking into account the current status of research on the roadbed of low and medium-speed maglev low placement structure. The following conclusions are obtained:

(1) By simulating the actual load, it is found that the magnitude of stress acting on the surface of the subgrade at different speeds has an insignificant influence, and the difference is within 10%. Therefore, the most unfavorable load condition (speed of 160 km/h) is used for the calculations to obtain the dynamic stress of the subgrade surface with a value of 13.61 kPa. The maximum stress occurs at the middle of the longitudinal rail bearing beam. The depth of influence of dynamic load is about 1.5 m calculated by the principle that the ratio of dynamic stress to the self-weight stress of the roadbed is 0.2. When the surface filler is group A filler, the influence depth of the bottom filler is coarse-grained soil and improved soil increases to 1.6 m and 1.7 m, respectively. When

the surface filler is graded gravel and the bottom layer is gravel soil, the influence depth of dynamic load is the smallest (1.46 m), and the stress attenuation to the bottom of the bed is about 36.63%.

(2) The distribution of dynamic deformation on the surface of the subgrade bed is uniform in the horizontal direction within the range of the base (2 m). The maximum deformation is concentrated mainly in the range of 0.5 m on both sides of the central axis, the maximum value of the dynamic deformation distribution along the longitudinal direction occurs in the middle of the rail beam position, and the deformation at the internode position is reduced. The minimum dynamic deformation is 0.322 mm for a surface filler of graded gravel and a bottom layer of gravel soil. The dynamic strain is analyzed by the two indexes of maximum dynamic strain and average dynamic strain. The maximum dynamic strain meets the limit under all working conditions, and the average dynamic strain meets the requirements except for the two working conditions where the bottom layer is gravel soil.

(3) By summarizing the working conditions determined by the above indicators, when the thickness of the base bed is 1.5 m, the surface layer is graded crushed stone or group A filler, and the bottom layer uses crushed stone soil. In this case, the bed can meet the dynamic stress, dynamic deformation, and dynamic strain indicators. The change in the thickness of the subgrade has a certain influence on the dynamic response of the subgrade. Among the relevant factors, the influence on the dynamic strain is the largest. When the thickness of 1.5 m meets the requirements, the average dynamic strain obtained by further reducing the thickness of the subgrade exceeds the limit.

Through the above conclusions, it is recommended that the thickness of the base bed is set at 1.5 m, the surface layer of filler is graded gravel or group A filler, and the bottom layer uses gravel soil.

Data Availability

The data involved are contained in the article.

Conflicts of Interest

The authors declare that they have no conflicts of interest.

Acknowledgments

This research was funded by China Railway Construction Co. Ltd, Grant no. 2018-A01, and funded by National Natural Science Foundation of China, Grant no. 51978588.

References

[1] L. Luguang Yan, "Development and application of the maglev transportation system," *IEEE Transactions on Applied Superconductivity*, vol. 18, no. 2, pp. 92–99, 2008.

[2] J. S. Wang, S. Y. Wang, Y. W. Zeng et al., "The present status of the high temperature superconducting Maglev vehicle in China," *Superconductor Science and Technology*, vol. 18, no. 2, pp. S215–S218, 2005.

[3] M. Zhai, Z. Long, and X. Li, "Calculation and evaluation of load performance of magnetic levitation system in medium-low speed maglev train," *International Journal of Applied Electromagnetics and Mechanics*, vol. 61, no. 4, pp. 519–536, 2019.

[4] Y. Sun, H. Qiang, J. Xu, and G. Lin, "Internet of Things-Based Online Condition Monitor and Improved Adaptive Fuzzy Control for a Medium-Low-Speed Maglev Train System," *IEEE Transactions on Industrial Informatics*, vol. 16, no. 4, 2020.

[5] X. Lu, Y. Li, M. Wu, J. Zuo, and W. Hu, "Rail temperature rise characteristics caused by linear eddy current brake of high-speed train," *Journal of Traffic and Transportation Engineering*, vol. 1, no. 6, pp. 448–456, 2014.

[6] J. Hu, W. Ma, X. Chen, and S. Luo, "Levitation Stability and Hopf Bifurcation of EMS Maglev Trains," *Mathematical Problems in Engineering*, vol. 2020, Article ID 2936838, 12 pages, 2020.

[7] H. Yu, J. Jiao, E. Houston, and Z. R. Peng, "Evaluating the relationship between rail transit and industrial agglomeration: an observation from the Dallas-fort worth region, TX," *Journal of Transport Geography*, vol. 67, 2018.

[8] B. Zeng, "The adaptability and the improvement in engineering of the lower - medium speed maglev transit system," *Journal of Railway Engineering Society*, vol. 33, no. 10, pp. 111–115, 2016.

[9] J. Sadeghi, H. Liravi, and M. H. Esmaeili, "Experimental investigation on loading pattern of railway concrete slabs," *Construction and Building Materials*, vol. 153, pp. 481–495, 2017.

[10] J. A. Sadeghi and M. H. Esmaeili, "Effectiveness of Track Stiffness Reduction in Attenuation of Metro Induced Vibrations Received by Historical Buildings," *Latin American Journal of Solids and Structures*, vol. 15, no. 11, 2018.

[11] P. Leng, J. Li, and Y. Jin, "Kinematics modeling and analysis of mid-low speed maglev vehicle with screw and product of exponential theory," *Symmetry*, vol. 11, no. 10, p. 1201, 2019.

[12] J. Geng, *Theory and Experimental R Esearch of Key Parameters Design on Simpliy-Supported Track Girders of Low to Medium Speed Malev line*, Southwest Jiaotong University, Sichuan, China, 2018.

[13] C. Wen-Feng, X. U. Xi-Jiang, W. U. Cheng-Jin, and Y. Ping, *Research on Key Technologies in Track Design of Zhuzhou Medium and Low Speed Maglev Transit Test Line*, Railway Standard Design, Uttar Pradesh, India, 2015, In Chinese.

[14] De Ping-Yang, J. Liu, Li. Xiao-Zhen, and Y. Ping, "Investigation of dynamic factors of low and medium speed maglev simply-supported guideway beam," *Bridge Construction*, vol. 46, no. 4, pp. 79–84, 2016, In Chinese.

[15] P. Yang, Yu-L. Zhan, Li. Xiao-Zhen, and Y. Ping, "Study of track beam stiffness of medium and low speed maglev test line," *World Bridges*, vol. 44, no. 3, pp. 58–62, 2016, In Chinese.

[16] B. S. Gao and F. Z. Xiao, "Dynamic characteristics analysis of low set line structure of medium and low speed maglev transit," *HIGH SPEED RAILWAY TECHNOLOGY*, vol. 6, no. 4, pp. 36–39+76, 2015, In Chinese.

[17] Li. Xiao-Zhen, J. Geng, D. X. Wang, X. Zhang, and L. Lin, "Study on vertical coupling vibration of low-medium speed maglev train and at-ground-structure system," *Engineering Mechanics*, vol. 34, no. 12, pp. 210–218+247, 2017, In Chinese.

[18] D.-X. Wang, *Study on Space Coupling Vibration of Low-Medium Speed Maglev Train and At-Ground structure*, Southwest Jiaotong University, Sichuan, China, 2015.
[19] Z. Ding, "Optimization of key technical standards for ground structure of Changsha maglev express," *Railway Standard Design*, vol. 63, no. 6, pp. 6–10, 2019.
[20] P. Han, "Comparison and analysis of main technical standards of Germany and China high speed railway subgrade," *Journal of Railway Engineering*, vol. 34, no. 4, pp. 21–24, 2017.
[21] D. Liang, K. Zhang, Q. Jiang, and Y. Wang, "A novel analytic method to calculate the equivalent stray capacitance of the low-speed maglev train's suspension electromagnet," *Energies*, vol. 13, no. 20, p. 5469, 2020.
[22] N. Hu, G.-L. Dai, B. Yan, and K. Liu, "Recent development of design and construction of medium and long span high-speed railway bridges in China," *Engineering Structures*, vol. 74, pp. 233–241, 2014.
[23] S. Maximov, F. Gonzalez-Montañez, R. Escarela-Perez, J. C. Olivares-Galvan, and H. Ascencion-Mestiza, "Analytical analysis of magnetic levitation systems with harmonic voltage input," *Actuators*, vol. 9, no. 3, p. 82, 2020.
[24] S. Bhowmick and G.-R. Liu, "Three dimensional CS-FEM phase-field modeling technique for brittle fracture in elastic solids," *Applied Sciences*, vol. 8, no. 12, p. 2488, 2018.
[25] O. Hibi, "Automatically operated maglev public transport line in Nagoya," *ELEKTRISCHE BAHNEN-CHARLOTTENBURG THEN BERLIN THEN MUNCHEN*, vol. 104, no. 10, p. 480, 2006.
[26] D. Y. Doh Young Park, B. C. Byung Chun Shin, and H. Hyungsuk Han, "Korea's urban maglev program," *Proceedings of the IEEE*, vol. 97, no. 11, pp. 1886–1891, 2009.
[27] J. Guardo, "Magnetic levitation transport system," *U.S. Patent Application*, vol. 301, pp. 26–4, 2007.
[28] K. Xie, *Medium and Low Speed Maglev Based on UM and ANSYS Co-simulationcoupled Vibration Analysis of Vehicle-Track Beam system*, Southwest Jiaotong University, Sichuan, China, 2019.
[29] Y. Ming, *Research on Changsha Medium and Low Speed Maglev Gauges*, Railway Standard Design, Lucknow, Uttar, vol. 63, no. 2, p. 7, 2017.
[30] Q. L. Jiang, J. S. Lian, and D. K. Yue, "Mechanical Coupling Analysis of Single EMS Module," *Journal of The China Railway Society*, 2005.
[31] S. Li-Wei, "Research on the Lightweight of the Beam of Maglev Train," *Journal of Jiamusi University(Natural ence Edition)*, 2018.
[32] Z. Lin, "Tangshan mid and low-speed maglev test line contact rail reformed——the replacement of steel-aluminum contact rail engineering practice," *Modern Urban Transit*, vol. 8, no. 1, pp. 83–92, 2012.
[33] M. Li, *Research on Coupling Vibration of Mid-low Speed Maglev Vehicle on Light Switch Steel beam*, Southwest Jiaotong University, Sichuan, China, 2018.
[34] *Code for Design of Railway Earth Structure TB10001-2016*.
[35] H. Xie, *Engineering Application of Medium and Low Speed Maglev Traffic system*, pp. 60–77, China railway publishing house CO. LTD, China, 2018.
[36] J. Sadeghi and M. H. Esmaeili, "Safe distance of cultural and historical buildings from subway lines," *Soil Dynamics and Earthquake Engineering*, vol. 96, pp. 89–103, 2017.
[37] M. H. Esmaeili, M. Naeimi, B. Soltani, and M. Afsartaha, "Reducing slab track vibrations by using asphalt concrete in the substructure," in *Proceedings of the Joint Rail Conference American Society of Mechanical Engineers (ASME)*, Columbia, SC, USA, April 2016.
[38] *Basic Technical Parameters of Changsha Maglev vehicle(CS_XT-JK-000 A)2014-04-30*.
[39] TB 10621-2014, *Code for Design of High Speed Railway*.

Hindawi
Advances in Civil Engineering
Volume 2022, Article ID 9801222, 18 pages
https://doi.org/10.1155/2022/9801222

Research Article

Axial Compression Test and Bearing Capacity Analysis of Biaxial Prestressed Angle Steel Plate Fully Wrapped Reinforced Concrete Short Column

Zhenhua Ren, Xiantao Zeng, Yaqian Shen, and Huanlin Huang

Hunan Key Laboratory for Intelligent Disaster Prevention-Mitigation and Ecological Restoration in Civil Engineering, Hunan Institute of Engineering, Xiangtan 411104, China

Correspondence should be addressed to Xiantao Zeng; xtzeng63@163.com

Received 4 November 2021; Accepted 14 March 2022; Published 9 April 2022

Academic Editor: Wenjie Ge

A new external reinforcement method is proposed in this research by using the prestressed angle steel plate to fully wrap a reinforced concrete column with a rectangular cross section. To study the axial compression characteristics of the new proposed structure, twenty pieces of the concrete columns were built using the normal reinforcement: five control columns and fifteen reinforced concrete columns, with three groups of different prestressed angle steel plates. These columns were tested under axial compression after the completion of the reinforcement. The experimental results showed that the ultimate load-bearing capacities of the three groups of the reinforced concrete columns with different prestress levels were increased by 35.6%, 52.7%, and 61.7% compared with the control columns. Both the ultimate strain and the deformation were improved significantly. The load-bearing capacity equation of the reinforced column was deduced based on the unified strength theory, and the accuracy of the equation was validated. Moreover, a finite element simulation was performed for the new structure, and the simulation results were in good agreement with the test results. Simulation results are in good agreement with the experimental results.

1. Introduction

The most direct method of concrete column reinforcement is transverse reinforcement and axial reinforcement of concrete column; the transverse reinforcement increases the cross section area of concrete, and the stress lag phenomenon exists in the material after addition. Axial reinforcement also increases the transverse dimensions of concrete columns. The prestressed strip reinforcement method can overcome the stress and strain lag and enhance the reinforcement effect; the concrete column is strengthened by applying prestress to the transverse constraint, which makes the concrete in the active three-way compression state, gives full play to its bearing capacity, and then improves the bearing capacity and deformation performance of the concrete column; however, the poor force transmission performance at the joint surface will lead to the poor force of the whole specimen.

Similar to the prestressed strip method, the reinforcement method of using a prestressed angle steel plate for a concrete column with a rectangular cross section was invented by Ren et al. [1]. They conducted a theoretical analysis on the load-bearing capacity of a reinforced concrete column to obtain the calculation formula for short columns. It is well known that a circular concrete column covered with a steel tube has the advantages of high bearing capacity, good seismic performance, light structural weight, and great convenience for construction [2]. A reinforced concrete column using a prestressed angle steel plate has all the advantages of a concrete column covered by a steel tube. Therefore, the research on the axial compression performance of a steel-tube concrete column is the prerequisite for understanding the performance of an angle steel plate's concrete column. Liang et al. [3] analyzed the ultimate bearing capacity of a steel tube by using thick-wall cylinder theory and double-shear unified strength theory, and they

analyzed the load-bearing capacity of a concrete column by using the Drucker-Prager yield theory with the constraint of a steel tube. Their analysis focused on the axially loaded condition of a short concrete column, and they considered the contribution of the vertical stress of a steel tube in a state of yielding to the load-bearing capacity. Their result provided a new method for calculating the ultimate bearing capacity of circular-steel-tube short concrete columns under axial compression. Qin et al. [4] studied the impacts of the concrete strength grade, the steel pipe wall thickness, and the additional amount of steel fiber on the load-carrying performance of short concrete columns. Their research results showed that as the strength grade of the concrete core increased, the ductility of the column deteriorated, and the steel tube could effectively prevent further damage to the concrete core. Moreover, the addition of steel fibers could significantly improve the ultimate strength and the load-bearing capacity in the stationary stage of a steel-tube concrete column. As the steel content in the steel tube increased, the protective constraint effect for the concrete core was enhanced.

Many scholars have investigated reinforced steel-tube concrete columns in recent years. Han et al. [5] conducted experimental research and a theoretical analysis on the axial compression performance of a reinforced steel-tube concrete column. They studied the mechanical behavior, deformation capacity, and failure mode of a short concrete column, and they provided the experimental results for the deformation and ultimate load-bearing capacity, as well as a calculation method for the axial load-bearing capacity. Lu et al. [6] and Gao et al. [7] studied the impacts of various parameters on the load-bearing capacity and ductility of this type of concrete column. They found that different reinforcement methods, the steel tube's wall thickness, and the fly ash replacement ratio had significant impacts on the load-bearing capacity and ductility of the concrete column. Hu [8] carried out axial compression and bias compression failure tests as well as finite element analysis on the load-bearing capacity of a reinforced steel-tube concrete column, and Hu proposed a calculation method for the axial compression load-bearing capacity considering the effect of the initial stress.

The reinforcement method for winding reinforced polymer fibers [9–12] has the advantages of high efficiency, high strength, convenient construction, strong corrosion resistance, wide applications, and small impacts on a structure. Ma et al. [13] carried out comparison tests with axial compression for reinforced circular concrete columns that were wrapped by carbon fiber-reinforced polymers (CFRP) for concrete in a strength range of C40 to C60. They found that the CFRP could effectively constrain the concrete column and improve the compressive properties of the concrete. They also proposed a calculation model for the ultimate compressive strength of the axial compression and the peak strain for a CFRP constrained concrete column. Moreover, they developed a stress-strain relationship model to analyze the improvement effect of the CFRP constraint on the axial compression load-bearing capacity of the concrete column. They analyzed the influences of different factors on the energy density for the axial compression failure of the CFRP concrete column. However, because polymer fiber cloth is a type of anisotropic material, its strength and elastic modulus in the fiber direction are much greater than those in the perpendicular direction. Therefore, this material cannot significantly improve the ultimate load-bearing capacity of a reinforced concrete column.

The reinforcement method of using a prestressed steel strip [14–16] can further improve the load-bearing capacity and deformation performance of a concrete column. Zhang et al. [17] conducted experiments on the mechanical properties of this type of concrete column and found that the failure mode of this type of column was basically the same as that of an unreinforced specimen, while the load for generating the initial crack was higher for the reinforced specimen. Additionally, the prestressed steel strip could significantly enhance the axial stiffness of the reinforced specimen during compression and greatly improve the deformation resistance capability during biased compression.

The rectangular reinforced concrete column with the prestressed angle steel plate is a new product invented by the authors. Its cross section is shown in Figure 1. It is composed of four pieces of angle steel plates that can essentially wrap an entire concrete column. The four sides of each angle steel plate are provided with flanges. The circumferential prestress is applied to the concrete column via the axial flange bolts on the angle steel plate to make the four steel plates and the concrete column into a new structure similar to the steel-tube concrete column. The circumferential constraints given by the angle steel plates can improve the load-bearing capacity of the concrete column. This new reinforcement method has been granted a national invention patent in China (patent no. ZL201610919619.1). The structure is novel in design, and there has been no published research on its performance.

2. Materials and Methods

2.1. Materials and Specimen Design. The design strength grade of the concrete used in the test was C30. According to the *Standard for Test Method of Mechanical Properties on Ordinary Concrete* (GB/T50081-2016) [18], the same batch of the concrete as the rectangular column specimens was selected to conduct the compressive property test. The average compressive strength of the concrete was 30.75 MPa.

The concrete column had a square cross section with a side length of 220 mm and a height of 1000 mm. It was a short column with a slenderness ratio of 4.5, as shown in Figure 2(a). A total of twenty columns were designed for the test, among which five control columns were denoted as CC, and the remaining fifteen columns were divided into three groups of concrete columns having different prestress levels, denoted as RC0, RC2, and RC3.

As shown in Figure 2(b), the material 8Φ12HRBE400E was used for longitudinal reinforcement. According to the *Test Methods of Steel for Reinforcement of Concrete* (GB/T28900-2012), the yield strength of the longitudinal reinforcement was 380 MPa. The material Φ6HPB300 was used for the stirrup with spacing $s = 65$ mm. The yield strength of the stirrup was 275 MPa.

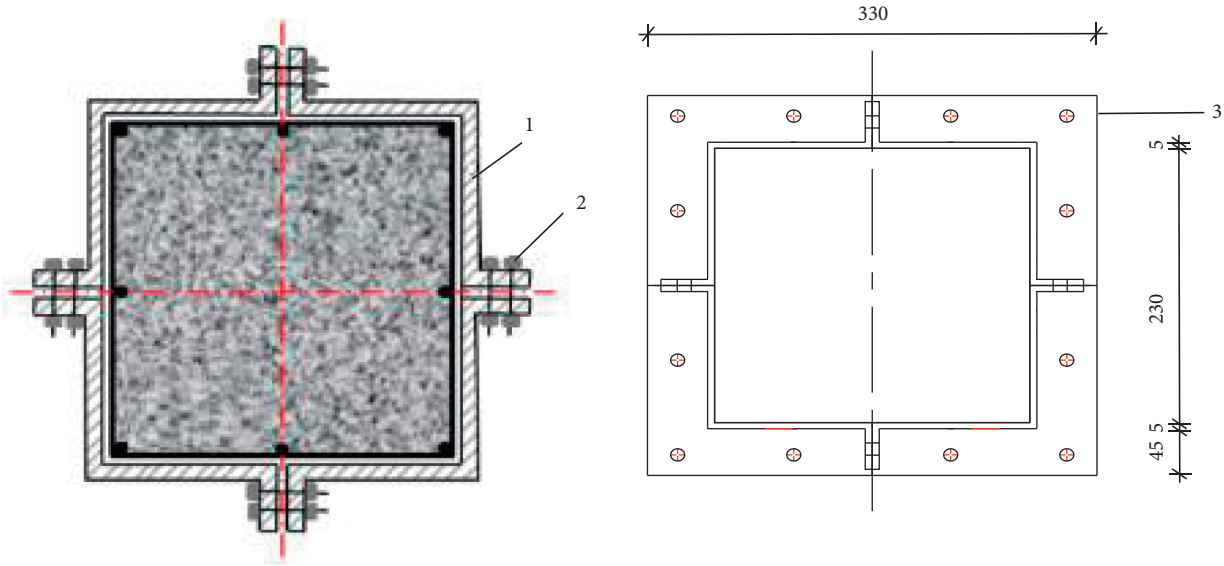

Figure 1: Schematic diagram of reinforcement method.

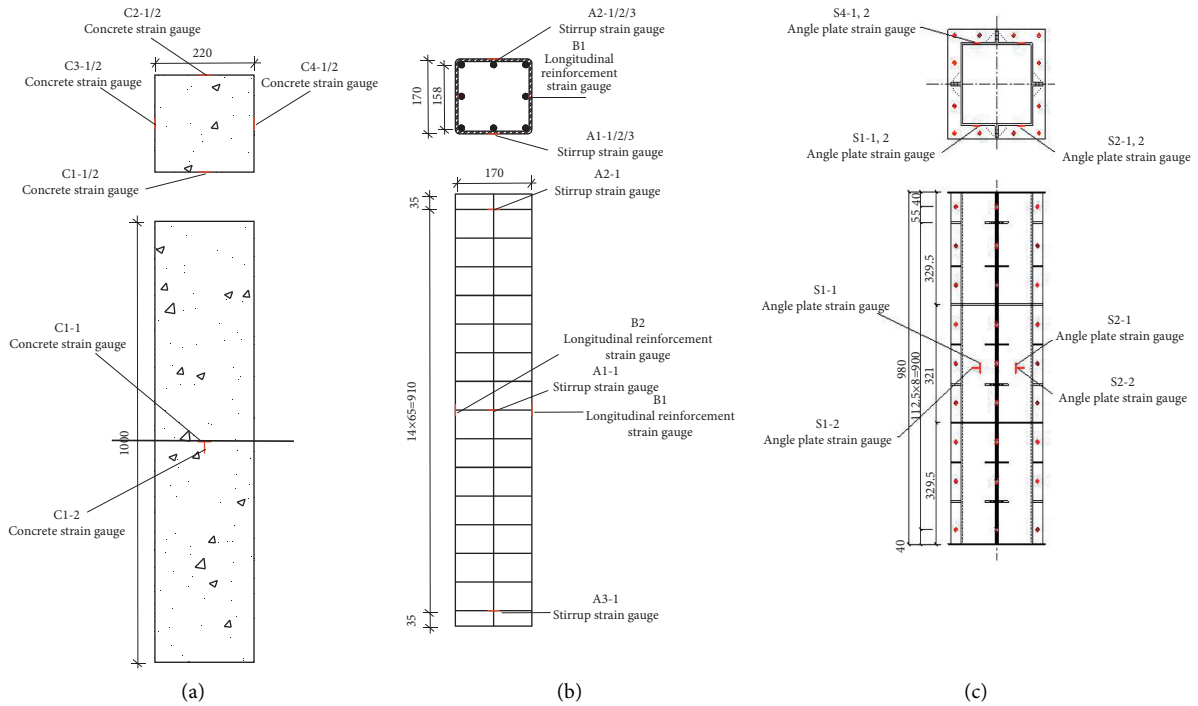

Figure 2: Details of specimens. (a) Concrete. (b) Steel bar. (c) Angle steel plate.

As shown in Figure 2(c), the steel type of the angle steel plate was Q235, the length was 980 mm, and the steel plate thickness was 5 mm. Each single column was strengthened by four pieces of angle steel plates. The four sides of each angle steel plate had flanges and bolt holes. The bolts used in the connections were 8.8 Grade M12 with a diameter of 12 mm. Nine bolts were arranged longitudinally at the joint of the angle steel plate's flange, and a total of 36 bolts were required for each concrete column. To ensure that the circumferential prestress was exerted by the angle steel plates to the concrete column, the four plates did not form a complete square cross section after being closed, and a 6 mm gap was reserved between two adjacent plates, as shown in Figure 2.

Four groups of axial compression tests for the short columns reinforced with the prestressed steel plates were carried out, including the following:

(1) Control column tests without reinforcement

(2) Prestressed column tests including the three following schemes

Scheme 1. The steel plate was fastened on the column without the prestress. The bolts were gently tightened with an ordinary wrench to make the steel plate barely stick to the concrete column. This scheme essentially reflected a reinforced concrete column covered by a steel sleeve.

Scheme 2. The confining pressure of the steel plate on the concrete column was the same as that of the stirrup inside the column on the concrete core, as shown in Figure 3; that is, $\sigma_{r1} = \sigma_{r2}$ (σ_{r1} and σ_{r2} are shown in Figures 3(b) and 3(f), where σ_{r1} is the confining pressure of the steel plate on the concrete column). The wall thickness of the steel plate was much less than the side length of the concrete column. The steel plate thickness was $t = 5$ mm. The cross-sectional area of the steel plate wall was $A_{s1} = 4400\,\text{mm}^2$. The column side length was $b0 = 220$ mm. The concrete column's protective layer thickness was 25 mm. The side length of the concrete core (i.e., the spacing within the stirrup) was 158 mm. The concrete core area was $A_{cor} = 24964\,\text{mm}^2$. The cross-sectional area of the concrete column was $A = 48400\,\text{mm}^2$. The converted area of the stirrup was $A_{ss0} = 274.77\,\text{mm}^2$. Therefore, the constraint stress σ_{r2} of the stirrup acting on the concrete core of the column was calculated with [19]

$$\sigma_{r2} = \frac{f_{yv} \cdot A_{ss0}}{2A_{cor}} = \frac{270 \times 274.77}{2 \times 24964} = 1.49\,\frac{\text{N}}{\text{mm}^2}, \quad (1)$$

where f_{yv} is the design value of the stirrup's tensile strength: $f_{yv} = 270$ MPa. When the confining pressure given by the steel plate to the column was equal to the confining pressure given by the stirrup to the concrete core, there was the following relationship:

$$\sigma_{r1} = \sigma_{r2}. \quad (2)$$

The circumferential tensile stress in the steel plate could be calculated as follows:

$$\sigma_\theta = 2\sigma_{r2}\frac{A}{A_{s1}} = 2 \times 1.49 \times \frac{48400}{4400} = 32.78\,\frac{\text{N}}{\text{mm}^2}. \quad (3)$$

Scheme 3. : The prestress was designed to be the same as the design value of the tensile strength of the fastening bolt. The tensile force sustained by the steel plate was greater than that in Scheme 2. It was assumed that the design value of the axial tensile bearing capacity of a single bolt was N_t^b. Then

$$N_t^b = A_{\text{eff}} f_t^b = 84.3 \times 400 = 33270N, \quad (4)$$

where A_{eff} is the cross-sectional area under the stress of a single bolt: $A_{\text{eff}} = 84.3\,\text{mm}^2$. The parameter f_t^b is the designed tensile strength of the bolt: $f_{\text{t}}^b = 400$ MPa. The number of bolts in each row on the steel plate was nine. Therefore,

$$\sigma_\theta = \frac{N_t^b \times 9}{t \cdot l} = \frac{33270 \times 9}{5 \times 980} = 61.11\,\frac{\text{N}}{\text{mm}^2}, \quad (5)$$

where t is the steel plate thickness: $t = 5$ mm; l is the steel plate height: $l = 980$ mm. The grouping of the test specimens and their prestress values are listed in Table 1.

2.2. Specimen Preparation. The specimen procurement is shown in Figure 4. The steel bars were cut, welded, and bent according to the specification requirements. The processed steel bars were welded and bundled with wires. The leveling steel pad was welded. The steel bars were ground. The strain gauges were pasted on the steel bars and numbered. The concrete was stirred and prepared according to the requirement of the mixture ratio. The concrete prototype was fully vibrated and compacted after pouring and underwent standard concrete curing of 28 days. Water was sprayed on the concrete once every hour in the early stage, once every three hours in the middle stage, and once every five hours in the late stage. After the concrete specimens reached the standard curing period, they were treated with experimental preprocessing procedures such as top leveling and attaching concrete strain gauges and then used in the experiment.

2.3. Loading Program. The YAJ-10000 computer-controlled large electrohydraulic servo compression and shear test machine in the Structure Laboratory of the Construction Engineering Test Center at Zhongnan Forestry University was used in the experiment. It was used to carry out the axial compression test for the short rectangular concrete columns reinforced with prestressed steel plates. The strain gauge measurement locations were on the upper, middle, and lower parts of the concrete columns, as well as on the longitudinal steel bars, the stirrups, the concrete surface, and the outer surfaces of the steel plates. On each concrete column, there were two strain gauge measurement locations on each longitudinal steel bar, six locations on the stirrup, and either four locations on the concrete surface of the control column or four locations on the outer surfaces of the steel plates of the reinforced column. There were twelve strain gauge measurement locations in total. The load was applied in the test according to the Standard for *Test Method of Concrete Structures* (GB/T50152-2012). There were three stages in the test:

(i) Preloading stage: The specimen was first placed in the center of the test device to avoid eccentric compression. The preload was set at 10% of the estimated ultimate load level. The purpose of this stage was to check the safety and reliability of the loading device, check for any abnormal functions of the instrument, and adjust the specimen for mechanical alignment and automatic leveling.

(ii) Standard loading stage: The load was applied with a loading rate of 2 kN/s at the seven following steps: 20%, 40%, 60%, 70%, 80%, 90%, and 95% of the predicted ultimate load level. Each step was held for five minutes.

(iii) Destruction stage: After the load reached 95% of the ultimate load level, the load was not added in steps. Instead, the load was added by displacement control with continuous data acquisition. The load was further increased at a rate of 1 kN/s until the specimen was destroyed. When the load reading on the dial of the test machine decreased sharply, the

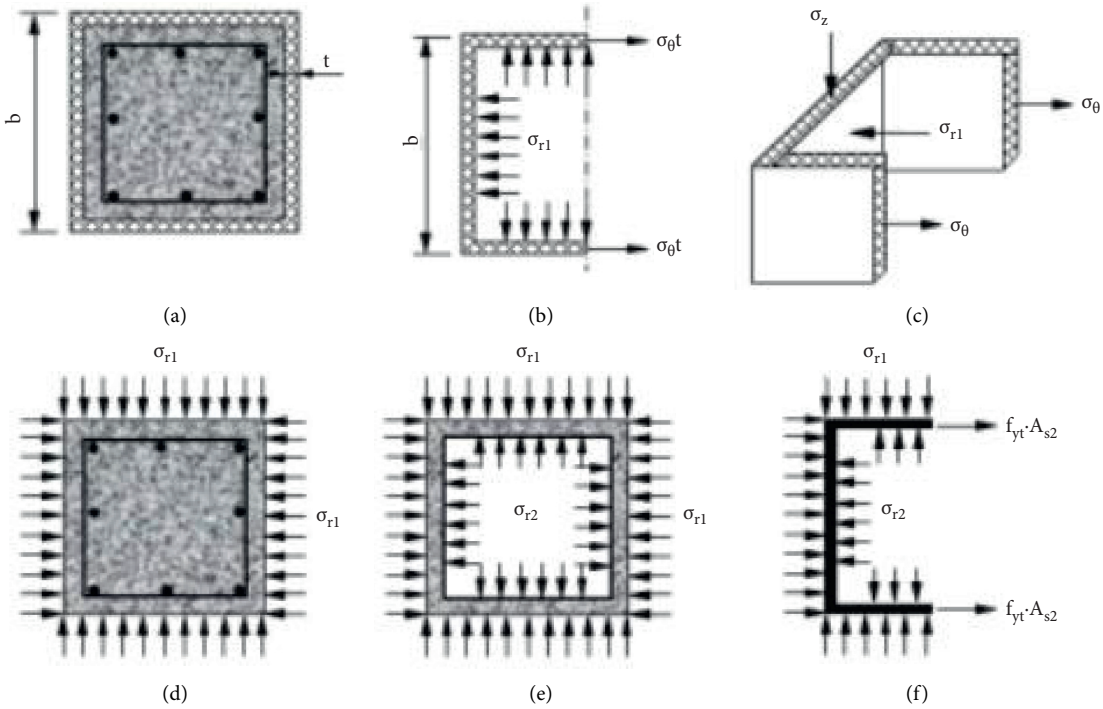

Figure 3: Stress diagram after reinforcement. (a) Column section. (b) Angle plate plane stress. (c) Stereoscopic loading of angle plates. (d) Section overall stress. (e) Protective layer stress. (f) Force of stirrup.

Table 1: Details of specimens.

Methods	Number	Scheme	σ_θ (MPa)	Quantity (pillar)
No reinforcement	RC-1	No angle steel plate	0	5
Reinforcement	RC-2-1	Scheme 1	0	5
	RC-2-2	Scheme 2	32.78	5
	RC-2-3	Scheme 3	61.11	5
Total				20

specimen was close to its ultimate load state and the test was ended. The test loading device is shown in Figure 5.

3. Experimental Results and Phenomena

3.1. Experimental Results. The main test results of the reinforced concrete columns are shown in Table 2. The ultimate load of group RC0 increased by 35.6% on average, and the ultimate load-bearing capacity increased by 43.2% at most. The ultimate load of group RC2 increased by 52.7% on average, and the ultimate load-bearing capacity increased by 56.5% at most. The ultimate load of group RC3 increased by 61.7% on average, and the ultimate load-bearing capacity increased by 73.4% at most. As the prestress increased continuously, the ultimate load-bearing capacity increased significantly. The failure location in the concrete column was mainly concentrated in the middle and lower parts of the column. The steel plates and flanges of groups RC2 and RC3 were deformed and bent, and their bolts began to yield. Because there was a gap between the flanges, the concrete and the steel plate squeezed each other during the axial compression process, resulting in the most serious broken event for the concrete in the gap. Therefore, the concrete in the flange gap was the weak link for compression damage.

3.2. Experimental Phenomena. The concrete column's failure stages in the test included the following: (1) The reinforcement steel bars had yield failures, resulting in a stripping phenomenon between the concrete and the steel bars. (2) The concrete was crushed in a large area, resulting in the bending of the steel plate with the extrusion of the concrete. (3) The concrete completely lost its load-bearing capacity, resulting in deformations in the steel plate's belly and the flange as well as yielding of some bolts.

The control columns were the specimens without reinforcement. In their initial loading stage, the reinforcement steel bars and the concrete were both in the elastic range, and the compressive strain increased uniformly. When the load was increased to approximately 30% of the ultimate load level, subtle longitudinal cracks began to appear at both ends of the column around the corners. When the load was increased to approximately 85% of the ultimate load level,

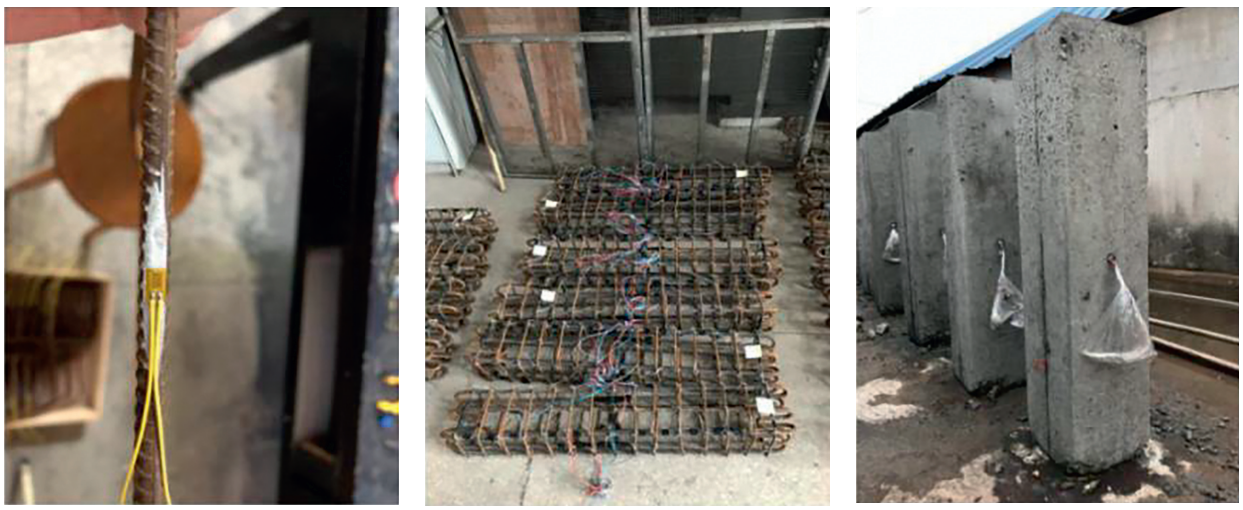

(a) (b) (c)

Figure 4: Process of specimen fabrication. (a) Bonding strain gauges. (b) Reinforcement cage processing. (c) Room temperature maintenance of concrete.

there was an obvious cracking sound and the cracks gradually became wide and extended continuously to the middle. When the load was close to the failure load level, the surface layer of the concrete began to peel off slowly along the cracks, and most of the concrete at the column's corners was crushed. Additionally, the load reading in the dial of the test machine decreased sharply and the specimen was destroyed. These processes are shown in Figure 6(a).

The RC0 column specimens were strengthened by the zero prestress in the steel plates. In the initial loading stage, the concrete column was in the elastic range, and the compressive strain increased uniformly. The load-displacement curve was linear and ascending. The specimen did not have obvious changes in appearance. When the load increased, the concrete column began to have a subtle cracking sound. When the load was increased to approximately 30% of the ultimate load level, the cracking sound was heard everywhere, but the steel plate on the outer surface had no obvious changes.

When the load was increased to approximately 80%, the cracking sound of the concrete core was heard, along with the shooting sound of the cracks when they hit the steel plates. Until the specimen was destroyed, the steel plates did not change significantly, and the upper and lower ends of the reserved compression height of 10 mm were completely pressed. The steel plates were taken off after the load was removed. Obvious cracks were noticed on both sides of the concrete column. When the concrete was struck with a hammer, the concrete in the crushed area immediately peeled off. These processes are shown in Figure 6(b).

The RC2 column specimens were equivalent to the stirrup-reinforced concrete column. In their initial loading stage, the performance of the specimens was similar to that of RC0. When the load was increased to 90%, there were no obvious changes in the steel plates, but the flanges began to be partially stretched and bent. After the load was removed and the steel plates were taken off, it was found that the concrete in the flange gap was seriously damaged. There were obvious and widespread cracks on both sides of the concrete. When the concrete was struck by a rubber hammer, the concrete in the crushed area immediately peeled off. These processes are shown in Figures 6(c) and 6(e).

The RC3 column specimens were designed to have the prestress equal to the design value of the tensile strength of the fastening bolt. In their initial loading stage, the performance of the specimens was similar to that of RC2. When the load was increased to 90%, the steel plate started to have slight bending, and the flanges of the steel plates were seriously strained and bent. Moreover, some bolts reached their yield strength and the damaged bolts jumped out of the screw holes due to the yield fracture. After the load was removed and the steel plates were disassembled, it was found that the concrete in the flange gap was seriously damaged in a powder form. There were obvious and widespread cracks on both sides of the concrete. When the concrete was struck with a hammer, the concrete in the crushed area immediately peeled off. These processes are shown in Figures 6(d) and 6(f).

4. Bearing Capacity Analysis of the New Structure

One control group and three test groups were arranged in the experiment, namely, CC, RC0, RC2, and RC3. The impacts of the prestressed steel plates on the compressive properties of the reinforced concrete columns were studied. According to Table 2, the average test value of each group of specimens was taken. Compared with groups CC, RC0, and RC2, group RC3 increased the load-bearing capacities by 61.7%, 19.2%, and 5.9%, respectively, demonstrating the most significant reinforcement effect. Compared with groups CC and RC0, group RC2 increased the load-bearing capacities by 52.7% and 12.6%, respectively. Compared with group CC, group RC0 increased the load-bearing capacity by

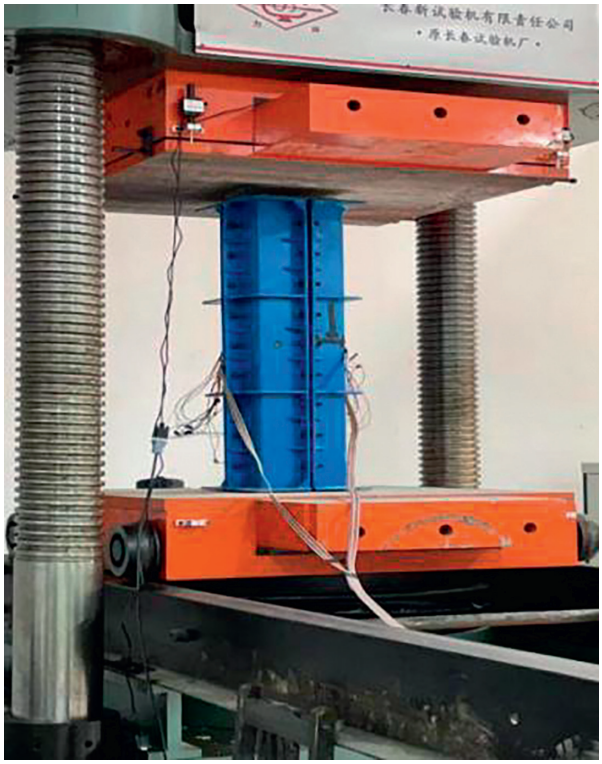

Figure 5: Testing machine.

Table 2: Main results of the test.

Number	N_u(kN)	Increase rate (%)	Failure mode
CC-1	1534	—	Cover concrete spalling, concrete crushing
CC-2	1270	—	
CC-3	1402	—	
CC-4	1445	—	
CC-5	1398	—	
RC0-1	1814	28.7	Steel bar bending, concrete crushing
RC0-2	1853	31.4	
RC0-3	1941	37.7	
RC0-4	1934	37.2	
RC0-5	2019	43.2	
RC2-1	2152	52.6	Axial compression failure of column and deformation of angle plate
RC2-2	2026	43.7	
RC2-3	2181	54.7	
RC2-4	2196	55.8	
RC2-5	2206	56.5	
RC3-1	2444	73.4	Axial compression failure of column, deformation of angle plate and yield of bolt
RC3-2	2443	73.3	
RC3-3	2172	54.1	
RC3-4	2106	49.4	
RC3-5	2233	58.4	

35.6%. The compressive load-bearing capacity of reinforced concrete columns with prestressed steel plates has not been investigated by previous researchers. The authors analyzed the axial compression mechanisms based on their invention patent and the unified strength theory for short column with the longitudinal reinforcement, stirrup, and steel plates. The roles of the steel plate and stirrup in constraining the concrete were studied. A calculation formula for the axial bearing capacity was derived. The calculation results were compared with the test results to validate the formula.

In 1991, Yu established a unified strength theory applicable to different materials based on the double-shear strength theory, using a double-shear element as the mechanics model and considering the influence of the intermediate principal stress. Its mathematical expression is as follows [20]:

(a) (b) (c)

(d) (e) (f)

Figure 6: Failure modes of typical specimens. (a) CC-2. (b) RC0-1. (c) RC2-2. (d) RC3-1. (e) RC2-2. (f) RC3-1.

$$\left.\begin{aligned} F &= \sigma_1 - \frac{\alpha}{1+\beta}\left(\beta\sigma_2 + \sigma_3\right) = \sigma_{ts}\sigma_2 \le \frac{\sigma_1 + \alpha\sigma_3}{1+\alpha} \\ F' &= \frac{1}{1+\beta}\left(\sigma_1 + \beta\sigma_2\right) - \alpha\sigma_3 = \sigma_{ts}\sigma_2 \ge \frac{\sigma_1 + \alpha\sigma_3}{1+\alpha} \\ \beta &= \frac{(1+\alpha)\tau_s - \sigma_{ts}}{\sigma_{ts} - \tau_s} = \frac{1+\alpha-B}{B-1} \\ a &= \frac{\sigma_{ts}}{\sigma_{cs}} B = \frac{\sigma_{ts}}{\tau_s} \end{aligned}\right\}, \quad (6)$$

where F, F' is the theoretical function of principal stress intensity. σ_1, σ_2, and σ_3 are the first, second, and third principal stresses, taking tensile stress as positive and compressive stress as negative. σ_{ts}, σ_{cs}, and τ_s are tensile yield strength, compressive yield strength, and shear yield strength of materials, respectively. β is the weighted parameter reflecting the influence of the intermediate shear stress and the corresponding normal stress on the material yield or failure, $0 \le \beta \le 1$. B is the shear stress coefficient.

4.1. Stress Mechanisms. When the concrete column was reinforced by the angle steel plate or the prestressed angle steel plate, the column was similar to the reinforced concrete column with the square steel tube. Its structural process and cross section are shown in Figure 3. It was a column with prestressed confining pressure. The differences between this column and the square-steel-tube concrete column included the following: (1) The four steel plates were prestressed, and the prestress could be adjusted according to the need. (2) The square steel sleeve formed by the four steel plates had no forces in the axial direction of the column. (3) There were gaps in the flange connections of the four steel plates. (4) The concrete column was reinforced by steel bars, and the addition of the four steel plates formed a steel sleeve around the concrete column.

The stress mechanisms of the short concrete column with the steel plates under axial compression were as follows. The concrete core was in a triaxial stress state subject to the constraints of the steel plates and the stirrup. The outer layer of the concrete between the steel plate and the stirrup was constrained by the steel plate and in a triaxial state. The prestressed steel plates were added to the reinforced concrete column. The axial pressure was almost zero. There was tensile stress in the circumferential direction. There was

compression stress (prestress) in the radial direction. The longitudinal steel bars were subject to axial compression.

4.2. Stress in the Angle Steel Plate. As shown in Figure 3, the thickness of the steel plate was t, and the confining pressure of the steel plate on the concrete column was σ_{r1}. The loading condition of the steel plate is shown in Figures 3(b) and 3(c). Because the steel plate could not be pushed too tightly at both ends of the concrete column, the axial compressive stress of the steel plate could be assumed to be. The radial compressive stress was σ_{r1}, and the tensile stress was σ_θ. Then

$$\begin{aligned} \sigma_z &= \frac{N_1}{A_{s1}} = 0, \\ \sigma_{r1} &= -\sigma_r \\ \sigma_\theta &= \frac{\sigma_{r1} b}{2t}, \end{aligned} \tag{7}$$

where N_1 is the axial pressure sustained by the steel plate, which could be approximately zero. As_1 is the cross-sectional area of the steel plate, which was approximately equal to. The parameter is the lateral constraint stress produced by the steel plate on the concrete. The parameter b is twice the width of the steel plate. The parameter t is the wall thickness of the steel plate. The steel plate used for concrete columns is generally very thin, satisfying $b/t \geq 20$, and hence can be regarded as a thin-walled steel pipe, and $|\sigma_r|/\sigma_\theta = (2t/b) \ll 1$, $|\sigma_r| \ll \sigma_\theta$. According to the operating principle of the steel plate, as the concrete strain continuously developed, the circumferential tensile stress σ_θ of the steel plate increased, and the axial compressive stress σ_z gradually decreased. The loading condition of the steel plate changed from mainly sustaining the axial compressive stress to mainly bearing the circumferential tensile stress, and $\sigma_\theta > \sigma_z$. Therefore, the principal stress of the thin-walled steel pipe was

$$\sigma_1 = \sigma_\theta \quad \sigma_2 = \sigma_{r1}\, \sigma_3 = \sigma_z. \tag{8}$$

Substituting the above equation into the discriminant formula of the unified strength theory produced

$$\frac{\sigma_1 + \alpha\sigma_3}{1+\alpha} = \frac{\sigma_\theta + \alpha\sigma_z}{1+\alpha} > 0 > \sigma_2 = \sigma_{r1}. \tag{9}$$

Equation (1) of the unified strength theory was used in combination with Equation (2) and the three principal stresses. The following simplified formula was obtained:

$$\sigma_z = -\frac{1+\beta}{\alpha}\left[\sigma_{ts} - \left(\frac{b}{2t} + \frac{\alpha\beta}{1+\beta}\right)\sigma_{r1}\right]. \tag{10}$$

$$N_1 = \sigma_z A_{s1}. \tag{11}$$

Normally, σ_z is 0, so N_1 is 0.

4.3. Stirrup Stress. The stress conditions of the stirrup and the concrete core in the column are shown in Figure 3(f). When the axial distance between the continuous spiral stirrups or the octagonal stirrups in the compressed column was small, the concrete core could be effectively constrained, and the constrained stress was [21]

$$\sigma_{r2} = \frac{2 f_{yt} \cdot A_{s2}}{s \cdot b_{\text{cor}}}, \tag{12}$$

where σ_{r2} is the constraint stress generated by the stirrup acting on the concrete core, and f_{yt} and A_{s2} are the yield strength and the cross-sectional area of the stirrup, respectively. The parameters s and b_{cor} are the longitudinal spacing and the inner diameter of the stirrup, respectively. Because the force exerted by the steel plate on the stirrup through the protective layer of the concrete was σ_{r1}, the following relationship was obtained from the force balance shown in Figure 3(f):

$$\begin{aligned} (\sigma_{r2} - \sigma_{r1}) &= \frac{2 f_{yt} \cdot A_{s2}}{s \cdot b_{\text{cor}}}, \\ \sigma_{r2} &= \frac{2 f_{yt} A_{s2}}{s \cdot b_{\text{cor}}} + \sigma_{r1}. \end{aligned} \tag{13}$$

4.4. Concrete Load-Bearing Capacity

4.4.1. Before Reinforcement of the Concrete Column. The protective layer of the concrete outside the stirrup was free and only acted as a protective layer. The concrete core in the stirrup was in a triaxial state of stress. The compressive strength of the concrete core could be considered according to the strength of the triaxial compression. Therefore, $f_c' = f_c + 4\sigma_{r2}$, where σ_{r2} is the passive lateral compressive stress (i.e., radial compressive stress) generated by the stirrup on the concrete core. When the stirrup's strain reached the tensile yield strength, the following could be derived:

$$\sigma_{r2} = \frac{f_{yt} \cdot A_{ss0}}{2A_{\text{cor}}}, \tag{14}$$

where A_{cor} is the area of the concrete core counted from the stirrup's inner edge and A_{sso} is the converted area of the stirrup:

$$A_{\text{sso}} = \frac{4 \cdot b_{\text{cor}} \cdot A_{s2}}{s}. \tag{15}$$

4.4.2. After the Concrete Column Reinforced by the Prestressed Steel Plate. The protective layer of the concrete between the steel plate and the stirrup was subjected to the inward force σ_{r1} restrained by the steel plate and to the expansion force (with the same magnitude as σ_{r1}) exerted by the stirrup, as shown in Figure 3(e). The concrete protective layer was equivalent to a stressed cylinder with an inner radius of $b_{\text{cor}}/2$ and an outer radius of $b/2$, subject to an inward stress σ_{r1} and an outward stress σ_{r1}. The stress distribution had to be axisymmetric, and its expression was [22]

$$\sigma_r = \sigma_\theta = \sigma_{r1}. \tag{16}$$

The compressive strength of the outer concrete layer with the triaxial stress, f_{c1}', was

$$f_{c1}' = f_{cy} + k\sigma_{r1}. \tag{17}$$

Then the axial load-bearing capacity of the outer concrete layer, N_2, was

$$N_2 = \left(f_{cy} + k\sigma_{r1}\right)A_{c1} = \left(f_{cy} + k\sigma_{r1}\right)\left[(b)^2 - (b_{\text{cor}})^2\right], \tag{18}$$

where A_{c1} is the cross-sectional area of the outer concrete layer and $A_{c1} = [(b)^2 - (b_{\text{cor}})^2]$. The concrete core was subjected to the dual constraints of the steel plate and the stirrup [23–25] and was in the triaxial stress state. The calculation formula of the axial compressive strength of the concrete for the triaxial stress state was deduced from the unified strength theory in the literature [26] as follows:

$$f_c' = f_{cy} + k\sigma_{r2}. \tag{19}$$

Here, f_c' is the compressive strength of the concrete in the triaxial stress state; $k = (1 + \sin(\phi))(1 - \sin(\phi))$. The parameter ϕ is the internal friction angle of the concrete. k was between 1.0 and 7.0, as determined by testing. When $k = 4.0$, $\phi = 36.87$. The parameter σ_{r2} is the lateral constraint stress of the concrete core, and f_{cy} is the uniaxial compressive strength of the concrete. For the columns with a square cross section, f_{cy} is the uniaxial compressive strength of the prismatic body.

The load-bearing capacity of the concrete core was

$$\begin{aligned} N_3 &= \left(f_{cy} + k\frac{2f_{yt}A_{s2}}{s \cdot b_{\text{cor}}} + k\sigma_{r1}\right)A_{\text{cor}} \\ &= \left(f_{cy} + k\frac{2f_{yt}A_{s2}}{s \cdot b_{\text{cor}}} + k\sigma_{r1}\right)(b_{\text{cor}})^2, \end{aligned} \tag{20}$$

where s is the stirrup spacing and A_{cor} is the cross-sectional area of the concrete core: $A_{\text{cor}} = (b_{\text{cor}})^2$.

4.5. Load-Bearing Capacity of the Longitudinal Reinforcement Steel Bars. When the short reinforced concrete circular column with a steel tube reached the ultimate axial compression bearing capacity, the longitudinal reinforcement steel bars yielded. Therefore, their axial compression bearing capacity N_4 was given by

$$N_4 = f_{ys}A_{s3}, \tag{21}$$

where f_{ys} is the yield strength of the longitudinal reinforcement steel bar and A_{s3} is the cross-sectional area of the reinforcement steel bar.

4.6. Unified Solution of Axial Compression Bearing Capacity. The axial compression bearing capacity N of the short reinforced concrete column with a steel tube was composed of the bearing capacities provided by the steel tube, the outer layer of the concrete, the concrete core, and the longitudinal reinforcement steel bars; that is,

$$N = N_1 + N_2 + N_3 + N_4. \tag{22}$$

After substituting equations (11), (18), (20), and (21) into (22), the unified solution of the axial compression bearing capacity of the short reinforced concrete column with a steel tube was

$$\begin{aligned} N = &-\frac{1+\beta}{\alpha}\sigma_{ts}A_{s1} + f_{cy}\left(A_{c1} + A_{\text{cor}}\right) + k\frac{2f_{yt}A_{s2}}{s \cdot b_{\text{cor}}}A_{\text{cor}} \\ &+ f_{ys}A_{s3} + \left[k\left(A_{c1} + A_{\text{cor}}\right) + \frac{1+\beta}{\alpha}\left(\frac{b}{2t} + \frac{\alpha\beta}{1+\beta}\right)A_{s1}\right]\sigma_{r1}. \end{aligned} \tag{23}$$

When $N_1 = 0$, the equation became

$$\begin{aligned} N = &f_{cy}\left(A_{c1} + A_{\text{cor}}\right) + k\frac{2f_{yt}A_{s2}}{s \cdot b_{\text{cor}}}A_{\text{cor}} \\ &+ f_{ys}A_{s3} + k\left(A_{c1} + A_{\text{cor}}\right)\sigma_{r1}. \end{aligned} \tag{24}$$

The load-bearing capacity was a function of the lateral constraint stress σ_{r1}, because when the circumferential tensile stress of the thin steel plate reached the extreme value $\sigma_{ts} = f_y$, its lateral constraint force also reached the extreme value, and, from $\sigma_\theta = (\sigma_{r1}b/2t) \le \sigma_s = f_y$, the following was obtained:

$$\sigma_{r1} \le \frac{2tf_y}{b}, \tag{25}$$

where f_{y} is the yield strength of the steel plate. Substituting (19) into (18), the maximum axial load-bearing capacity N_{u} was obtained:

$$\begin{aligned} N_u = &-\frac{1+\beta}{\alpha}f_yA_{s1} + f_{cy}\left(A_{c1} + A_{cor}\right) + k\frac{2f_{yt}A_{s2}}{s \cdot b_{cor}}A_{cor} + f_{ys}A_{s3} \\ &+ \left[k\left(A_{c1} + A_{cor}\right) + \frac{1+\beta}{\alpha}\left(\frac{b}{2t} + \frac{\alpha\beta}{1+\beta}\right)A_{s1}\right]\frac{2tf_y}{b}. \end{aligned} \tag{26}$$

When $As_2 = 0$ and $As_3 = 0$, (26) was simplified to the calculation formula of the axial compression bearing capacity of the ordinary short concrete column with a square steel sleeve, given by

$$N_u = -\frac{1+\beta}{\alpha} f_y A_{s1} + f_{cy}\left(A_{c1} + A_{\text{cor}}\right) + \left[k\left(A_{c1} + A_{\text{cor}}\right) + \frac{1+\beta}{\alpha}\left(\frac{b}{2t} + \frac{\alpha\beta}{1+\beta}\right)A_{s1}\right]\frac{2tf_y}{b} = 2b\pi t^2 f_y + \left(f_{cy} + k\frac{2tf_y}{d}\right)A_c. \tag{27}$$

The calculation results obtained using (27) are shown in Table 3.

The load-bearing capacity test results showed that as the prestressed steel plate increased, the load-bearing capacity of the short reinforced concrete column increased significantly. The experimental result was compared with the calculated result given by (27), and the results matched very closely, indicating that the formula could provide guidance for the bearing capacity calculation.

5. Finite Element Analysis of the New Structures

5.1. Finite Element Model Setup

5.1.1. Constitutive Model of the Concrete. The short concrete column reinforced with the steel plate was similar to the steel-tube concrete column in the constitutive model. When the prestress was zero, the columns were equivalent, and the axial compression force of the internal concrete core was a type of passive force that increased with the increase of the vertical axial compression. When the axial compression was small, the concrete column was approximately subject to a unidirectional force. The concrete core did not expand, and the transverse strain was small, with negligible circumferential pressure. When the axial pressure acting on the internal concrete increased, the transverse strain increased and the concrete continued to expand to squeeze the steel plate, producing transverse deformation of the steel plate. The internal concrete was compressed from three directions due to the axial force and the circumferential constraint force.

When the prestress was applied, the steel plate provided an active confining pressure to the concrete core, forming a two-way forcing condition. After the concrete core began to bear the axial pressure, the steel plate produced a lateral constraint effect on the internal concrete column. With the axial pressure exerted by the end of the column, the concrete column was subject to a triaxial state of stress.

Therefore, according to the stress characteristics of the short concrete column, the plastic damage constitutive model suitable for a steel-tube concrete column [27] was used for the new structure in this research. The model was modified based on the unified calculation formula of the stress-strain relationship curve of the axially symmetric triaxial compression of the concrete with different strength grades as follows:

$$y = \begin{cases} \dfrac{A_3 x + (B_3 - 1)x^2}{1 + (A_3 - 2)x + B_3 x^2}, & x \le 1, \\ \dfrac{x}{\alpha_3 (x-1)^2 + x}, & x > 1, \end{cases} \tag{28}$$

where $y = \sigma_{Lc}/f_c^*$, $x = \varepsilon_{Lc}/\varepsilon_f \sigma_{Lc}$ is the axial stress of the concrete, ε_{Lc} is the axial strain of the concrete, f_c^* is the axial ultimate strength of the concrete during the triaxial compression, and ε_f is the axis peak strain of concrete. $f_c^*/f_c = 1 + 3.4\sigma_{Lc}/f_c$, $\varepsilon_f = \varepsilon_c(1 + 3.4\sigma_{Lc}/f_c)[1 + 4.8(A_1 - 1)(\sigma_{Lc}/f_c)^{0.5}]$, $A_3 = A_1[1 + 4.8(A_1 - 1)(\sigma_{Lc}/f_c)^{0.5}]$, and $A_1 = 9.1 f_{cu}^{-4/9}$. B_3 is a physical quantity controlling the attenuation of the elastic modulus of the curve in the rising section. According to the definition of the elastic modulus of the concrete, the rising section was basically a straight line before $\sigma_{Lc} = 0.4 f_c$; that is, when $x = 0.4 f_c^*/A_3$, $y = 0.4 f_c/f_c^*$, B_3 could be obtained as follows:

$$B_3 = \frac{y + (A_3 - 2)xy - (A_3 - x)x}{(1-y)x^2}, \tag{29}$$

where α_3 is the parameter of the descending section of the curve: $\alpha_3 = \alpha_1 = 0.15$. The secant expression of Poisson's ratio of the concrete is expressed as

$$v_c = \begin{cases} v_0, & x \le 1, y \le y_a, \\ v_f - (v_f - v_0)\sqrt{1 - \left(\dfrac{y - y_a}{1 - y_a}\right)^2}, & x \le 1, y_a < y < 1, \\ v_f, & x \ge 1, y < 1, \end{cases} \tag{30}$$

where $v_0 = 0.2$, v_0, v_f are the initial Poisson's ratio of the concrete and the secant value of Poisson's ratio at failure. According to the analysis of the short concrete columns, $v_f = 1 - 0.0025(f_{cu} - 20)$, $y_a = 0.3 + 0.002(f_{cu} - 20)$ was satisfactory for accurate simulations.

5.1.2. Constitutive Model of Steel. The ideal steel elastic-plastic model was used to model the constitutive relationship of steel. The steel materials in the test included the longitudinal reinforcement steel bar, the stirrup, and the angle steel plate. Due to their similar properties, the constitutive relationship curves of these steel materials were the same.

Table 3: Bearing capacity test results of each group.

Number	N_c (kN)	$\overline{N_t}$ (kN)	Error (%)
CC	1461.38	1409.80	--
RC0	1930.98	1912.04	0.98
RC2	2219.44	2152.22	3.03
RC3	2469.19	2279.91	7.67

Note: N_c and $\overline{N_t}$, respectively, are the calculated value and average test value of specimen bearing capacity.

The relationship was an ideal elastic stage before the steel material reached the yield strength, and the relationship entered the plastic stage after the material reached the yield strength. Its expression is shown as follows:

$$\begin{cases} \sigma_s = E_s\varepsilon_s, & \left(\varepsilon_s \le \varepsilon_y\right), \\ \sigma_s = f_y, & \left(\varepsilon_s > \varepsilon_y\right). \end{cases} \tag{31}$$

The following assumptions were adopted in the finite element simulation:

(1) There was limited slip between the angle steel plate and the concrete.

(2) The stress-strain relationships of steel and concrete were determined according to equation (31).

(3) Only the longitudinal equilibrium and the deformation coordination were considered

5.2. Finite Element Calculation Model

5.2.1. Element Type Selection. `The research object was the internal concrete core. Therefore, the angle steel plate was simplified to an equivalent steel sleeve, and the influence of the high-strength bolt connection was ignored. The shell element (S4) of the fully integrated form of the four nodes was used for the angle steel plate. The three-dimensional solid element (C3D8R) with the reduced integral form of the eight nodes was used for the concrete core. The truss element of T3D2 was used for the reinforcement steel bars.

5.2.2. Model Setup and Mesh Division. Different parts in the finite element model were defined with the constitutive models and the section characteristics according to different material types, including the concrete, the reinforcement steel bar, the angle steel plate, and the upper and lower cushion blocks. The simulation parameters of the concrete column were the same as the parameters used in the test, that is, a rectangular section of 220 mm $\times$ 220 mm, a column height of 1000 mm, a longitudinal length of the reinforcement steel bar of 980 mm, a steel sleeve (equivalent angle steel plate) length of 980 mm, and a stirrup side length of 170 mm. An entity is the mapping object of the component in an assembly. An entity can be independent or dependent. The components were defined as dependent entities, and grid division in the assembly was not possible for the components. Therefore, grid division was conducted for each component separately in this research. According to the finite element computational time, an appropriate mesh density was selected in mesh division. The meshing result is shown in Figure 7.

5.2.3. Section Contact Definition. When the contact surface was defined in the finite element model, the embedded contact between the reinforced skeleton and the concrete was selected without considering the influence of the bond-slip. The interface model between the angle steel plate and the concrete was composed of the normal and tangential bond-slips. The "hard" contact was selected to model the normal contact between the angle steel plate and the concrete core. The coulomb friction model was used to simulate the tangential force transfer. The nested model was used to simulate the interface between the reinforcement steel bar and the concrete, and the steel bar was assumed to be nested into the concrete as a whole. The Tie binding model was selected to simulate the contact surface between the upper or lower pad block and the concrete.

5.2.4. Boundary Condition Definition and Loading Simulation. In the boundary condition definition of the finite element model, it was necessary to define the boundary conditions of the two cushion blocks. A fixed constraint boundary condition was added to the bottom pad of the column. The constraint condition for the upper pad was set to move only along the z-axis.

The experimental test required prestress during the loading process. Therefore, three analysis steps were simulated in the model: Initially we have Step 1 and Step 2. In the initial stage, the constraints were set up on various contact surfaces. The prestress exerted by the high-strength bolts in the test was simplified in the simulation into the circumferential confining pressure exerted on the steel sleeve. Therefore, the circumferential pressure was exerted on the short column in Step 1. The pressure was produced with direct uniform distribution. The axial loading process was simulated in Step 2. The loading method was displacement loading, which was achieved by applying a surface load on the upper pad of the concrete column.

During the loading process in the test, the prestresses were the pretightening forces exerted by the high-strength bolts, which were 0 MPa, 179.5 MPa, and 340 MPa. According to (1) and (5) for the confining pressure of the angle steel plate, the uniform distributed loads exerted on the equivalent side steel sleeve were 0 N/mm^2, 1.49 N/mm^2, and 2.78 N/mm^2.

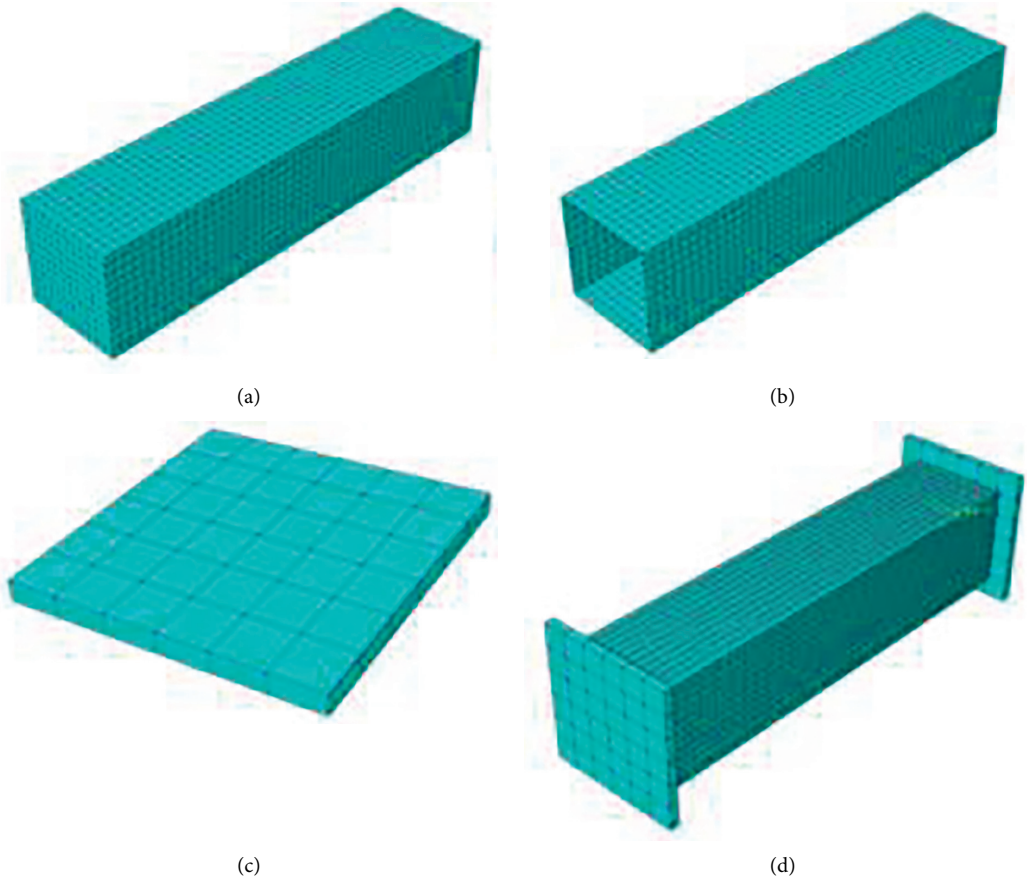

Figure 7: Model mesh subdivision. (a) Concrete. (b) Angle steel plate. (c) Cushion block. (d) Whole model.

5.2.5. Finite Element Solution. After the above operations were completed, the finite element calculation was started. During the simulation, the computational process was monitored by using related functions in ABAQUS. When the software reported an error, the problem was diagnosed according to the system prompt and the model was modified to fix the problem.

5.3. Analysis of Finite Element Simulation Results

5.3.1. Validation of Finite Element Simulation. Table 4 shows that the ultimate bearing capacity of each specimen was obtained through finite element simulation. The simulation data and the test data were very close when compared, with an error within 5%, meeting engineering calculation requirements. N_m in Table 4 is the simulated ultimate load and N_t is the tested ultimate load.

Figure 8 shows the curves of the load versus vertical displacement of the four groups of specimens. With the reinforcement effect of the confining pressure given by the steel plates, when the specimen reached the maximum bearing capacity, the curve retained a slow decline and tended to level off. When the simulation result of this type of curve was compared with the test results for all the groups of specimens, there was a small difference.

5.3.2. Finite Element Analysis Results. In order to further study the stress characteristics of the short concrete column reinforced with the steel plate under axial compression, ABAQUS was used to perform finite element analysis to obtain the stress variations of the steel plate and the stress distribution chart with the ultimate load, as shown in Figure 9.

The stress distribution maps of RC1, RC2, and RC3 were analyzed. The maximum stress was concentrated in the corner of the rectangular angle steel plate. The first location of the buckling deformation was concentrated in the middle and upper regions of the steel plate. Compared with RC2, as the RC3 prestress increased, the coverage range of the maximum stress on the RC3 steel plate increased and was distributed in the middle area of the component.

Figures 10–13 show the plastic PEMAG charts of the CC, RC1, RC2, and RC3 specimens, which recorded the plastic strains of the concrete columns when the bearing capacities reached the failure loads in the deformation process. By comparing the CC columns with reinforced columns, it was found that the plastic strain in the red area of the CC columns in the control group was small, while the plastic strains of the RC1–RC3 columns were increased 1-2-fold, indicating that the proposed reinforcement method could improve the ductility of the concrete columns.

Table 4: Comparison of experimental and calculated values.

Number	f_c (MPa)	Prestress (MPa)	N_m/kN	N_t/kN	N_m/N_t
CC	30.1	—	1413.56	1409.80	1.02
RC1	30.1	0	1955.22	1912.04	1.02
RC2	30.1	179.5	2171.83	2152.22	1.01
RC3	30.1	340	2271,39	2279.91	1.00

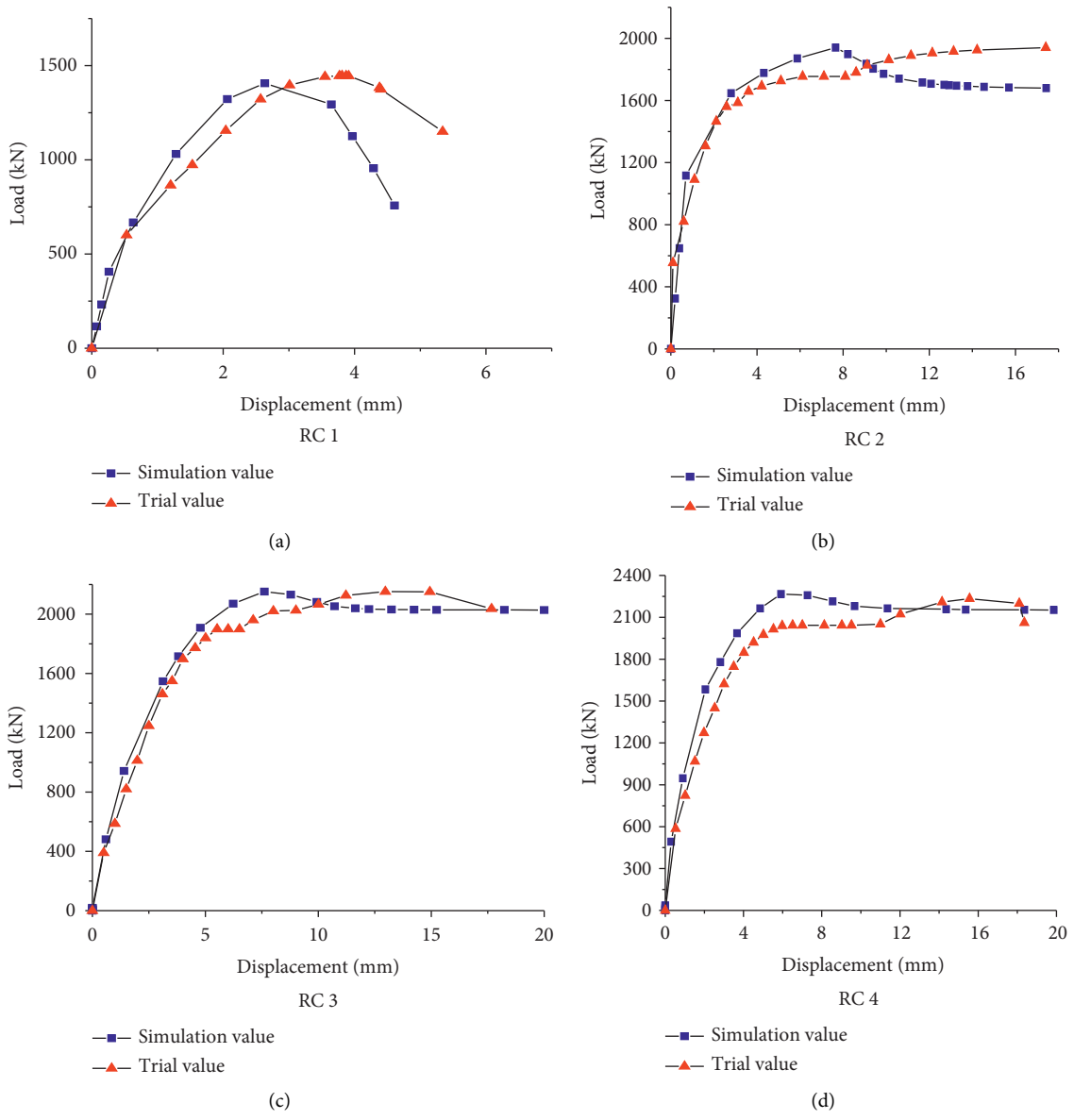

Figure 8: Comparison of load-displacement curves between test and simulation. (a) RC1, (b) RC2, (c) RC3, (d) RC4.

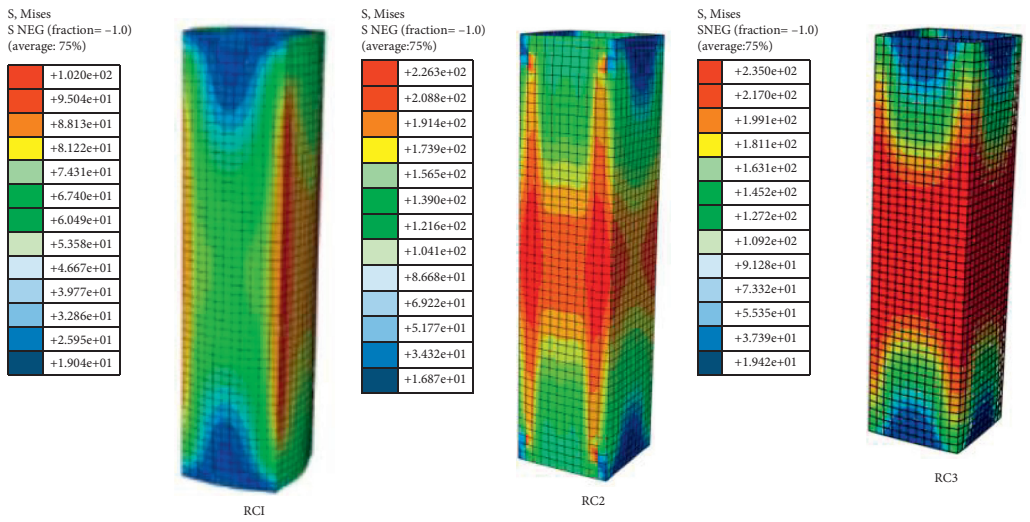

Figure 9: Stress nephogram of angle plate.

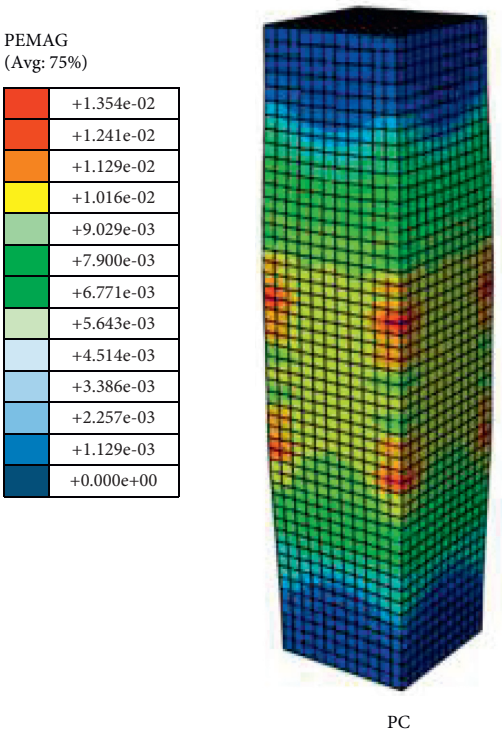

Figure 10: Strain cloud picture of CC (MPa).

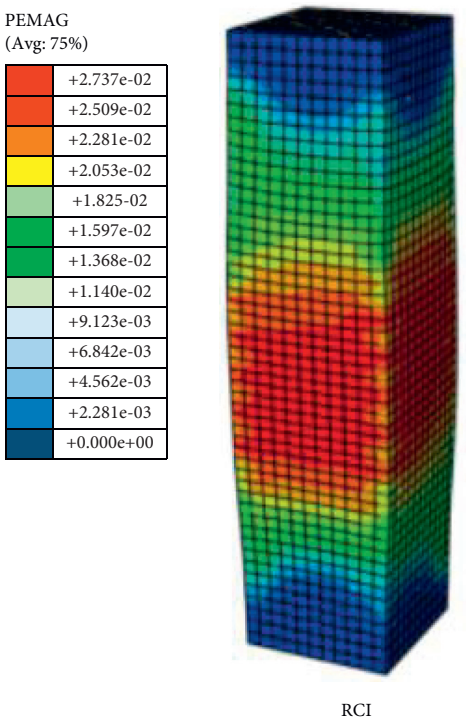

Figure 11: Strain cloud picture of RC1 (MPa).

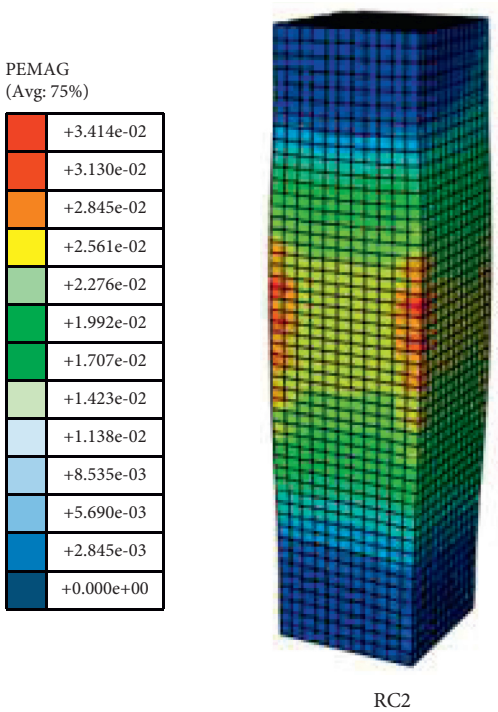

Figure 12: Strain cloud picture of RC2 (MPa).

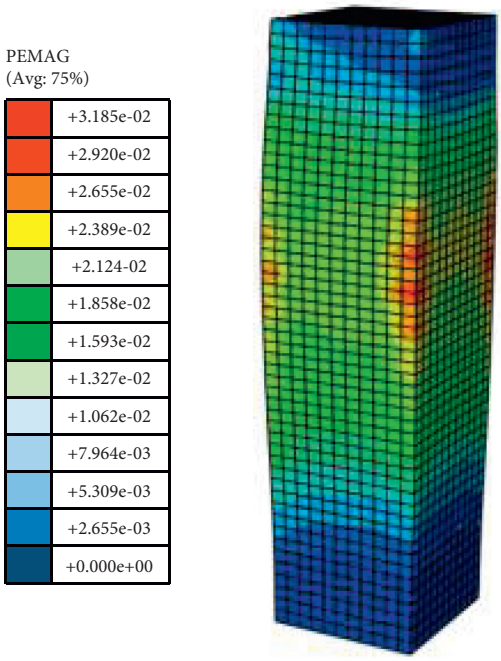

Figure 13: Strain cloud picture of RC3 (MPa).

6. Conclusions

The axial compression load-bearing capacity and mechanical properties of short concrete columns reinforced with prestressed angle steel plates were studied with the axial compression test of 20 specimen columns. Conclusions were drawn as follows:

(1) Compared with the control columns, the ultimate load-bearing capacity of each group of the reinforced columns was significantly increased (RC3 > RC2 > RC0 > CC). With the unidirectional compression, as the steel plate's prestress increased, the duration of the elastic stage was increased, indicating an increase in the stiffness. When the ultimate load was reached, the curve of load versus displacement declined more gently for the specimen with a greater prestress, showing increased ductility with an increase in the prestress.

(2) The curve of load versus strain of the reinforcement steel bar showed that a greater prestress resulted in an increase in the peak strain of the concrete in the elastic stage, that is, the strain corresponding to the ultimate load. However, a greater prestress also led to a greater deformation of the concrete, indicating that the prestressed angle steel plate could not effectively constrain the deformation of the concrete column.

(3) The test results were compared with the calculation results given by Equation (25). The comparison validated the good accuracy of the formula for the proposed new structure. The formula could provide design guidance for the calculation of the load-bearing capacity of the reinforced concrete columns.

(4) The finite element simulation accurately reflected the stress conditions of the concrete columns. The failure characteristics of the concrete columns simulated by the finite element model were in good agreement with the test results.

Data Availability

The data used to support the findings of this study are all included within the article.

Disclosure

The patent number is ZL201610919619.1.

Conflicts of Interest

The authors declare that they have no conflicts of interest.

Authors' Contributions

Conceptualization was done by Z. R. and X. Z.; methodology was developed by Z. R.; software was provided by Q. S.; validation was performed by X. Z.; formal analysis was performed by X. Z.; investigation was performed by Z. R. and X. Z.; resources was provided by Z. R. and X. Z.; data curation was performed by Q. S.; original draft was written by X. Z.; reviewing and editing were done by X. Z. and H. H.; visualization was performed by Z. R.; supervision was done by X. Z.; project administration was done by Z. R. and X. Z.; funding acquisition was done by Z. R. and X. Z. All authors have read and agreed to the published version of the manuscript.

Acknowledgments

This research was funded by the Fundamental Research Funds for the Key Project of Research and Development Plan of Hunan Province (2020SK2109) and National Natural Science Foundation of Hunan Province (2021JJ50106). The project was supported by Hunan Key Laboratory of Intelligent Disaster Prevention and Mitigation and Ecological Restoration in Civil Engineering, Catastrophe and Reinforcement of Dangerous Engineering Structures, Hunan Provincial Engineering Research Center.

References

[1] Z. H. Ren, X. T. Zeng, W. J. Qu, and Q. Liang, "Analysis of axial compression bearing capacity of rectangular concrete short columns strengthened with prestressed angle steel plate," *Building Structure*, vol. 48, no. 14, pp. 84–89+93, 2018.

[2] S. H. Cai, *Modern Steel Tube Confined Concrete Structures*, pp. 3–7, China Communications Press, Beijing, China, 2003.

[3] B. L. Liang and J. X. Liu, "Ultimate bearing capacity of concrete-filled circular steel tubular short columns under axial compression," *Journal og Shanghai Jiaotong University*, vol. 44, no. 6, pp. 749–753, 2010.

[4] Y. Qin, P. T. Wu, L. Huang, and Y. Lv, "Experimental study on the short columns of steel tube ultra-high performance concrete under axial compression," *Journal of Tianjin Chengjian University*, vol. 26, no. 04, pp. 254–259, 2020.

[5] J. S. Han, D. Yuli, Z. D. Xu, S. P. Cong, and W. R. Cheng, "Analysis of axial compression performance for reinforcement concrete-filled tubular steel," *Journal of civil, architectural &environmental engineering*, vol. 31, no. 03, pp. 11–17, 2009.

[6] Y. Y. Lu, H. Liang, S. Li, and X. Yin, "Experimental study on behavior of square RC columns strengthened with self-compacting concrete filled square steel tubes under axial load," *Journal of Building Structures*, vol. 36, no. 07, pp. 43–50, 2015.

[7] C. Y. Gao, Y. X. Duan, H. Zhang, and H. G. Yang, "Experimental study on the bearing capacity of circular tubed reinforced concrete short column under axial compression," *Building Structure*, vol. 47, no. 2, pp. 48–52, 2017.

[8] X. Hu, *Research on Compressive Performance and Bearing Capacity of RC Short Columns Strengthened with Circular Steel Jacketing*, Southwest Jiaotong University, Chengdu, China, 2014.

[9] J. Gao, *Performance Investigation of FRP Strengthened Reinforced concrete Circular Columns under Axial Compressive Loading*, Zhengzhou University, Zhengzhou, China, 2014.

[10] S. P. Yin, C. Peng, and S. X. Ai, "Research on the axial compression properties of concrete columns strengthened with textile reinforced concrete," *Journal of Sichuan University (Engineering Science Edition)*, vol. 48, no. 4, pp. 85–95, 2016.

[11] Y. Y. Lu, J. Y. Shi, and G. F. Zhao, "Experimental research on concrete columns strengthened with the combination of CFRP and angle steel," *Journal of Building Structures*, vol. 24, no. 5, pp. 18–23, 2003.

[12] L. Zeng, L. Li, J. Chen, X. Yang, and S. Peng, "Experimental study on concrete columns strengthened with non-adhesive carbon fibre spirals under axial compression," *Journal of Building Structures*, vol. 37, no. 5, pp. 283–290, 2016.

[13] Y. F. Ma, *Experimental Study on High-Strength concrete Restrained by CFRP Sheet under Axial Loading*, Hebei United University, Tangshan, China, 2014.

[14] L. J. Hao, *Research on Axial Compression Performance of concrete Column Strengthened by Prestressed Steel belt Reinforced*, Xi'an University of Architecture and Technology, Xi'an, China, 2014.

[15] Y. Zhao, *The Experimental Study on Axial Compression Performance of concrete Square Columns Strengthened with Prestressed Steel Strip*, Xi'an University of Architecture and Technology, Xi'an, China, 2014.

[16] B. Zhang, Y. Yang, Y. Liu, and L. J. Hao, "Experimental study on axial compression performance of reinforced concrete column retrofitted by prestressed steel strip," *Journal of Engineering Mechanics*, vol. 33, no. 3, pp. 104–111, 2016.

[17] L. Zhang, G. R. Ning, J. H. Li, and Y. Yang, "Experimental study of reinforced concrete columns strengthened by prestressed steel strips," *Industrial Construction*, vol. 46, no. 3, pp. 155–159, 2016.

[18] GB/T 50081-2002, *Standard for Test Method of Mechanical Properties on Ordinary concrete, Ministry of Construction PRC,General Administration of Quality Supervision*, Quarantine and Inspection, Beijing, China, 2002.

[19] P. Shen, *Design Theory for Concrete Structure*, Higher Education Press, Beijing, 4th edition, 2012.

[20] Y. U. Mao-hong, *Unified Strength Theory and Its Applications*, Springer Press, Berlin, 2004.

[21] Z. H. Guo and X. D. Shi, *Reinforced Concrete Theory and Analysis*, Tsinghua University Press, Beijing, 2003.

[22] Z. L. Xu, *Elasticity*, Vol. I, Higher Education Press, , Beijing, 2006.

[23] Z. Q. Zhang, J. H. Zhao, Y. F. Zhang, and X. W. Li, "Axial bearing capacity of composite concrete-filled steel tubular columns," *Journal of Chang'an University (Natural Science Edition)*, vol. 30, no. 1, pp. 67–70, 2010.

[24] J. H. Zhao and . Meng, "Bearing capacity of concrete-filled double-skin steel-tube stub column," *Journal of Chang'an University (Natural Science Edition)*, vol. 29, no. 1, pp. 70–74, 2009.

[25] Y. Zhai, J. H. Zhao, L. Ji, and X. Y. Wei, "Unified Solutions on axial compressive strength of concrete filled steel tube," *Journal of Chang'an University (Natural Science Edition)*, vol. 26, no. 3, pp. 55–58, 2006.

[26] J. H. Zhao, *Strength Theory and Engineering Application*, Science Press, Beijing, 2003.

[27] S. Wang, X. Jiang, and Y. Bai, "Nonlinear finite element analysis of axially loaded concrete-filled steel tubular stub columns," *Sciencepaper Online*, vol. 4, no. 07, pp. 472–479, 2009.

Hindawi
Advances in Civil Engineering
Volume 2022, Article ID 3831580, 11 pages
https://doi.org/10.1155/2022/3831580

Research Article

A Comparative Analysis by Experimental Investigations on Normal and Ground Ultrafine Mineral Admixtures in Arresting Permeation in High-Strength Concrete

B. Karthikeyan,[1] **Senthil Kumaran Selvaraj**,[2] **G. Dhinakaran**,[1] **G. Sundaramali**,[2] **Natarajan Muthuswamy**,[3] **and Velmurugan Paramasivam**[4]

[1]*School of Civil Engineering, SASTRA Deemed to be University, Thanjavur 613401, Tamilnadu, India*
[2]*Department of Manufacturing Engineering, School of Mechanical Engineering (SMEC), Vellore Institute of Technology (VIT), Vellore 632014, Tamilnadu, India*
[3]*Department of Thermal and Energy Engineering, School of Mechanical Engineering (SMEC), Vellore Institute of Technology (VIT), Vellore 632014, Tamilnadu, India*
[4]*School of Mechanical and Automotive Engineering, College of Engineering and Technology, Dilla University, P.O. Box 419, Dilla, Ethiopia*

Correspondence should be addressed to Senthil Kumaran Selvaraj; senthilkumaran.s@vit.ac.in and Velmurugan Paramasivam; drvelmuruganp@du.edu.et

Received 10 November 2021; Revised 27 December 2021; Accepted 18 January 2022; Published 2 February 2022

Academic Editor: Wenjie Ge

This paper discusses the permeation characteristics of concrete made by increasing the fineness of the conventional mineral admixtures and using them as a partial substitute for cement. Silica fume and metakaolin ground to ultrafine state and ceramic powder obtained from grinding waste ceramic tiles were used as mineral admixtures. The mixes were designed for a compressive strength of 50 MPa and were prepared for both binary and ternary blended cases. Binary blended specimens were cast, partially replacing cement with unground silica fume, ground silica fume, unground metakaolin, and ground metakaolin separately in different replacement proportions. Ternary blended mixes were prepared using ceramic powder in 4%, 9%, and 14% and with silica fume in a constant level of 1% percentage. All the cast specimens were compared against the control concrete. A deeper comparative analysis was also made by comparing the performance of specimens made with unground mineral admixtures with that of ground mineral admixtures. Various parameters such as resistance against water absorption, percentage of voids, and sorptivity characteristics were studied. It was observed that increasing the fineness helps fill up the pores, thereby improving the resistance to permeation action.

1. Introduction

The pore structure of concrete is considered one of the significant characteristics of concrete as it plays a vital role in assessing the mechanical and durability properties of concrete [1]. Pore structure, in general, includes pores of all types such as air voids, capillary pores, and gel pores. The presence of pores in concrete causes permeation of fluid particles into the concrete and, if permitted for a more extended period, may threaten the stability of the structures. Permeability of concrete is arrived at by measuring the flow of any fluid, mainly water, under pressure gradient [2]. Resistance to permeation is an essential property in high-performance concrete. It plays a significant role in estimating the performance of the concrete as it affects the durability of the structures, especially those exposed to aggressive environments. The presence of pores in concrete leads to the permeation of water, salt, and other natural agents, resulting finally in the deterioration of concrete. This can be controlled by incorporating more refined supplementary cementitious materials available as industrial by-products. Silica fume and metakaolin are the commonly

used supplementary cementitious materials among those possessing pozzolanic nature.

Many reports are available in justifying the capability of such supplementary cementitious materials in resisting permeability and improveing performance. Poon et al. [3] reported that comparing the concrete with silica fume and metakaolin, the metakaolin-based concrete resulted in dense matrix possessing low porosity characteristics.

In addition to the industrial by-products used as supplementary cementitious materials, a few authors have used industrial dumped wastes such as both in cement and fine aggregate to enhance the durability characteristics of concrete. Karthikeyan and Dhinakaran [4] have carried out works with construction waste ceramic powder and reported that strength development was better in 15% replacement of ceramic powder for cement, and it was mentioned that the improvement in strength is mainly due to the pore-filling effect. Karthikeyan et al. [5] developed a high=strength concrete using dumped iron ore tailings as fine aggregate and reported that the iron ore tailings can be used up to a maximum replacement level of 30% for fine aggregate, and the authors also mentioned that waste utilization in concrete with suitable adaptation of fibres can yield better strength and durability.

Adding to the earlier research works of using conventional mineral admixtures in a typical form, many research works were completed and many are still in progress with nanosized mineral admixtures in making a densely packed concrete structure to arrest the permeation, and a few are presented in this section. Jo et al. [6] in their experimental research stated that mixing nano-SiO_2 to cement improved the early age and 28-day strength of the cement mortars due to the increased surface area, thereby increasing the rate of pozzolanic reaction which ultimately led to an increase in strength. Pacheco-Torgal et al. [7] developed high-performance concrete with nanoparticles, and their report discussed the use of nanoparticles in concrete and their benefits, and also, it suggested suitable methods to improve the mechanical properties of high-performance concrete. Actually, Ali et al. [8–10] contributed more to the research on using nanosized mineral admixtures such as ZnO_2 and TiO_2 in regular as well as self-compacting concrete.

Though the use of nanosized mineral admixture provided a densely packed concrete matrix, thereby reducing the permeation characteristics, the cost involved is too high, so the ultrafine mineral admixtures were tried by many researchers to make the concrete economically feasible and durable, and few of them are discussed here. Karthikeyan and Dhinakaran [11, 12] developed a high-strength concrete by blending ultrafine TiO_2 with silica fume and presented its behavior in both fiber-reinforced and -unreinforced concrete specimens. Karthikeyan and Dhinakaran [13, 14] tried using the conventional mineral admixtures in their ultrafine state. They found that there was undoubtedly an improvement in the mechanical and durability properties when the size of the conventional supplementary cementitious mineral admixtures reduced to an ultrafine state. Chai et al. [15] carried out works with ground fly ash to prepare high-strength concrete. Felekoğlu et al. [16] performed experimental investigations by grinding coarse fly ash and optimizing the fineness to attain a high strength. Teng et al. [17] used ultrafine ground granulated blast furnace slag to improve high-strength concrete's mechanical and durability properties.

Although, the discussed literature presents a clear view about the contribution of ultrafine mineral admixtures in offering better strength properties, other durability properties such as permeation, presence of voids, and their effects on the pore structure of the concrete need proper experimental validation. It is essential to check whether durability properties such as the strength and performance of concrete made with ultrafine mineral admixtures depend on pore presence, size, and distribution in the concrete. The total volume of pores present in a mix affects the strength and elasticity of concrete [18]. Niu et al. [19] discussed the pore-filling capability of superfine slag in cement paste. It is reported that the use of superfine slag decreased the presence of voids and resulted in better porosity behavior and more overdue to their complete hydration, and the strength of mortars increased. This paper presents the experimental investigations adopted in studying the durability characteristics of concrete made with ultrafine mineral admixtures and the effect due to size reduction in filling up the pores.

In the present study, the permeation characteristics of specimens made with normal silica fume and metakaolin were compared with those of specimens made with ultrafine silica fume and ultrafine metakaolin. The ultrafine state was obtained by grinding the commonly available silica fume and metakaolin using a ball mill. The main focus of this study is to assess the capability of ground silica fume and ground metakaolin in resisting the permeability and porosity properties. A permeability test was conducted through the sorptivity method. Based on the sorptivity, porosity, and water absorption test results, the replacement levels required for attaining durability and the comparison in the permeation resisting characteristics of ground and unground specimens were discussed. In addition to ground/unground silica fume, ground/unground metakaolin, to implement waste utilization specimens using ceramic powder, was also made, and the results were also discussed.

1.1. Research Scope and Significance. This paper reports the permeation characteristics of high-strength concrete with ultrafine mineral admixtures. Though many works were reported in strengthening the pore structure using nanosized and ultrafine cementitious materials, limited works were carried out on silica fume due to their finer size and other industrial wastes such as ceramic powder. In this work, the use of the ultrafine mineral admixtures, especially with silica fume, metakaolin, and ceramic powder, and their effect in protecting the pore structure were studied by performing various tests such as sorptivity and porosity tests.

2. Materials Used

2.1. Basic Materials. OPC confirming to ASTM C150 [20] was used in the present research. Table 1 presents the composition of cement. River sand possessing physical

Table 1: Compounds of cement and other mineral admixtures obtained from XRF.

Compounds	Concentration in percentage			
	Cement	Silica fume	Metakaolin	Ceramic powder
SiO_2	23	97.36	53.67	55.80
MgO	0.4	0.79	0.09	4.28
Al_2O_3	0.6	0.53	43.34	19.13
SO_3	2.5	0.51	0.27	0.54
Fe_2O_3	4	0.15	0.46	7.88
CaO	62	0.14	0.37	7.85
P_2O_5	—	0.09	0.12	0.13
Na_2O	—	0.06	0.12	1.17
Cl	—	0.02	0.02	0.13
K_2O	—	0.29	0.17	1.36
MnO	—	0.01	—	0.04

properties such as fineness modulus 2.60 and a specific gravity of 2.63 was used as fine aggregate. Well-graded coarse aggregate, which was locally available and of standard size greater than 4.75 mm and less than 12.5 mm with fineness modulus 2.72, was used.

2.2. Silica Fume. Silica fume (SiO_2), a by-product obtained from ferrosilicon industry, was used as one of the mineral admixtures. It is a very fine powder with more than 95% of the particles having a size less than 1 μm. The silica fume used in this study was received from Oriental Exporters, Navi Mumbai, Maharashtra, India. Silica fume was used in unground (as supplied) ultrafine states (after grinding in the planetary ball mill). The components of silica fume were found using an XRF analyzer, and Table 1 shows the composition.

2.3. Metakaolin. Metakaolin is derived from purified kaolin clay, formed by calcining purified kaolinite at a temperature range between 650°C and 700°C. Kaolinite is hydrous aluminium silicate and is represented chemically as $Al_2O_3.2SiO_2.2H_2O$. Metakaolin is finer than cement particles but coarser than silica fume. Table 1 shows the chemical composition of the metakaolin.

2.4. Ceramic Powder. Industrial by-products such as silica fume, fly ash, and GGBFS are usually pozzolanic and have many chemical components similar to cement. The use of such mineral admixtures in concrete can help in reducing the cement content without affecting the strength characteristics. They indeed help in increasing the long-term strength of concrete. On the other hand, other industrial wastes such as marble, granite, and ceramic powders cannot be expected to exert pozzolanic behavior but can act as inert materials. However, in an excellent powder form, a homogeneous mixture can be arrived at using them. The ceramic powder used in the present work was prepared by grinding waste ceramic tiles in a ball mill. The ceramic powder that is coarser than cement was finely ground to a size much less than that of cement. Though they cannot exert a better pozzolanic characteristic, they can act as fillers in concrete. The specific gravity of ceramic powder is 2.182. The components of ceramic powder are shown in Table 1.

2.5. Superplasticizer. The superplasticizer CONPLAST SP 430 obtained from FOSROC company was used to induce the workability. It was used in a dosage of 1.5 litres per 100 kg of cement depending on the required workability.

2.6. Ultrafine Silica Fume and Metakaolin. Silica fume and metakaolin were ground using a planetary ball mill of 320 rpm. Zirconium balls of size 10 mm were used for the grinding process. The balls were added in different time durations, and only 18 balls were used initially. 20 minutes later, the number of balls was increased to 26. Figure 1 shows the zirconium balls used while grinding metakaolin. The grinding efficiency of the mill is affected by various factors such as the materials to be ground, the ratio of the material to the balls used for grinding, and the grinding ball size. The quantity of the material was judged by trial and error only [25–27]. So, the material silica fume/metakaolin was ground individually for 1 hour in 100 g and 50 g, and the effect of grinding was observed.

2.7. Ultrafine Ceramic Powder. The ceramic powder was prepared by breaking ceramic tiles into smaller pieces by feeding into a jaw crusher and then grinding waste ceramic tile in a dry ball mill. The ceramic powder was made by grinding waste ceramic tiles in a jaw crusher, making them into less-coarse particles first. Then, the less-coarse particles were fed into a dry ball mill and 7 numbers of 30 mm diameter steel balls, each weighing 400 g. The grinding process was continued for 30 minutes, 45 minutes, and 60 minutes. A 75-micron sieve was used to collect only the particles that are finer than cement. A particle size analyzer was used to categorize the samples ground for different durations, and the finer samples were used for the research. Figures 2–4 depict the process involved in grinding ceramic tiles. The components were found using X-ray fluorescence (XRF) and are presented in Table 1 to ensure that the ceramic particles also possess chemical properties similar to those of cement and are helpful for a partial replacement for cement.

2.8. Mixture Proportions. The research was conducted for two types of mixes, namely, binary and ternary mix. Among the binary mix category, silica fume, metakaolin, and ceramic powder were used as mineral admixtures as partial substitutes for cement in both unground and ultrafine states. In ternary mix, ceramic powder and silica fume were blended with cement. The mineral admixtures were used to partially replace cement in 5%, 10%, and 15%. The mixes were proportioned with a water-cement ratio (w/c) of 0.3. A control mixture without adding supplementary cementitious materials was cast to compare with other mixes. A total of 19 mixes including one control mix, 15 binary mixes (UGSF5, UGSF10, UGSF15, UFSF5, UFSF10, UFSF15, UGMK5, UGMK10, UGMK15, UFMK5, UFMK10,

Figure 1: Zirconium balls and metakaolin during grinding.

Figure 2: Waste ceramic tiles from construction sites.

Figure 3: Jaw crusher for crushing tiles.

Figure 4: Ultrafine ceramic powders after grinding in a planetary ball.

UFMK15, CP5, CP10, and CP15), and 3 ternary mixes (CSF5, CSF10, and CSF15) were made. The main objective of this research work is to check the pore-filling capability due to the increase in the fineness of the mineral admixtures. So, mixes were made using the mineral admixtures in their unground state (UGSF and UGMK) and ground state (GSF and GMK). Ceramic powder (CP) was used in its fine ground state both in binary mixes and ternary mixes. In ternary mixes, the ceramic powder was used in a larger proportion by 4%, 9%, and 14% to encourage waste utilization. Sometimes, ceramic powder may behave like an inert material that can only fill pores and cannot provide necessary pozzolanic action. So, silica fume was added in a minor amount of 1% to induce pozzolanic action and possess cementitious properties. The mix was named CSF. The mix design was carried out by the ACI method, and the mix proportion obtained was 1 : 1.04 : 2.13 : 0.3 (cement: fine aggregate: coarse aggregate: w/c) with a suitable addition of superplasticizer. The methodology is illustrated in Figure 5. Tables 2 and 3 show the mix details adopted.

3. Experimental Investigations

3.1. Sorptivity. Sorption is the absorption of water under capillary suction. This test will help in assessing the quantum of water absorbed in the pores of the specimen under capillary suction. Cylindrical specimens of size 100 mm (d) × 50 mm (h) were cast and used for the present work. The specimens after finishing their 28-day period of normal curing were dried in an oven at about 110°C. Then, the oven-heated specimens were kept in a sealed container to cool them in an ambient temperature. The specimen surfaces were covered with nonporous insulation tape except the bottom surface as shown in Figure 6. Specimens were kept in water only 3 to 5 mm from the bottom surface to ensure entry of water only through the bottom. The mass of the specimen at the periodical interval was taken in accordance with ASTM C1585 [21]. The volume of water absorbed had been calculated by dividing the total mass of the specimen by the nominal surface area and by the density of water. These obtained values were then plotted against the square root of time, and the water sorptivity coefficient of concrete is the slope of line of the best fit.

3.2. Porosity Test. The durability test for the specimen was conducted by performing a porosity test. The test was performed in accordance with ASTM C642-13 [22]. Cylinder specimens of size 100 mm (dia) × 50 mm (thick) were cast for various replacement percentages of cement and are kept for 28 days curing. After obtaining the weights of all these specimens at different conditions such as oven-dried weight and saturated weight after keeping in water for 24 hours, as specified in the codal provisions, the percentage of voids (porosity) of the specimen was calculated.

4. Results and Discussion

4.1. Size Reduction by Grinding. Ultrafine silica fume and metakaolin were obtained by subjecting the mineral admixtures separately to different hours of grinding in a

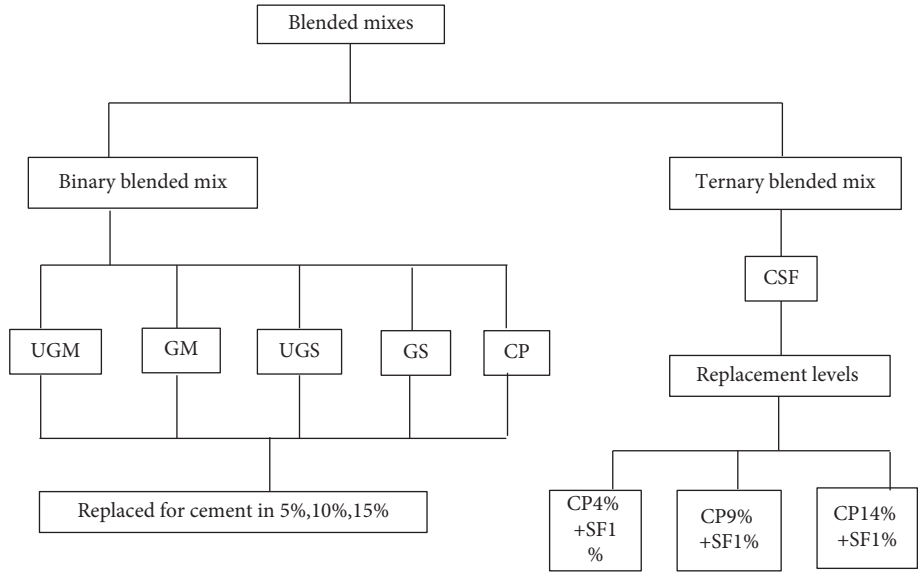

Figure 5: Pictorial representation of the mix proportions adopted.

Table 2: Mix proportion: binary mix (cement and any one mineral admixture).

Parameters	Mix reference					
	Cement (kg/m^3)	SF (kg/m^3)	MK (kg/m^3)	CP (kg/m^3)	Fine aggregate (kg/m^3)	Coarse aggregate (kg/m^3)
CONTROL	522.57	—	—	—	544.18	1113.84
UGSF5	496.44	26.13	—	—		
UGSF10	470.31	52.26	—	—		
UGSF15	444.18	78.38	—	—		
UGMK5	496.44	—	26.13	—		
UGMK10	470.31	—	52.26	—		
UGMK15	444.18	—	78.38	—		
GSF5	496.44	26.13	—	—		
GSF10	470.31	52.26	—	—		
GSF15	444.18	78.38	—	—		
GMK5	496.44	—	26.13	—		
GMK10	470.31	—	52.26	—		
GMK15	444.18	—	78.38	—		
CP5	496.44	—	—	26.13		
CP10	470.31	—	—	52.26		
CP15	444.18	—	—	78.38		

Table 3: Mix proportion: ternary (cement + SF + CP).

Parameters	Mix reference				
	Cement (kg/m^3)	CP (kg/m^3)	SF (kg/m^3)	Fine aggregate (kg/m^3)	Coarse aggregate (kg/m^3)
CONTROL	522.57	—	—	544.18	1113.84
CSF5	496.44	25.085	1.045		
CSF10	470.31	50.17	2.09		
CSF15	444.18	75.24	3.14		

planetary ball mill using zirconium balls. Initially when the ball mill is loaded with its full capacity, the percentage reduction in size was only 20.84%; later, the quantity was reduced to 50%, and a greater percentage of reduction in size about 75.39% from the original size of microsilica was obtained. Table 4 presents the average diameter size details for which the maximum reduction was obtained. The same procedure was adopted for grinding metakaolin also. It can be seen that major reduction in size of about 75.83% was obtained when 50 g of metakaolin was subjected to grinding for 1 hour. The particle size of the ceramic powder checked by using a zeta analyzer and reported as average diameter ensures that their size is less than the size of cement. It is shown in Table 4 and in Figures 7–11. As the particles reached ultrafine size at one hour of grinding,

Figure 6: Specimens for the sorptivity test.

Table 4: Reduction in size after grinding.

Sl. no.	Sample type	Duration of grinding (hours)	Size (nm)	Percentage variation in size
1	UGSF	—	638	75.39% decrease in size
2	GSF	1	157	
3	UGMK	—	1738	75.83% decrease in size
4	GMK	1	420	
5	CP	1	2481	—

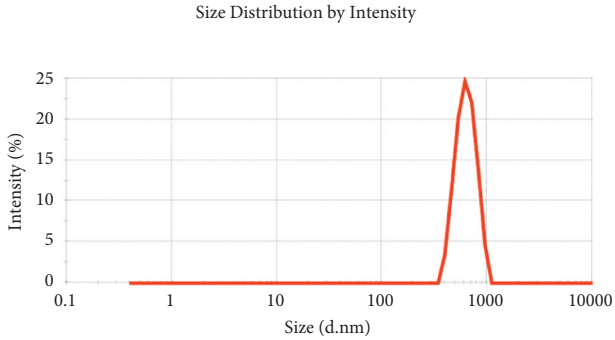

Figure 7: Particle size distribution graph of UGSF.

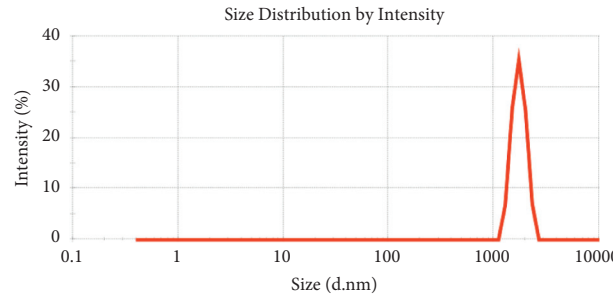

Figure 9: Particle size distribution graph of UGMK.

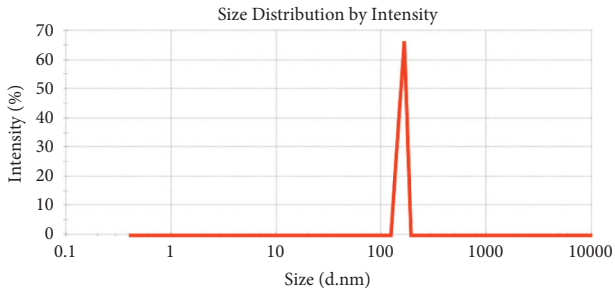

Figure 8: Particle size distribution graph of GSF.

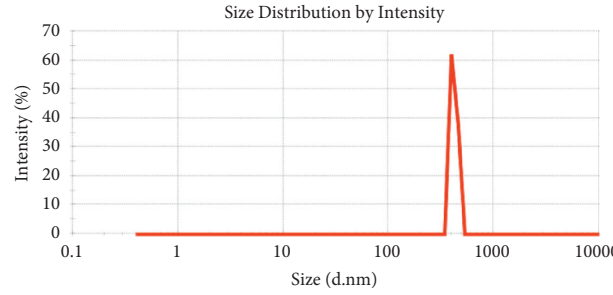

Figure 10: Particle size distribution graph of GMK.

the experiments were carried out with samples ground for one hour only, fixing that as the optimum duration for obtaining finer particles.

4.2. Water Absorption and Sorption Coefficient of SF-Blended Binary Mix. All the SF-mixed specimens showed less water absorption than control by 0.52%, 0.54%, and 0.55% for UGSF5, UGSF10, and UGSF15 specimens. GSF specimens performed well and have shown better resistance in resisting water permeation showing a much less value than the control and UGSF specimens. The reduction in water absorption is due to the filling of the pores by the ground fine-sized silica fume which had made the concrete a densely packed one, thus resisting further water absorption. The

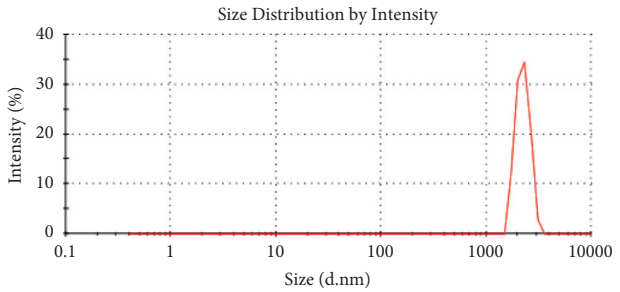

Figure 11: Particle size distribution graph of CP.

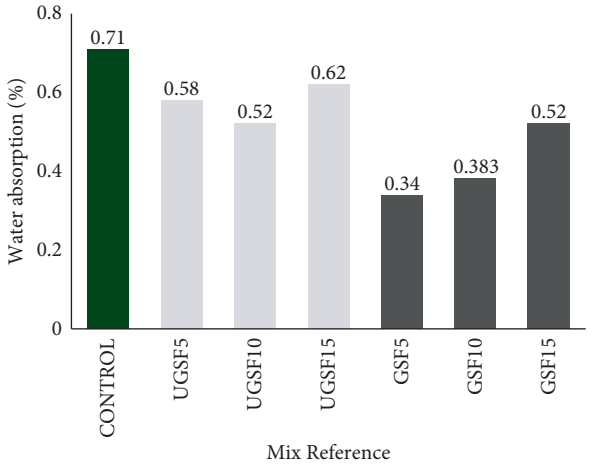

Figure 12: Water absorption values of SF.

Table 5: Sorption coefficient.

Specimen	Replacement levels Sorption coefficient			
	0	5	10	15
CONTROL	0.008	—	—	—
UGSF	—	0.004	0.018	0.029
GSF	—	0.005	0.002	0.002
UGMK	—	0.008	0.006	0.005
GMK	—	0.008	0.007	0.009
CP	—	0.01	0.011	0.007
CSF	—	0.241	0.141	0.074

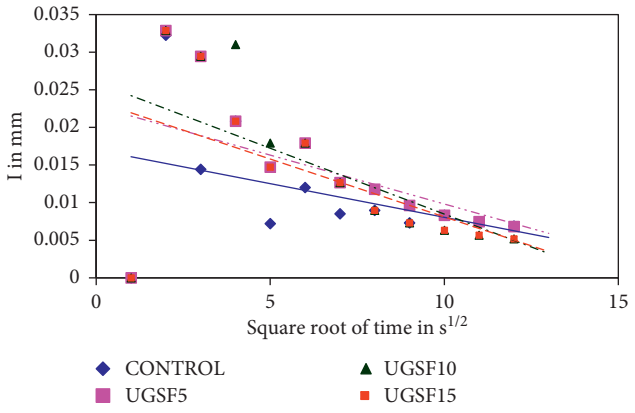

Figure 13: Sorption coefficient of UGSF.

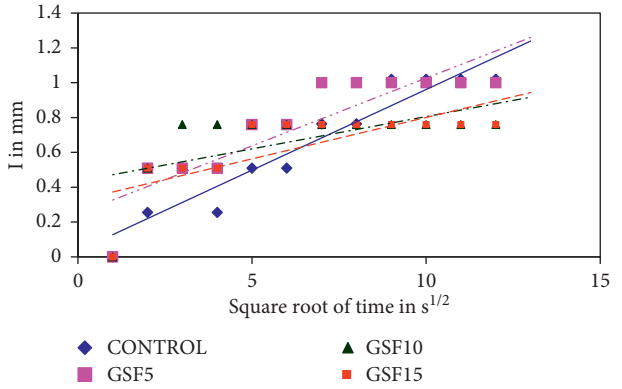

Figure 14: Sorption coefficient of GSF.

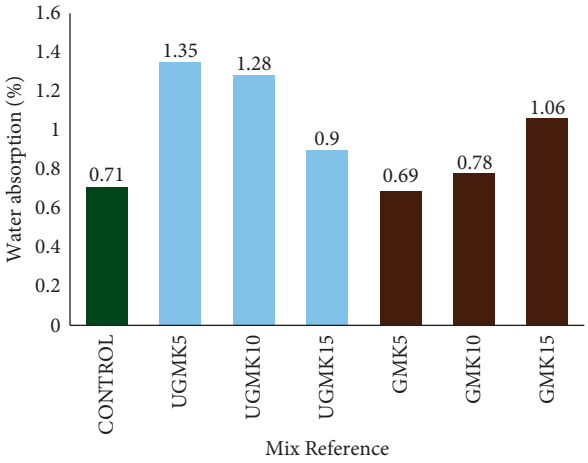

Figure 15: Water absorption values of MK.

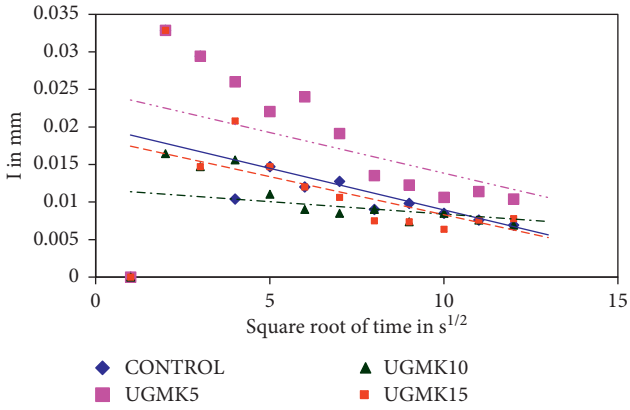

Figure 16: Sorption coefficient of UGMK.

effect of ground silica fume GSF in water absorption has already been discussed by the authors in their earlier work [4]; here, it is compared with the UGSF, and it is found that the specimen with GSF performs well in resisting the water absorption. Figure 12 shows the variation in the percentage of water absorption of specimens with SF.

On comparing our results with other research works [23], it was observed that when SF was used as a mineral

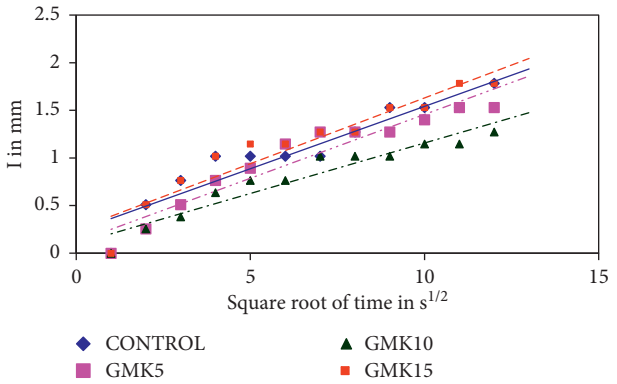

Figure 17: Sorption coefficient of GMK.

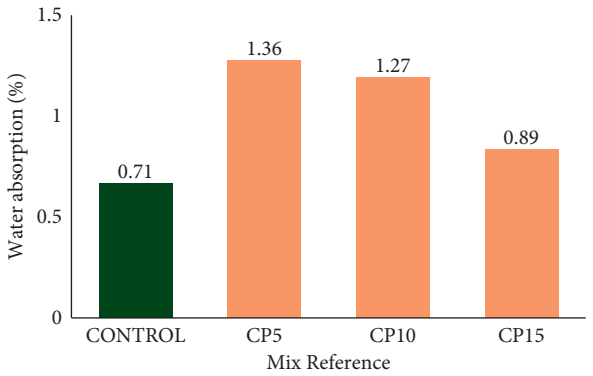

Figure 18: Water absorption values of CP.

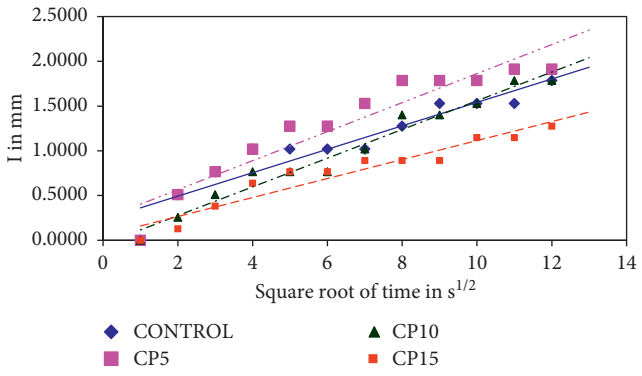

Figure 19: Sorption coefficient of CP.

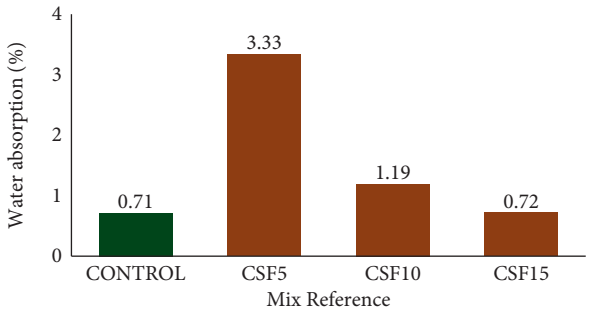

Figure 20: Water absorption values of CSF.

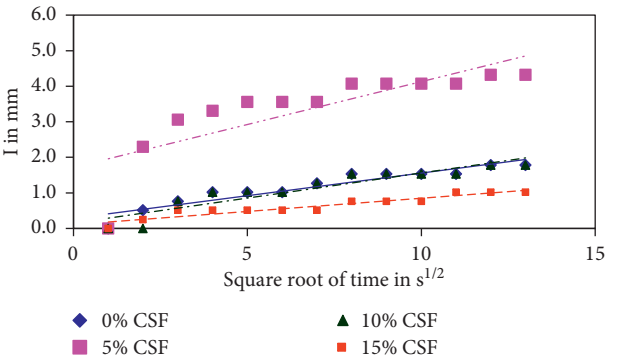

Figure 21: Sorption coefficient of CSF.

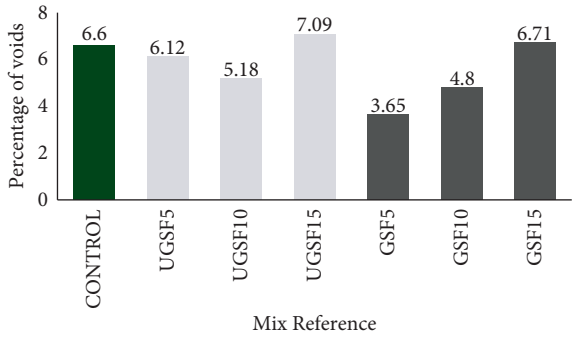

Figure 22: Porosity: SF.

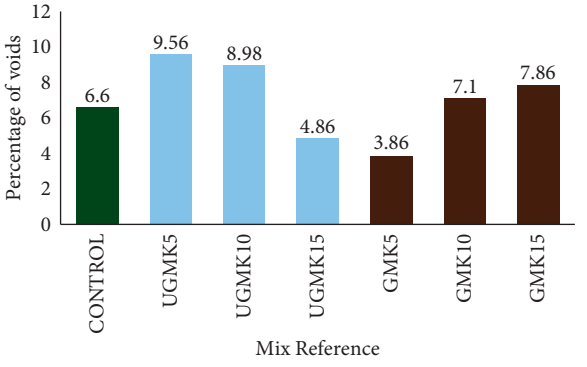

Figure 23: Porosity: MK.

admixture, the absorption values varied between 2.9% and 4.8%; here, all the water absorption values are less than 1% indicating a low water absorption percentage. On referring Table 5 and Figures 13 and 14, it is understood that the sorptivity specimens with UGSF showed higher values than GSF, but the values are well within the limit. UGSF15 also has shown the higher sorption values which means it has let more water to pass inside making it weak. Among the GSF-mixed specimens, GSF10 has shown a less sorptivity value of 0.002, and it indicates that the GSF10 has packed well the pores of concrete which would increase the strength and GSF has shown a higher sorption value, and higher sorption value indicates that the water permeation was more. GSF15 use with finer material in concrete did not improve the water

permeation as a major number of finer particles have dissolved or might have been wasted in the mixing process as air dust. As the water absorption characteristics of GSF 5 were less compared to those of GSF10 and GSF 15, the sorption coefficient values of GSF 10 and GSF15 were very less among all SF-mixed specimens. But, as discussed earlier, the sorption values involve large decimal values and the rounded values are presented in Table 5. It is just an indication to identify whether the permeation is under control; moreover, use of finer materials requires more water as the specific surface is increased which will affect the strength of concrete, so on an overall observation, GSF 5 can be considered as an optimum mix among all.

4.3. Water Absorption and Sorption Coefficient of MK-Blended Binary Mix. Figure 15 illustrates the water absorption values of different specimens from which it is understood that the ultrafine ground particles are unable to fill the pores and less water absorption was shown by UGMK15 specimens.

It is reported by Khatib et al. [24] that when metakaolin was used as a mineral admixture in the normal state, the water absorption values ranged between 4.2% and 5.4%. On comparing those with present experimental results, it was noted that water absorption values were less and the highest values are reported in UGMK and were found to be only 1.28% and 1.35%. The details are illustrated in Figure 14. From Table 5, it is clear MK-based specimens showed less sorption values irrespective of the nature whether unground and ground. The less sorption values indicate that the pores are properly packed. The less sorption values will lead to high strength, and it can be referred from the mechanical properties discussed by the same authors [13]. Much difference in sorption coefficient values was not identified among UGMK and GMK specimens. Though the sorption and water absorption characteristics are based on the masses of the specimens in water, the results are little contradictory as UGMK specimens show high water absorption than GMK and the difference was found to be less in sorption values. Sorption values use more decimal digits, and the difference can be noted when larger decimal digits were considered. But, it is clear that the effect of grinding has improved the water permeation resistance. Figures 16 and 17 show the sorption coefficient of UGMK- and GMK-based concrete specimens.

4.4. Water Absorption and Sorption Coefficient of CP-Blended Binary Mix. On observing the water absorption characteristics of the ceramic powder-mixed concrete specimen, it was found that CP15 has absorbed water less of about 0.88% than CP5 and CP10 for which the water absorption values were found to be 1.35% and 1.25%, respectively. Figure 17 shows the percentage of water absorbed by CP-mixed specimens compared with control. The sorption values of the specimens cast with CP are shown in Figure 16, and from Table 5, it is evident that the difference between CP5 and CP10 sorption values is very less. On comparing this with the strength results of Karthikeyan and Dhinakaran [11], it is evident that CP15 has exhibited more strength of 58.8 MPa than CP5 or CP10. CP is not finer than silica fume or MK, so its water absorption values are more than those of the specimens made with GSF, UGSF, GMK, or UGMK. But, among the ceramic-based concrete specimens, CP 15 has shown better water-resisting characteristics and lower sorption value which indicates that, with ceramic powder, a better resisting mix is possible with use of larger quantity of ceramic powder. Figures 18 and 19 show the percentage of water absorption and sorption values of CP with different replacement percentages compared with control.

4.5. Water Absorption and Sorption Coefficient of CSF-Blended Mix. Among ternary blended mix, CSF15 has shown a less water absorption of 0.72% and a lower sorption coefficient of 0.074 making it better than the other ternary blended mixes CSF5 and CSF10 which have shown a water absorption of 3.33% and 1.18% and sorptivity values of 0.241 and 141. This improvement in the mixes compared with those made with cement and CP alone on reduced water absorption and lower sorption coefficient is due to the addition of 1% finer SF along with CP in all the mixes. The presence of cement, SF, and CP provided a densely packed mix filling up the pores, and the water permeation was controlled. Figures 20 and 21 illustrate these details. On comparing these results with the strength results of Karthikeyan and Dhinakaran [4], it can be seen that the trend observed in compressive strength and tensile strength is repeated as in the previous cases also, CSF15 performed better than CSF5 and CSF10.

4.6. Sorptivity: Overall View. According to Güneyisi et al. [2], the increase in SF and MK content resulted in lower sorptivity in concrete. A similar result was obtained in the present work also and was due to the modification of microstructure and secondary hydration. The pozzolanaic materials such as SF or MK have the tendency to improve the pore-filling capability by reactions with the calcium hydroxide evolved during hydration, thereby making the interfacial transition zone dense, and in addition to this, the ultrafine property has helped them to some extent in filling up the pores and increasing strength or water absorption characteristics. The CP-blended mixes are not expected to show high pozzolanic reactions, and the resistance to water absorption is mainly compared with that of those made with UGSF, GSF, UGMK, and GMK, but this can be rectified on using them with other finer materials such as SF in suitable proportion, and this resulted in a better sorption coefficient for the CP-mixed specimens as to the pores got filled effectively.

4.7. Void Percentage in SF-Blended Binary Mix and Ternary Mix. Figure 22 shows the voids percentage for various mixes. The porosity values of all the specimens mostly reflected the water absorption results and also helped to arrive at a proper justification for the water absorption values. Control concrete showed a void percentage of 6.6. Though the finer silica fume helps in filling the pores in concrete,

sometimes, it may also get dissolved and get dispersed in the mix. This problem has occurred when the finer particles were added in large replacement levels such as 15% for UGSF and GSF-mixed specimens; they were unable to fill the gap of cement left over and were unable to control the formation of pores and showed a higher porosity among GSF specimens. The SF particles either got dispersed or dissolved making the concrete vulnerable to air voids which convey that the addition of finer particles may not yield better results. Other SF-mixed specimens UGSF5, UGSF10, GSF5, and GSF10 have restricted the presence of air voids and protected the specimens from being affected with pores. The specimen made with UGSF in all combinations (5%, 10%, and 15%) showed only moderate porosity value making it a possible supplementary material for cement.

4.8. Porosity: Void Percentage in MK-Blended Binary Mix. MK-mixed specimens, though cannot fill the pores as SF fills because of their size being coarser than SF, have put up a decent effort in filling up the pores due to their ability to form additional calcium silicate gel during hydration. UGMK when added in lower quantity has not much effect in filling the pores, and the porosity values were more than those of the control specimens; on slowly increasing the replacement, the results turned to be good for UGMK, and the one with 15% replacement showed a better filling capacity with less porosity values than control. Ground MK specimens have shown porosity values which reflected the water absorption and compressive strength values. A much less value of 3.86% was seen for GMK5, and the values of other GMK specimens showed a gradual increase in porosity as the replacement levels were increased. The void percentage was nominal for GMK 5 and GMK 10 and was higher for GMK15. So, adding ultrafine particles more in the mix affected the specimen by making it more porous. So, GMK 5 and GMK 10 were found to be better with nominal void percentages. These details are illustrated in Figure 23.

5. Conclusions

The following were the conclusions obtained from the experiments conducted:

(1) Using ultrafine mineral admixtures made with conventional mineral admixtures such as SF and MK in more significant replacement levels affected the water permeation resistance as the specimens dragged more water into them due to an increased specific surface area.

(2) Considering the UGMK and GMK specimens, samples with less replacement of GMK showed better resistance to water permeation. The water absorption and porosity values gradually increased from GMK5 to GMK 15.

(3) On comparing all the tests, GMK5 showed better resistance to water and air void permeation.

(4) The sorption values of GSF5, GSF10, and GSF15 were minor. The water absorption and porosity characteristics gradually increased, with GSF5 possessing lower water absorption and void percentage and GSF15 having higher values.

(5) Though GSF10 and GSF15 possessed lower sorption values, the values increased as finer particles were added to the mix. The presence of more ultrafine particles increased the water requirement of the mix due to their increased specific surface area. So, GSF 5 is considered an optimum replacement level among the blends made with UGSF and GSF.

(6) Among the binary blended mixes, GSF5, GMK5, and CP15 are the identified optimum mixtures resisting water absorption and air voids.

(7) In the ternary blended mixes, CSF15 showed better permeation resistance characteristics with less sorption coefficient and low water absorption and is identified as the optimum mix in this category.

(8) Also, adding CP in a significantly less quantity of 5% or 10% in binary or ternary blended mixes was ineffective in improving the resistance to water permeation.

Abbreviations

OPC: Ordinary Portland cement
C: Control concrete
SF: Silica fume
UGSF: Unground silica fume
GSF: Ground silica fume
UGMK: Unground metakaolin
GMK: Ground metakaolin
CP: Ceramic powder
CSF: Silica fume blended with ceramic powder.

Data Availability

All data are included in the manuscript.

Conflicts of Interest

The authors declare no conflicts of interest.

References

[1] T. Gonen and S. Yazicioglu, "The influence of compaction pores on sorptivity and carbonation of concrete," *Construction and Building Materials*, vol. 21, no. 5, pp. 1040–1045, 2007.

[2] E. Güneyisi, K. Mermerdaş, and K. Mermerdas, "Strength deterioration of plain and metakaolin concretes in aggressive sulfate environments," *Journal of Materials in Civil Engineering*, vol. 22, no. 4, pp. 403–407, 2010.

[3] C. S. Poon, S. C. Kou, and L. Lam, "Compressive strength, chloride diffusivity and pore structure of high performance metakaolin and silica fume concrete," *Construction and Building Materials*, vol. 20, no. 10, pp. 858–865, 2006.

[4] B. Karthikeyan and G. Dhinakaran, "Strength and durability studies on high strength concrete using ceramic waste powder," *Structural Engineering & Mechanics*, vol. 61, no. No.2, pp. 171–181, 2017.

[5] B. Karthikeyan, R. Kathyayini, V. Aravindh kumar, V. Uthra, and S. Senthil Kumaran, "Effect of dumped iron ore tailing waste as fine aggregate with steel and basalt fibre in improving the performance of concrete," *Materials Today Proceedings*, vol. 46, pp. 7624–7632, 2021.

[6] B.-W. Jo, C.-H. kim, G.-h. Tae, and J.-B. Park, "Characteristics of cement mortar with nano-SiO2 particles," *Construction and Building Materials*, vol. 21, no. 6, pp. 1351–1355, 2007.

[7] F. Pacheco-Torgal, S. Miraldo, Y. Ding, and J. A. Labrincha, "Targeting HPC with the help of nanoparticles: an overview," *Construction and Building Materials*, vol. 38, pp. 365–370, 2013.

[8] N. Ali and S. Riahi, "TiO_2 nanoparticles effects on physical, thermal and mechanical properties of self-compacting concrete with ground granulated blast furnace slag as binder," *Energy and Buildings*, vol. 43, pp. 995–1002, 2011.

[9] S. Riahi and A. Nazari, "RETRACTED: physical, mechanical and thermal properties of concrete in different curing media containing ZnO2 nanoparticles," *Energy and Buildings*, vol. 43, no. 8, pp. 1977–1984, 2011.

[10] N. Ali and S. Riahi, "The effects of ZnO2 nano-particles on split tensile strength of self-compacting concrete," *Journal of Experimental Nanoscience*, vol. 7, pp. 491–512, 2012.

[11] B. Karthikeyan and G. Dhinakaran, "Influence of ultrafine TiO2 and silica fume on performance of unreinforced and fiber reinforced concrete," *Construction and Building Materials*, vol. 161, pp. 570–576, 2018.

[12] B. Karthikeyan, A Subin, and T Muthulakshmi, "High strength concrete using Ultra-fine TiO_2 and Basalt fiber- A study on Mechanical and Durability characteristics," *The Romanian Journal of Materials*, vol. 50, no. 1, pp. 51–58, 2020.

[13] B. Karthikeyan and G Dhinakaran, "Effect of ultra-fine SiO_2 and metakaolin on high strength concrete in aggressive environment," *Scientia Iranica*, vol. 24, no. 1, pp. 1–10, 2017.

[14] B. Karthikeyan, N. Chidambaram, J. Srikanth, and G. Dhinakaran, "Mechanical properties and micro structure characteristics of ternary blended concrete with ceramic powder and SiO_2," *Asian Journal of Scientific Research*, vol. 8, no. 3, pp. 291–303, 2015.

[15] J. Chai, K. Kiattikomol, V. Sata, and T. Leekeeratikul, "Use of ground coarse fly ash as a replacement of condensed silica fume in producing high-strength concrete," *Cement and Concrete Research*, vol. 34, pp. 549–555, 2004.

[16] B. Felekoğlu, S. Türkel, and H. Kalyoncu, "Optimization of fineness to maximize the strength activity of high-calcium ground fly ash-Portland cement composites," *Construction and Building Materials*, vol. 23, pp. 2053–2061, 2009.

[17] S. Teng, T. Y. D. Lim, and B. Sabet Divsholi, "Durability and mechanical properties of high strength concrete incorporating ultra fine Ground Granulated Blast-furnace Slag," *Construction and Building Materials*, vol. 40, pp. 875–881, 2013.

[18] L. Basheer, J. Kropp, and D. J. Cleland, "Assessment of the durability of concrete from its permeation properties: a review," *Construction and Building Materials*, vol. 15, no. 2-3, pp. 93–103, 2001.

[19] Q. Niu, N. Feng, J. Yang, and X. Zheng, "Effect of superfine slag powder on cement properties," *Cement and Concrete Research*, vol. 32, no. 4, pp. 615–621, 2002.

[20] ASTM150, *Standard Specification for Portland Cement*, ASTM International, West Conshohocken, PA, USA, 2006.

[21] ASTM C 1585-13, *Standard Test Method for Measurement of Rate of Absorption of Water by Hydraulic-Cement Concretes*, ASTM International, West Conshohocken, PA, USA, 2011.

[22] ASTM C 642-13, *Standard Test Method for Density, Absorption, and Voids in Hardened Concrete*, ASTM International, West Conshohocken, PA, USA, 2021.

[23] H. Abdul Razak, H. K. Chai, and H. S. Wong, "Near surface characteristics of concrete containing supplementary cementing materials," *Cement and Concrete Composites*, vol. 26, no. 7, pp. 883–889, 2004.

[24] J. M. Khatib, R. M. Clay, and R. M. Clay, "Absorption characteristics of metakaolin concrete," *Cement and Concrete Research*, vol. 34, no. 1, pp. 19–29, 2004.

[25] V. V Kumar and S. S Kumaran, "Friction material composite: types of brake friction material formulations and effects of various ingredients on brake performance-a review," *Materials Research Express*, vol. 6, 2019.

[26] S. Senthil Kumaran, S. Muthukumaran, D. Venkateswarlu, G. K. Balaji, and S. Vinodh, "Eco-friendly aspects associated with friction welding of tube-to-tube plate using an external tool process," *International Journal of Sustainable Engineering*, vol. 5, no. 2, pp. 120–127, 2012.

[27] S. Senthil Kumaran and A. Daniel Das, "Friction welding joints of SA 213 tube to SA 387 tube plate boiler grade materials by using clearance and interference fit method," *Materials Today Proceedings*, vol. 5, no. 2, pp. 8557–8566, 2018.

Hindawi
Advances in Civil Engineering
Volume 2022, Article ID 4038344, 10 pages
https://doi.org/10.1155/2022/4038344

Research Article

Mechanical and Durability Studies on Ficus exasperata Leaf Ash Concrete

K. S. Elango,[1] B. Prabu,[2] S. Sathish,[3] Alagar Karthick,[4,5] V. Sampathkumar,[6] Sanjeev Kumar,[7] V. Mohanavel,[8] M. Ravichandran,[9] M. Muhibbullah,[10] and Sameh M. Osman[11]

[1]*Department of Civil Engineering, KPR Institute of Engineering and Technology, Coimbatore 641407, Tamil Nadu, India*
[2]*Department of Civil Engineering, Sona College of Technology, Salem 636005, Tamil Nadu, India*
[3]*Department of Mechanical Engineering, KPR Institute of Engineering and Technology, Coimbatore, Tamil Nadu, India*
[4]*Renewable Energy Lab, Department of Electrical and Electronics Engineering, KPR Institute of Engineering and Technology, Coimbatore 641407, Tamil Nadu, India*
[5]*Departamento de Quimica Organica, Universidad de Cordoba, Edificio Marie Curie (C-3), Ctra Nnal IV-A, Km 396, E14014, Cordoba, Spain*
[6]*Department of Civil Engineering, Sathyabama Institute of Science and Technology, Chennai 600119, Tamil Nadu, India*
[7]*Department of Civil Engineering, Graphic Era Deemed to Be University, Bell Road, Clement Town 248002, Dehradun, Uttarakhand, India*
[8]*Centre for Materials Engineering and Regenerative Medicine, Bharath Institute of Higher Education and Research, Chennai 600073, Tamil Nadu, India*
[9]*Department of Mechanical Engineering, K. Ramakrishnan College of Engineering, Trichy 621112, Tamil Nadu, India*
[10]*Department of Electrical and Electronic Engineering, Bangladesh University, Dhaka 1207, Bangladesh*
[11]*Chemistry Department, College of Science, King Saud University, P.O. Box 2455, Riyadh 11451, Saudi Arabia*

Correspondence should be addressed to M. Muhibbullah; m.muhibbullah@bu.edu.bd

Received 23 October 2021; Revised 31 December 2021; Accepted 3 January 2022; Published 20 January 2022

Academic Editor: Wenjie Ge

This paper reports the effect of snake grass (SG) fibers in Ficus exasperata Leaf Ash (FELA) concrete. Snake grass fibers of percentages 0.5, 1, 1.5, and 2 were used in this investigation. Tests of compressive strength, split tensile strength, and flexural strength and durability studies of salt resistance, sulphate resistance, and impact energy resistance were determined, and the test results are discussed in detail. Test results revealed that FELA ash of 15% replacement in cement showed remarkable binding property. Moreover, incorporation of snake grass fiber in concrete improves the strength, postcracking resistance, and energy absorption. It is also observed that 1.5% snake grass fiber incorporation in concrete exhibited better strength properties and energy absorption property than 0.5% and 1%. Also, beyond 1.5%, there is significant reduction in workability property. Regardless of durability property, the mix containing 1.5% snake grass fiber has shown better resistance against durability when compared with other mixes. It is also observed that penetration of chloride and sulphate ions made slight deterioration at sharp edges. Moreover, test results revealed that applications of FELA concrete with snake grass fiber can be effectively expanded in the construction industry.

1. Introduction

Concrete is the most widely used material next to water all over the world. The construction activity can be enhanced by focusing attention towards sustainability in addition to performance and functional ability. The main objective of the sustainable growth is to ensure the benefits for future generation without affecting the needs of the present generation [1, 2]. Binder is an essential material that combines some materials together to develop a cohesive mechanically

or chemically by adhesion or cohesion. In construction work, Portland cement is used as a binder in concrete which holds aggregates together [3]. Portland cement can be categorized into various types of cement according to the raw materials used and use of additives and adjustment of chemical composition. In fact, Ordinary Portland Cement (OPC) is the most important type which is commercially available everywhere and another choice known as Portland Pozzolana Cement (PPC) is increasingly in use in this decade due to its high performance [4]. Infrastructural development makes concrete be used in wide applications because of its enhanced compressive strength which is an added advantage. It also has few limitations such as lack in toughness and lesser tensile strength. During application of load, occurrence of cracks is observed and the crack scale is in different extent under every magnitude of load. Mechanical and durability properties of the concrete have improved when concrete is blended with fly ash, lime stone powder, and rice husk ash in the percentage of 20, 10, and 5 [1]. At fracture point of view, concrete with no reinforcement has demonstrated lesser tensile strength and minimal strain [2]. Concrete brittleness gets weakened when crumb rubber content is increased inside concrete [5]. Higher ductility and toughness have been observed in Engineered Cementitious Composite (ECC). The volume of fiber addition by 2% produces 3% increment in maximum tensile strain [6–8]. ECC with nonexistence of coarse aggregate has improved brittleness owing to the presence of coarse aggregate but affects the fiber distribution in concrete [9]. Fiber is a tiny material which acts as reinforcing element in concrete. The parameter aspect ratio (length to its diameter) illustrates the shape of fiber and aspect ratio is typically ranging from 20 to 150. Fibers are broadly classified as metallic fibers, mineral fibers, synthetic fibers, and natural fibers. Fibers such as low carbon steel, stainless steel, galvanized iron, and aluminum are belonging to metallic fiber category while asbestos, glass, and carbon come under the category of mineral fibers. Synthesized polymers of tiny molecules are bonded together to form synthetic fibers and few synthetic fibers are polyester, nylon, polypropylene, and polyethylene. Natural fibers are formed due to geological processes or from plants and animal bodies. Apart from static loads, concrete structure is also subjected to impact loads due to earthquakes, machine vibration, natural calamities, and so on. Impact load in the structures makes concrete fail suddenly but when fibers are incorporated in the concrete structure it overcomes the brittle failure [3, 10]. Also, energy absorption property increased with inclusion of silica fume materials, steel fibers, and polypropylene fibers. Hybrid fibers result in overall improvement and higher performance and produce better mechanical properties [11]. The presence of carbohydrate content in cementitious material improves the service life of structures and secondary cementitious material with silica reaction improves strength in concrete [12]. 15% replacement of *Ficus exasperata* Leaf Ash shows better mechanical property and when the replacement percentage has increased, strength gets decreased [4, 13–16]. Increased compressive strength of cement paste enhances the compressive strength of the concrete and addition of nanosilica (NS) modifies the microstructure property of hardened cementitious paste [17]. Inclusion of mineral admixtures in high volume boosts the concrete strength. Specimens cured under steam curing and high pressure steam curing possess improved compressive strength compared to other curing conditions [18]. Better filler property is observed in Ennore sand having grade I (70%) and grade II (30%) [19]. Fiber orientation influences the mechanical properties of the concrete [20]. Steel fibers packed with high density accomplish high compressive strength [21]. More researches are being carried out utilizing various fibers like steel fibers, polypropylene fibers, and carbon fibers. Nevertheless, limited researches have been carried out using steel fiber and snake grass fibers. In this present study, an attempt has been made to investigate the mechanical and impact resistance properties of concrete containing different percentages of snake grass hybrid fibers and feasibility of using *Ficus exasperata* Leaf Ash in concrete as a partial replacement for Ordinary Portland Cement (OPC) [22]. Steel fiber addition in concrete improves impact energy absorption capacity [23]. Supplementary cementitious materials (SCMs) such as rice husk ash, fly ash, bottom ash, and ground granulated blast furnace slag in concrete increase strength and durability properties and they also make concrete more economical and environmentally friendly. Inclusion of steel fibers increases the ductility and energy absorption property in concrete. In addition, addition of various fibers in the concrete exhibits various kinds of action in the behaving property [24]. Three kinds of actions include toughening, reinforcing, and anticracking. Upon environmental exposure, cracks formation takes place in the structures. Major cracks formed in the structure are of shrinkage cracks. Those cracks can be arrested and the action of preventing or arresting the crack generation in the structures is called anticracking. Moreover, mechanical properties of the concrete can be improved by inclusion of the fibers and the effect caused due to cracks can be minimized or arrested. The action taking place due to this effect is known as reinforcing action. Further, it also increases the toughness property of the concrete and it refers to toughening action. During the use of steel fibers, compaction using vibrator can be preferred for even distribution of fibers which can increase the concrete density that indirectly improves the mechanical properties of the concrete. In order to improve the ductile property in concrete, fibers can be added in optimum percentage [25]. Volume addition of fibers by 2% increases the tensile strength of concrete by 3%. Engineered Cement Composite (ECC) incorporation instead of coarse aggregates enhances the fiber distribution in the concrete. Fly ash (FA) addition in ECC greatly reduces the emission percentage of carbon dioxide and also improves the toughness and ductility. It is noticed that FA addition greatly decreases the heat of hydration and it also makes the concrete economical [26].

2. Materials

2.1. Cement and Aggregates. Ordinary Portland Cement (OPC) grade 53 with specific gravity of 3.10, fineness of 3.05%, and consistency of 31% has been used in this study.

Initial setting time and final setting time have been recorded and it is found to be 85 and 290 minutes, respectively. Crushed blue granite metal (coarse aggregate (CA)) having a specific gravity of 2.72 and M-sand (fine aggregate (FA)) with a specific gravity of 2.65 are used. OPC grade-53 cement and coarse aggregates were purchased in APAT Crushers, Erode, Tamil Nadu, India.

2.2. Fibers. Snake grass fibers (*Sansevieria ehrenbergii*) having a diameter of 45 μm and tensile strength ranging 240–450 MPa have been used in this present study (Figure 1). Furthermore, to know the morphological behavior, scanning electron microscope study on snake grass fiber has been carried out at PSG College of Technology, Coimbatore, Tamil Nadu, India (Figure 2). The scanning electron microscope (SEM) image revealed that the shape of the fiber cross section is round and it is mainly used to determine the strength of the fiber. The snake grass fiber has very low density associated with other biofibers like flax, sea grass, and oil palm but has higher density than elephant grass, ramie, and petiole bark. The transverse and the longitudinal direction of fiber diameter are around 20–240 μm and 25–250 μm using optical microscopy.

2.3. Ficus exasperata Leaf Ash (FELA). *Ficus exasperata* leaf (sand paper tree) was gathered from Palakkad district, Kerala (Figure 3). Gathered leaves were dried at natural sunlight and heated over at muffle furnace at a temperature of 500°C and while heating, the ash was subjected to calcination. The ash obtained after calcination was sieved through 90 microns (μ) to attain the required fineness. In order to investigate the presence of chemical compounds in FELA, chemical properties have been studied at Sona College of Technology, Salem, Tamil Nadu, India. FELA comprises 81.45% SiO_2, 5.88% CaO, 3.78% SO_3, 3.02% K_2O, 1.85% Al_2O_3, and 1.95% Fe_2O_3 [4]. The chemical test results proved that FELA can be effectively used as supplementary cementitious material since it satisfies the requirement for cementitious material through SiO_2 percentage in the ash content. Furthermore, to observe the morphological behavior of FELA, scanning electron microscope test has been carried out on calcined *Ficus exasperata* Leaf Ash at Karunya University, Coimbatore, Tamil Nadu, India. The SEM image of FELA proved that the particles present are in spherical and round shape (Figure 4).

2.4. Mix Design. The grade used in this present study is M25 and the mix design has been carried out in accordance with IS 10262–2009 [27, 28]. Mix produced without snake grass fiber and *Ficus exasperata* Leaf Ash is considered as conventional control mix and designated as CC. Four mixes were prepared with different percentages of snake grass fiber. The percentage of snake grass fiber used was 0.5, 1, 1.5, and 2 by concrete volume. In order to prepare FELA-SG concrete, coarse aggregate and fine aggregate are mixed thoroughly in dry state for 60 seconds. FELA ash (15% weight of total cement) was added with the dry mix and thorough mixing was carried out for two minutes. In continuation with the process, potable water available at KPR Institute of Engineering and Technology (KPRIET) college laboratory was added and homogenously mixed for five minutes. Snake grass fibers of specified amount required as per mix design were added and mixed carefully in order to achieve consistent distribution inside the concrete. Table 1 shows the mix proportion achieved for various mixes. Mix ID MSG represents the mix produced with snake grass fiber and the value mentioned in suffix of each mix ID shows the percentage of snake grass fiber used.

Figure 1: Extracted fiber of *Sansevieria ehrenbergii* plant.

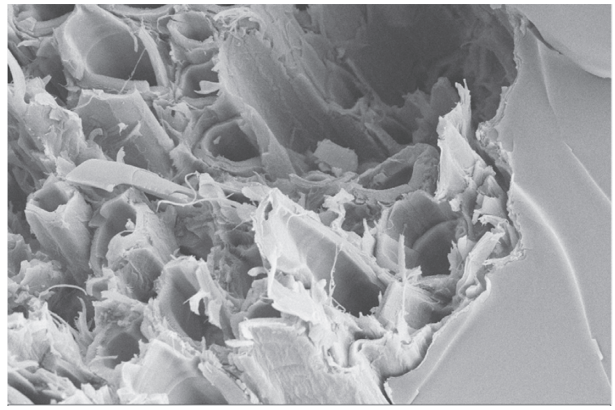

Figure 2: Scanning electron microscope image of *Sansevieria ehrenbergii* fiber.

Figure 3: *Ficus exasperata* leaf before drying process.

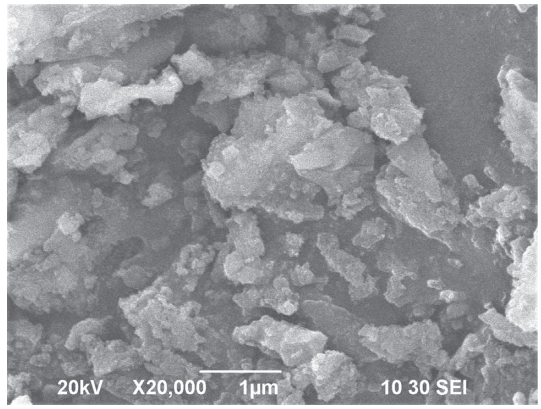

Figure 4: Scanning electron microscope image of calcined *Ficus exasperata* Leaf Ash.

Table 1: Mix proportion of various mixes.

Mix ID	Cement		FELA		Snake grass fiber		Fine aggregate (kg/m^3)	Coarse aggregate (kg/m^3)
	%	kg/m^3	%	kg/m^3	%	kg/m^3		
CC	0	428	0	—	0	—	518.50	1195.60
MSG0.5	85	364	15	64	0.5	2.15	518.50	1195.60
MSG1.0	85	364	15	64	1	4.30	518.50	1195.60
MSG1.5	85	364	15	64	1.5	6.45	518.50	1195.60
MSG2.0	85	364	15	64	2	8.60	518.50	1195.60

3. Experimental Program

3.1. Mechanical Properties. Totally 30 cubes (150 mm × 150 mm × 150 mm), cylinders (150 mm in diameter and 300 mm in height), and beams (100 mm × 100 mm × 500 mm) are cast to study the compressive, split tensile, and flexural strength of concrete made with FELA and SG fibers. Among all the tests, compressive strength test has more importance because, in most of the structural applications, concrete is subjected to compressive stress rather than tensile stress. The load was applied gradually without shock and continuously increased at the rate of 14 N/sq.mm/min until achieving the resistance of the specimen. Average of three cubes was tested for each mix to study the compressive strength properties at the age of 7 and 28 days. Regardless of split tensile strength, the cylindrical specimen was kept horizontally in compression testing machine between the platens so that applying of load leads to failure of the cylindrical specimen along the vertical diameter. It should also be ensured that upper platen is parallel with lower platen. Load on the specimen was applied gradually at a nominal rate in the range of 1.2 N/sq.mm/min. Flexural strength was determined by keeping the specimen mounted on the two roller beds of 38 mm diameter and the center to center distance between the two rollers was kept as 400 mm. The load was applied at the compression surface of the specimen through the couple of rollers mounted above at the distance of 133 mm from center to center. Load was applied uniformly at the rate of 1.80 kN/min till the specimen gets failed [29, 30].

3.2. Durability Properties. The durability tests such as resistance against salt and sulphate attack were conducted on the concrete cube specimens of 100 mm × 100 mm × 100 mm. The 28-day cured cube specimens were dried in room temperature and the weight (W_1) of the cubes was measured. Then, the specimens were immersed in NaCl salt solution with 3.5% concentration (equivalent to sea water). Chloride solution was prepared in plastic tubs and covered temporarily to arrest the evaporation and dust formation. The pH value of the solution was monitored periodically and the solution was replaced every month. Specimens were also tested against sulphate attack. The test procedure was the same as that of chloride (NaCl) attack. The specimens were immersed in magnesium sulphate ($MgSO_4$) solution with 5% concentration. $MgSO_4$ was selected since it is more aggressive than $CaSO_4$. The immersed specimens in salt and sulphate solution were taken out at the age of 28, 56, 90, and 180 days for examination. The examinations such as visual appearance, change in weight (W_2), and residual compressive strength studies were done to know the properties of the concrete subjected to salt attack.

Percentage of loss in weight can be calculated using the following equation:

$$\text{percentage of weight loss}\,(\%) = \frac{W_1 - W_2}{W_1}, \tag{1}$$

where W_1 is the specimen weight before exposure to solution in kg and W_2 is the specimen weight before exposure to solution in kg.

3.3. Impact Energy Test. The cylindrical specimen of size 150 mm in diameter and 64 mm in height was cast to know the impact energy absorption capacity [24, 31]. This test was conducted in accordance with ACI 544.2R-89 (reapproved in 2009) [32] at the age of 28 days and 56 days. Base plate with lugs was used to support the specimen cast with PVC pipe of 63.5 mm in diameter which was kept above the specimen through steel ball of 63.5 mm which falls on the specimen. The number of blows taken for the first crack and final failure crack was noticed and impact resistance energy has been calculated using (2). Test setup used for determining impact energy is represented schematically in Figure 5.

$$E_{\text{imp}} = \text{N.m.g.h}, \tag{2}$$

where E_{imp} is the impact energy in *J*, *N* is the number of blows, *m* is the mass of drop hammer in kg, $g = 9.81\ \text{m/s}^2$, and *h* is the releasing height of drop hammer in *m*.

4. Results and Discussion

4.1. Mechanical Properties. Mechanical properties such as compressive strength, split tensile strength, and flexural strength were performed and test results are tabulated in Table 2. Also, statistical analysis for all the mixes was also done to know the normal distribution of results.

Test results at the age of 28 days revealed that the mix made with 0.5%, 1%, and 1.5% snake grass fiber exhibited higher strength properties than the conventional control mix. When compared to CC, compressive strength of FELA concrete increased by 11.11%, 22%, and 22.9% for the mixes having 0.5%, 1%, and 1.5% SG fibers. This can be attributed to the fact that the addition of fibers made significant effect on improvement of test results. It has also been observed that when the SG fiber addition is increased beyond 2%, there has been a decrease in compressive strength properties. The decrement of compressive strength is due to poor workability, when high percentage fibers are added, which indirectly affected the cohesiveness and led to balling effect. However, the mix with suitable admixture for workability could show remarkable strength properties with 2% SG fiber addition [33]. Regardless of split tensile strength, the trend observed in compressive strength property is as follows. The mix made with 0.5%, 1%, and 1.5% has shown 5.17%, 21.3%, and 31% higher split tensile strength than the conventional control mix. Furthermore, 5.52%, 13.2%, and 17.4% lesser flexural strength could be observed compared to conventional control mix having 0.5%, 1%, and 1.5% SG fibers. In both cases, when the percentage addition of SG fibers was increased by 1.5%, there was a gradual decrease in strength properties. This is due to deprived workability. Performed statistical analysis proved that better distribution of test results are noticed on all the test parameters. Test results arrived are graphically Figure 6 represented Figure 7 in Figure 8. In addition, regression analysis has also been carried out to understand the relationship between the mechanical property and the percentage of fiber addition in the concrete and the same is shown in (3)–(5). Moreover, to measure the fitness of the curve, R^2 value is determined and mentioned in

$$R^2 = 0.952, \text{fck}\,(28) = 27.90 + 10.34\text{sg} - 3.14\text{sg}^2, R^2 = 0.952, \tag{3}$$

$$R^2 = 0.953, \text{fst}\,(28) = 2.80 + 1.072\text{sg} - 0.35\text{sg}^2, R^2 = 0.953, \tag{4}$$

$$R^2 = 0.950, \text{fct}\,(28) = 3.58 + 0.73\text{sg} - 0.22\text{sg}^2, R^2 = 0.950, \tag{5}$$

where fck is the compressive strength at 28 days (MPa), fst is the split tensile strength at 28 days (MPa), fct is the flexural strength at 28 days (MPa), and sg is the percentage of snake grass fiber (%).

4.2. Durability Properties. Specimens subjected to salt and sulphate attack have been examined visually and mechanically. Test results revealed that the concrete produced with *Ficus exasperata* Leaf ash and snake grass fiber has better resistance against salt and sulphate attack and the results are presented in Table 3. Results compared were noticed at the age of 180 days. Test results demonstrated that, when compared to control mix, mix $MSG_{0.5}$ shows 0.85-fold lesser percentage of weight retention when subjected to salt attack solution. Similarly lesser percentage of weight retention was observed in the mixes made with 1.0 and 2.0% snake grass fibers. $MSG_{1.5}$ has demonstrated 0.45-fold increase in percentage of weight retention when compared to control mix. The same trend of results was observed in the specimens when subjected to magnesium sulphate attack solution. At the age of 180 days, residual compressive strength was determined. Test results exhibited that $MSG_{1.5}$ mix showed better retention in compressive strength than conventional control mix. The same trend was observed in percentage of weight retention property. Upon visual observation, all the mixes immersed in NaCl solution have no change in color whereas specimens which are soaked in $MgSO_4$ solution showed slight whitish layer appearance. This can be attributed to the fact that displayed calcium in the cement matrix shows whitish appearance when immersed in magnesium sulphate solution. Moreover, slight deterioration at sharp edges observed is due to the effect of chemical solutions. The penetration of chloride and sulphate ions in the concrete mix makes the matrix bonding disintegrate and leads to deterioration at sharp edges and this occurred since edges contain mortar portion rather than concrete portion. It was also noticed that incorporation of FELA has magnanimous effect on improving the durability properties.

4.3. Impact Resistance Energy. Impact energy test results are noticed at the age of 28 days and 56 days and the results are shown in Table 4 and graphically represented in Figure 9. Test results revealed that the mix with 1.5% snake grass fiber showed higher impact energy resistance than the mix made with 0.5% and 1%. It is also been noticed that when the percentage addition of fiber exceeds 1.5%, there was a gradual decrement in impact energy property. This can be attributed to the fact that the increase in fiber content results in lesser workability and lesser impact energy property. This

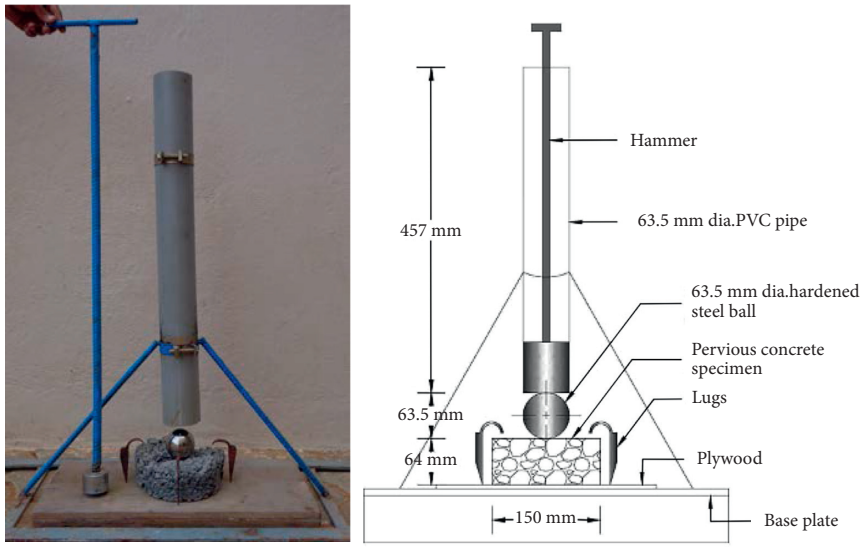

Figure 5: Impact energy test setup. (a) Figure. (b) Schematic figure.

Table 2: Strength properties of various mixes.

Mix ID	Age at testing	Compressive strength (MPa)		Split tensile strength (MPa)		Flexural strength (MPa)	
		Mean	SD	Mean	SD	Mean	SD
CC	7	20.50	1.51	1.95	0.18	3.10	0.33
	28	28.35	1.38	2.90	0.23	3.62	0.43
$MSG_{0.5}$	7	23.20	1.03	2.35	0.17	3.27	0.29
	28	31.50	2.03	3.05	0.24	3.82	0.26
$MSG_{1.0}$	7	25.35	0.74	2.60	0.14	3.40	0.25
	28	34.85	1.79	3.52	0.24	4.10	0.30
$MSG_{1.5}$	7	28.25	1.01	2.94	0.05	3.65	0.10
	28	37.50	1.28	3.80	0.18	4.25	0.35
$MSG_{2.0}$	7	26.50	1.00	2.60	0.20	3.50	0.37
	28	35.50	1.88	3.42	0.33	4.12	0.45

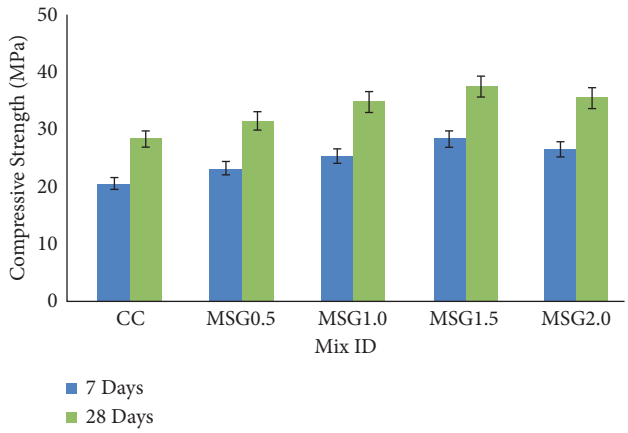

Figure 6: Compressive strength of various mixes.

same trend of results is observed in compressive strength property as well. It is evident that impact energy resistance has a direct relationship with compressive strength. Specimens subjected to impact force are shown in Figure 10 and the observed failure pattern during failure crack is clearly visible.

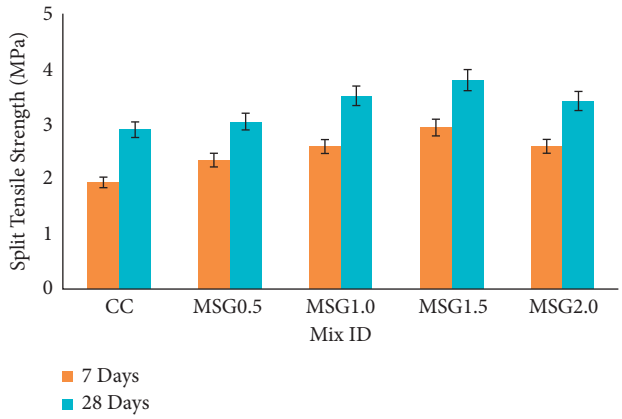

Figure 7: Split tensile strength of various mixes.

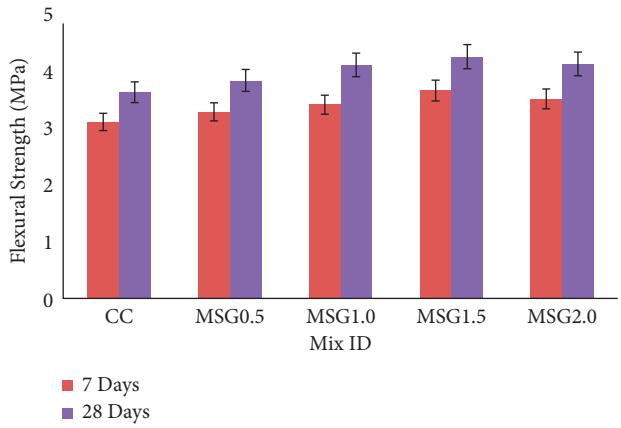

Figure 8: Flexural strength of various mixes.

Table 3: Durability properties of various mixes.

Mix ID	Percentage of weight retention at 180 days		Residual compressive strength at 180 days (%)	
	NaCl	$MgSO_4$	NaCl	$MgSO_4$
CC	97.48	97.15	2.45	2.32
$MSG_{0.5}$	96.60	95.20	2.52	2.40
$MSG_{1.0}$	96.65	95.70	2.58	2.52
$MSG_{1.5}$	97.90	96.50	2.85	2.78
$MSG_{2.0}$	95.29	94.50	2.20	2.00

Table 4: Impact energy of various mixes.

Mix ID	Number of blows (N)				Impact energy (Nm)			
	28 days		56 days		28 days		56 days	
	First crack	Failure crack	First crack	Failure crack	First crack	Failure crack	First crack	Failure crack
CC	455	462	578	596	2040	2071	2591	2672
$MSG_{0.5}$	467	478	586	602	2094	2143	2627	2699
$MSG_{1.0}$	472	485	599	613	2116	2174	2685	2748
$MSG_{1.5}$	488	493	610	621	2188	2210	2735	2784
$MSG_{2.0}$	471	478	602	607	2112	2143	2699	2721

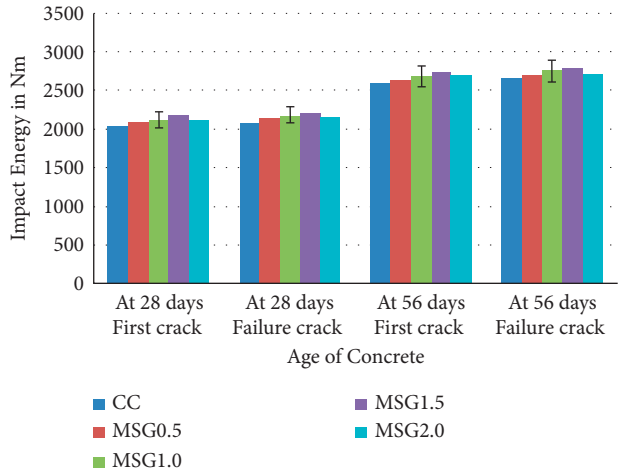

Figure 9: Impact energy of various mixes.

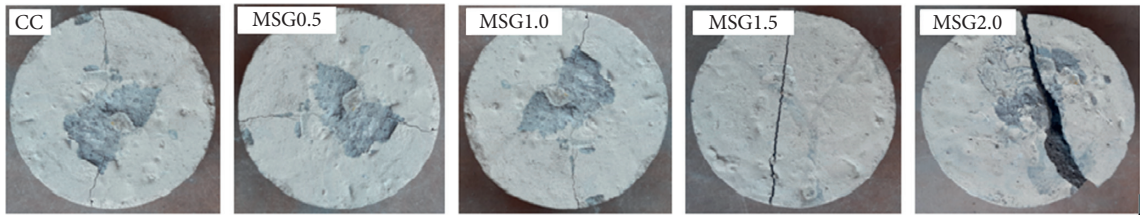

Figure 10: Specimens tested against impact force.

5. Conclusion

The mechanical properties such as compressive strength, split tensile strength, flexural strength, and impact energy resistance and durability properties such as salt resistance and sulphate resistance were demonstrated and the following conclusions are drawn:

(1) Ordinary Portland Cement replaced with 15% of FELA has shown improved and excellent mechanical and durability properties. Furthermore, it is observed that chemical composition confirms the feasibility of using FELA as mineral admixture in concrete.

(2) Snake grass fibers, in addition to FELA concrete, showed remarkable mechanical and impact resistance properties. This can be attributed to the fact that round morphological structure influenced and improved strength properties which is confirmed by microstructural study.

(3) It was observed that concrete with 1.5% of snake grass fibers possessed higher strength and impact energy than concrete containing 0.5% and 1% snake grass fibers. 22.9% increase in compressive strength was noticed in $MSG_{1.5}$ when compared to conventional control mix.

(4) There was a gradual decrease in strength and impact energy when addition of snake grass fibers exceeded 1.5%. This can be attributed to the fact that when the amount of fiber addition increases, it shows lesser workability and results in decrease in strength and impact resistance property. The specimens with 15% of FELA and 1.5% of snake grass have demonstrated better performance in terms of mechanical properties and impact energy and also have better postcracking resistance than conventional control mix.

(5) Regardless of durability properties, among all mixes, $MSG_{1.5}$ has demonstrated better strength and weight retention against chloride and sulphate solution attack. This can be attributed to the fact that concrete with 1.5% addition of SG fibers showed denser effect when compared to other mixes that would act as barrier medium for penetration of chloride and sulphate ions.

(6) From the test results, it was evident that concrete made with *Ficus exasperata* Leaf Ash as a partial replacement for cement showed better strength and durability properties and it can be used for sustainable construction practices.

Data Availability

The data used to support the findings of this study are included within the article.

Conflicts of Interest

The authors declare that there are no conflicts of interest regarding the publication of this article.

Acknowledgments

Alagar Karthick gratefully acknowledges group FQM-383 from Universidad de Cordoba, Spain, for the provision of an honorary visiting research position in the group. This project was funded by the Researchers Supporting Project (no. RSP-2021/405), King Saud University, Riyadh, Saudi Arabia.

References

[1] P. Kathirvel, V. Saraswathy, S. P. Karthik, and A. S. S. Sekar, "Strength and durability properties of quaternary cement concrete made with fly ash, rice husk ash and limestone powder," *Arabian Journal for Science and Engineering*, vol. 38, no. 3, pp. 589–598, 2013.

[2] K. S. Elango and V. Revathi, "Fal-G binder pervious concrete," *Construction and Building Materials*, vol. 140, pp. 91–99, 2017.

[3] K. S. Elango and V. Revathi, "Properties of PPC binder pervious concrete," *International Journal of Advances in Engineering & Technology*, vol. 7, no. 2, pp. 444–448, 2016.

[4] K. S. Elango, P. R. Remya, D. Vivek, R. Gopi, and R. Saravanakumar, "Strength and durability studies on Ficus Exasperata leaf ash concrete," *Materials Today Proceedings*, vol. 37, no. 11, 2020.

[5] A. R. Khaloo, M. Dehestani, and P. Rahmatabadi, "Mechanical properties of concrete containing a high volume of tire-rubber particles," *Waste Management*, vol. 28, no. 12, pp. 2472–2482, 2008.

[6] V. C. Li, "On Engineered Cementitious Composites (ECC): a review of the material and its applications," *Transportation Research Record Journal of the Transportation Research Board*, vol. 2164, pp. 1–8, 2010.

[7] S. Wang, C. Wu, and V. C. Li, "Tensile strain-hardening behaviour of polyvinyl alcohol engineered cementitious composite (PVA-ECC)," *ACI Materials Journal*, vol. 98, no. 6, pp. 483–492, 2001.

[8] R. Dharmaraj, A. Karthick, G. K. Arunvivek et al., "Novel approach to handling microfiber-rich dye effluent for sustainable water conservation," *Advances in Civil Engineering*, vol. 2021, Article ID 1323472, 10 pages, 2021.

[9] M. A. Chowdhury, M. M. Islam, and Z. Ibna Zahid, "Finite element modeling of compressive and splitting tensile behavior of plain concrete and steel fiber reinforced concrete cylinder specimens," *Advances in Civil Engineering*, vol. 2016, pp. 1–11, Article ID 6579434, 2016.

[10] K. Khaloo, "Mechanical properties of normal to high strength steel fiber reinforced concrete," *Cement, Concrete and Aggregates*, vol. 18, pp. 92–97, 1996.

[11] M. Bentur, *Fibre Reinforced Cementitious Composites*, Taylor & Francis, Oxfordshire, UK, 2007.

[12] R. Dharmaraj, G. K. Arunvivek, A. Karthick, V. Mohanavel, B. Perumal, and S. Rajkumar, "Investigation of mechanical and durability properties of concrete mixed with water exposed to a magnetic field," *Advances in Civil Engineering*, vol. 2021, Article ID 2821419, 14 pages, 2021.

[13] K. S. Elango and V. Revathi, "Infiltration and clogging characteristics of pervious concrete," *Asian Journal of Civil Engineering*, vol. 20, no. 8, pp. 1119–1127, 2019.

[14] L. Zheng, X. S. Huo, and Y. Yuan, "Strength, modulus of elasticity, and brittleness index of rubberized concrete," *Journal of Materials in Civil Engineering*, vol. 20, no. 11, pp. 692–699, 2008.

[15] F. Hernández-Olivares, G. Barluenga, M. Bollati, and B. Witoszek, "Static and dynamic behaviour of recycled tyre rubber-filled concrete," *Cement and Concrete Research*, vol. 32, no. 10, pp. 1587–1596, 2002.

[16] K. S. Elango, R. Gopi, C. Jayaguru, D. Vivek, R. Saravanakumar, and V. Rajeshkumar, "Experimental investigation on concrete beams reinforced with basalt fiber reinforced polymer bars," *Materials Today Proceedings*, vol. 45, no. 2, 2020.

[17] B. S. Mohammed, M. S. Liew, W. S. Alaloul, V. C. Khed, C. Y. Hoong, and M. Adamu, "Properties of nano-silica modified pervious concrete," *Case Studies in Construction Materials*, vol. 8, pp. 409–422, 2018.

[18] H. Yazici, "Effect of curing conditions on compressive strength of ultra high strength concrete with high volume mineral admixtures," *Building and Environment*, vol. 42, no. 5, pp. 2083–2089, 2007.

[19] P. R. Prem, B. H. Bharatkumar, and N. R. Iyer, "Influence of curing regimes on compressive strength of ultra high performance concrete," *Sadhana*, vol. 38, no. 6, pp. 1421–1431, 2013.

[20] J. Michels, "Matija Gams "Preliminary study on the influence of fibre orientation in fibre reinforced mortars"," *Građevinar*, vol. 8, pp. 645–655, 2016.

[21] K. Wille, A. E. Naaman, S. El-Tawil, and G. J. Parra-Montesinos, "Ultra-high performance concrete and fiber reinforced concrete: achieving strength and ductility without heat curing," *Materials and Structures*, vol. 45, no. 3, pp. 309–324, 2011.

[22] K. S. Elango, D. Vivek, G. KrishnaPrakash, M. J. Paranidharan, S. Pradeep, and M. Prabhukesavaraj, "Strength and permeability studies on PPC binder pervious concrete using palm jaggery as an admixture," *Materials Today Proceedings*, vol. 37, pp. 2329–2333, 2020.

[23] M. C. Nataraja, T. S. Nagaraj, and S. B. Basavaraja, "Reproportioning of steel fibre reinforced concrete mixes and their impact resistance," *Cement and Concrete Research*, vol. 35, no. 12, pp. 2350–2359, 2005.

[24] R. Kanagavel and A. Kalidass, "Mechanical Properties of hybrid fibre reinforced quaternary concrete," *Građevinar*, vol. 69, no. 1, pp. 1–10, 2017.

[25] P. Zhang, S. Han, S. Ng, and X.-H. Wang, "Fiber-Reinforced concrete with application in Civil engineering," *Advances in Civil Engineering*, vol. 2018, pp. 1–4, Article ID 1698905, 2018.

[26] Y. Wang, J. Chen, D. Gao, and E. Huang, "Mechanical properties of steel fibers and nanosilica modified crumb rubber concrete," *Advances in Civil Engineering*, vol. 2018, pp. 1–10, Article ID 6715813, 2018.

[27] Bureau of Indian Standards, *Indian Standard Guidelines for concrete Mix Design Proportioning*, Bureau of Indian Standards, New Delhi, India, 2009.

[28] Bureau of Indian Standards, *Indian Standard Methods of Sampling and Analysis of Concrete*, Bureau of Indian Standards, New Delhi, India, 1999.

[29] Bureau of Indian Standards, *Indian Standard Methods of Tests for Strength of Concrete*, Bureau of Indian Standards, New Delhi, India, 1999.

[30] Bureau of Indian Standards, *Indian Standard Splitting Tensile Strength of Concrete- Method of Test*, Bureau of Indian Standards, New Delhi, India, 1999.

[31] K. S. Elango and V. Revathi, "Mechanical and durability studies on pervious concrete using different types of binders," *Romanian Journal of Materials*, vol. 50, no. 2, pp. 258–267, 2020.

[32] ACI Committee 544, "Measurement of Properties of Fiber Reinforced Concrete," *American Concrete Institute*, vol. 85, no. 6, pp. 583–593, 1998.

[33] R. Navilesh, S. P. Shankar, Vivekan, and A. Gutteder, "Study on hybrid fiber reinforced concrete," *International Research Journal of Engineering and Technology*, vol. 4, no. 6, 2017.

Hindawi
Advances in Civil Engineering
Volume 2022, Article ID 7346620, 13 pages
https://doi.org/10.1155/2022/7346620

Research Article

Effect of Axial Compression Ratio on Seismic and Self-Centering Performance of Unbonded Prestressed Concrete Columns

Yun Shi,[1,2] **Guanglin Yuan**,[1] **and Hao Zhu**[2]

[1]*School of Mechanics and Civil Engineering, China University of Mining and Technology, Xuzhou 221008, Jiangsu, China*
[2]*School of Civil Engineering and Architecture, Suqian University, Suqian 223800, Jiangsu, China*

Correspondence should be addressed to Yun Shi; sqshiyun@qq.com

Received 29 October 2021; Accepted 17 December 2021; Published 18 January 2022

Academic Editor: Wenjie Ge

To explore the influence of the applied axial compression ratio and preloaded axial compression ratio on the seismic performance of unbonded prestressed concrete columns, pseudo-static tests were carried out on four prestressed columns and one ordinary column in this study. The seismic performance indexes of test columns were studied and analyzed, including failure modes, hysteresis curves, skeleton curves, stiffness, ductility, and energy dissipation. The test results show that compared with concrete columns with ordinary reinforcement, the hysteresis curve of reinforced concrete columns with prestressed tendons has a pinch phenomenon to a certain extent, and the energy dissipation performance becomes worse. For the prestressed columns, the greater the applied axial compression ratio, the worse the fullness of hysteresis curves and the energy dissipation performance, the greater the residual displacement, the faster the strength attenuation, and the worse the self-centering performance. For the posttensioned unbonded prestressed concrete columns, the greater the preloaded axial compression ratio, the worse the energy dissipation performance of the test column, the slower the strength attenuation, and the better the self-centering performance.

1. Introduction

The previous analysis of earthquake disasters has shown that building structures after the earthquake can produce large residual deformation. Many building structures are not damaged but difficult to repair due to large residual displacement and have to be demolished and rebuilt, resulting in resource waste and property loss [1]. Therefore, the development and research of a building with small residual deformation after an earthquake are an important direction of building development in the future [2–10]. At present, the common methods to improve the self-resetting performance of specimens are adding unbonded prestressed reinforcement, adding viscous damper, setting unbonded high-strength reinforcement, and so on. Unbonded prestressed tendons are widely used because of their advantages of convenient construction and low cost. The existing research has shown that when unbonded prestressed tendons are added to the ordinary reinforced concrete columns for applying the prestress, the high-strength elastic recovery characteristics of prestressed tendons can be used to effectively reduce the residual displacement of structures or members and obtain good self-centering performance.

Roke [11] conducted the time history analysis of three central braced frame structures with different positions of prestressed tendons and found that this structure has a good self-centering effect. Luo Haiyan [12] carried out comparative tests of three concrete columns with unbonded partially prestressed tendons and one concrete column with ordinary reinforcement. It was found that the prestress level has an important influence on the performance of the specimens. Yang Yiming et al. [13] performed pseudo-static tests of two RC frame column base joints equipped with unbonded prestressed tendons and energy dissipation damper. It was reported that the axial compression ratio has an important impact on the seismic performance and self-centering performance of RC frame column base joints. Through the above research, it can be found that the axial compression ratio is an important factor affecting the seismic and self-centering performance of reinforced

concrete frame columns. However, there is no research on the specific influence law of the applied axial compression ratio and preloaded axial compression ratio on their performance. In this study, four concrete columns with posttensioned unbonded prestressed tendons and one ordinary reinforced concrete column were designed at a reduced scale of 1/2, and pseudo-static loading tests on these columns were performed to analyze their energy dissipation performance, strength attenuation, and self-centering performance.

2. Experimental Investigation

2.1. Description of Specimens. In this test, four concrete columns with posttensioned unbonded prestressed tendons (marked as PURC) and one ordinary reinforced concrete column (marked as PTRC) were designed and fabricated in the proportion of 1/2. The column height was 1200 mm, and the section size was 300 mm × 300 mm. Table 1 and Table 2 show the axial compression ratio of the test piece, and Figure 1 shows the size and reinforcement of the test piece. The C40 concrete was used, and the measured compressive strength of the cube was 44.5 MPa. The longitudinal main reinforcement was HRB400 grade, with a diameter of 20 mm, the measured yield strength of 536.2 MPa, elongation of 19%, and elastic modulus of 2.00×10^5 MPa. The stirrup was HPB300 grade, with the measured yield strength of 371.0 MPa and elastic modulus of 2.10×10^5 MPa. In this study, $\zeta = N_p/f_c A$ and $\eta = N/f_c A$, where ζ is the preloaded axial compression ratio, η is the applied axial compression ratio, N_p is the axial pressure exerted by prestressed tendons, N is the applied axial pressure, f_c is the design value of concrete compressive strength, and A is the column section area.

2.2. Prestressed Tendon Tensioning. To exert the prestress, four $\Phi^S 15.2$ ($f_{ptk} = 1860\ \mathrm{N \cdot mm^{-2}}$) 1×7 steel strands were uniformly arranged at the four corners of the column section during the production of the column specimens. To ensure the flatness of the upper and lower sides of specimens, one end of the prestressed tendons was pretensioned at the column top and embedded in the concrete. The steel strand was covered with a thin steel pipe and fixed at the design position through the perforated steel plate at the column top and the column bottom to avoid the shift of the steel strand during the pouring and vibrating of concrete. To obtain the smooth bottom of test columns for the subsequent test, a groove of 300 mm × 400 mm × 150 mm was reserved at the bottom of the column during the fabrication for tensioning and anchoring prestressed steel strand, and the single-hole tool anchor was used.

The size of the prestressed members used in this test was smaller than that in the actual project; moreover, the reduction in length can cause a large amount of prestress loss [14]. To solve this problem, a support foot device developed by the China University of Mining and Technology was used to supplement the tension by the insert gasket [15]. Figure 2 shows the specific operation process, and Table 3 shows the detailed tension control stress.

2.3. Loading Device and Loading System. The test was conducted in Jiangsu Key Laboratory Environmental Impact and Structural Safety in Engineering, China University of Mining and Technology. The electrohydraulic servo loading structure test machine was used for pseudo-static loading under low-cycle repeated loading [16]. Figure 3 shows the loading device. The vertical load was applied to the design value through two hydraulic jacks at the top of the column, and the horizontal load was applied by the actuator at the top of the column.

The load-displacement control mode was adopted in the loading process. The loading system was as follows: the yield displacement Δ of each test column was obtained by the load control with an increase of 10 kN. After the test column yielded, the loading was performed according to the controlled displacement of 1Δ, 2Δ, 3Δ, and so on. Before the test column yielded, load control and displacement control were cycled once; after the test column yielded, displacement control was loaded for three times at each level. When the load dropped below 85% of the maximum load value, the specimen was considered to be destroyed and the test was terminated.

3. Experimental Phenomenon and Failure Mode

Figure 4 shows the final failure modes of test columns. The loading failure process of test columns is described as follows:

(1) Specimen PTRC-1. After formal loading, the test column showed significant elastic characteristics before yielding. When the horizontal force was applied to 56.8 kN, the first horizontal crack appeared on the right side of the column 130 mm from the base. When the controlled displacement was 18 mm, cracks on the front and rear sides extended obliquely and vertically, and multiple through cracks appeared on the left and right sides. The through cracks were clearly observed during the unloading. When the controlled displacement was 27 mm, a small area of damage was generated in the concrete of the column corner, and vertical cracks appeared in the middle of the left and right sides of the column body. The specimen reached the limit state, and the horizontal force had an extreme value (200.71 kN in the forward direction and 173.20 kN in the reverse direction). When the controlled displacement was 54 mm, the horizontal load dropped below 85% of the ultimate load value. After the test termination, the failure mode of the test column was mainly the flexural shear failure, showing good ductility characteristics.

(2) Specimen PURC-1. After formal loading, when the load was added to 59.3 kN, the first horizontal crack appeared on the right side of the column 75 mm from the base. When the controlled displacement was 18 mm, vertical cracks were gradually produced in the bottom beam during the first cycle, and the horizontal cracks continued to extend and develop. When the controlled displacement was 27 mm, the

Table 1: Design parameters of specimens.

Specimen number	Section size mm × mm	Concrete strength grade	Longitudinal reinforcement	Reinforcement ratio ρ_t/%	Column stirrup	Prestressed tendons	Effective prestress	Shear span ratio λ
PTRC-1	300 × 300	C40	8 Φ 20	2.79	Φ8@50/100	-	-	3.5
PURC-1	300 × 300	C40	8 Φ 20	2.79	Φ8@50/100	$4\Phi^S15.2$	0.65 f_{ptk}	3.5
PURC-2	300 × 300	C40	8 Φ 20	2.79	Φ8@50/100	$4\Phi^S15.2$	0.65 f_{ptk}	3.5
PURC-3	300 × 300	C40	8 Φ 20	2.79	Φ8@50/100	$4\Phi^S15.2$	0.65 f_{ptk}	3.5
PURC-4	300 × 300	C40	8 Φ 20	2.79	Φ8@50/100	$4\Phi^S15.2$	0.45 f_{ptk}	3.5

Table 2: Axial compression ratios of specimens.

Specimen number	Axial compression ratio n	Preloaded axial compression ratio ζ	Applied axial compression ratio η	Applied axial compression kN
PTRC-1	0.15	—	0.15	238.05
PURC-1	0.55	0.40	0.15	238.05
PURC-2	0.45	0.40	0.05	79.35
PURC-3	0.65	0.40	0.25	396.75
PURC-4	0.40	0.25	0.15	238.05

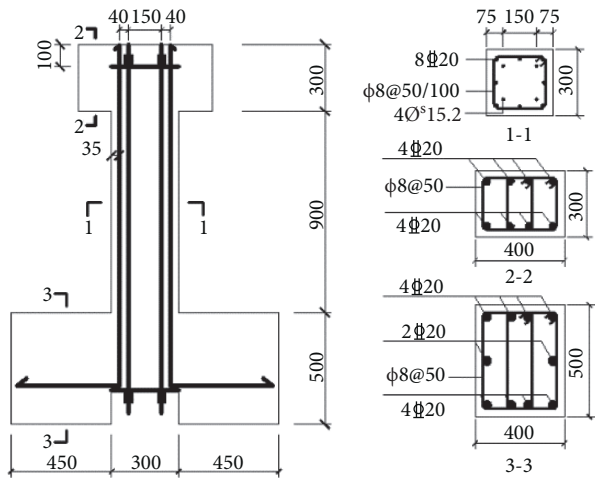

Figure 1: Size and section reinforcement of test columns (mm).

specimen reached the limit state during the first cycle, and the horizontal force had an extreme value (201.06 kN in the forward direction and 195.19 kN in the reverse direction). When the controlled displacement was 54 mm, the horizontal load of the test column dropped below 85% of the ultimate load, and the test was terminated.

(3) Specimen PURC-2. After formal loading, when the load was increased to 53.2 kN, the first horizontal crack was produced at the connection between the column body and the base. When the controlled displacement was ±27 mm, the cracks on the column body were widened and the four cracks extended vertically. During the cycle under the controlled displacement of 30 mm, new cracks were no longer generated and the load peak appeared (198.50 kN in the forward direction and 203.57 kN in the reverse direction). When the controlled displacement was 60 mm, the horizontal load of the test column dropped below 85% of the ultimate load, and the test was terminated.

(4) Specimen PURC-3. After formal loading, when the load was added to 76.4 kN, multiple horizontal cracks were generated on the right side of the column 50 mm, 150 mm, 250 mm, and 375 mm away from the base. When the controlled displacement was ±24 mm, the vertical crack perpendicular to the horizontal crack began to appear. When the controlled

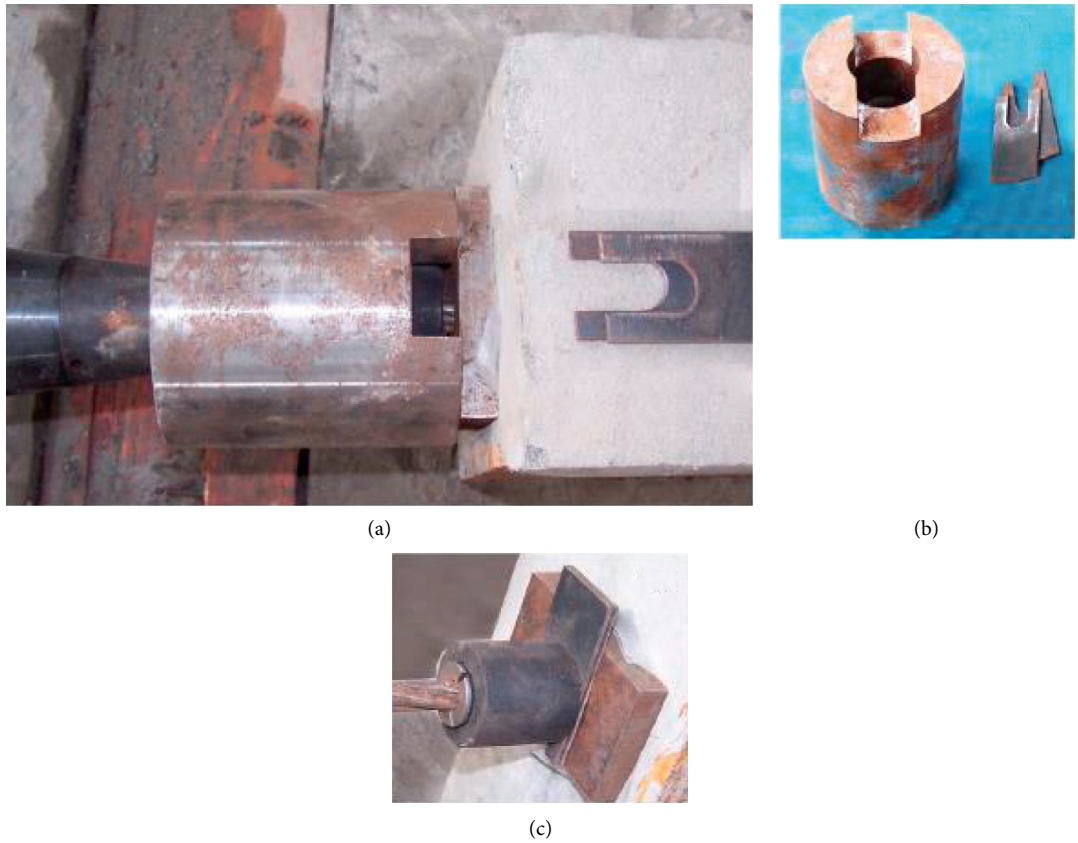

(a) (b) (c)

Figure 2: Insert gasket for tension supplement. (a) Insert gasket for tension supplement and (b) brace angle and gasket (c) after tension supplement [15].

Table 3: Tensioning data of prestressed tendons.

Specimen No.	PTRC-1	PURC-1	PURC-2	PURC-3	PURC-4
Prestress loss/$(N \cdot mm^{-2})$	—	60.06	60.06	60.06	50.82
Tension control force/ kN	—	176.40	176.40	176.40	149.26

displacement was ±32 mm, the specimen reached the limit state during the first cycle, and the extreme value of the horizontal force was obtained (211.16 kN in the forward direction and 209.83 kN in the reverse direction). After that, the bearing capacity decreased continuously with the failure of the specimen. When the controlled displacement was 48 mm, the horizontal load of the test column dropped below 85% of the ultimate load, and the test was ended.

(5) Specimen PURC-4. After formal loading, when the load was 59.3 kN, the first horizontal crack appeared on the right cylindrical surface 160 mm away from the base. When the controlled displacement was 27 mm, the new cracks were not generated. During the first loading of 0⟶27 mm, the load peak appeared (192.14 kN in the forward direction and 192.46 kN in the reverse direction), the concrete at the column corner of the left foot began to crush, the cracks developed vertically, and a main vertical crack was formed in the middle of the left and right sides. When the controlled displacement was 54 mm, the horizontal load of the test column dropped below 85% of the ultimate load, and the test was ended.

4. Experimental Results and Discussion

4.1. Hysteresis Curves. The hysteresis curves of different specimens are compared (Figure 5). It can be seen that:

(1) At the initial stage of loading, the hysteresis curve of each specimen approximates a straight line, indicating that the specimen is in the elastic stage at this time. With the increase in load and displacement, the area of the hysteresis loop increases continuously, and the hysteresis curve no longer grows as a straight line. It indicates that the specimen enters the elastic-plastic stage. After unloading, the residual displacement increases, the plastic damage develops, and the energy dissipation performance is improved.

(2) Hysteresis curves of PURC-1-PURC-4 and PTRC-1 are compared. It can be found that there is an obvious pinch phenomenon in hysteresis curves of

Figure 3: Test loading device.

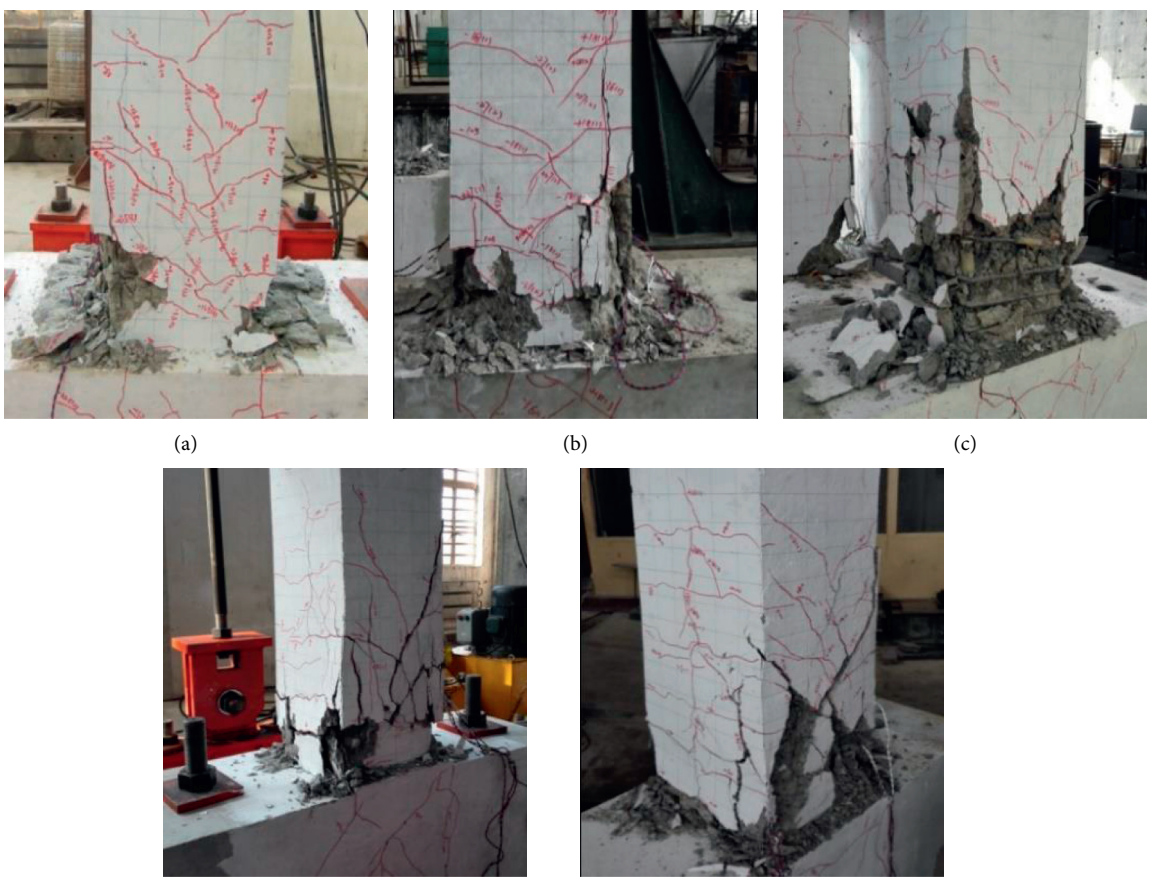

Figure 4: Failure modes of specimens. (a) PTRC-1. (b) PURC-1. (c) PURC-2. (d) PURC-3. (e) PURC-4.

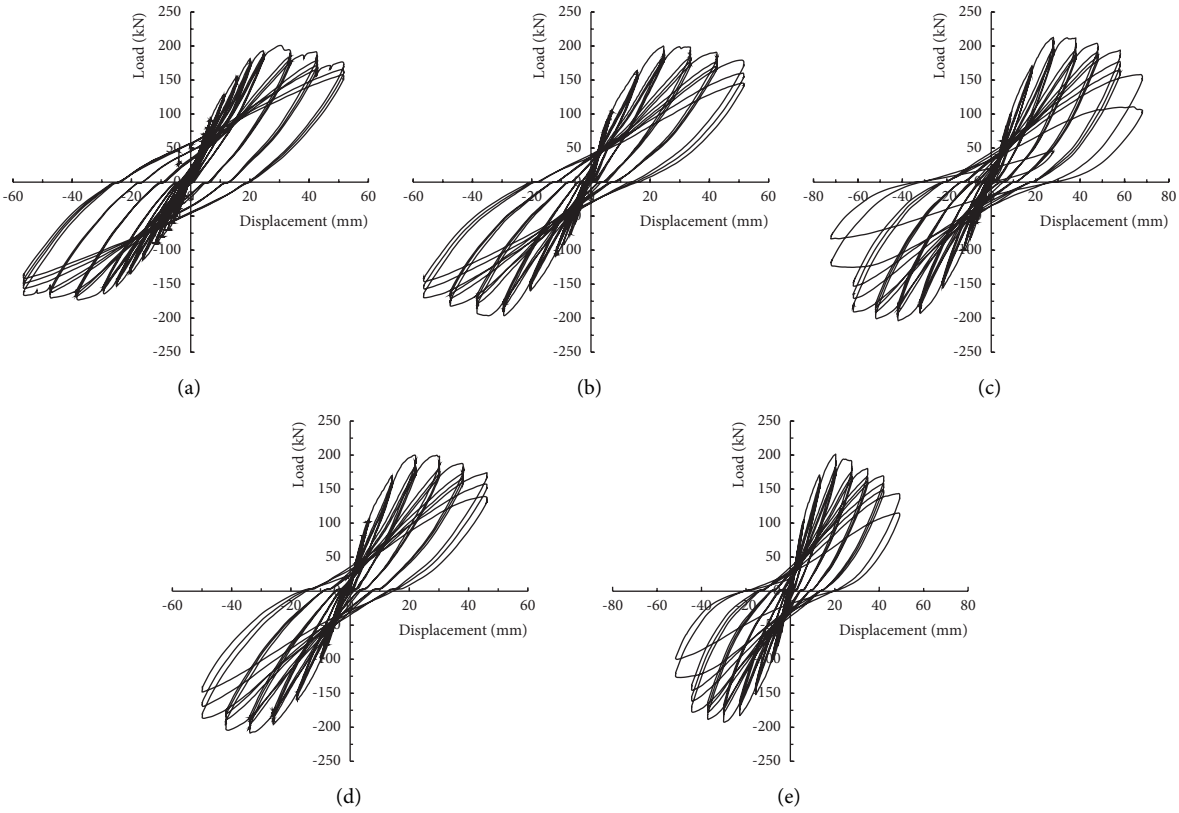

Figure 5: Hysteresis curves of specimens. (a) PTRC-1. (b) PURC-1. (c) PURC-2 and PURC-p3. (d) PURC-4.

specimens with posttensioned unbonded prestressed tendons, and the peak load of these specimens is increased by 5.97%, 7.53%, 12.59%, and 2.86%, respectively. It shows that the addition of posttensioned unbonded prestressed tendons can reduce the energy dissipation performance of concrete columns, but cannot significantly improve their bearing capacity.

(3) Hysteresis curves of PURC-2, PURC-1, and PURC-3 are compared. Under the same preloaded axial compression ratio of specimens, when the applied axial compression ratio increases from 0.05, 0.15, to 0.25, the fullness of hysteresis curve becomes worse, the limit displacement becomes smaller, and the load after yield decreases faster. It indicates that the energy dissipation performance of posttensioned unbonded prestressed concrete columns becomes worse with the increase in the applied axial compression ratio.

(4) Hysteresis curves of PURC-1 and PURC-4 are compared. Under the same applied axial compression ratio of the specimen, when the preloaded axial compression ratio is 0.4 and 0.25, the fullness of the hysteresis curve of PURC-4 is relatively good, and the limit displacements of PURC-1 and PURC-4 are similar. It indicates that the greater the preloaded axial compression ratio, the lower the energy consumption capacity of the specimen.

4.2. Skeleton Curves. Figure 6 shows skeleton curves of test columns. The skeleton curves of test columns are compared.

(1) By comparing skeleton curves of PTRC-1 and PURC-1, it is found that the rising section and falling section of the skeleton curve of PTRC-1 are steep, and the initial stiffness is large, while the falling section of the curve of PURC-1 is relatively gentle. This is because when the prestress is applied to the test column, the column is compacted, which is conducive to improve its stiffness. However, after the peak load, the concrete damage is accelerated and the bearing capacity is degraded rapidly due to the pressure of prestressed tendons.

(2) By comparing the skeleton curves of PURC-1, PURC-2, and PURC-3, it can be seen that the rising and falling sections of the skeleton curve of PURC-3 are the steepest, with the largest initial stiffness and the smallest ultimate displacement; the rising section and the falling section of the skeleton curve of the PURC-2 are the most gentle, with the smallest initial stiffness and the largest limit displacement. It indicates that the greater the applied axial compression ratio, the smaller the ultimate displacement of the posttensioned unbonded prestressed concrete column and the more significant the ductility reduction.

(3) By comparing the skeleton curves of PURC-1 and PURC-4, it can be seen that the rising section of the

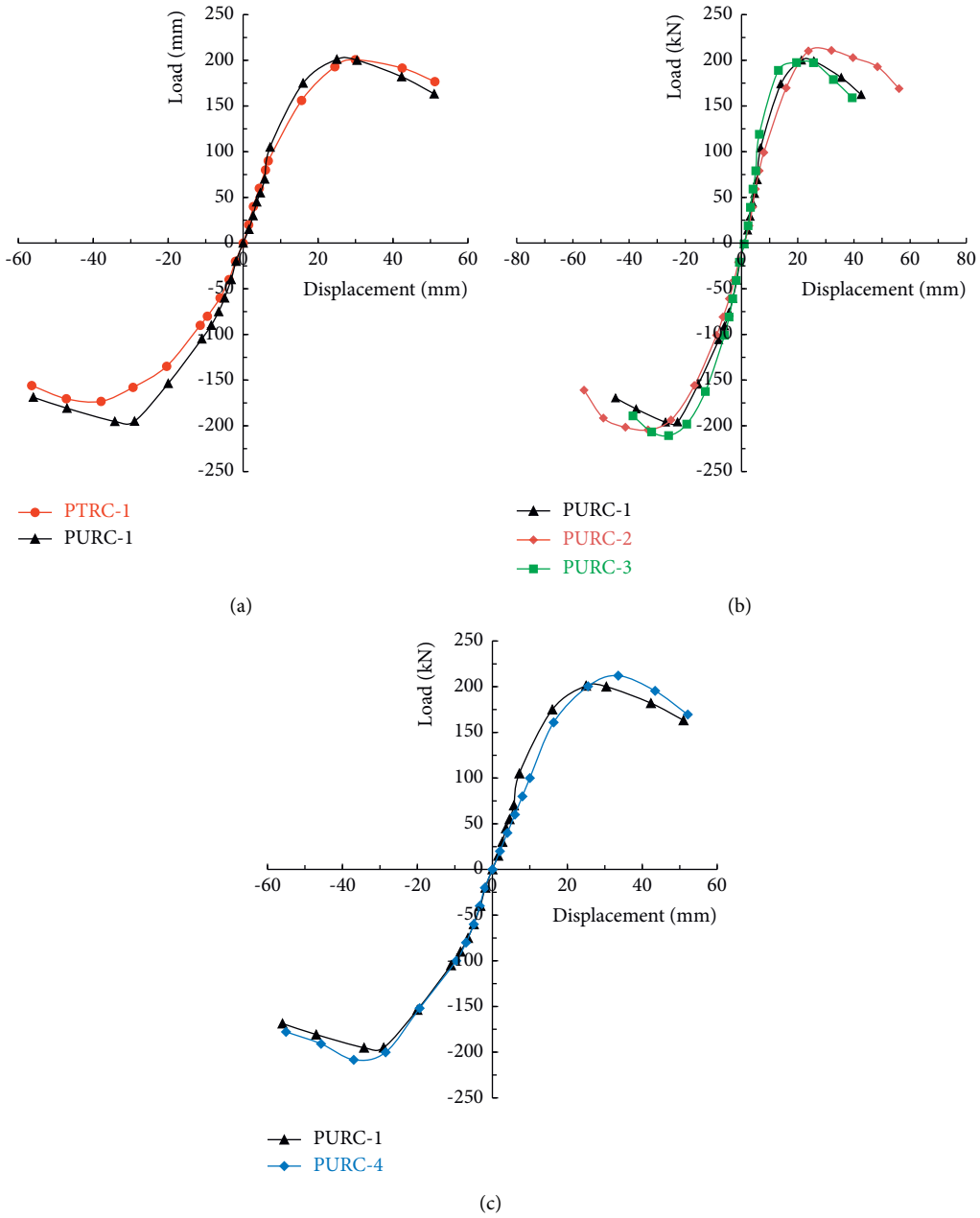

Figure 6: Skeleton curves of specimens. (a) PTRC-1 and PURC-1. (b) PURC-1, PURC-2, and PURC-3. (c) PURC-1 and PURC-4.

skeleton curve of PURC-4 is relatively gentle, the limit displacement is large, and its ductility is good.

4.3. Stiffness Degradation. Under the condition of pseudo-static test, the stiffness degradation characteristics of structures or members are usually characterized by loop stiffness:

$$K_j = \frac{\sum_{i=1}^{n} V_j^i}{\sum_{i=1}^{n} \Delta_j^i}, \quad (1)$$

where K_j is the stiffness under the jth level load; V_j^i is the average value of forward and reverse loads under the jth level load at the ith cycle; and Δ_j^i is the average value of forward and reverse displacement under the jth level load at the ith cycle. Figure 7 shows the skeleton curves of different specimens.

As shown in Figure 7, it is concluded that

(1) The stiffness degradation curves of all specimens are smooth without sudden change, indicating that the damage of posttensioned unbonded prestressed concrete develops stably under seismic load.

(2) Compared with ordinary reinforced concrete columns, the columns with posttensioned unbonded prestressed tendons present higher initial stiffness, but rapid stiffness loss after loading. It suggests that

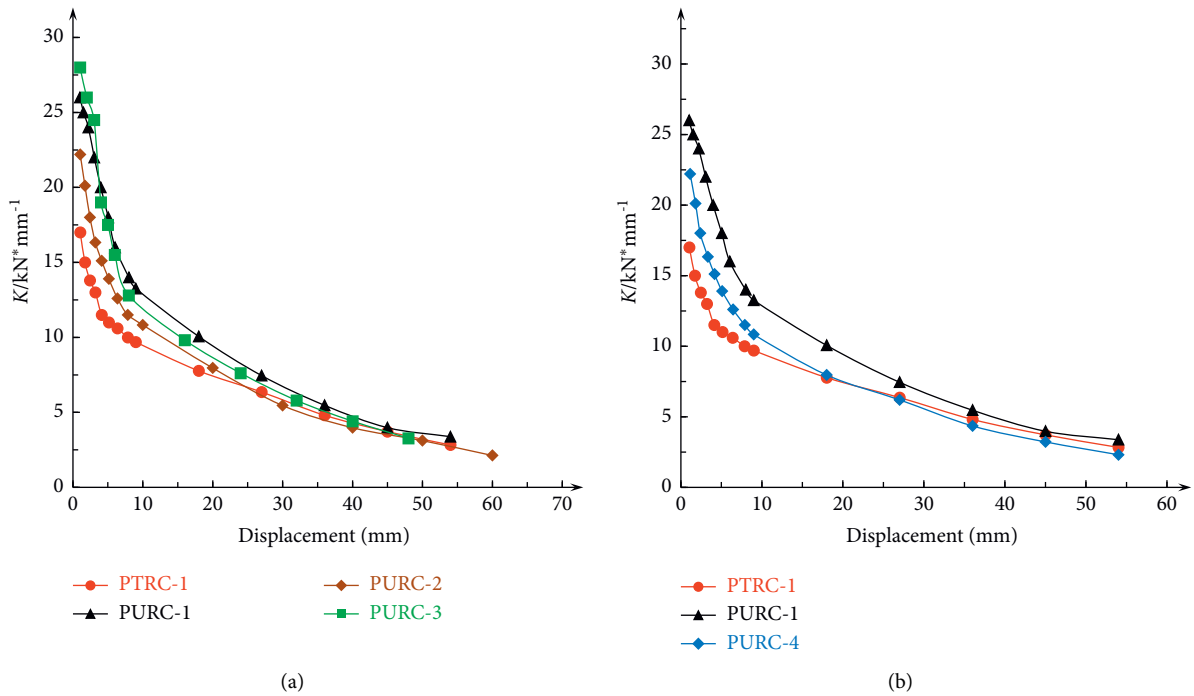

Figure 7: Stiffness degradation curves of specimens.

the prestressing can accelerate the damage of specimens.

(3) As shown in Figure 7(a), the effect of applied axial pressure ratio on stiffness degradation is significant. The greater the applied axial pressure ratio, the faster the stiffness degradation. As shown in Figure 7(b), the change in preloaded axial compression ratio before the specimen yielding has little effect on the stiffness degradation rate of the specimen; after the specimen yielding, the stiffness degradation of the specimen with a high preloaded axial compression ratio is accelerated. It shows that the greater the applied axial compression ratio, the faster the damage of the specimen and the faster the stiffness degradation. Besides, the preloaded axial compression ratio rarely affects the damage rate of the specimen before yielding, but accelerates the damage rate of the specimen after yielding and the stiffness degradation is accelerated.

4.4. Bearing Capacity

4.4.1. Test Value of Bearing Capacity. Tables 4 and 5 show the load, displacement, displacement angle, and displacement ductility coefficient of different characteristic points of the specimen. The yield displacement is obtained by the energy method [17], and the ultimate load and displacement are the corresponding load and displacement values when the load drops to 85% of the peak load. The experimental results show that

(1) By comparing the PTRC-1 with PURC-1-1 and PURC-1-4, it can be found that the yield displacement of concrete columns with unbonded prestressed tendons increases, while the addition of unbonded prestressed tendons rarely affects the peak load, peak displacement, ultimate load, and ultimate displacement. Compared with PTRC-1, the yield displacement of PURC-1 and PURC-4 increases by 36.31% and 26.18%, respectively. The three specimens enter the yield state at the displacement angle of 1/37–1/36 and fail at the displacement angle of 1/22–1/21. This is because for large eccentric compression members, the reinforcement in the tensile area first yields, and then, the concrete in the compression area is damaged by compression, but the existence of preload slows down the yield of reinforcement in the tensile area, resulting in the increase in yield load and displacement of the specimen; however, after the specimen yields, the prestressed tendons basically stop working. At this time, the specimen can be approximately equivalent to an ordinary reinforced concrete column. Therefore, the peak load, peak displacement, ultimate load, and ultimate displacement of PURC-1 and PURC-4 are not significantly different from those of PTRC-1.

(2) The test values of PURC-1, PURC-2, and PURC-3 are also analyzed. Compared with PURC-2, the yield load of PURC-1 and PURC-3 increases by 19.39% and 22.20%, and their yield displacement decreases by 9.88% and 9.70%; the peak load of PURC-1 and PURC-3 increases by 2.64% and 11.63%, and their peak displacement decreases by 13.43% and 25.30%; the ultimate load of PURC-1 and PURC-3 increases by 3.71% and 10.19%, and their ultimate displacement decreases by 12.57% and 17.52%, respectively.

Table 4: Ductility coefficients of the specimens.

Specimen No.	Loading direction	Yield load P_y/kN	Yield displacement Δ_y/mm	Peak load P_b/kN	Peak displacement Δ_b/mm	Ultimate load P_u/kN	Ultimate displacement Δ_u/mm	Ductility coefficient $u = \Delta_u/\Delta_y$	Ductility coefficient average
PTRC-1	Forward direction	168.29	11.22	200.71	29.92	170.60	51.16	4.56	4.75
	Reverse direction	−160.80	−12.07	−173.20	−32.92	−147.22	−59.52	4.93	
PURC-1	Forward direction	178.26	15.73	201.06	25.00	170.90	53.84	3.22	3.29
	Reverse direction	−188.98	−16.02	−195.19	−30.24	−165.91	−56.94	3.35	
PURC-2	Forward direction	153.26	17.35	188.50	28.02	160.23	62.86	3.62	3.60
	Reverse direction	−154.33	−17.89	−193.57	−35.85	−164.53	−63.83	3.57	
PURC-3	Forward direction	189.97	15.22	211.16	22.82	179.47	53.53	2.94	2.92
	Reverse direction	−185.96	−16.59	−219.83	−24.90	−178.36	−50.97	2.90	
PURC-4	Forward direction	161.42	14.45	192.14	27.56	163.32	54.05	3.29	3.41
	Reverse direction	−163.77	−14.94	−192.46	−34.99	−163.59	−59.57	3.52	

Table 5: Average value of load and displacement angle of specimens.

Specimen number	Yield load P_y/kN	Average yield displacement Δ_y/mm	$\theta_y = \Delta_y/H$	Average peak load P_b/kN	Average peak displacement Δ_b/mm	$\theta_b = \Delta_b/H$	Average ultimate load P_u/kN	Average ultimate displacement Δ_u/mm	$\theta_u = \Delta_u/H$
PTRC-1	164.55	11.65	1/99	186.96	31.42	1/37	158.91	55.34	1/21
PURC-1	183.62	15.88	1/72	198.13	27.62	1/42	168.41	55.39	1/21
PURC-2	153.80	17.62	1/65	193.04	31.94	1/36	162.38	63.35	1/18
PURC-3	187.97	15.91	1/68	215.50	23.86	1/48	178.92	52.25	1/22
PURC-4	162.60	14.70	1/69	192.30	31.28	1/37	163.46	56.81	1/20

It shows that under the same preloaded axial compression ratio, the greater the applied axial compression ratio, the greater the yield load, peak load, and ultimate load, and the smaller the yield displacement, peak displacement, and ultimate displacement.

4.4.2. Bearing Capacity Attenuation. Under the control of displacement amplitude at the same level, the bearing capacity of the specimen after yielding decreases with the increase in loading times, which is called bearing capacity attenuation. The bearing capacity attenuation Φ_i can be expressed as follows:

$$\Phi_i = \frac{P_{j-i}}{P_{j-1}}, \tag{2}$$

where P_{j-i} is the peak load value of the ith cycle under the jth level displacement amplitude; P_{j-1} is the peak load value of the first cycle under the jth level displacement amplitude.

Figure 8 shows the strength attenuation of different specimens. It can be found that:

(1) The strength attenuation of each specimen increases with the increase in loading displacement; during the same level displacement loading cycle, the attenuation degree of the third loading is less than that of the second loading.

(2) The average attenuation rates of PURC-1, PTRC-1, PTRC-2, PTRC-3, and PTRC-4 before failure are 4.70%, 6.16%, 5.98%, 7.13%, and 7.46%; their maximum strength attenuation rates are 10.05%, 10.23%, 10.14%, 10.21%, and 11.93%, and the corresponding displacement angles are 1/23, 1/29, 1/26, 1/26, and 1/39, respectively. It can be found that the strength attenuation of prestressed reinforced concrete columns is faster than that of the ordinary columns. Comparing PURC-1 and PURC-4, it can be found that the average attenuation rate of PURC-4 is 21.10% higher than that of PURC-1, and the maximum attenuation rate of PURC-4 is 16.62% higher

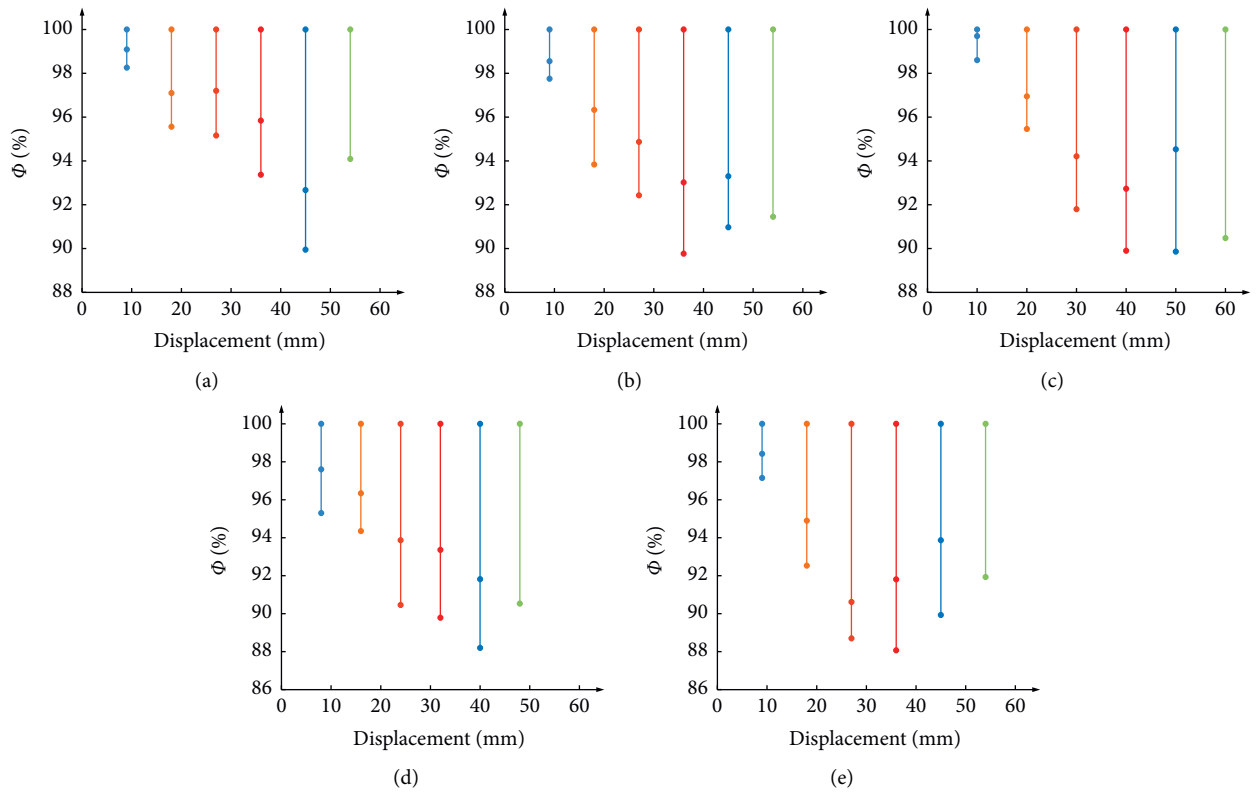

Figure 8: Strength attenuation of each specimen. (a) PTRC-1. (b) PURC-1. (c) PURC-2. (d) PURC-3. (e) PURC-4.

than that of PURC-1. It indicates that for the specimen with a small preloaded axial compression ratio, the faster the strength attenuation, the smaller the maximum strength attenuation rate. This is because during the loading process, with the increase in displacement, the deformation of prestressed tendons increases, and the preloaded axial pressure gradually increases; for the specimens with a small preloaded axial compression ratio, the prestressed tendons quit work in the later stage. By comparing PURC-1, PURC-2, and PURC-3, it can be found that the greater the applied axial compression ratio, the greater the strength attenuation rate and maximum amplitude of the specimen.

4.5. Ductility and Energy Dissipation. Ductility refers to the deformation capacity of a certain section of a structure or component from the beginning of yield to the maximum bearing capacity. The calculation equation of ductility is as follows:

$$u = \frac{\Delta_u}{\Delta_y}, \tag{3}$$

where u is ductility coefficient; Δ_u is the ultimate displacement of the structure or member under load; and Δ_y is the yield displacement of the structure or member under load. The yield displacement is determined by the energy method. Based on the test data and calculation results, the ductility coefficient and displacement angle of each test column are obtained, as shown in Tables 4 and 5, Table 4 shows the ductility coefficients of the specimens, and Table 5 shows the average value of load and displacement angle of specimens. The energy dissipation performance can be measured by the equivalent damping coefficient h_e, and the calculation results are shown in Figure 9.

As shown in Tables 4 and 5, the ductility of the column with unbonded prestressed tendons is worse than that of an ordinary reinforced concrete column. Through the data comparison of PURC-1, PURC-2, and PURC-3, it can be found that the greater the applied axial compression ratio, the smaller the displacement ductility coefficient of the test column; through the data comparison of PURC-1 and PURC-4, it can be found that the larger the preloaded axial compression ratio, the smaller the displacement ductility coefficient of the test column.

As shown in Figure 9, the energy dissipation coefficient of the column with unbonded prestressed tendons is less than that of ordinary reinforced concrete column. It indicates that the addition of prestressed tendons can lead to the deterioration of the energy dissipation performance of the member. Regardless of the axial compression ratio, the greater the loading displacement of each test column, the greater the equivalent damping coefficient; the larger the applied axial compression ratio and preloaded axial compression ratio of each test column, the smaller the equivalent damping coefficient. It shows that the increase in the applied axial compression ratio and the preloaded axial compression ratio leads to the deterioration of the energy dissipation capacity of the column.

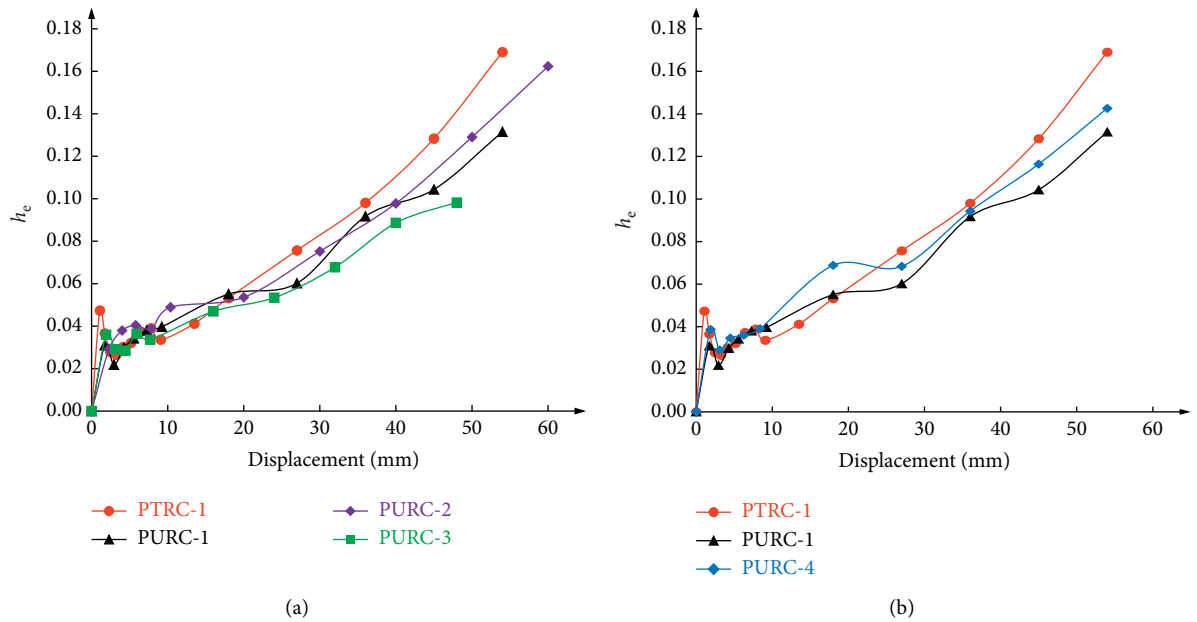

Figure 9: Comparison of equivalent damping coefficients.

4.6. Self-Centering Performance. The self-centering performance of a structure or member refers to its recovery performance to the initial state after applying the load. To intuitively reflect the self-centering performance of test columns, the self-centering capability coefficient γ is used, and it can be calculated as follows:

$$\gamma = 1 - \frac{\Delta_r}{\Delta_m}, \tag{4}$$

where γ is the self-centering capability coefficient; Δ_r is the residual displacement of the structure or member after the load; and Δ_m is the maximum displacement of the structure or member under load. Figure 10 shows the changing curve of the self-centering capability coefficient of test columns.

As shown in Figure 10, it is concluded that

(1) The concrete column with unbonded prestressed tendons has a large self-centering capability coefficient and strong self-centering performance, which can reduce the residual displacement of the test column. When the loading displacement is +54 mm, the residual displacement of PURC-1 is 34.10% less than that of PTRC-1, and the reduction capacity coefficient of PURC-1 is 1.3 times larger than that of PTRC-1.

(2) When the displacement is small, the self-centering capability coefficient of the specimen is relatively stable with a small changing trend, and the self-centering capability curve is basically parallel to the x-axis. When the loading displacement increases, the self-centering capability coefficient of the test column decreases gradually. The greater the loading displacement, the faster the reduction in the self-centering capability coefficient.

(3) At the beginning of loading, the larger the applied axial pressure ratio of the test column, the larger the initial self-centering capability coefficient. However, with the increase in the loading displacement, the decline rate of the self-centering capability coefficient accelerates, the changing curve of the self-centering capability coefficient becomes steeper and steeper, and the self-centering capability coefficient of the column with a large applied axial pressure ratio is gradually smaller than that of the column with a small applied axial pressure ratio. It shows that the excessive applied axial compression ratio is not conducive to maintain the self-centering performance of prestressed concrete columns after damage. This is because the restoring force of the test column is provided by the prestressed tendons and the main reinforcement. The greater the applied axial pressure ratio, the more work the restoring force needs to overcome the axial pressure in the process of specimen recovery.

(4) The larger the preloaded axial compression ratio, the smaller the residual displacement of the test column, and the larger the self-centering capability coefficient. This is because the greater the prestress, the greater the restoring force provided. Besides, the preloaded axial compression ratio has little effect on the reduction rate of the self-centering coefficient of the test column.

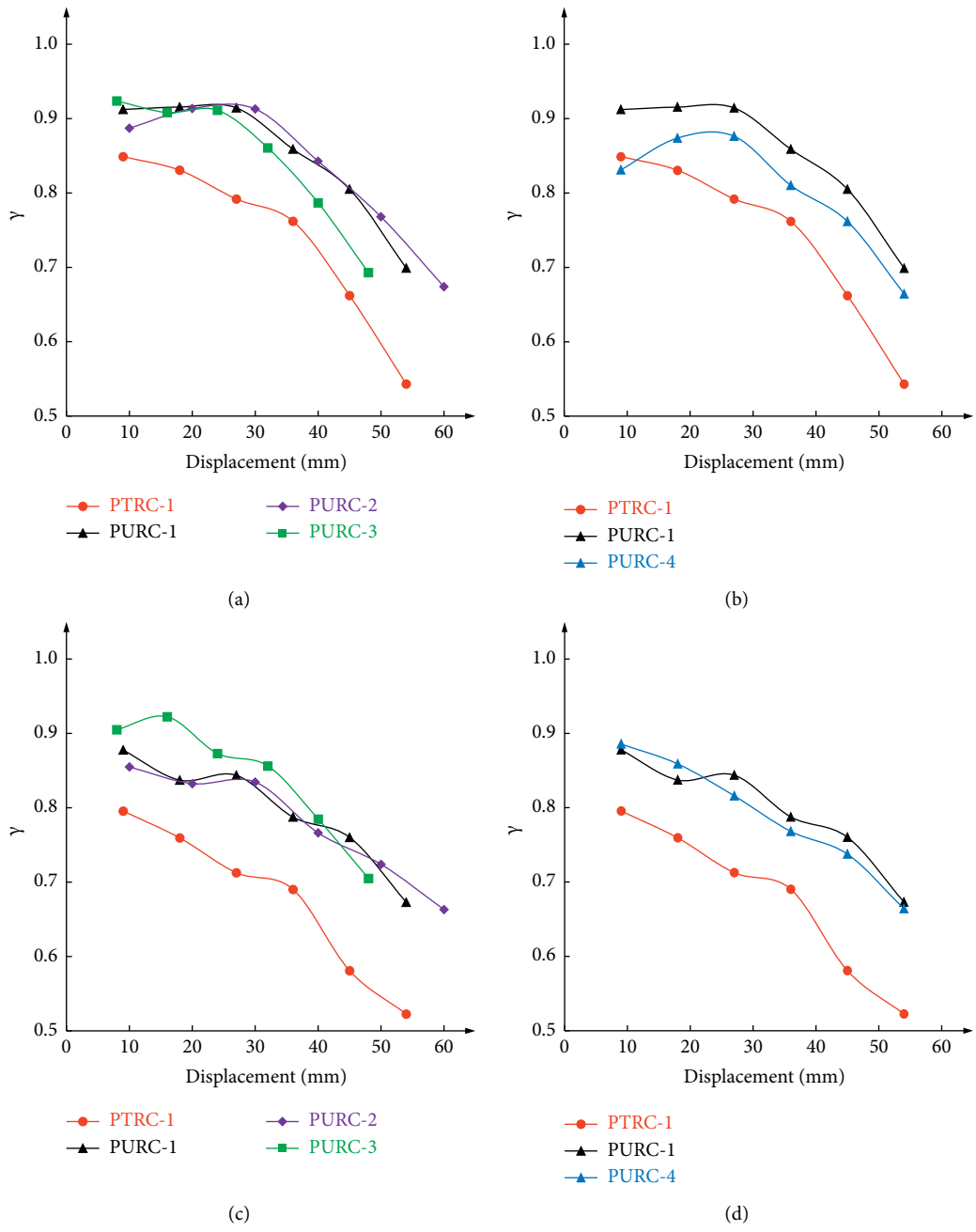

Figure 10: Self-centering capability coefficient of specimens. *Note*. (a) and (b) present the self-centering capability coefficients of specimens under the forward loading; (c) and (d) present the self-centering capability coefficients of specimens under the reverse loading.

5. Conclusion

In this test, the low-cycle repeated loading tests were conducted on one ordinary reinforced concrete column and four reinforced concrete columns with posttensioned unbonded prestressed tendons under different axial compression ratios. The conclusions are obtained as follows:

(1) Adding posttensioned unbonded prestressed tendons to ordinary reinforced concrete columns can lead to poor energy dissipation performance, but it can effectively improve the self-centering performance of the test columns and reduce the residual displacement of the columns.

(2) Axial compression ratio is an important factor affecting the seismic performance of test columns. With the increase in the applied axial compression ratio, the bearing capacity and initial stiffness of the column increase, but the ductility and energy dissipation performance become worse, and the stiffness and bearing capacity decay faster. The increase in the preloaded axial compression ratio can deteriorate the ductility and energy dissipation

performance of columns, but rarely affects the bearing capacity of columns. Besides, the increase in the preloaded axial compression ratio can reduce the attenuation rate of bearing capacity.

(3) The elastic displacement angle of each test column is between 1/21 and 1/18, which meets the design requirement that the displacement angle between elastic-plastic layers is not less than 1/50 under rare earthquake action. It indicates that the posttensioned unbonded prestressed concrete column has good collapse resistance.

(4) The average strength attenuation rate of each test column under all levels of loading displacement amplitude is not more than 8%, and the maximum strength attenuation rate is not more than 12%. It indicates that the posttensioned unbonded prestressed concrete column has good seismic bearing capacity under earthquake.

(5) The axial compression ratio has an important influence on the self-centering performance of posttensioned unbonded prestressed concrete columns. The larger the applied axial pressure ratio, the better the initial self-centering performance of the column, but the faster the self-centering performance attenuation in the later stage of loading, the worse the self-centering performance. The greater the preloaded axial compression ratio, the better the self-centering performance of the column. Besides, the preloaded axial compression ratio has no significant effect on the attenuation rate of self-centering performance.

Data Availability

The data used to support the findings of this study are included within the article.

Conflicts of Interest

The authors declare that they have no conflicts of interest.

Acknowledgments

The work in this study was supported by the Natural Science Foundation of the Jiangsu Higher Education Institutions of China (20KJB560012). The authors would like to acknowledge the support of the organizations for providing photographs and advice.

References

[1] J. F. Jia, B. Wei, and J. P. Ou, "Test for seismic performance of prefabricated self-centering bridge piers with external replaceable energy dissipator," *Journal of Vibration and Shock*, vol. 40, no. 5, pp. 154–162, 2021.

[2] E. Xiong, K. Zu, J. Wang, and Q. Zhang, "Seismic performance analysis of self-centering concentrically braced steel frame structures," *World Earthquake Engineering*, vol. 36, no. 3, pp. 69–79, 2020.

[3] J. Erochko, C. Christopoulos, and R. Tremblay, "Design and testing of an enhanced-elongation telescoping self-centering energy-dissipative brace," *Journal of Structural Engineering*, vol. 141, no. 6, 2015.

[4] C.-C. Chou, W.-J. Tsai, and P.-T. Chung, "Development and validation tests of a dual-core self-centering sandwiched buckling-restrained brace (SC-SBRB) for seismic resistance," *Engineering Structures*, vol. 121, pp. 30–41, 2016.

[5] D. J. Miller, L. A. Fahnestock, and M. R. Eatherton, "Development and experimental validation of a nickel-titanium shape memory alloy self-centering buckling-restrained brace," *Engineering Structures*, vol. 40, pp. 288–298, 2012.

[6] Z. Zhou, Q. Xie, X. C. Lei, X. He, and S. Meng, "Experimental investigation of the hysteresis performance of dual-tube self-centering buckling-restrained braces with composite tendons," *Journal of Composites for Construction*, vol. 19, no. 6, Article ID 4015011, 2015.

[7] C. Fang, M. C. H. Yam, T.-M. Chan, W. Wang, X. Yang, and X. Lin, "A study of hybrid self-centring connections equipped with shape memory alloy washers and bolts," *Engineering Structures*, vol. 164, pp. 155–168, 2018.

[8] H. Y. Luo, Q. Li, and Z. B. Wang, "Experimental study on restoring performance of unbonded partially prestressed concrete columns," *China Concrete and Cement Products*, vol. 7, pp. 44–48, 2013.

[9] L. Lu, Y. L. Ye, and W. Q. Xia, "Study on the seismic performance of a 3D external prestressed self-centering reinforced concrete frame by shaking test," *China Civil Engineering Journal*, vol. 53, no. S2, pp. 68–73+108, 2020.

[10] H. Qian, J. t. Xu, and J. t. Zhu, "Numerical simulation of mechanical behaviors of the innovative self-centering coupling beam damper," *World Earthquake Engineering*, vol. 36, no. 4, pp. 121–129, 2020.

[11] D. Roke, R. Sause, J. M. Ricles, and N. Gonner, "Design concepts for damage-free seismic-resistant self-centering steel concentrically-braced frames," in *Proceedings of the 14th World Conference on Earthquake Engineering*, pp. 1–10, Beijing, China, October 2009.

[12] H. Y. Luo, *Research on the Influence of the Degree of Prestress to Re-centering Behavior of Unbonded Partially Prestressed concrete Columns*, Yangzhou University, Yangzhou, China, 2008.

[13] Y. M. Yang, P. Yang, and H. J. Gao, "Experimental study on the seismic behavior of self-centering RC frame column base joints under different axial compressive ratios," *Journal of Tianjin University*, vol. 53, no. 5, pp. 542–550, 2020.

[14] F. M. Li, *Effect of Steel Strands Corrosion on Prestressed concrete Structures under Chloride Environment*, China University of Mining and Technology, Beijing, China, 2008.

[15] China University of Mining and Technology, *A Tensioning Support Foot Device: 200720035651*, China University of Mining and Technology, Xuzhou, China, 2008.

[16] China Academy of Building Research, *Specification For Seismic Test of Buildings: JGJ/T101-2015*, China Architecture & Building Press, Beijin, China, 2015.

[17] J. Yan, Z. L. Li, and G. Zuo, "An experimental study on the seismic performance of welded closed stirrup concrete columns," *Journal of Vibration and Shock*, vol. 37, no. 24, pp. 148–157+171, 2018.

Hindawi
Advances in Civil Engineering
Volume 2021, Article ID 6733402, 12 pages
https://doi.org/10.1155/2021/6733402

Research Article

Flexural Behaviour of RC Beams with a Circular Opening at the Flexural Zone and Shear Zone Strengthened Using Steel Plates

J. Branesh Robert,[1] **R. Angeline Prabhavathy**,[1] **P. S. Joanna**,[1] **S. Christopher Ezhil Singh**,[2] **Sivaraj Murugan**,[3] **S. Rajkumar**,[3] **and Shubham Sharma**[4]

[1]*Department of Civil Engineering, Hindustan Institute of Technology and Science, Padur, Chennai, Tamil Nadu 603103, India*
[2]*Department of Mechanical Engineering, Vimal Jyothi Engineering College, Kannur, Kerala 670632, India*
[3]*Department of Mechanical Engineering, Faculty of Manufacturing, Hawassa University, Hawassa, Ethiopia*
[4]*Department of Mechanical Engineering, IK Gujral Punjab Technical University, Main Campus, Kapurthala 144603, India*

Correspondence should be addressed to Sivaraj Murugan; msivaraj2014@gmail.com

Received 6 July 2021; Revised 29 September 2021; Accepted 8 October 2021; Published 2 December 2021

Academic Editor: Wenjie Ge

In this paper, an investigation on the behaviour of RC beams with circular openings in the flexural zone and shear zone strengthened using steel plates is presented. Totally seven beams were cast: a control beam, one beam with a circular opening of size of one-third the depth of the beam (100 mmϕ) in the flexural zone, one beam with opening strengthened using the steel plate, one beam with a circular opening of size of 100 mmϕ in the shear zone, one beam with an opening in the shear zone strengthened using the steel plate, one beam with two circular openings of size of 100 mmϕ in the shear zone, and another beam with two openings in the shear zone strengthened using the steel plate. The experiments were conducted in a loading frame of 400 kN capacity. The beams were subjected to two-point loading. The ultimate load carrying capacity reduced marginally by 1.78% and 2.8% compared to that of the control beam when a circular opening of 100 mmϕ was provided in the flexural zone and shear zone, respectively, and when the opening was strengthened with steel plates, it reduced by 3.04% and 25%, respectively, but the ductility increased when steel plates were provided. Beams with an opening of size of one-third the depth of the beam (100 mmϕ) in the flexural zone strengthened with the steel plate can be provided, as the load carrying capacity is only marginally reduced compared to the control beam, and the ductility is more when compared with beams with unstrengthened openings.

1. Introduction

In high-rise framed structures, providing service ducts is necessary for various purposes. If the ducts placed under the beams are covered by a false ceiling, the height of each floor increases, resulting in a considerable increase of the total height. The service ducts are provided through openings in RC beams. As a result, the stiffness decreases, which reduces the load carrying capacity and causes excessive deflection under the service load. Many researchers have studied the strengthening of RC beam with openings which increased the load capacity effectively. In order to enhance the shear capacity and regain the strength of the beams with openings, numerous strengthening techniques were suggested. FRP can play a key part in reinforcing and strengthening the structures. The reinforced concrete beams with openings can be strengthened by CFRP sheets, GFRP sheets, laminates, rods, fabrics, and so forth with different strengthening schemes. The load carrying capacity of the reinforced concrete beams with openings increases when strengthened externally with CFRP sheets in RC T-section deep beams [1], fibre reinforced polymer sheets in RC beams [2], unidirectional CFRP fabrics in RC T-beams [3], and NSM (near surface mounted) GFRP rods saturated with epoxy in RC self-compacting concrete deep beams [4]. CFRP laminates fully wrapped around the openings in RC beams with large openings [5], CFRP and GFRP sheets both around and inside the opening [6], CFRP strips with different

orientation and axis in RC deep beams [7], inclined and vertical configurations of bonding steel plate in beams with circular opening at the shear zone [8], and end anchor system with epoxy [9] are used. The reinforced concrete beam with openings strengthened by CFRP laminates at the flexural region increases the stiffness of beam [9]. Fibre reinforced concrete beams with opening indicate that the location of opening, web reinforcement, and fibre content affect the shear strength, tensile strength, and the behaviour of deep beams [10]. The FRC specimens with strengthened boundaries attain higher strength compared to the design load and exhibit ductile failure [11]. The shear capacity of the beam increases when the openings are strengthened with mild steel strips that are 3 mm thick in reinforced concrete T-beams. The beam deflection significantly reduced in RC beams, when inclined and vertical configurations of bonding steel plate were used for strengthening the circular opening at the shear zone [8] and the CFRP sheets were used in the openings [2]. The midspan deflection at the initial stage is not affected by the size of the openings but the formation of diagonal cracks near the opening affects the beam [12].

The strengthening techniques that are very effective in preventing and controlling the formation of cracks around the opening in reinforced concrete beams with openings are externally installed FRP rods placed diagonally in full length [13], strengthening with fibre reinforced polymer sheets, strengthening with glass fibre reinforced polymer wrapping around the opening [14], and strengthening by CFRP strips with different orientation [7].

Shear compression failure occurs in RC T-section deep beams strengthened externally with CFRP sheets due to partial elimination of CFRP sheets and U-wrapped anchorage CFRP sheets [15]. The steel fibre reinforced concrete beams with openings and high moment-to-shear ratio demonstrate ductile behaviour. The beams with low moment-to-shear ratio fail due to shear cracking [16]. Steel fibre reinforced concrete deep beams with large openings and the boundary regions near the supports of specimens strengthened with steel cages formed by steel reinforced bars exhibit a ductile mode of failure [17]. Strengthening using the inclined configuration of the bonding steel plate instead of the vertical configuration in RC beams with circular opening at the shear zone changes the mode of failure from shear mode to flexural mode. The FRC specimens with strengthened boundaries exhibit ductile failure [11]. Sudden failure due to the formation of diagonal shear cracks in the top and bottom chords of the opening and detachment of CFRP wrapper from the concrete surface occur in reinforced concrete deep beams with openings strengthened by CFRP sheets [18].

Many retrofitting techniques are used in reinforced concrete beams without openings. Few of them are discussed and they can be used for reinforced concrete beams with openings in the future. A relatively thin reinforced U-shaped concrete jacket made of self-compacting concrete to repair the shear damaged RC beams restores the load carrying capacity with respect to the initial samples, enhances the overall structural performance, and alters their failure mode to a more ductile one. Jacketed beams exhibit pure flexural and enhanced ductile behaviour, whereas the corresponding initially tested beams demonstrate typical brittle shear response [19]. Another study presents a simpler approach for analysing the interface slippage distribution for jacketed RC beams that can be manipulated by engineers to accurately plot the load-deflection curves of jacketed RC beams taking into account slip impact [20]. A new retrofitting technique to upgrade the structural behaviour of shear-critical rectangular and T-shaped reinforced concrete (RC) deep beams without steel stirrups using CFRP ropes as shear reinforcement exhibits increased capacity and significant improvement in the overall behaviour compared to the control beams. The catastrophic brittle failure of the beams is prevented by altering the shear failure to a ductile flexural one [21]. The repair of heavily damaged shear-critical reinforced concrete beams jacketed with mild steel small diameter U-shaped transverse stirrups examined experimentally in thin, U-shaped cement mortar jacketing showed reduced brittleness and increased deflections at failure up to six times compared to the initially tested specimens and can alter the failure mode from brittle shear to ductile flexural under certain circumstances [22]. The beam retrofitting technique by injecting grout infilled prefabricated fibre reinforced polymer (FRP) jacket is better to repair flexural components with damage on the top rather than at the bottom of the member [23]. A promising strengthening approach is the application of externally bonded fibre reinforced polymer (EB-FRP) as a shear transverse enhancement used in vulnerable reinforced concrete (RC) beams [15]. U-jacketing in shear-critical T-beams seems to undergo premature debonding failures, resulting in significant reduction of the predictable strength. Strengthening RC beams with the U-jacketing technique using galvanised welded steel wire mesh (SWM) and thin self-compacting concrete layer is one of the most recent techniques. It is found that the utilisation of SWM has a significant influence on ductility [24]. A reinforced concrete shear-critical beam with continuous rectangular spiral reinforcement as transverse reinforcement enhances the bearing capacity and improves the shear performance. An advanced rectangular spiral reinforcement with inclined vertical links as shear reinforcement improves the postpeak deformation ductility compared to the control beams [25].

Numerical analysis using 3D finite element (FE) modelling can be used as an engineering tool, as accurate results can be obtained in a relatively short time. A smeared crack model for the postcracking behaviour of slender and deep flexural and shear-critical steel fibre reinforced concrete (SFRC) beams under tension, using the fracture characteristics of the composite material, accurately predicts the load versus deformation cyclic envelope and the influence of the fibres on the overall hysteretic performance [26]. A new constitutive hypoelastic-brittle model of concrete based on the smeared cracking approach and a method including the tension stiffening effect in connection with the bond properties between concrete and steel (TS) are developed, which accurately predict the ultimate load capacity [27]. A parametric study on reinforced concrete beams with openings in the shear zone strengthened using orthotropic

CFRP analysed by finite element method (ANSYS9) taking the maximum strain values for concrete and steel at failure loads of different opening sizes shows that the proposed model is efficient [28]. The brittle crack model offers an approximate but reliable way for modelling of concrete. The FE simulation (ABAQUS) results are favourable when compared to those observed in experiments. A study was performed by beams with spiral reinforcement under monotonic loading. However, these beams showed a rather ductile response, whereas the other beams showed brittle shear failure [29].

The literatures pertaining to the repair and retrofitting of reinforced concrete beams, deep beams, and strengthening of reinforced concrete beams with openings using different techniques like steel fibres, FRP, CFRP, GFRP, stirrups, and the finite element modelling of reinforced concrete beams with openings and their comparison with the experimental investigation are reviewed. All the strengthening methods are practically very difficult, very expensive, and time consuming and require interruption of use of the structure, while works are being carried out. Hence, there is an urgent need for the development of an improved, low cost, less disruptive technique, which makes the necessary strengthening of structures economically viable.

Almost all the researchers investigated about the external reinforcement or externally strengthened beams with openings. Some literatures discuss the use of steel plates placed externally in the form of strips to strengthen the beams with openings. Hence, strengthening to the openings in reinforced concrete beams with steel plates kept inside the openings during casting and connected using shear connectors was proposed.

No research has been conducted on RC beams with circular openings strengthened using steel plates in the flexural zone and shear zone and such beams are investigated to study their behaviour with respect to the ultimate load capacity, load-deflection behaviour, and the mode of failure.

Besides, there is no proper finite element analysis carried out on strengthened beams with openings. Therefore, this paper presents the finite element modelling of beams with openings strengthened with steel plates kept inside the openings using ABAQUS software.

A new method has been developed for strengthening the RC beams with circular openings in the flexural zone and shear zone using steel plates connected using shear connectors around the openings placed during casting of the beam. The use of steel plates around the openings for strengthening the RC beams with circular openings has not been reported so far. The outcome of this work represents promising data for further studies to be conducted in large scale to improve the load capacity of the RC beams with openings in construction works.

2. Experimental Investigations

2.1. Materials. In this study, cement OPC (grade no.53) meeting the requirements of IS 12269 and having specific gravity of 3.15 was used. The fine aggregate used in the concrete mix was M sand. Blue granite crushed stone aggregates of 20 mm size were used as coarse aggregate. Potable water without any suspended particles and impurities was used for the purpose of mixing of concrete. The mechanical properties such as specific gravity of the materials and gradation of soil were found out conducting the specific gravity test and the sieve analysis. The most commonly used grade of concrete in construction M20 grade concrete and Fe 415 steel were used. The mix design of concrete was carried out as per IS code 10262.

2.2. Test Specimen Details. In this experimental programme, totally seven beams were cast with the same cross section which included a control beam, one beam with circular opening of size of one-third the depth of the beam (100 mmϕ) in the flexural zone, one beam with opening (100 mmϕ) strengthened using steel plate, one beam with an opening (100 mmϕ) in the shear zone, one beam with an opening (100 mmϕ) in the shear zone strengthened using steel plate, one beam with two openings of size of 100 mmϕ in the shear zone, and one beam with two openings (100 mmϕ) in the shear zone strengthened using steel plate. The test specimens were of rectangular cross section having the dimensions of 150 mm width, 300 mm depth, and 2000 mm length tested under two-point loading. Each beam had a longitudinal reinforcement of 3 numbers of 12 mm dia. bars at the bottom, 2 numbers of 10 mm dia. bars at the top, and 8 mm dia. stirrups at 200 mm centre to centre spacing used as shear reinforcement. The reinforcement details of the test specimens are shown in Figure 1. 4 mm thick steel plates with shear connectors were used for strengthening the opening region. The circular opening was created by a circular steel plate inserted in the beam before casting of concrete. The details of the test specimens are shown in Table 1. Figure 2 shows the moulding, casting, and curing of beam specimens.

2.3. Test Setup. The test setup consists of a loading frame of 400 kN capacity with a hydraulic jack and a strain indicator. The edges of the beams were simply supported on roller supports placed 100 mm away from the face of the support. The beams were subjected to two concentrated static loads and subsequently increased till failure. Instrumentation included linear variable differential transducers (LVDT) with 0.01 mm accuracy for deflection measurement at the midspan of the beam and at 2 positions at a distance of 400 mm from the midspan on either side. The load was measured by a load cell with 0.05 kN accuracy attached to the hydraulic jack and used for the measurement of applied loads. The load and corresponding deflection measurements were recorded continuously during the performed tests. The strain gauges were placed at the midspan and around the openings to measure the strains in the beams. Figure 3 shows the schematic diagram of the test setup. The test setup for the reinforced concrete beam without openings is shown in Figure 4.

3. Results and Discussion

3.1. Effect of Providing the Circular Opening with and without the Steel Plate in Beams on the Load-Deflection Behaviour. The load-deflection behaviour of control beam and beams with openings of 100 mm ϕ (D/3 size) strengthened with

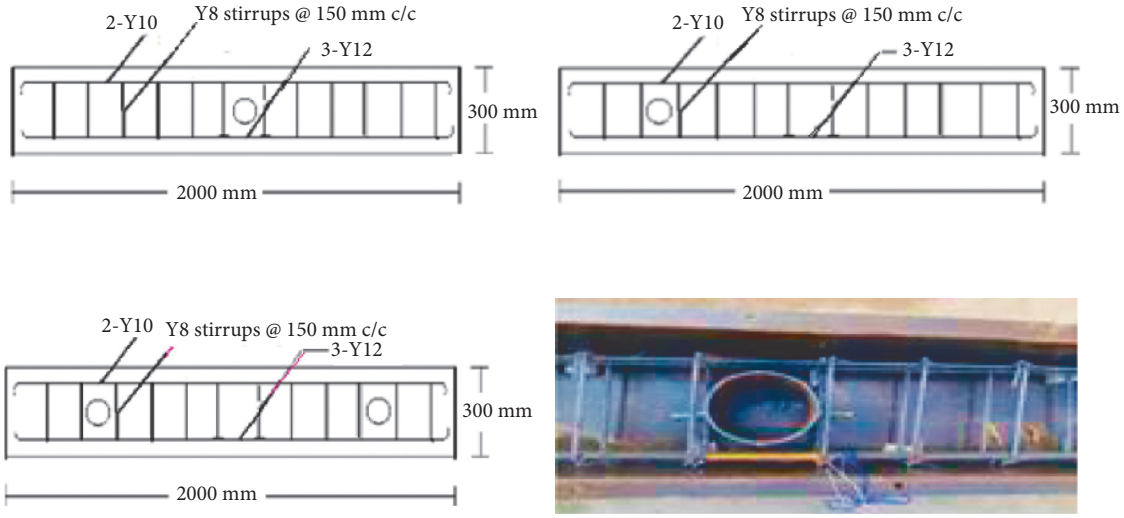

Figure 1: Reinforcement details of the beam with a circular opening.

Table 1: Details of beam specimens.

S. no.	Specimen details	Name of the specimen	Opening size
1	Control beam	CB	—
2	Beam with an opening at the flexural zone	BCOF	100 mm
3	Beam with an opening at the shear zone	BCOS1	100 mm
4	Beam with 2 openings at the shear zone	BCOS2	100 mm
5	Beam with an opening at the flexural zone (strengthened by the steel plate)	BCFSP	100 mm
6	Beam with an opening at the shear zone (strengthened by the steel plate)	BCSSP1	100 mm
7	Beam with 2 openings at the shear zone (strengthened by the steel plate)	BCSSP2	100 mm

(a)

(b)

Figure 2: Moulding, casting, and curing of beams. (a) Reinforcement detailing with steel plates for strengthening the opening, casting, and curing. (b) Cast beam specimens with an opening.

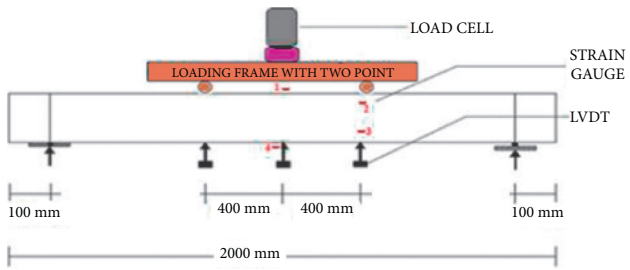

Figure 3: Test setup of the beams.

Figure 4: Test setup of the control beam.

steel plates in the flexural and shear zones is shown in Figure 5.

From Figure 5, it can be seen that the beams with openings when strengthened with steel plates exhibit more ductility and the load capacity of beams with opening (100 mm ϕ) in the flexural and shear zones was higher compared to beams strengthened with steel plates but the ductility was less.

3.2. Effect of Providing the Circular Opening in the Flexural Zone and Shear Zone of the Beam. The load versus deflection behaviour of the beams with opening (100 mmϕ) in the flexural and shear zones is shown in Figure 6. When 2 circular openings of 100 mmϕ were provided near the supports, the ultimate load was reduced by 13.2% compared to the control beam, whereas provision of a small opening in the flexural zone as well as an opening in the shear zone marginally decreased the ultimate load.

The ultimate loads, crack load, and deflection of the control beam and RC beams having opening (100 mmϕ) are shown in Table 2.

3.3. Effect of Providing the Circular Opening with the Steel Plate in the Flexural Zone and Shear Zone. The control beam carries an ultimate load of 151.5 kN and the maximum deflection is 21 mm. Figure 7 shows the load versus deflection behaviour of beams with opening (100 mmϕ) in the flexural and shear zones with steel plates. The beams with steel plates did not fail in a brittle manner. The beam BCFSP showed a marginal reduction in the load capacity compared to control beam and the ductility is more when compared with other beams with unstrengthened openings.

3.4. Effect of Providing the Steel Plate in the Opening (100 mmϕ) Provided at the Midspan (Flexural Zone) of the Beam. The load-deflection behaviour of beams with

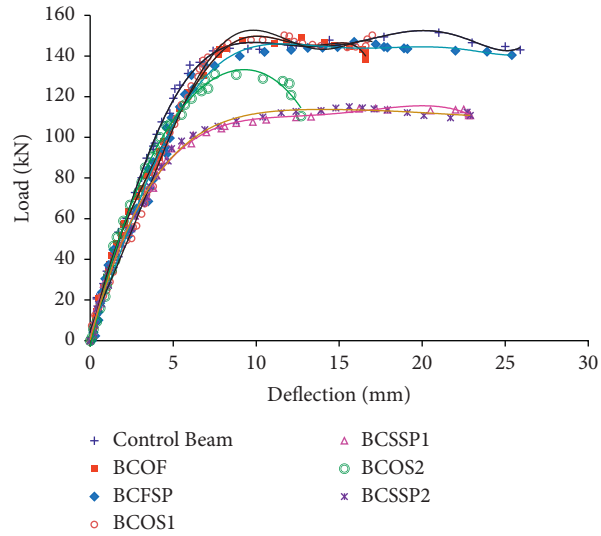

Figure 5: Load versus deflection behaviour of beams with the opening (100 mmϕ) in the flexural and shear zones with and without steel plates.

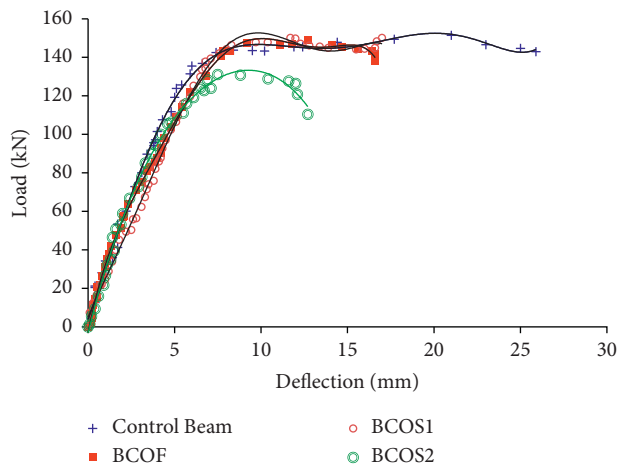

Figure 6: Load versus deflection behaviour of beams with the opening (100 mmϕ) in the flexural and shear zones.

opening (100 mmϕ) at the midspan (flexural zone) strengthened with steel plate is shown in Figure 8. The ultimate load of beam BCOF is 148.8 kN and, in beam BCFSP, when the opening was strengthened using steel plate, the ultimate load is 146.9 kN. When a circular opening of 100 mmϕ was provided at the flexural zone, for beam BCOF, the ultimate load reduced marginally (1.78%) compared to control beam and, for beam BCFSP, it reduced by 3.04%.

3.5. Effect of Providing the Steel Plate in the Opening (100 mmϕ) Provided at the Shear Zone. The ultimate load of beam with opening (100 mmϕ) at the shear zone strengthened with steel plate was reduced by 1.26% compared to the beam without strengthening because of the formation of cracks in the flexural zone due to the provision of steel plate

Table 2: Load and deflection results.

S. no.	Beam description	Crack load (kN)	Ultimate load (kN)	Deflection (mm)
1	Control beam (CB)	34.5	151.5	21
2	BCOF	41.8	148.8	12.7
3	BCFSP	37.2	146.9	15.9
4	BCOS1	29.5	150.1	17
5	BCSSP1	22.1	114.2	17.2
6	BCOS2	29.8	131.5	15.7
7	BCSSP2	21.7	115.1	15.6

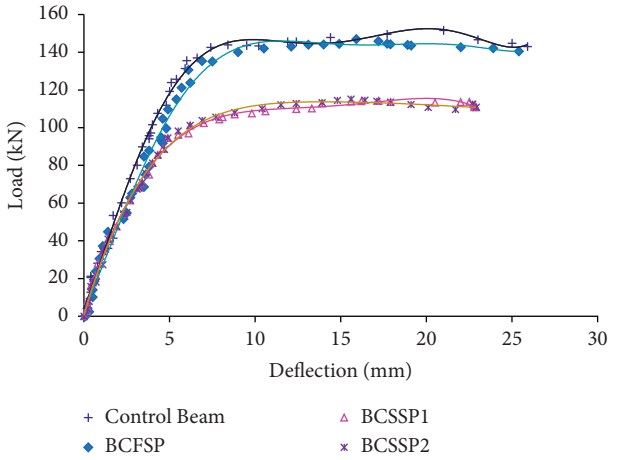

Figure 7: Load versus deflection behaviour of beams with the opening (100 mmϕ) in the flexural and shear zones strengthened with the steel plate.

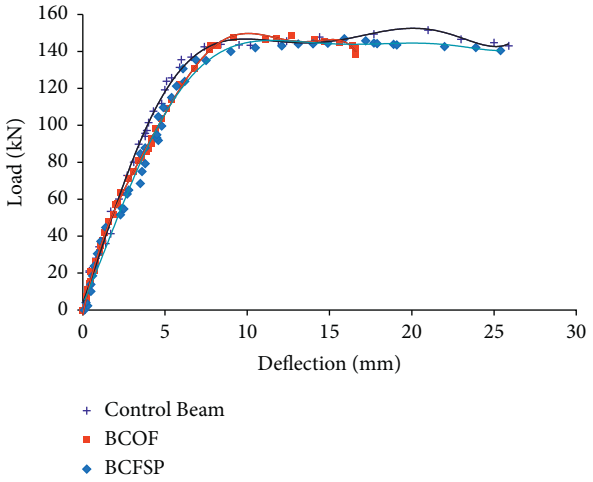

Figure 8: Load versus deflection behaviour of beams with the opening (100 mmϕ) provided at the midspan (flexural zone) of the beam.

around the opening at the shear zone. Figure 9 shows the load versus deflection behaviour of beams with an opening (100 mmϕ) in the shear zone with steel plates. The ultimate load of the beam with opening (100 mmϕ) near the support (BCOS1) was 147.2 kN and when the opening was strengthened using steel plate (BCSSP1), the ultimate load was 113.5 kN. The ultimate load reduced marginally by 2.8% for beam BCOS1 and reduced by 25% when the opening was

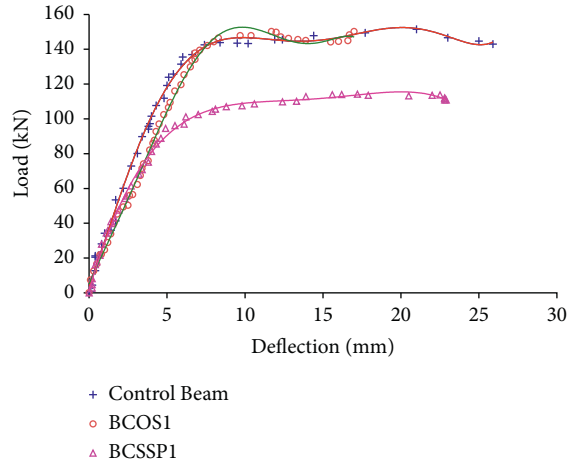

Figure 9: Load versus deflection behaviour of beams with the opening (100 mmϕ) provided at the shear zone with steel plates.

strengthened with steel plates, compared to the control beam. The ultimate load reduced marginally by 23% for beam BCSSP1 compared to the beam without strengthening as flexural cracks were formed earlier at the midspan due to strengthening of the openings in the shear zone.

3.6. Effect of Providing the Steel Plate for 2 Circular Openings (100 mmϕ) Provided at the Shear Zone of the Beam. The ultimate load of the beam with 2 openings (100 mmϕ) near the support (BCOS2) is 131.5 kN and, for beam BCSSP2, the ultimate load is 115.1 kN. Figure 10 shows the load versus deflection behaviour of beams BCOS2 and BCSSP2.

When 2 circular openings of 100 mmϕ were provided in the shear zone, the ultimate load reduced by 13.2% compared to the control beam and when the openings were strengthened with steel plates, it was reduced by 24% because flexural cracks were formed in the flexural zone.

When steel plates were provided around the openings in the shear zone, the diagonal shear cracks around the openings reduced to a larger extent and the flexural cracks appeared. The load carrying capacity of the beam reduced due to the earlier formation of flexural cracks but the ductility of the beams increases when steel plates are provided around the openings.

3.7. Failure Patterns of the Control Beam, BCOF, and BCFSP. Two modes of failure were observed in the tested beam specimens. The first mode is a diagonal breakup that happens when the diagonal crack originates from the opening

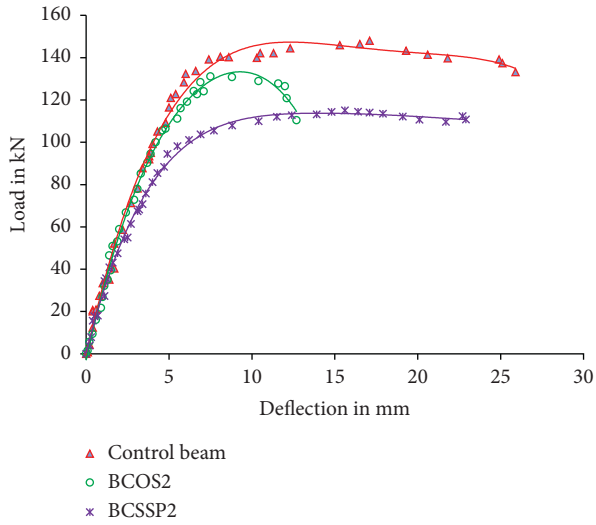

Figure 10: Load versus deflection behaviour of beams BCOS2 and BCSSP2.

corners and spreads in the direction of the load and support provided. The second mode is the shear compressive failure that occurs when the diagonal fracture is formed in the shear span, leading to excessive tension in the openings.

Figures 11 and 12 show the failure pattern of the control beam and the beam BCOF, respectively. The flexural cracks were formed first in the tension zone at a load of 34.5 kN for control beam and 41.8 kN for BCOF and propagated vertically.

Figure 13 shows the failure pattern of the beam BCFSP. For the beam BCFSP, the first crack appeared in the tension zone at a load of 37.2 kN. Steel plates provided around the openings resist the concentration of stress at the sides of the openings leading to reduction in crack formation in the flexural zone. However, diagonal shear cracks were formed in the shear zone because the flexural zone was strengthened using steel plate.

3.8. Failure Pattern of Beams BCOS1 and BCSSP1. The first crack appeared in the tension zone at a load of 23.5 kN for BCOS1 and diagonal shear cracks were noticed on the sides of the opening as shown in Figure 14. For the beam BCSSP1, when the opening was strengthened with steel plate in the shear zone, the first crack appeared in the tension zone at a load of 22.1 kN and flexural cracks occurred in the beam as shown in Figure 14, which resulted in considerable reduction in the load carrying capacity. There was a considerable reduction of diagonal cracks around the openings when the opening was strengthened in the shear zone using steel plate.

3.9. Modelling and Analysis of Beams with Circular Openings. The FEM package ABAQUS was used to create the models of the tested specimens. A nonlinear 3D FE analysis has been performed to predict the response of RC beams with circular openings in the flexural and shear zones subjected to static loading.

Concrete was assumed to be homogeneous and isotropic. Eight-node isoparametric element was used for idealisation of concrete. The reinforcement was represented by two-node truss element.

This model uses the fracture characteristics of the material taking into account the constitutive laws. The constitutive model used for concrete is formulated for stress and strain increments and it can be considered as a hypoelastic-brittle model proposed to characterise concrete deformability. The constitutive model used for steel is generalised elastic-plastic with tension stiffening effect. At first, the beam was modelled as a 3D deformable model. The element type used to model concrete was solid continuum, 3-dimensional, 8-node C3D8 element. Then the longitudinal reinforcement was also modelled as a 3D deformable model using simple truss elements. The 3-dimensional 2-node truss elements (T3D2) were selected for the simulation of main reinforcement (longitudinal steel bars) and transverse reinforcement (stirrups). The top reinforcement 2 nos. of Y10 bars, bottom reinforcement 3 nos. of Y12 bars, and the 6 mm dia. stirrups were also modelled using the 3D truss element. The steel plates were modelled as the 3D deformable shell element.

The material properties employed in the model are defined in ABAQUS, such as the properties of concrete and steel reinforcement. The ABAQUS model of concrete mainly consists of two material modelling techniques, concrete damaged plasticity (CDP) model and concrete smeared cracking. For plain and reinforced concrete models, both can be employed. In this work, the plasticity model for concrete damage is utilised to simulate the concrete.

The material properties were defined in the beam models. For concrete, the mass density, Young's modulus, and Poisson's ratio values were assigned. The values of the steel modulus of elasticity Es, yield stress, corresponding plastic strain, and Poisson's ratio were also used in the FE analysis according to the test data of the steel reinforcement. Modelling of steel reinforcement such as stirrups and steel longitudinal bars was done taking the modulus of elasticity and Poisson's ratio as 200×10^3 MPa and 0.3, respectively. The yield stress "fy" and the ultimate stress "fu" are defined in the model. The steel plates and supporting plates are designed as linear isotropic material with the elasticity modulus of steel equivalent to 200×10^3 MPa. The thickness of the steel plate was assigned. A section was created for every part given in the model, the profile names were given, and the material names were assigned.

3.9.1. Boundary Conditions. Every element's node has three degrees of freedom with x, y, and z (global coordinate system) translation. The supports were positioned at a particular distance from each edge and the edges remained free. The boundary conditions were taken as one end roller supported and another end simply supported. Concerning the boundary conditions for the supports, a line of nodes was constrained in the Ux, Uy, and Uz directions at the left side while at the right support, the translation in the X and Y directions was limited and hence functions as a roller.

Figure 11: Failure pattern of the control beam.

Figure 12: Failure pattern of beam BCOF.

Figure 13: Failure pattern of beam BCFSP.

3.9.2. Modelling of Interfaces. In order to ensure the correct interfacial activity between the two different surfaces concrete and steel plate, the interfacial element is employed. Embedded contact is regarded for the interaction between reinforcement and concrete. The bond between reinforcement and concrete is modelled using the embedded option, the ABAQUS feature "truss in solid" for which solid and truss element nodes do not have to be in the same location. Hence, regular and coarse meshes can be used in the analysis.

Normally, the mesh size is taken in proportion to the aggregate size. Meshing depends on the type of element. The mesh was taken as 10 mm for the reinforcement bars as the element part was small and for beams, the bigger solid element, the mesh size adopted was 20 mm for the solid element.

Every part in the model was assembled, the type of analysis was taken as static and the increments and the loads as mechanical and the load type as pressure were assigned. The data are checked for error and finally submitted for analysis. Using this model, the failure pattern of the beam with openings and the deflection values were obtained.

The modes of failure observed in the models of the beam specimens are diagonal crack which originates from the opening and spreads in the direction of the load and flexural failure in the tension zone of the beam models. Figure 15 shows the simulation of FE models for steel reinforcement and steel plates in the models using the FE software ABAQUS, the deflection pattern and the failure pattern of the control beam, and the beams with circular opening in the flexural zone and the shear zone.

The analytical loads, analytical deflection, experimental deflection, and ratio of analytical and experimental deflection of the control beam and RC beams having opening (100 mmϕ) are shown in Table 3.

The finite element results demonstrate that the beam's actual behaviour is observed in the finite element models. Furthermore, the results show that the experimental beams can anticipate likely fractures occurring in the FE model to a high degree of accuracy. In addition, comparison of the experimental and the numerical results shows that, in both linear and nonlinear parts of the behaviour, the numerical models with strengthened openings are stiffer than the tested beams with strengthened openings. There is a good

(a)

(b)

Figure 14: Failure pattern of beams (a) BCOS1 and (b) BCSSP1.

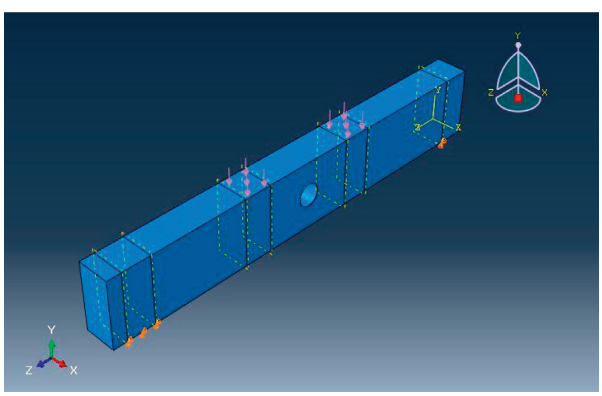

(a)

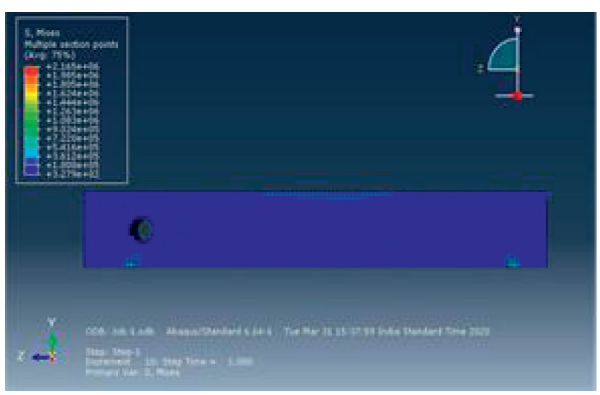

(b)

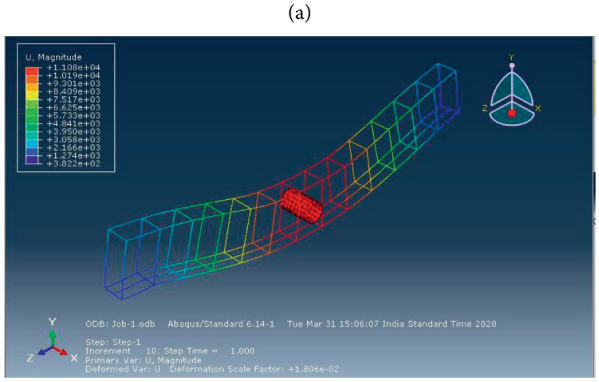

(c)

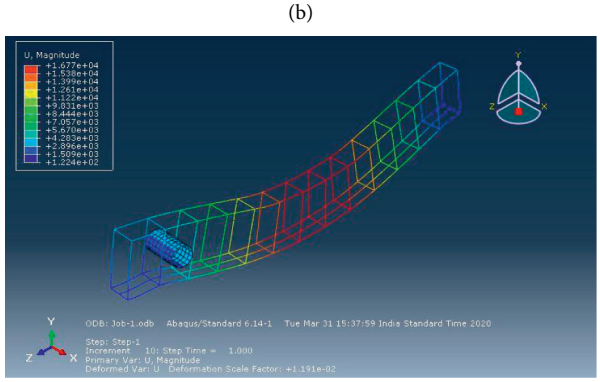

(d)

Figure 15: Continued.

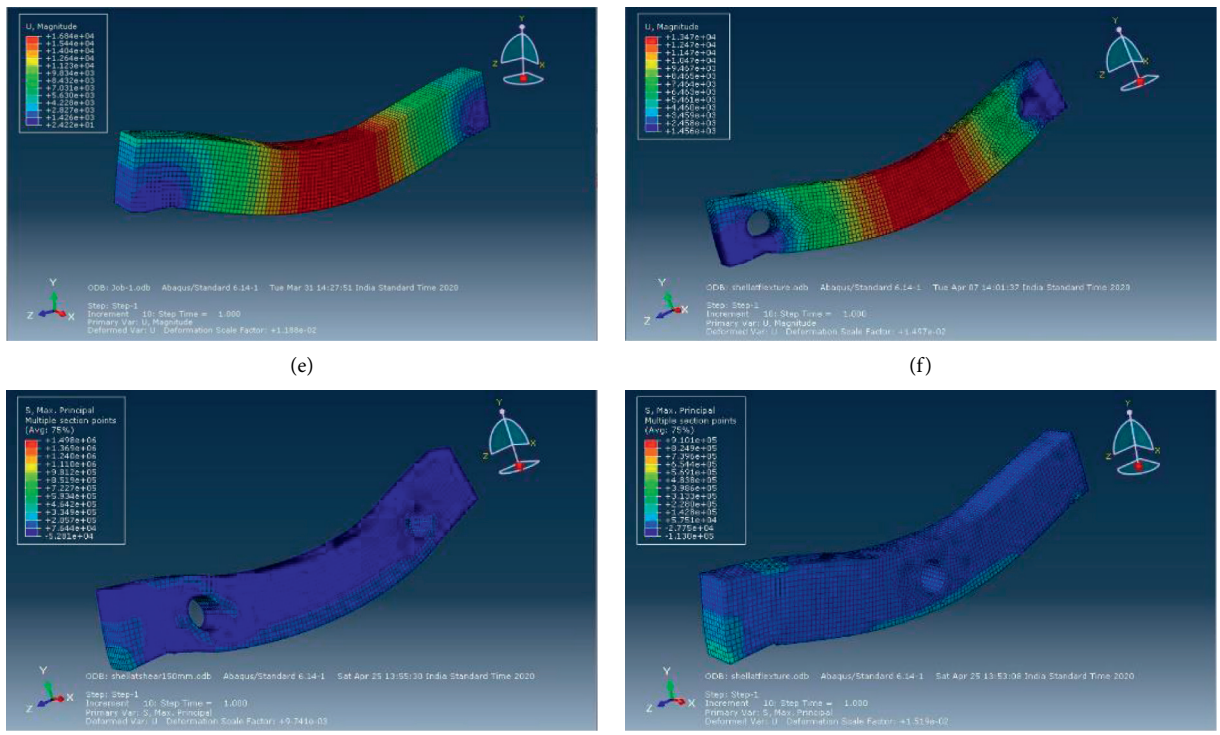

(e) (f)

(g) (h)

Figure 15: Analytical modelling of beams with circular openings in the flexural and shear zone. (a) Model with load points and supports. (b) Meshed model. (c) Reinforcement model of beam BCFSP. (d) Reinforcement model of beam BCOS1. (e) Deflection pattern for the control beam. (f) Deflection pattern for beam BCOS2. (g) Failure pattern for beam BCOS2. (h) Failure pattern for beam BCOF.

Table 3: Comparison of analytical and experimental deflection.

S. no.	Beam description	Load $P_{\text{Anal.}}$	Analytical deflection $\delta_{\text{Anal. (mm)}}$	Exper. deflection $\delta_{\text{Exp. (mm)}}$)	Ratio of $\delta_{\text{Anal}}/\delta_{\text{Exp}}$
1	CB	151.1	18.5	21	0.88
2	BCOF	148.8	13.3	12.7	1.05
3	BCFSP	146.9	14.1	15.9	0.89
4	BCOS1	147.2	17.15	16.9	1.02
5	BCSSP1	114.5	16.65	16.2	1.03
6	BCOS2	131.5	15.13	15.7	0.96
7	BCSSP2	115.1	14.75	15.6	0.95

agreement between the experimental and analytical models which allows the use of the finite element models for parametric studies related to beams with openings.

3.9.3. Effect of Providing Steel Plates around the Opening. Generally steel plates enhance the beam capacity. Earlier, when the experiments were conducted in beams using river sand, having circular opening strengthened using steel plates, an increase in the load capacity of 1.4 times and 70% was observed when two openings were provided in the shear zone and one opening was provided in the flexural zone, respectively, compared to the unstrengthened beams. When M sand was used instead of river sand, the first flexural crack occurred earlier, and the failure loads were reduced for the beams with circular openings in the shear zone strengthened using steel plates when compared to beams with unstrengthened openings in the shear zone. This may be due to M sand which was attributed to the earlier cracking of the beam in the flexural zone and caused the reduction in the load bearing capacity of the beam strengthened with steel plates. When the number of openings is raised from one to two as well, further reduction in the load carrying capacity was observed. However, steel plates improved the ductility of the beams before failure of the beams. The location of the opening affects the strength of the member to a greater extent.

This leads to the conclusion that the beams with circular opening of size of one-third the depth of the beam (100 mmϕ) in the flexural zone strengthened with steel plate can be provided as the load carrying capacity is marginally reduced when compared to the control beam and the ductility is increased by 103% when compared with the beam with unstrengthened opening.

4. Conclusion

(i) When a circular opening of one-third the depth of the beam (100 mmϕ) was provided in the flexural zone, the ultimate load reduced marginally by 1.78% and when the beam with opening was strengthened with steel plate, it reduced by 3.04%, when compared to the control beam.

(ii) Cracks formed were lesser in the case of beams with openings strengthened using steel plate when compared to the beams with openings without steel plate.

(iii) When the openings in the shear zone were strengthened with steel plates, the beams exhibited more ductility but resulted in the occurrence of flexural cracks leading to a considerable reduction in the load carrying capacity.

(iv) The finite element results demonstrate that the beam's actual behaviour is found in the finite element models. Furthermore, the results show that the experimental beams can anticipate likely fractures occurring in the FE model to a high degree of accuracy. In addition, comparison of the experimental and the numerical results shows that, in both linear and nonlinear parts of the behaviour, the numerical models with strengthened openings are stiffer than the tested beams with strengthened openings. There is a good agreement between the experimental model and the analytical model which allows the use of the finite element models for parametric studies related to beams with openings.

(v) Beam strength is greatly impacted by the number of openings.

(vi) It is concluded that the beam with opening of one-third the depth of the beam (100 mmϕ) in the flexural zone strengthened with steel plate can be provided as the load carrying capacity is marginally reduced when compared to the control beam and the ductility is increased by 103% when compared with the beam with unstrengthened opening.

Data Availability

The data used to support the findings of this study are available from the corresponding author upon request.

Conflicts of Interest

The authors declare that they have no conflicts of interest.

References

[1] H. K. Lee, S. H. Cheong, S. K. Ha, and C. G. Lee, "Behaviour and performance of RC T-section deep beams externally strengthened in shear with CFRP sheets," *Composite Structures*, vol. 93, no. 2, 2010.

[2] H. A. Abdalla, A. M. Torkey, H. A. Haggag, and A. F. Abu-Amira, "Design against cracking at openings in reinforced concrete beams strengthened with composite sheets," *Composite Structures*, vol. 60, no. 2, pp. 197–204, 2003.

[3] S. A. G. Aly, Y. H. Hammad, G. T. Abdel-Rahman, and M. Said, "Behavior of RC beams with strengthened openings in D-region," in *Proceedings of the 9th Arab Structural Engineering Conference*, pp. 163–174, Abu Dhabi, UAE, December 2003.

[4] K. M. Heiza, N. N. Meleka, and N. Y. Elwkad, "Shear strengthening of self-compacting reinforced concrete deep beams with external bonded layers," *Concrete Research Letters*, vol. 3, no. 4, pp. 507–527, 2012.

[5] S. C. Chin, N. Shafiq, and M. F. Nuruddin, "Strengthening of RC beams with large openings in shear by CFRP laminates: experiment and 2D nonlinear finite element analysis," *Research Journal of Applied Sciences, Engineering and Technology*, vol. 4, no. 9, pp. 1172–1180, 2012.

[6] R. Diggikar, S. Mangalgi, and R. Harsoor, "Behavior of RCC beam with rectangular opening strengthened by CFRP and GFRP sheets," in *Proceedings of the International conference on recent innovations in civil engineering*, pp. 25–27, Delhi, India, October 2013.

[7] B. S. Abduljalil, "Shear resistance of reinforced concrete deep beams with opening strengthened by CFRP strips," *Journal of Engineering and Development*, vol. 18, no. 1, pp. 14–32, 2014.

[8] G. Hassein Abed, *Effects of Temperature on the Adhesive Bonding in Steel Beams Reinforced with CFRP Composites*, Doctoral dissertation, University of Southampton, Southampton, England, 2012.

[9] A. Y. Ali, A. A. Ibrahim, and R. F. Yousif, "Analysis of reinforced concrete beams with openings and strengthened by (CFRP) laminates," *Univ Babylon Mag*, vol. 19, no. 3, pp. 1098–1113, 2011.

[10] V. Vengatachalapathy and R. Ilangovan, "A study on steel fiber reinforced concrete deep beams with and without openings," *International Journal of Civil and Structural Engineering*, vol. 1, no. 3, pp. 509–517, 2010.

[11] M. A. Mansur, "Effect of openings on the behaviour and strength of R/C beams in shear," *Cement and Concrete Composites*, vol. 20, no. 6, pp. 477–486, 1998.

[12] B. Aykac, I. Kalkan, S. Aykac, and Y. E. Egriboz, "Flexural behavior of RC beams with regular square or circular web openings," *Engineering Structures*, vol. 56, pp. 2165–2174, 2013.

[13] A. Pimanmas, "Strengthening R/C beams with opening by externally installed FRP rods: behavior and analysis," *Composite Structures*, vol. 92, no. 8, pp. 1957–1976, 2010.

[14] S. Mondal, J. N. Bandyapadhya, and C. P. Gautam, "Strengthening and rehabilitation of reinforced concrete beams with opening," *International Journal of Civil and Structural Engineering*, vol. 2, no. 1, pp. 127–137, 2011.

[15] C. E. Chalioris, A. G. Zapris, and C. G. Karayannis, "U-Jacketing applications of fiber-reinforced polymers in reinforced concrete T-beams against shear-tests and design," *Fibers*, vol. 8, no. 2, p. 13, 2020.

[16] X. F. Nie, S. S. Zhang, J. G. Teng, and G. M. Chen, "Experimental study on RC T-section beams with an FRP-strengthened web opening," *Composite Structures*, vol. 185, pp. 273–285, 2018.

[17] D. R. Sahoo Carlos, A. Flores, and S.-H. Chao, "Behaviour of steel fibre-reinforced concrete deep beams with large opening," *ACI Structural Journal*, vol. 109, no. 2, pp. 193–204, 2012.

[18] T. El Maaddawy and S. Sherif, "FRP composites for shear strengthening of reinforced concrete deep beams with openings," *Composite Structures*, vol. 89, no. 1, pp. 60–69, 2009.

[19] C. E. Chalioris and C. N. Pourzitidis, "Rehabilitation of shear-damaged reinforced concrete beams using self-compacting concrete jacketing," *International Scholarly Research Notices*, vol. 2012, Article ID 816107, 2012.

[20] M. M. A. Alhadid and M. A. Youssef, "Analysis of reinforced concrete beams strengthened using concrete jackets," *Engineering Structures*, vol. 132, pp. 172–187, 2017.

[21] C. Chalioris, P.-M. Kosmidou, and N. Papadopoulos, "Investigation of a new strengthening technique for RC deep beams using carbon FRP ropes as transverse reinforcements," *Fibers*, vol. 6, no. 3, p. 52, 2018.

[22] C. Chalioris, V. Kytinou, M. Voutetaki, and N. Papadopoulos, "Repair of heavily damaged RC beams failing in shear using U-shaped mortar jackets," *Buildings*, vol. 9, no. 6, p. 146, 2019.

[23] A. A. Mohammed, A. C. Manalo, G. B. Maranan et al., "Effectiveness of a novel composite jacket in repairing damaged reinforced concrete structures subject to flexural loads," *Composite Structures*, vol. 233, Article ID 111634, 2020.

[24] M. A. Abu Maraq, B. A. Tayeh, M. M. Ziara, and R. Alyousef, "Flexural behavior of RC beams strengthened with steel wire mesh and self-compacting concrete jacketing - experimental investigation and test results," *Journal of Materials Research and Technology*, vol. 10, pp. 1002–1019, 2021.

[25] C. G. Karayannis and C. E. Chalioris, "Shear tests of reinforced concrete beams with continuous rectangular spiral reinforcement," *Construction and Building Materials*, vol. 46, pp. 86–97, 2013.

[26] V. Kytinou, C. Chalioris, C. Karayannis, and A. Elenas, "Effect of steel fibers on the hysteretic performance of concrete beams with steel reinforcement-Tests and analysis," *Materials*, vol. 13, no. 13, p. 2923, 2020.

[27] S. Dudziak, "Numerically efficient three-dimensional model for non-linear finite element analysis of reinforced concrete structures," *Materials*, vol. 14, no. 7, p. 1578, 2021.

[28] A. M. Mahmoud, "Strengthening of concrete beams having shear zone openings using orthotropic CFRP modeling," *Ain Shams Engineering Journal*, vol. 3, no. 3, pp. 177–190, 2012.

[29] C. G. Karayannis, C. E. Chalioris, and P. D. Mavroeidis, "Shear capacity of RC rectangular beams with continuous spiral transversal reinforcement," *WIT Transactions on Modelling and Simulation*, vol. 41, 2005.

Hindawi
Advances in Civil Engineering
Volume 2021, Article ID 2245885, 10 pages
https://doi.org/10.1155/2021/2245885

Research Article

A Comprehensive Flexural Analysis for Sustainable Concrete Structure Reinforced by Embedded Parts

Yuantian Sun,[1,2] **Junfei Zhang**,[3] **Yunchao Tang**,[4] **Yufei Wang**,[5] **Junbo Sun**,[6,7] **and Xiangyu Wang**[7]

[1]*Ningbo Zhongchun High Tech Co., Ltd., Ningbo 315100, China*
[2]*School of Mines, Key Laboratory of Deep Coal Resource Mining of the Ministry of Education, China University of Mining and Technology, Xuzhou, Jiangsu 221116, China*
[3]*School of Civil and Transportation Engineering, Hebei University of Technology, 5340 Xiping Road, Beichen District, Tianjin 300401, China*
[4]*College of Urban and Rural Construction, Zhongkai University of Agriculture and Engineering, Guangzhou 510225, China*
[5]*Chongqing University Industrial Technology Research Institute, Chongqing University, Chongqing 400045, China*
[6]*Institute for Smart City of Chongqing University in Liyang, Chongqing University, Chongqing, Jiangsu 213300, China*
[7]*School of Design and Built Environment, Curtin University, Perth, WA 6102, Australia*

Correspondence should be addressed to Junbo Sun; junbo.sun@curtin.edu.au

Received 28 August 2021; Accepted 3 November 2021; Published 23 November 2021

Academic Editor: Wenjie Ge

In this research, the plate embedded parts and grooved embedded parts reinforced concrete structures were investigated. Two types of plate embedded parts and three types of grooved embedded parts experienced coating treatment to enable sustainable function. Later, the ultimate failure capacity by bending experiments was conducted and compared with the theoretically calculated results. Moreover, three grooved embedded parts were simulated by ABAQUS to compare the results with the experimental exploration results, which was in close agreement with the theoretically calculated results and finite element analysis results. The result indicated that the failure modes of the embedded specimens under the five working conditions are all concrete vertebral failure. The plate-type embedded components were proved to exhibit higher ultimate bearing capacity than the grooved embedded parts. Moreover, the flexural and shear capacity of these five types of embedded parts has not been fully developed. The ultimate flexural and shear capacity of these five types of embedded parts could be further explored by adjusting the higher concrete grade.

1. Introduction

As the construction industry develops rapidly, the mechanical properties of the concrete have attached more attention [1, 2]. Consequently, the reinforced concrete (RC) structures have been widely used in constructions with the advantages of high sustainability, excellent mechanical strength, and considerable deformability resistance [3, 4]. However, the ordinary RC structures cannot meet the increasing demand of engineering specifically for the formworks in structure nodes [5–7]. This phenomenon points to the need for novel RC structures for filling structure nodes' formworks and producing high-quality constructions [8].

The application of sustainable embedded parts in steel-concrete composite structure joints has been used extensively as a promising material [9]. The embedded parts' structure comprising Halfen channel embedded parts and plate embedded parts are raising attention and can be the feasible solutions towards current drawbacks [10]. The embedded parts' structures do not depend on the secondary construction of the ground in constructions with the advantages of the convenient assembly procedure, low cost, and labor [11]. Stout et al. [12] patented a method for making

cast-in-place concrete structures to reveal integrally bounded confines in the structure. Stout et al. [13] also explored a void-creating device to be embedded in a concrete structure, aiming at defining a labyrinth of passageways with the concrete structure, which revealed the passage procedure for service parts through the interior parts within the concrete.

At present, drawing, shearing, and seismic resistance are major concerns for embedded parts worldwide. In engineering application, the slot embedded parts, bearing the bending force and shear force in most cases as the joint of the steel-concrete structure [14]. However, few studies have been conducted on the bending-shear test performance of slot embedded parts. Moreover, despite the embedded parts being widely used, there are few standard designs for slot embedded parts.

In this study, a novel coating treatment was conducted upon three kinds of HALFEN channel embedded parts and two kinds of plate embedded parts to reveal the sustainable function. The bending-shear experiments were carried out with different specifications to analyze the ultimate bearing capacity and failure modes. Under the actual test conditions, the theoretical calculation and finite element analysis using ABAQUS were carried out on the flexural and shear test to determine the reliability of the HALFEN channel embedded parts in the practical application. The study can be regarded as a guideline in this research area.

2. Experimental Study

2.1. Experimental Design. 15 specimens for two types of embedded parts were analyzed comprising A-1, A-2, B-1, B-2, and B-3. The A group was the structure reinforced by embedded plate and the B group means the grooved embedded parts corresponded to three different types of grooved embedded parts. Each batch contains three samples and the loading configurations are constant. Specifically, A-1 and A-2 were each reinforced by a 150 mm × 150 mm × 10 mm and a 150 mm × 150 mm × 20 mm anchor plate separately. Meanwhile, the embedded plate was welded by 4 steel bar anchor legs (200 mm in length and 20 mm in diameter) and the anchor legs were also welded to an I-beam (150 mm) with different distances towards edges (10 mm for A-1 and 20 mm for A-2). For the B group, the specimen was reinforced by HALFEN groove (40 mm width and 22 mm height for B-1, 50 mm width and 30 mm height for B-2, and 52 mm width and 34 mm height for B-3). The groove was weld by 4 anchor legs with a length of 100 mm (overall length of 300 mm). The anchor legs were linked with 5 T bolts on the other side.

The concrete specimen sizes were 450 mm × 450 mm × 450 mm (A group) and 600 mm × 400 mm × 300 mm (B group). The design strength of all specimens was C30 and the embedded parts were Q345-type galvanized steel. The surface of the anchor plate was even with the concrete, embedding all anchor legs. The bending or shearing loads were applied to the I beam or *T* bolt, and the loading eccentricity was 40 mm from the anchor plate plane. The specimen parameters were demonstrated in Table 1.

2.2. Sustainable Treatment. All designed embedded parts experienced coating treatment to guarantee sufficient sustainability in-service lifespan. A self-developed Zn-A1-Mg-RE alloy on a small scale is utilized coating, as shown in Figure 1. This is because the alloy not only exhibits outstanding corrosion resistance but also fills the microcracks in the coating which enhances the mechanical performance. First, pure Zn strip at the content of 99.9% is sprayed onto the surface of embedded parts as a base by a high-velocity spraying gun (HAS-02) cooperated by a CDM system (AS3000) at 200 μm thickness. Later, the Zn-A1-Mg alloys are coated upon the surface of the embedded part with a thickness of 400 μm. The spraying current stands at 140 A, and spraying voltage employs 30 V. The spraying distance keeps at 250 mm and the air pressure is 0.65 MPa.

2.3. Loading Parameters. The 500t servo compression-testing machine is utilized to load the test specimens. Meanwhile, a self-control device is set on the upside of the specimen to prevent the sliding effect on the workbench. The structure diagram of the entire loading system and self-control device are, respectively, shown in Figure 2.

As for the loading procedure, the servo machine first utilized a 0.2 kN/s preload rate till the 10% yield load followed by a recovering process. After the inspection of the loading device and instrument, the servo machine applied uniaxial load at a rate of 0.4 kN/s with 50 mm eccentricity until failure. The loading value, as well as the strain data, was collected automatically by the servo machine and the static strain tester. Especially, both the circumscribed I-beam of plate-type and the circumscribed T-type bolt of slot-type built-in fitting obtained 4 anchor legs using 8 wires to connect with the static strain tester during loading. The loading procedure of plate-type built-in fitting and slot-type built-in fitting separately are illustrated in Figure 3.

3. Test Results

3.1. Mechanical Properties. The experimental results are shown in Figure 4. The average failure load of A-1 was 378.73 kN and was 78 kN higher than that of A-2(299.93 kN). The mean loading capacities for the B batch were 89.76 kN for the B-1 sample, 125.34 kN for the B-2 sample, and 105.63 kN for the B-3 sample.

3.2. Failure Mode. The failure modes and surface cracks for all five embedded specimens are denoted in Figure 5.

All the specimens were damaged by the concrete vertebral body with considerable cracks. For the embedded structures, the concrete around the groove began to crack slightly and then gradually expanded. After a specific threshold (98 kN for B-1 and 92 kN for B-2), the cracks on the original extend rapidly and terminally came into failure. Major cracks in the vertical direction on both sides of the middle groove steel were found, the bottom joint was protruded around the T-bolt and the upper part was pulled out due to the exerted force on the edge.

Table 1: Specimen parameters for A and B groups.

Group	Built-in type	Anchor number and size	Sample size (mm)	Circumscribed device
A-1	Plate-type	4 ∗ 100 ∗ 20	450 × 450 × 450	No. 14 I-beam
A-2	Plate-type	4 ∗ 100 ∗ 20	450 × 450 × 450	No. 14 I-beam
B-1	Slot-type	4 ∗ 100 ∗ 20	600 × 400 × 300	5 T-type bolts
B-2	Slot-type	4 ∗ 100 ∗ 20	600 × 400 × 300	5 T-type bolts
B-3	Slot-type	4 ∗ 100 ∗ 20	600 × 400 × 300	5 T-type bolts

Figure 1: Microscale set up of Zn-AI-Mg-RE coating.

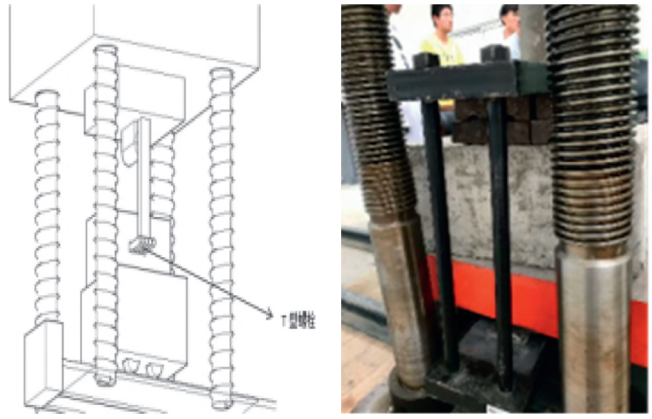

(a) (b)

Figure 2: (a) Servo testing machine structure diagram. (b) Self-control experiment device.

4. Theoretical Calculations

The bearing capacity of a section of embedded components is calculated according to CEN/TS 1992-4-3:2009 [15].

4.1. Design Calculation and Analysis of Plate Embedded Parts. As for the damage characteristics, when the force moment e/z is less than 0.3, the embedded parts are first crushed by concrete with general shear-bearing embedded parts. When the force moment e/z is more than 0.6, the embedded parts are all damaged by the pulled anchor leg. Otherwise, the embedded part failure is caused by the compound effect of crushed concrete or the pulled anchor leg. In this study, the eccentricity is 40 mm, and the vertical distance Z between the anchor legs is 130 mm. Therefore, the moment equals 0.3 and the theoretical damage characteristic ought to be a crushing effect to form vertebral body damage, which is consistent with the actual damage characteristics.

According to the experimental study and theoretical analysis of uniformly arranged bending-shear embedded parts with straight anchor legs, the strength of bending-shear embedded parts can be calculated according to the following equation [16, 17]:

(a) (b)

Figure 3: The built-in fitting for (a) plate-type and (b) slot-type.

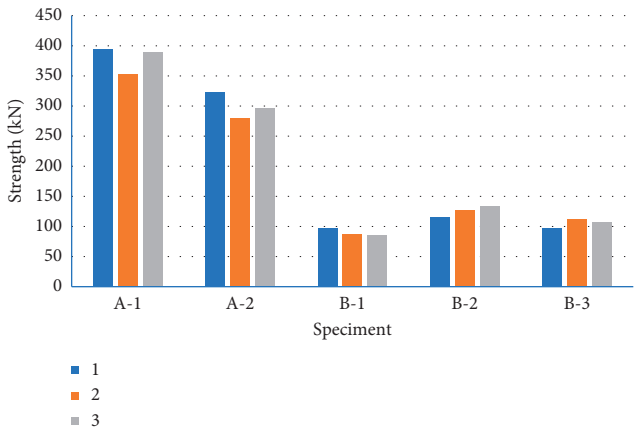

Figure 4: Experimental results of plate and groove embedded parts.

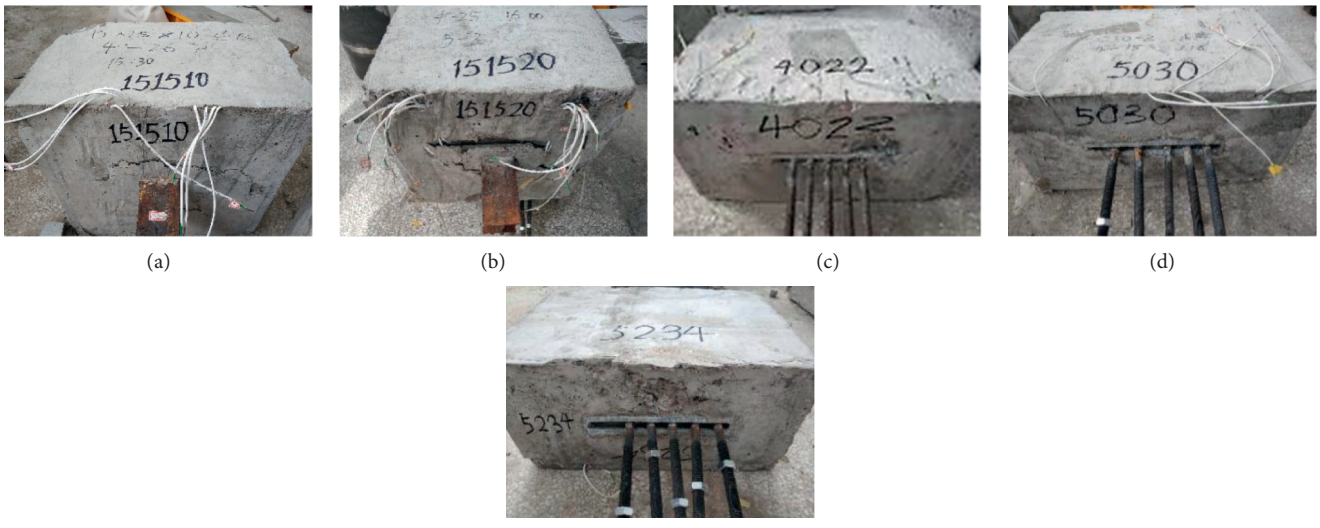

(a) (b) (c) (d)

(e)

Figure 5: Specimen failure form for (a) A-1, (b) A-2, (c) B-1, (d) B-2, and (e) B-3.

$$\frac{V}{V_{u_0}} + \frac{0.3M}{Mu0} = 1, \tag{1}$$

where $V/V_{u0} \geq 0.7$, or $(e/z) \leq 0.57(\alpha_a \alpha_b/\alpha_v)$.

According to the reliability analysis of embedded parts, the shear strength of embedded parts can be calculated according to equation (2) and the bending strength of embedded parts can be calculated according to equations (3) to (5):

$$v_{u0} = \alpha_v \alpha_r f_y A_s, \tag{2}$$

$$M_{u0} = 0.4\alpha_a \alpha_b \alpha_r f y A s z, \tag{3}$$

$$\alpha_v = (4 - 0.08d)\sqrt{\frac{f_c}{f_y}} \leq 0.7, \tag{4}$$

$$\alpha_a = \frac{l_a'}{l_a}, \tag{5}$$

where α_v symbols the shear strength coefficient of anchor legs, f_c is the design value of concrete compressive strength, f_y equals the design value of tensile strength of embedded anchor legs, d is the diameter of steel bars, α_r means the influence coefficient of the number of anchor legs, A_s is the section area for all anchor legs, α_a symbols the reduction coefficient of anchor length, α_b is the reduction factor of bending deformation of anchor plate which generally equals 1, l_a' is the actual length of the anchor leg (200), and l_a means the anchorage length (600) of tensile anchor legs is usually selected and calculated according to Table 2.

By combining the listed formulas, equation (6) is obtained shown as follows:

$$\frac{V}{\alpha_v \alpha_r f_y A_s} + \frac{M}{1.3\alpha_a \alpha_b \alpha_r f_y A_s z} = 1. \tag{6}$$

As the embedded parts met the structural requirements and the anchor plate can be considered as nonbending deformation, α_b thus equals 1. The embedded parts are equipped with two rows of anchor legs, and α_r is taken as 1. The design value of compressive strength of concrete specimens is 14.3 N/mm^2, and the design value of tensile strength of embedded anchor legs is 310 N/mm^2.

As a result, α_a = 1/3 and the shear strength coefficient of anchor legs α_v is 0.52. The theoretical calculation solution V is 148 kN, which is far lower than the experimental results of A-1 and A-2, meeting the safety considerations.

4.2. Practical Calculation and Analysis of Groove Embedded Parts. The embedded depth of the anchor leg was shallow, which is less than 150 mm. The failure form of the groove embedded structure was usually concrete cone failure, and the experimental results verified this assumption. According to CEN/TS 1992-4-3:2009 [15], the formula of a failure bearing capacity of the concrete cone is described as[18, 19]

$$N_{Rk,c} = N^0_{Rk,c} \times \alpha_{s,N} \times \alpha_{e,N} \times \alpha_{c,N} \times \varphi_{re,N} \times \varphi_{ucr,N}, \tag{7}$$

Table 2: The formula for calculating anchorage length.

Type of reinforcement	Strength grade of concrete			
	C15 (d)	C20 (d)	C25 (d)	≥C30
Crescent rebar	50	40	35	30d

where $N_{Rk,c}$ is the failure capacity of the concrete cone when a single anchor leg of groove-type embedded part is applied, $\alpha_{s,N}$, $\alpha_{e,N}$, and $\alpha_{c,N}$ are the adjacent anchor correction coefficient, boundary effect correction coefficient, and corner effect correction coefficient, respectively, and $\varphi_{ucr,N}$ is the cracking correction coefficient of concrete, and when noncracking concrete equals to1.4, $\varphi_{re,N}$ is the shadow of bearing capacity considering the peeling of surface concrete. The formula for calculating the response coefficient is expressed in equation (8). $N^0_{Rk,c}$ means the standard value of bearing capacity of concrete cone failure reinforced by single anchor legs of groove embedded parts under tension which is calculated as equation (9):

$$\phi_{re,N} = 0.5 + \frac{h_{ef}}{200} \leq 1, \tag{8}$$

$$N^0_{Rk,c} = 8.5 \times \alpha_{ch} \times \sqrt{f_{ck,\text{cube}}} \times h_{ef}^{1.5}, \tag{9}$$

where α_{ch} is the correction factor of channel steel to concrete cone less than 1, $f_{ck,\text{cube}}$ is the standard value of compressive strength of concrete cube (N/mm^2), and h_{ef} is the length of anchor leg of groove embedded parts.

According to the listed formulas, h_{ef} is 100 mm, and $\varphi_{re,N}$ is thus calculated as 1. When the specimen is C30, $f_{ck,\text{cube}}$ take 34.9 N/mm^2 and α_{ch} was chosen as 1; then, $N^0_{Rk,c}$ is calculated as 50.2 kN. The adjacent anchor repair coefficient, boundary effect repair coefficient, and corner effect repair coefficient $\alpha_{s,N}$, $\alpha_{e,N}$, and $\alpha_{c,N}$, are 1, 1.1, and 1.2, respectively, according to the actual situation. The concrete is noncracking concrete, and $\varphi_{ucr,N}$ is 1.4. As a result, $N_{Rk,c}$ is calculated as 102.1 kN, which is in close agreement with the experimental values.

5. Finite Element Simulation Analysis of Groove Embedded Parts Test

5.1. Establishment of the Finite Element Model for Slot Embedded Parts

5.1.1. Selection of Materials. The groove embedded components (B-1, B-2, and B-3) were simulated in finite element analysis consisting of steel plate, groove embedded parts, and concrete structure. The T-type bolt is simplified as a steel plate in modeling as its main function was to transmit force to embedded parts. The steel Poisson's ratio was 0.274, and the elastic modulus was $2.06 * 10^3$ MPa.

There were three constitutive models of concrete which are provided in ABAQUS including the brittle cracking model, dispersive cracking model, and damage-plasticity model [20, 21]. The plastic damage model of concrete is adopted in this paper because it was able to simulate the mechanical behavior of concrete under

monotonous, reciprocating, and dynamic loads under low hydrostatic pressure and has good convergence. As for the uniaxial constitutive relationship of concrete, it was based on the damage-plasticity mode and consisted of the elastic section, strengthening section, and softening section. Poisson's ratio took 0.167 in the elastic section. The inelastic strain and damage constitutive relationship are demonstrated in equations (10) and (11) [22, 23]:

$$\varepsilon_{c,\text{in}} = \frac{\varepsilon - \sigma}{E_0}, \tag{10}$$

$$\sigma = (1 - d)D_0 : \left(\varepsilon - \varepsilon^{\text{pl}}\right) = D : \left(\varepsilon - \varepsilon^{\text{pl}}\right), \tag{11}$$

where E_0 means the initial modulus of elasticity, D_0 is the initial elastic stiffness, D symbols the degraded elastic stiffness, and d is the damaging factor variable within the domain of 0 and 1.

The uniaxial tension constitutive relation defined the peak stress f_t as $0.35f_{cu}^{0.55}$ and the softening section when the strain exceeds the ultimate strain ε_{cu}. Meanwhile, the ultimate tensile strain and the corresponding residual stress in the tension-softening section of concrete have a great influence on the convergence of the calculation. The residual stress is thus defined as $0.13f_t$. Other related parameters are selected according to the measured values. The plastic nonlinear model is difficult to converge in the calculation. Considering that plastic deformation hardly occurs in the noncontact parts (concrete and embedded part), this area post minor impact towards test results. Therefore, the noncontact region is set as linear elastic material, and the contact part between concrete and embedded parts is defined as plastic material.

5.1.2. Interaction and Boundary Conditions. The binding constraints were established at the contact areas between the steel plate and the embedded parts. To facilitate the loading, a reference point was set on the upper surface of the steel plate followed by a kinematic coupling procedure. To coincide with the test results, some surface-to-surface contact pairs were set. Specifically, the steel plate with larger stiffness was set as the main surface and the concrete part was set as the slave surface. Moreover, the finite slip formula was utilized to define the finite element contact because the relative displacement between the embedded parts and the concrete may be arbitrary. The tangential and normal behaviors were mainly considered in the contact properties and the Coulomb friction was adopted in the friction model and the friction coefficient was 0.4.

The model was placed on the loading table of the press with a clamp on the opposite side of the embedded part. The load was applied smoothly on the bolt to transfer the force to the embedded part. According to the experimental setting, three degrees-of-freedom constraints were applied to the concrete bottom and the displacement constraints were utilized for the steel plate.

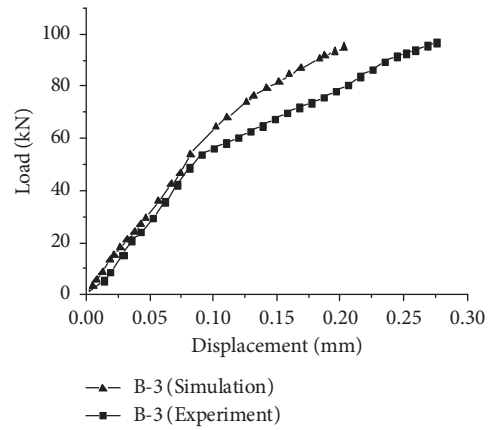

Figure 6: Comparison diagram of displacement load curve of B-3.

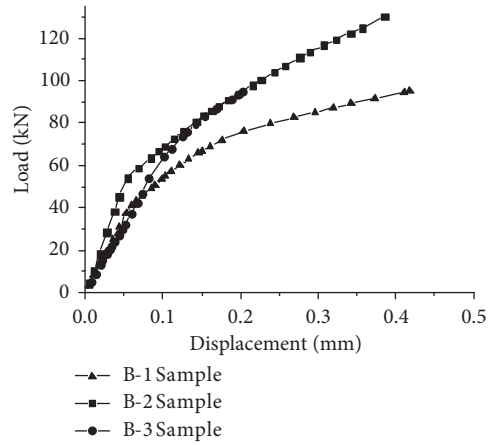

Figure 7: Simulated displacement load curve of three specimens.

5.1.3. Mesh Generation. In this paper, the 8-node hexahedron reduction integral entity element C3D8R was used in the plastic nonlinearity analysis. The embedded component was in 8 mm mesh size and the concrete unit was 30 mm; the contact interface unit was in 7 mm.

5.2. Finite Element Analysis Results. Figure 6 is the comparison of displacement load curve measured in the experiment and simulated by the finite element method. The experimental results of the embedded parts were in close agreement with the finite element analysis results. The displacement load-curve comparison obtained by finite element simulation is shown in Figure 7. It can be seen that the groove embedded parts have obvious elastic and plastic stages and are verified with the mechanical bearing capacity in the experiments.

Figure 8 demonstrates the concrete stress cloud diagram for the simulated B group specimens. The stress distribution on the upper surface in the finite element analysis was consistent with the damaged area of the concrete vertebral surface in experiments. When the embedded parts were subjected to bending and shearing force, the T-bolt would be pulled on the upper side, and we exert relatively large

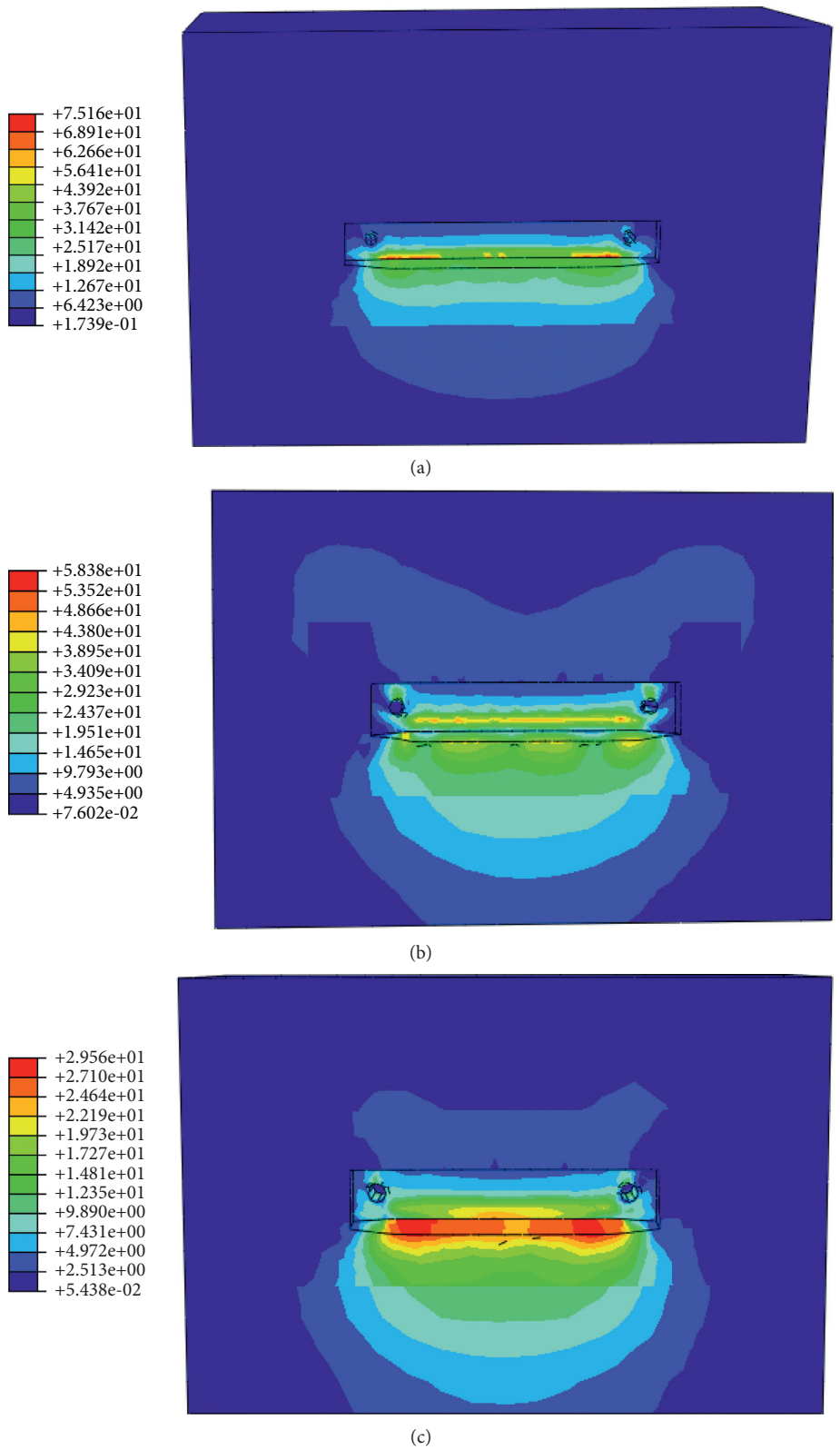

Figure 8: Concrete stress cloud diagram. (a) B-1, (b) B-2, and (c) B-3 (unit: MPa).

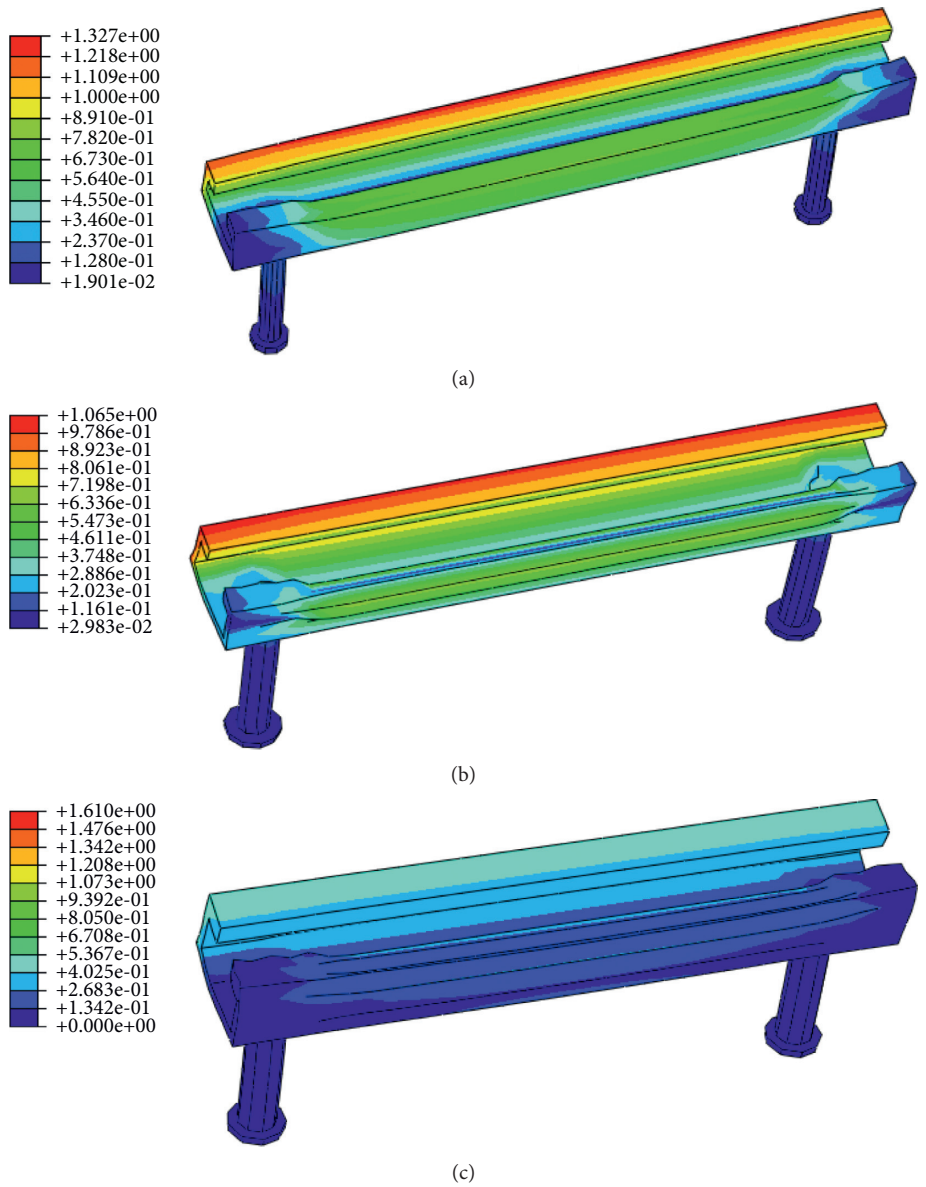

Figure 9: The embedded parts deformation diagram for (a) B-1, (b) B-2, and (c) B-3 (unit: mm).

compressive pressure on the lower side of the channel. When the displacement occurred upon T-bolt, the anchor leg in concrete would be pulled out slowly. Thereby, the punching effect upon the interaction between the anchor leg end and the concrete would increase. According to the stress cloud diagrams, the obvious stress concentration phenomenon was found at the interfaces for all three specimens, which was in agreement with the vertebral destruction caused by concrete in the mechanical experiments.

Figure 9 shows the deformation diagrams for the groove embedded parts' reinforced concretes. The displacement load-curve comparison figure obtained by finite element simulation is shown in Figure 10. From the listed figures, the maximum stresses for the simulated samples occurred at the bolt-channel steel interface and the anchor leg end. For the B-1 sample, the maximum stress reached 272.8 MPa and was mainly at the connection between T-type bolts and groove steel. The groove-type embedded part was still in an elastic state, while the maximum stress of concrete stood at 75.16 MPa at the end of the anchor leg, exceeding the compressive ultimate limit. The B-2 sample obtains the maximum stress of 268 MPa also at the connection surface between T-type bolts and groove steel. Meanwhile, the groove-type embedded parts have not fully kept the plastic state, but the concrete's maximum stress (58.38 MPa) has already reached the compressive limit at the end of anchor legs. For the B-3 specimen, the HALFEN groove's peak stress was simulated as 281.8 MPa at the connection part between channel steel and T-type bolts. Simultaneously, both the embedded parts and the concrete component did not exceed the plastic level threshold. The works can lay the foundation for future artificial intelligence optimization works.

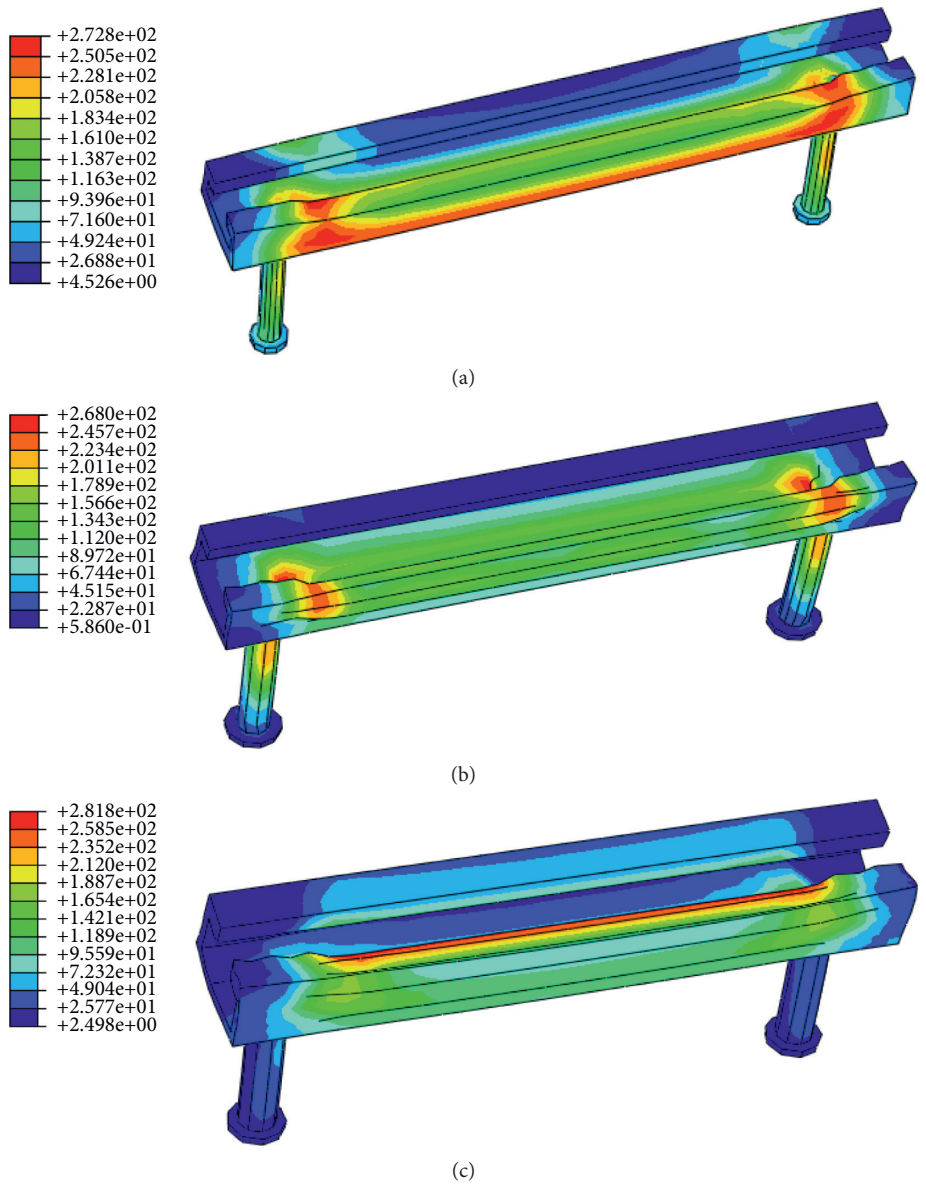

Figure 10: The embedded stress diagram for (a) B-1, (b) B-2, and (c) B-3 (unit: MPa).

6. Conclusion

The purpose of the study was to investigate the reliability of sustainable plate embedded parts and grooved embedded parts' reinforced concrete structures. The main conclusions of the study can be summarized as follows:

(1) The self-developed Zn-A1-Mg-RE coating enhances the sustainability performance of the embedded parts, which benefits the whole concrete structure of a longer service life span. The plate embedded parts supplied higher bearing capacity and the HALFEN groove with 50 mm width and 30 mm height was the most suitable category in reinforcing works.

(2) The theoretical calculation of failure bearing capacity for both plate embedded parts and grooved embedded parts reinforced concrete structures was consistent with the experimental results. The failure modes for embedded parts' reinforced concrete structures were the destruction of concrete vertebrae with obvious cracks.

(3) Based on the finite element analysis of three groove embedded specimens, the concrete at the end of the anchor leg had an obvious stress concentration phenomenon, which was consistent with the phenomenon of vertebral body destruction caused by concrete in the experiment. The finite element simulations were in according to the experimental results and theoretical calculation results.

Data Availability

All data used to support the study are included within the article.

Conflicts of Interest

The authors declare that they have no conflicts of interest.

Acknowledgments

This research was supported by the projects of "the Fundamental Research Funds for the Central Universities (2020ZDPY0221 and 2021QN1003),""National Natural Science Foundation of China (52104106 and 52174089)" and Basic Research Program of Xuzhou (KC21017).

References

[1] S. O. Hong and C. J. Aldrete, "Simple method for upgrading an existing reinforced-concrete structure," *Practice Periodical on Structural Design and Construction*, vol. 1, no. 1, pp. 47–50, 1996.

[2] K. M. A. Hossain, M. Lachemi, M. Sammour, and M. Sonebi, "Influence of polyvinyl alcohol, steel, and hybrid fibers on fresh and rheological properties of self-consolidating concrete," *Journal of Materials in Civil Engineering*, vol. 24, no. 9, pp. 1211–1220, 2012.

[3] D. Hu and K. Ma, "A study on reliability of reinforced concrete structure," *Journal of Building Structures*, vol. 14, 1987.

[4] R. Pucinotti, "Reinforced concrete structure: non destructive in situ strength assessment of concrete," *Construction and Building Materials*, vol. 75, no. 75, pp. 331–341, 2015.

[5] L. Hu, Y. Wang, P. Feng, H. Wang, and H. Qiang, "Debonding development in cracked steel plates strengthened by CFRP laminates under fatigue loading: experimental and boundary element method analysis," *Thin-Walled Structures*, vol. 166, Article ID 108038, 2021.

[6] L. Hu and P. Feng, "Prestressed CFRP-reinforced steel columns under axial and eccentric compression," *Composite Structures*, vol. 268, Article ID 113940, 2021.

[7] L. Hu, P. Feng, and X.-L. Zhao, "Fatigue design of CFRP strengthened steel members," *Thin-Walled Structures*, vol. 119, pp. 482–498, 2017.

[8] F. Aslani and S. Nejadi, "Bond behavior of reinforcement in conventional and self-compacting concrete," *Advances in Structural Engineering*, vol. 15, no. 12, pp. 2033–2051, 2012.

[9] L. Gerola, "Connecting horizontal panels and vertical panels in prefabricated buildings," Google Patents, 1972.

[10] L. L. Hu, X. L. Zhao, and P. Feng, "Fatigue behavior of cracked high-strength steel plates strengthened by CFRP sheets," *Journal of Composites for Construction*, vol. 20, no. 6, Article ID 04016043, 2016.

[11] R. Böllinghaus, "Transport anchor for embedding in prefabricated reinforced concrete parts," Google Patents, 2002.

[12] R. K. Stout, "Method for making cast-in-place concrete structures," Google Patents, 1975.

[13] R. K. Stout, "Void creating device to be embedded in a concrete structure," Google Patents, 1975.

[14] B. Zoubek, M. Fischinger, and T. Isakovic, "Estimation of the cyclic capacity of beam-to-column dowel connections in precast industrial buildings," *Bulletin of Earthquake Engineering*, vol. 13, no. 7, pp. 1–24, 2014.

[15] D. Standards, *Design of Fastenings for Use in Concrete - Part 4-3: Anchor Channels*, 1992.

[16] X. Liu, M. A. Bradford, and A. Ataei, "Flexural performance of innovative sustainable composite steel-concrete beams," *Engineering Structures*, vol. 130, pp. 282–296, 2017.

[17] P. K. Sarker, "Bond strength of reinforcing steel embedded in fly ash-based geopolymer concrete," *Materials and Structures*, vol. 44, no. 5, pp. 1021–1030, 2011.

[18] P. Valeri, M. F. Ruiz, and A. Muttoni, "Modelling of textile reinforced concrete in bending and shear with elastic-cracked stress fields," *Engineering Structures*, vol. 215, Article ID 110664, 2020.

[19] B. Han, Y. Wang, S. Dong et al., "Smart concretes and structures: a review," *Journal of Intelligent Material Systems and Structures*, vol. 26, no. 11, pp. 1303–1345, 2015.

[20] K. Hibbitt, *Sorensen. ABAQUS/Standard User Subroutines Reference Manual*, Sorensen, Inc, Chicago, IL, USA, 2002.

[21] A. Jawdhari and I. Harik, "Finite element analysis of RC beams strengthened in flexure with CFRP rod panels," *Construction and Building Materials*, vol. 163, pp. 751–766, 2018.

[22] W. Demin and H. Fukang, "Investigation for plastic damage constitutive models of the concrete material," *Procedia engineering*, vol. 210, pp. 71–78, 2017.

[23] T. Supaviriyakit, P. Pornpongsaroj, and A. Pimanmas, "Finite element analysis of FRP-strengthened RC beams," *Songklanakarin Journal of Science and Technology*, vol. 26, no. 4, pp. 497–507, 2004.

Hindawi
Advances in Civil Engineering
Volume 2021, Article ID 1992084, 12 pages
https://doi.org/10.1155/2021/1992084

Research Article

Experimental Research on Axial Compression of Reinforced Concrete Short Circular Columns Strengthened with Prestressed Semicircular Steel Plates

Zhenhua Ren,[1] Yaqian Shen,[1] Xiantao Zeng,[1] and Yuantian Sun[2]

[1]*Hunan Provincial Key Laboratory of Intelligent Disaster Prevention-Mitigation and Ecological Restoration in Civil Engineering, Hunan Institute of Engineering, Hunan, Xiangtan 411104, China*
[2]*School of Mines, Key Laboratory of Deep Coal Resource Mining, Ministry of Education of China, China University of Mining and Technology, Xuzhou 221116, China*

Correspondence should be addressed to Xiantao Zeng; xtzeng63@163.com

Received 7 September 2021; Accepted 1 November 2021; Published 23 November 2021

Academic Editor: Wenjie Ge

According to the statistics of relevant departments, the total area of various existing buildings in China is at least 10 billion m^2, of which about one-third of the houses have reached the design life and the safety reserve is insufficient. It is not economical to demolish these houses and rebuild them, and the benefits of new buildings are far less than those of extending the service life of old buildings through reinforcement. Therefore, reinforcement technology is increasingly indispensable. Currently varying methods for the prestressed reinforcement of concrete columns are developed, but they are generally not practical. Strengthening concrete columns with prestressed semicircular steel plate is a new prestressed strengthening technology. In this article, the experimental study on the axial compression of a reinforced concrete circular section short column strengthened with prestressed semicircular steel plate is carried out by combining experimental and numerical simulation methods, and the calculation formula of the bearing capacity of the reinforced short column is established by finite element analysis.

1. Introduction

The application of prestress reinforcement in a building structure improves the force performance of the original structure by enhancing crack resistance, structural carrying capacity, and durability [1–3]. Currently varying methods for the prestressed reinforcement of concrete columns are developed comprising prestressed rod, prestressed strip, and prestressed steel strand reinforcement methods [4–7]. However, the application of prestressed reinforcement technology in practical engineering is still in the preliminary stage. Zhang et al. [8] explored the anchorage-reinforced concrete column (similar to the clamp method) by the quasistatic test to find the circumferential prestressed steel strands and demonstrated good repair and improvement effect on the seismic performance of damaged columns. Prestressed steel strand has the advantages of convenient construction and short cycle and does not affect the use of the original structure during construction. It can also improve the bearing capacity, stiffness, and energy dissipation capacity of reinforced concrete columns. After reinforcement, the fire resistance, corrosion resistance, and aging resistance of the components are improved [9, 10]. Ge et al. [11] studied the seismic behavior of concrete columns strengthened by prestressed steel strand tensioning and anchoring. The test results show that the yield load and ultimate load were improved, but the concrete of the protective layer of the original column exposed to the prestressed steel strand is in the three-dimensional stress state, and the exposed concrete is still in the two-dimensional stress state, which makes the mechanical state of the concrete column more complex, which brings complexity to the design calculation, and the prestress of the steel strand is limited. Sun et al. [12] found a prestressed steel plate hoop to

reinforce bridge and effectively improve axial compression bearing capacity and deformation capacity of pier column. The axial compression performance tests of 16 reinforced columns and 2 contrast columns were carried out by Sun et al. [13] and Yong et al. [14]. The results show that the bearing capacity and deformation capacity of reinforced columns are improved under the conditions of constant spacing of steel strips, increasing or unchanged number of layers, and decreasing spacing. However, the column concrete between steel strips is exposed outside, which is not constrained by steel strips, leading to increased potential of early explosion [8, 15]. From the above research status, can we find a prestressed reinforcement method? It can not only improve the deformation resistance and bearing capacity of reinforced concrete columns, but also ensure that the stress of new and old structural layers is synchronized, the original structure is not destroyed, and the implementation is convenient.

Therefore, the prestressed semicircular steel plate is firstly proposed as a feasible solution toward the increased demand as shown in Figure 1. The main novelty is that two prestressed semicircular steel plates are installed on the side of the required strengthened cylinder, and the circumferential prestress is applied to the two semicircular steel plates by tightening the bolts. The prestress can be adjusted by tightening the bolts, so as to improve the bearing capacity of concrete columns without damaging the original column, and to achieve the purpose of rapid repair and reinforcement of concrete columns. As a result, compared to traditional reinforcement methods such as increasing section method [16, 17], steel casing method [18, 19], and CFRP reinforcement method [20, 21], the advantage can be concluded as follows: ①It does not increase the section of the column, nor add steel bars to the original column. ②Its core concrete is in the active three-way stress state before the force. ③The original concrete column has reinforcement according to the original bearing requirements. The reinforced concrete column is equivalent to the prestressed reinforced concrete-filled steel tube column, and its bearing capacity is higher than that of the concrete-filled steel tube column. ④The prestress can be adjusted to ensure the force synchronization of the original structure and the reinforced structure, and there will be no echelon damage. ⑤The reinforcement does not damage the structure of the original concrete column, nor does it reduce its bearing capacity. ⑥It is not necessary to unload the original concrete column and does not affect the use of the structure. The reinforcement construction can be implemented online and can be carried immediately after reinforcement. The structure demonstrates promising potential in intelligence manufacture owning to its superior advantages especially in the 3D printing domain [22–24].

In this article, the experimental study on the axial compression of the reinforced concrete circular section short column strengthened with prestressed semicircular steel plate is carried out by combining experimental and numerical simulation methods, and the calculation formula of bearing capacity of the reinforced short column is established by finite element analysis. In order to study the axial bearing capacity of strengthened concrete columns, the axial compression tests of 20 concrete columns were completed, including 5 comparative columns and 15 concrete columns. All specimens were strengthened by steel casing with varying prestressing values. The test results show that the bearing capacity of the reinforced concrete column is greatly improved by prestressed steel casing, and the ultimate bearing capacity is increased by 72.1%–109.9%. On the basis of the experimental study, the finite element models of the prestressed semicircular steel plate strengthened column were established by ABAQUS. The correctness of the finite element model is verified by the experimental results. Finally, the bearing capacity of the reinforced concrete column is analyzed theoretically, to propose the calculation formula for axial compression bearing capacity; compared with the experimental data, the theoretical calculation formula has outstanding accuracy, Through this test, it can provide experimental data for the eccentric compressive test, earthquake-resistant test, shear test, resistant explosion experiment, fatigue test, and stability test of the prestressed steel casing reinforcement method for strengthening the concrete column.

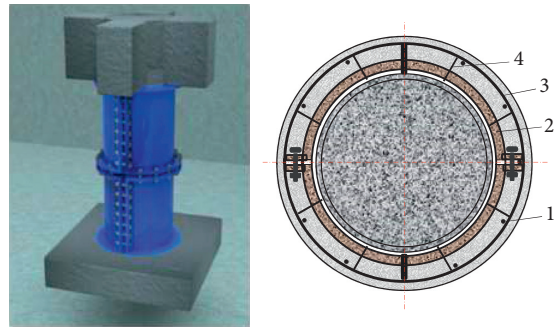

Figure 1: Schematic diagram of the reinforcement method. (1) Longitudinal bar; (2) semicircular steel plate; (3) stirrup; (4) radial structural bars.

2. Materials and Methods

2.1. Materials and Specimen Design. The concrete in this test is C30. According to Chinese Standard Test Method (GB/T50081-2016) [25], the same batch of concrete with the cylinder was selected for the compressive performance test of a concrete cube, and the average compressive strength of the concrete cube was 30.75 MPa.

As shown in Figure 2(a), 6C14HRB400E was selected as the longitudinal bar. According to the Steel Test Method for Reinforced Concrete (GB/T28900-2012) [26], the yield strength of the longitudinal bar was measured to be 541 MPa. The yield strength of the stirrup A6HPB300 is 332 MPa.

The test column is circular, 256 mm in diameter, and 1000 mm in height (Figure 2(b)). A total of 20 columns were designed in this experiment, of which 5 were the contrast columns, numbered RC-1 (the specific column numbers are RC-11 to RC-15), and the remaining 15 were divided into three groups of different prestressed reinforced concrete columns, numbered RC-2-1–RC-2-3 (the specific column numbers of each group are RC-2-11~RC-2-15).

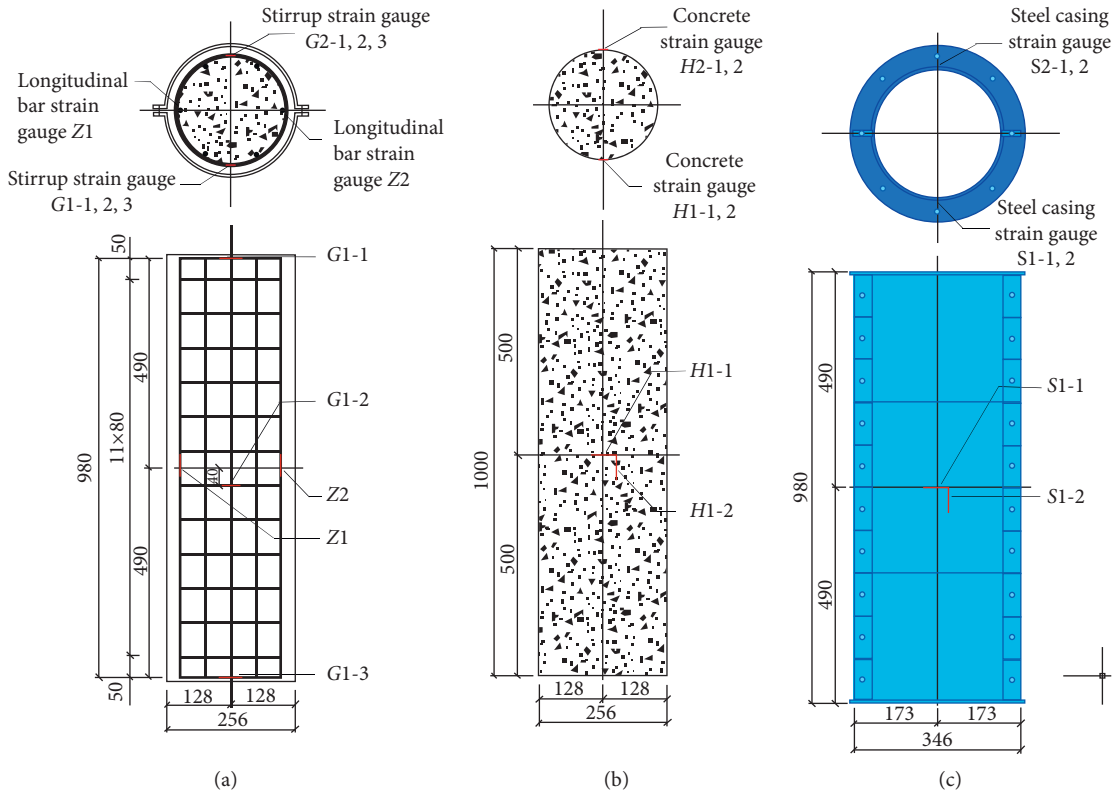

Figure 2: Details of specimens.

As shown in Figure 2(c), the inner diameter of the steel casing wall is 256 mm, the length is 980 mm, and the thickness of the steel plate is 5 mm. In order to make the steel casing successfully impose circumferential prestress on the concrete cylinder, the two semicircular steel plates cannot be closed into a complete circle, and the two semicircular steel plates should leave 6 mm ($256 \times \pi \times 0.01 \times 1.5 = 12$ mm, 0.01 is the ultimate tensile strain of steel, and 1.5 is the surplus coefficient) gaps in advance.

The nominal diameter was 12 mm, and the stress cross-sectional area of M12 bolt was 84.3 mm^2.

In order to measure the internal stress and deformation of the steel bar, concrete, and steel casing, strain gauges are affixed at the specific position of the specimen, and the specific position of the strain gauge is shown in Figure 2.

2.2. Loading Program. In order to study the mechanical properties and reinforcement effect of concrete columns strengthened with steel casting (steel cylinder formed by closing two semicircular steel plates) under precompression stress, four groups of axial compression tests of strengthened columns were carried out:

(1) Contrast column test of the unreinforced original column.

(2) According to the prestress value, the test of the reinforced column can be divided into the following three categories:

① In Scheme 1, the prestress value is 0, which means tightening the bolt gently with a common wrench so that the steel casing is just close to the surface of the concrete cylinder; therefore, reinforced columns are equivalent to reinforced concrete-filled steel tubular columns.

② In Scheme 2, the confining pressure of the semicircular steel plate on the concrete column is equivalent to that of the unreinforced column stirrup on core concrete. As shown in Figure 3, $p = \sigma_r$ (p is shown in Figure 3(c), and σ_r is the confining pressure of steel casing on concrete columns); therefore, $\sigma_3 = \sigma_r$ (Figure 3(c)).
Because the thickness of the semicircular steel plate is far less than the diameter of the concrete column, and the thickness of the steel plate is $t = 5$ mm, the cross-sectional area of the steel tube wall is $A_{s1} = 4097.70$ mm^2. When the diameter of the

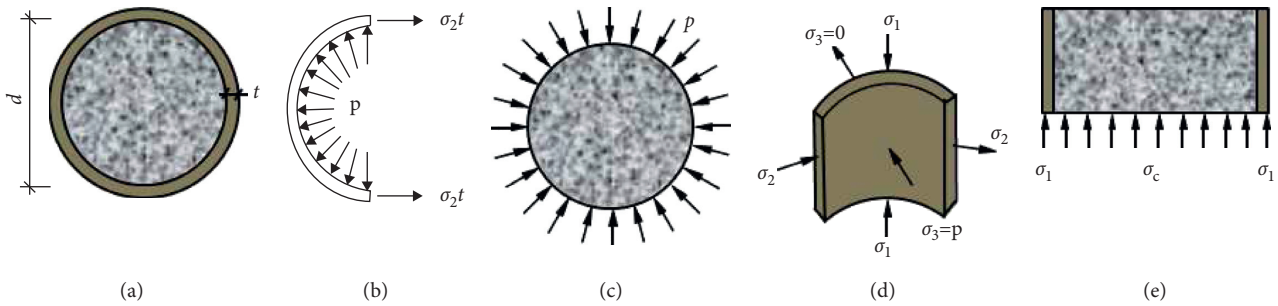

Figure 3: Stress diagram after reinforcement.

column is $d = 256$ mm and the thickness of the concrete cover is 25 mm, the diameter of core concrete (stirrup spacing) is 194 mm and the area of core concrete is $A_{cor} = 29544.26\ \text{mm}^2$. The cross-sectional area of concrete column $A = 51445.76\ \text{mm}^2$, and the stirrup conversion area is $A_{ss0} = 215.19\ \text{mm}^2$. Therefore, the constraint stress (σ_{r1}) of stirrup on the core concrete column can be calculated by the following formula [27, 28]:

$$\sigma_{r1} = \frac{f_{yv} \cdot A_{ss0}}{2A_{cor}} = \frac{270 \times 215.19}{2 \times 29544.26} = 0.983\ \frac{\text{N}}{\text{mm}^2}, \tag{1}$$

where f_{yv} is the design value of stirrup tensile strength, $f_{yv} = 270$ MPa. When the confining pressure of steel casing on the surface of the concrete column is equal to that of stirrup on core concrete before column reinforcement, there should be

$$\sigma_r = \sigma_{r1}. \tag{2}$$

At this time, the circumferential tensile stress in the steel casing plate can be obtained as follows:

$$\sigma_\theta = 2\sigma_r \frac{A}{A_{s1}} = 2 \times 0.983 \times \frac{51445.76}{4097.70} = 24.68\ \frac{\text{N}}{\text{mm}^2}. \tag{3}$$

③ In Scheme 3, the prestress value is equivalent to the prestress value required to make the bolt reach its tensile strength design value. At this time, the tensile force of the steel casing is larger than that of Scheme 2. The design value of the axial tensile connection bearing capacity of a single bolt is set as N_t^b:

$$N_t^b = A_{\text{eff}} f_t^b = 84.3 \times 400 = 33270\ \text{N}, \tag{4}$$

where A_{eff} is the stress section area of a single bolt, $A_{\text{eff}} = 84.3\ \text{mm}^2$. f_t^b is the tensile design strength of the bolt, $f_t^b = 400$ MPa. In addition, the number of bolts per row is 10:

$$\sigma_\theta = \frac{N_t^b \times 10}{t \cdot l} = \frac{33270 \times 10}{5 \times 980} = 67.90\ \frac{\text{N}}{\text{mm}^2}, \tag{5}$$

where t is the thickness of the steel casing plate, $t = 5$ mm and l is the height of steel casing, $l = 980$ mm. Therefore, the grouping scheme and the corresponding prestress values are listed in Table 1.

The loading method is full-section axial compression. The test is carried out on the microcomputer controlled electro-hydraulic servo press-shear testing machine. The strain of steel bars, steel casings, and concrete is measured by the static resistance strain gauge DH3818Y and dynamic signal acquisition and analysis system DHDAS. The cracks are observed with the naked eye of the magnifying glass and the flashlight. The testing machine is shown in Figure 4.

The test loading was carried out according to the *Standard Test Method for Concrete Structures* (GB/T50152-2012) [29]. After the reinforcement column is aligned, the preloading of $0.3N_u$ (predicted ultimate load value) was carried out, and the preloading was carried out 2-3 times. During the preloading period, the number of test equipment indicators needs to be carefully checked, and the abnormal phenomena should be eliminated in time. After the preload is completed. Then, remove all loads and start the formal test. The test device is shown in Figure 5. Pressurized loading was used in the test. Each stage was kept for 10 min, and the loading value of each stage was $0.2N_u$ (predicted ultimate load value) [30, 31]. The loading speed was 2 kN/s. When the loading value reached 0.8Nu, the loading value of each stage was $0.1N_u$. When the last stage was loaded, the loading speed was 1 kN/s. Until the ultimate load was reached and the pressure was kept, the loading was continuously and slowly until the specimen was destroyed. Among them, the strain data take the average value of 1 minute before the pressure was kept. Because the concrete column has 10 mm exposure in the upper and lower ends of the steel casing (Figure 5), the loading stops when the upper and lower loading plates contact the steel casing.

3. Results and Discussion

3.1. Main Results of the Test. The main test results are shown in Table 2. It can be seen from Table 2 that the ultimate load of strengthened columns increases differently with different prestress values. Compared with the contrast column, when the prestress value is $0\ \text{N/mm}^2$, the ultimate load of the strengthened column increases by 72.1%–92.4%; when the

Table 1: Details of specimens.

Methods	Number	Scheme	σ_θ (MPa)	Quantity (pillar)
No reinforcement	RC-1	No steel casing	0	5
Reinforcement	RC-2-1	Scheme 1	0	5
	RC-2-2	Scheme 2	24.68	5
	RC-2-3	Scheme 3	67.90	5
Total				20

Figure 4: Testing machine.

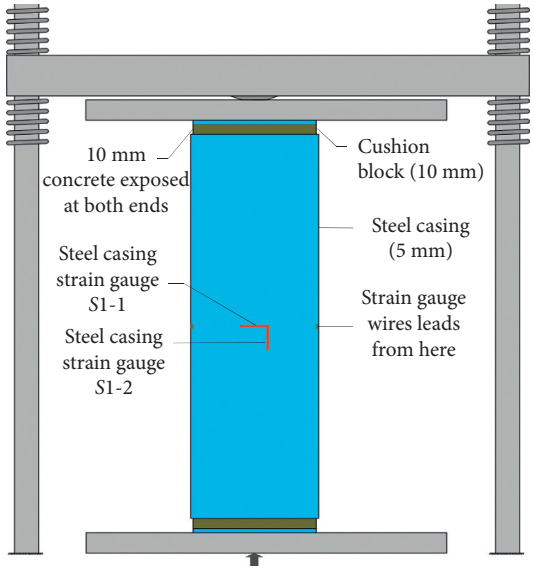

Figure 5: Diagram of specimen.

confining pressure of the semicircular steel plate on the concrete column is equivalent to that of the unreinforced column stirrup on core concrete, the ultimate load of the strengthened column increases by 95.0%–102.7%; when the prestress value is equivalent to the prestress value required to make the bolt reach its tensile strength design value, the ultimate load of the strengthened column increases by 97.5%–109.9%. It can be seen that, with the increase in the prestress value, the confinement effect of steel casing on concrete is more obvious, and the bearing capacity of concrete columns after reinforcement is slightly improved.

3.1.1. Phenomena. As shown in Figure 6, for RC-1, at the beginning of loading, two ends of the column due to stress concentration distribution crack. With the increase of load, because there is no restriction of steel casing, vertical cracks gradually appear in the surface of concrete cover. When the axial load reaches about 90% of its peak load, the vertical cracks continued to extend vertically, and the crack width increased. With a slight click, some cover concrete spalling. When the load reaches the maximum value, the head of the concrete column collapses in a large area, and the upper part of the specimen is bulging. Then, the bearing capacity decreases sharply. From the crack of the concrete column to the complete failure of the reinforced column, the whole process is relatively short, and the compression process shows the characteristics of brittle failure. For the three groups of concrete columns strengthened with steel casing, they have no obvious change at the initial stage of loading. When the load gradually increases, the appearance of steel casing has no obvious change, but its two vertical flanges have corrugated changes. Then, there was a crackling sound, which was due to the joint action of rib angle and bolt to make the vertical flange yield first. When the reinforced column reaches the ultimate bearing capacity, the weld position of the rib angle of the vertical flange is tear. Because the steel casing is restrained by the transverse flange during loading, the appearance of the steel casing still has no obvious change.

Figure 7 shows the internal failure mode diagram of the concrete cylinder after removing the steel plate. It can be seen that the failure of the ends of the column is more serious, which is due to the cushion plate that directly acts on the top of the concrete column during loading, and the end is not restrained by the steel casing. The ultimate compressive strain of concrete ε_{cu} is 0.0033; from this, the ultimate displacement value is 3.3 mm. Two ends of the reinforced column are compressed more than 10 mm, indicating that the confined concrete in the concrete column has been compressed. However, due to the circumferential constraint of the steel casing, the concrete column can still withstand axial pressure. Therefore, the prestressed steel casing can effectively restrict the concrete column. After loading, the steel casing is closely connected with the surface of the concrete cylinder, and it is very difficult to separate them. This shows that the Poisson displacement or lateral displacement of the concrete in the steel casing is obvious, and the steel casing ensures the integrity of the specimen and the effectiveness of the pressure transfer.

3.1.2. Failure Patterns of Specimens. There are two typical failure modes of concrete column: ①The top concrete is crushed and peeled off. ②Due to the constraint effect of the steel casing on the core concrete, the whole shearing destruction of the concrete will not appear, and even the cracked concrete will be re-extrusion under the constraint of

Table 2: Main results of the test.

Number		N_u (kN)	Increase rate (%)	Failure mode
RC-1	1	1471.50	—	Cover concrete spalling, concrete crushing, upper column drumming
	2	1553.30	—	
	3	1548.53	—	
	4	1612.32	—	
	5	1526.23	—	
RC-2-1	1	2654.89	72.1	Concrete cracking, no obvious phenomenon in the steel casing
	2	2910.25	88.7	
	3	2967.48	92.4	
	4	2938.08	90.5	
	5	2781.00	80.3	
RC-2-2	1	3017.00	95.6	Vertical flange weld cracking, concrete splitting
	2	3008.29	95.0	
	3	3026.02	96.2	
	4	3110.64	101.7	
	5	3125.31	102.7	
RC-2-3	1	3133.54	103.2	Bolt fracture, steel casing failure
	2	3146.81	104.0	
	3	3046.87	97.5	
	4	3237.70	109.9	
	5	3304.70	114.3	

(a) (b) (c) (d)

Figure 6: Failure modes of typical specimens.

the axial pressure and the steel casing. Due to the continuous occurrence of new corrugated bending of the vertical flange of the steel casing, cracks appear at the welds of the vertical flange, and the confining pressure is gradually weakened. On the premise of ensuring that no shear failure occurs, the reinforced column mainly occurs in two types of failure forms: the first type is axial compression failure; concrete columns in the compression zone are crushed and peeled off. The second type is the failure of the vertical flange of steel casing. From the cracking of reinforced columns under failure, two failure modes are ductile failure. Because the reinforced column has concrete spalling and clicking sound before failure, it shows that there are obvious signs before failure, and the failure form is reasonable.

(a) (b) (c) (d)

Figure 7: Internal failure mode of test column.

3.1.3. Load-Displacement Curve. Figure 8 shows the load-displacement curve of reinforced column. The curve can be divided into elastic section at the beginning of loading, inelastic section at 80% of ultimate load, and descending section after ultimate load. During the initial loading, all columns are in the elastic stage. Because fine stone concrete is poured between the steel casing and the concrete column to make them fit closely, the steel casing has a constraint effect on the core concrete. Therefore, with the increase of load, the greater the prestress value, the greater the slope of the strengthened column. As the load continues to increase, the constraint effect of steel casing on concrete becomes more obvious, and the bearing capacity of reinforced columns is also larger. Compared with the contrast column, the bearing capacities of RC2-1, RC2-2, and RC2-3 of the reinforced column were increased by 85%, 98%, and 106%, respectively. Because the steel casing has a strong constraint on concrete, the ultimate bearing capacity decreases slowly when it is destroyed, and for the specimens RC-1, RC2-1, RC2-2, and RC2-3, $\Delta_{max}/\Delta_{elastic}$ is 1.06, 2.57, 2.77, 3.48, respectively (Δ_{max} is the ultimate displacement, and $\Delta_{elastic}$ is the elastic displacement). It shows that the ductility of the new concrete structure increases with the increase of steel casing prestress.

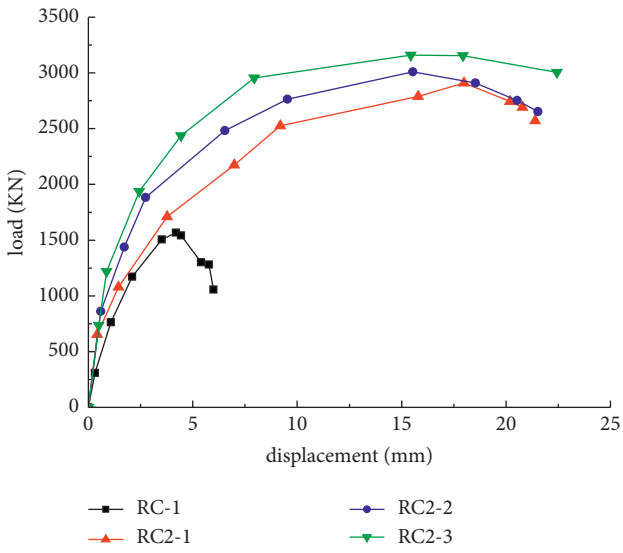

Figure 8: Load-displacement curves.

3.1.4. Load-Material Strain Curve. Figure 9 shows the load-strain curve of the concrete and steel casing. In the early stage of loading, the load-strain is linear, which indicates that the reinforced column is in the elastic stage. The strain of concrete and steel casing increases proportionally with the increase of load. When the load increases to 50%, the column cracks and works with cracks. With the increase of load, the strain of concrete increases and the transverse strain of steel casing also increases. The longitudinal strain of steel casing increases mainly due to the increase of transverse strain of steel casing. When the load is close to N_u, the slope of the curve continues to decrease, the stiffness of the specimen

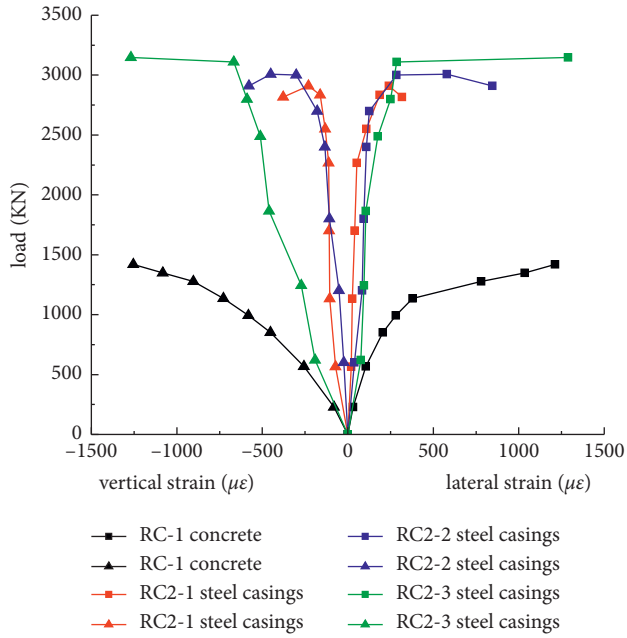

Figure 9: Load-strain curves of concrete and steel casings.

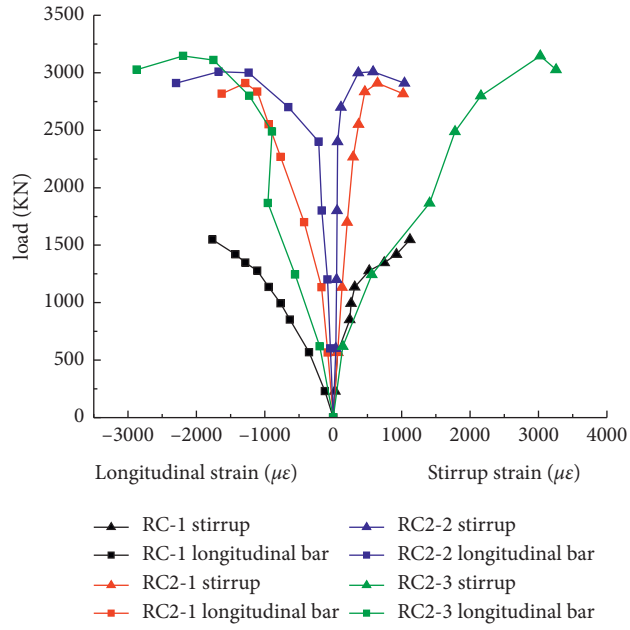

Figure 10: Load-strain curve of steel bar.

decreases, and the reinforced column is destroyed. When specimens RC2-1, RC2-2, and RC2-3 reach the ultimate load, the transverse strains of steel casing are 241, 580, and 1288 μ_ε, and the longitudinal strains are 231, 450, and 1268 μ_ε, respectively.

Figure 10 shows the load-strain curve of the steel bar of the reinforced column. With the increase in the steel casing prestress value, the constraint effect on the concrete column is stronger, and the increase of the peak strain of the steel bar (the strain corresponding to the ultimate load) is greater. When the specimens RC-1, RC2-1, RC2-2, and RC2-3 reach the ultimate load, the stirrup strains are 1120, 650, 584, and 3025 μ_ε, and the longitudinal reinforcement strains are 1767, 1284, 1675, and 2292 μ_ε, respectively. Comparing the reinforced columns RC2-1, RC2-2, and RC2-3, it is known that the prestressed semicircular steel plate reinforcement can improve the ultimate strain of concrete, and the concrete strain is related to the size of reinforcement prestress. The greater the prestress, the greater the ultimate strain of the reinforcement column. And the strain growth rate of the reinforced column is accelerated after the peak load, indicating that the prestressed semicircular steel plate reinforcement gives full play to the material properties of steel and concrete. It can be seen from the figure that the steel strain of the contrast column RC-1 decreases directly after reaching the ultimate load. Due to the transverse constraint force provided by the prestressed semicircular steel plate, the steel strain of the reinforced column decreased slowly after reaching the ultimate load.

3.2. Finite Element Analysis

3.2.1. Finite Element Modeling. In this article, ABAQUS software is used for finite element analysis. The steel skeleton and concrete are contacted by the embedded region without considering the influence of bond-slip, and it is assumed to be coordinated deformation. Although the steel casing and concrete column surface will produce relative slip in the actual test, many research results show that this relative slip has little effect on the constraint ability, so this article assumes that they are ideally connected and use tie contact. In the existing research field, the application method of steel casing prestress is still relatively rare. High strength bolts are used to apply prestress in the test, but, in the simulation, the equivalent substitution method is used to control prestress, and the prestress is equivalent to the pressure generated around the concrete column; that is, the contact element between the steel casing and the concrete transfers the interface pressure p, and the pressure perpendicular to the contact surface can be completely transferred between the interfaces. Only normal contact is considered between the cushion plate and the top surface of the concrete. Among them, the steel casing and two ends of the cushion plate are simulated by shell element S4R, and the concrete is simulated by three-dimensional solid element C3D8R.

The constitutive model of the concrete column strengthened with prestressed steel casing is similar to that of the concrete-filled steel tubular column. Therefore, the constitutive model of concrete in this simulation adopts the compression constitutive model of the concrete-filled steel tubular column in Liu Wei's study on the working mechanism of the concrete-filled steel tubular column under local compression [32]. The loading method adopts the vertical displacement loading of the upper part of the model. It is assumed that the lower part of the model is completely fixed, and the upper part constrains two translational and rotational degrees of freedom. The finite element model is shown in Figure 11.

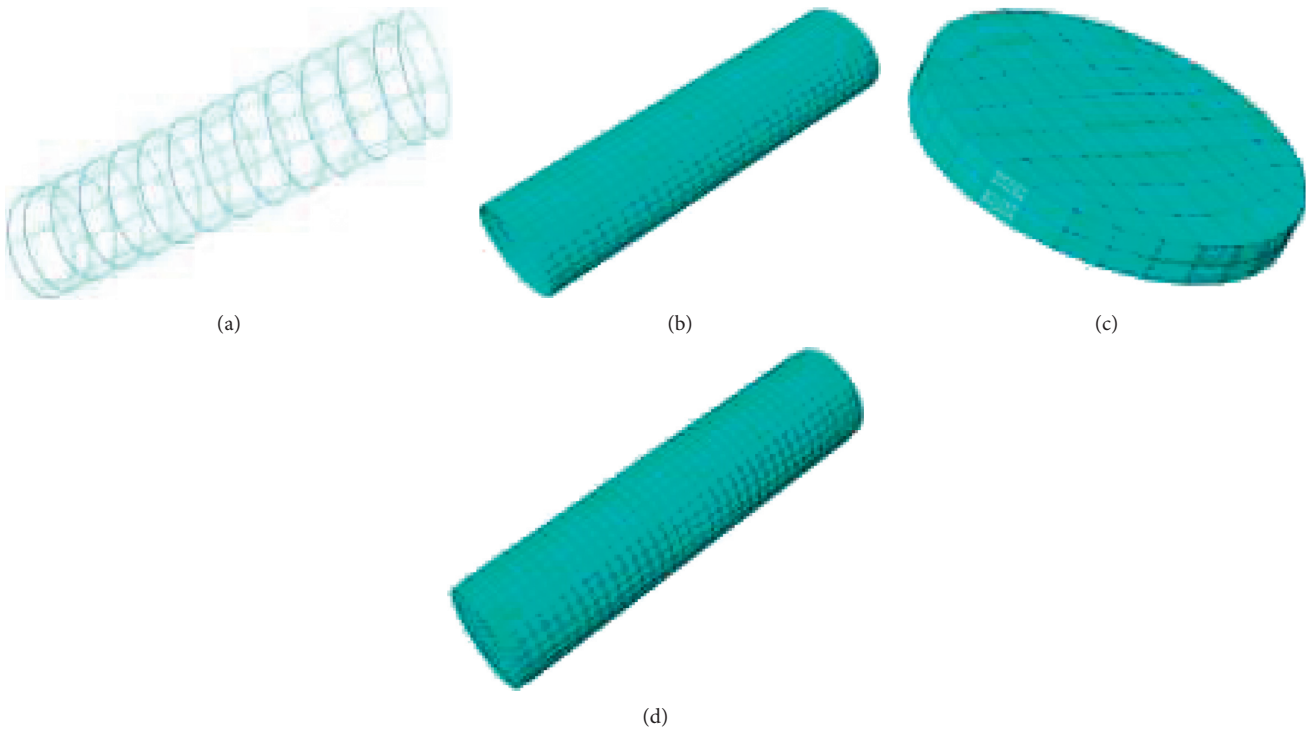

Figure 11: Model mesh subdivision. (a) Steel frame. (b) Steel casings. (c) Cushion block. (d) The whole specimen.

3.2.2. Results of Finite Element. Figure 12 shows the stress distribution nephogram of the steel casing when the reinforced column reaches the ultimate load when the prestress of the steel casing is 0 N/mm^2, 24.68 N/mm^2, and 67.90 N/mm^2, respectively. It can be seen from the figure that with the increase in the prestress value, the coverage of the maximum stress of the steel casing increases and is distributed in the middle area of the reinforced column. And with the increase in the prestress value, the compressive stress value increases, it shows that the steel casing has a good restraint effect, and the restraint effect is also obvious. There is a certain error between the finite element simulation and the test results; the main reason for the error is that there is a deviation between the application mode of prestress of reinforced columns and the actual situation during modeling. Moreover, the contact between steel casing and concrete is also complete contact in the ideal state, which is difficult to achieve in the actual project.

Figure 13 shows the load-displacement curve of the specimen obtained by the test and the finite element method. The real line represents the finite element value. The imaginary line represents the experimental value. It can be seen that the calculation results of the finite element model are consistent with the test results. The finite element analysis tends to be idealized. Therefore, the finite element analysis results are better than the test results. The comparison of specimen bearing capacity is shown in Table 3, $N_{FEM}/\overline{N}_{EXP}$ mean value is 1.026, and the standard deviation is 0.012, indicating that the finite element model established in this article can better simulate the stress characteristics of reinforced concrete columns strengthened with prestressed steel casing.

4. Calculation of Axial Compression Bearing Capacity

The prestressed steel casing reinforcement method studied in this article is a new reinforcement method. By prestressing the steel casing, the steel casing and the column needed to be strengthened are connected into a whole, so that they work together, thus significantly improving the bearing capacity of concrete columns.

Referring to the research results of Si et al. [33] in the axial compression test of damaged reinforced concrete columns strengthened with prestressed steel wires, after reinforcement, the bearing capacity of the reinforced column is composed of longitudinal reinforcement and confined concrete, and thus, the calculation formula of the bearing capacity of the reinforced column with prestressed steel wires is proposed:

$$N_u = \phi \cdot f_{c,c} A_c + f'_y A'_s,$$
$$f_{c,c} = b \cdot f_c, \tag{6}$$

where N_u is the ultimate bearing capacity of the composite strengthened member, kN; $f_{c,c}$ is the axial compressive strength of confined concrete, MPa; b is the prestressed winding improvement coefficient; f_c is the axial compressive strength of unconstrained concrete, MPa; A is the damage coefficient; A_c is the section area of compressive concrete, mm^2; f_y is the longitudinal reinforcement compressive

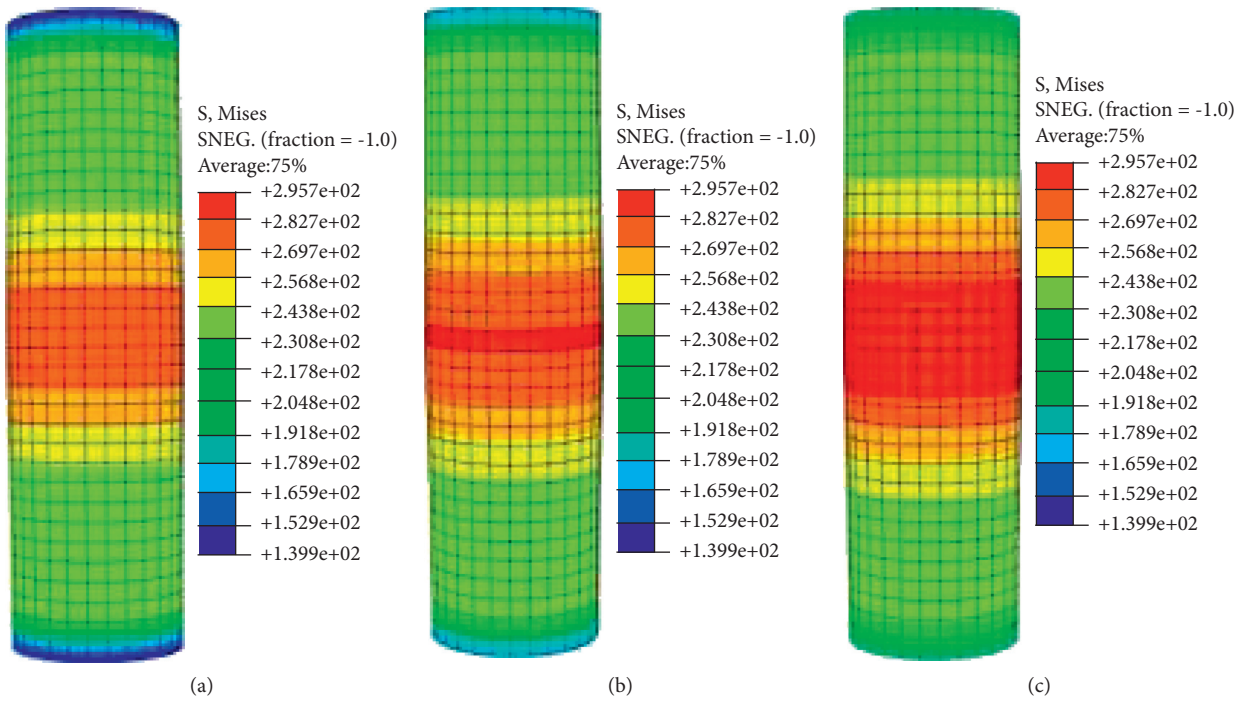

Figure 12: Strain cloud picture (MPa). (a) RC2-1. (b) RC2-2. (c) RC2-3.

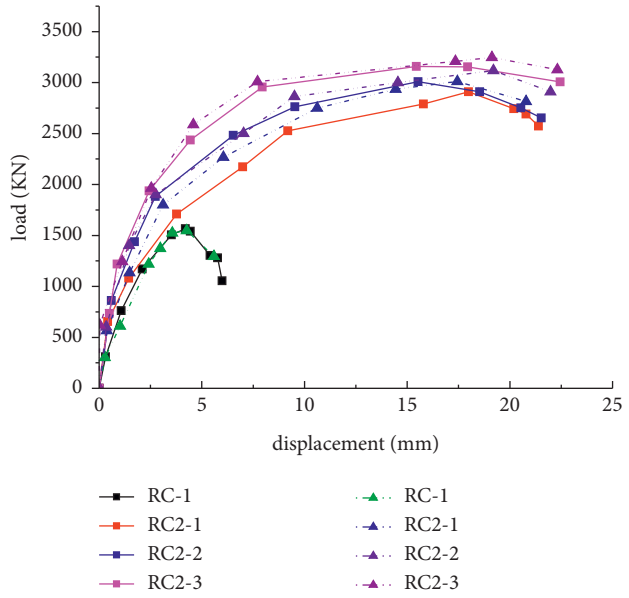

Figure 13: Load-displacement curve.

strength design value, MPa; and A_s is the longitudinal section area, mm^2.

Based on the derivation of Si Jianhui's calculation formula for the bearing capacity of reinforced members, it can be seen from Figure 5 that there are 10 mm left at the upper and lower ends of the concrete column without the constraint of steel plate. Therefore, the steel casing does not provide axial bearing capacity, but only provides one circumferential constraint force for the concrete column in this experiment. It can be seen that the increase in the bearing capacity of concrete columns strengthened with prestressed steel casing is mainly caused by the increase in the bearing capacity of concrete after being constrained [30, 34–36]. Due to the different prestress value, the ultimate compressive strain of confined concrete is different, and the strain of the steel bar is also different, so it is necessary to set up a composite reinforcement improvement coefficient. Since the specimens used in the test are all not under pressure before the test, the damage coefficient A can be taken as 1. Then calculation formula of the bearing capacity of concrete

Table 3: Comparison of experimental and calculated values.

Number	N_{EXP} (kN)						N_{FEM} (kN)	N_c (kN)	
	1	2	3	4	5	Average		Formula (7)	Error (%)
RC-1	1471.50	1553.30	1548.53	1612.32	1526.23	1542.38	1548.53	1419.67	8
RC-2-1	2654.89	2910.25	2967.48	2938.08	2781.00	2850.34	3010.25	2833.62	0.6
RC-2-2	3017.00	3008.29	3026.02	3110.64	3125.31	3057.45	3118.29	2921.90	4.4
RC-2-3	3133.54	3146.81	3046.87	3237.70	3304.70	3173.92	3246.81	3083.75	2.8

Note. N_{EXP} is the test bearing capacity. N_{FEM} is the bearing capacity of finite element analysis. N_C is the calculated bearing capacity.

columns strengthened with prestressed steel casing can be simplified as follows:

$$N_u = bf_cA_c + f'_yA'_s, \tag{7}$$

where b is the prestress increase coefficient, which is obtained by fitting from the relationship between prestress f and bearing capacity of steel casing by Origin software, $b = 0.005f + 3.40$.

The calculated results of formula (7) are compared with the experimental data and summarized in Table 3. It can be seen from Table 3 that the calculation results of formula (7) are in good agreement with the measured values.

5. Conclusions

In this article, the prestressed steel casing reinforcement method was proposed. Through the axial compression test and numerical simulation of 20 columns, the following preliminary conclusions can be drawn:

(1) Compared with the original column, the ultimate bearing capacity of reinforced concrete columns strengthened with prestressed steel casing is increased by 72.1%–109.9%, and the ductility is also greatly improved.

(2) The calculation formula of the axial compression bearing capacity of reinforced concrete columns strengthened with prestressed steel casing provided in this article has good applicability. Compared with the experimental values, the theoretical calculation formula has sufficient accuracy.

(3) The reinforcement effect of the prestressed steel casing reinforcement method is obvious, which is suitable for rapid repair and reinforcement of concrete columns that need to greatly improve the bearing capacity in a short time.

(4) ABAQUS software was used to model and analyze the test process. The results show that the finite element results are in good agreement with the test results. The comparative analysis results of models under different prestress levels show that when the prestress of steel casing is 0 N/mm^2, 24.68 N/mm^2, and 67.90 N/mm^2, the simulated bearing capacity increases by 94%, 101%, and 110%, respectively.

Data Availability

All data used to support the study are included within the article.

Consent

Not applicable.

Conflicts of Interest

The authors declare that they have no conflicts of interest.

Authors' Contributions

Z.R was responsible for methodology; Y.S was responsible for software and performed investigation; X.Z validated the data and prepared the original draft; Z.R and Y.S reviewed and edited the manuscript and helped with funding acquisition; Z.R and X.Z contributed to the project administration. All authors have read and agreed to the published version of the manuscript.

Acknowledgments

This research was funded by the Fundamental Research Funds for the Key Project of Research and Development Plan of Hunan Province 2020SK2109, National Natural Science Foundation of Hunan Province 2021JJ50106, National Natural Science Foundation of China 52104106, and Basic Research Program of Xuzhou (KC21017).

References

[1] Z. Ren, X. Zeng, and J. Sun, "Using two-way prestressed semicircular steel plate for construction of reinforced concrete cylinder column," *Complexity*, vol. 2018, Article ID 1481837, 10 pages, 2018.

[2] Y. Tang, W. Feng, Z. Chen, Y. Nong, S. Guan, and J. Sun, "Fracture behavior of a sustainable material: recycled concrete with waste crumb rubber subjected to elevated temperatures," *Journal of Cleaner Production*, vol. 318, Article ID 128553, 2021.

[3] Z. Ren, X. Zeng, J. Sun, and J. Wang, "Fracture properties of wide-notch concrete beams strengthened with near-surface mounted CFRP rebar," *KSCE Journal of Civil Engineering*, vol. 23, no. 11, pp. 4735–4746, 2019.

[4] B. Zhou, M. Zhang, L. Wang, and G. Ma, "Experimental study on mechanical property and microstructure of cement mortar reinforced with elaborately recycled GFRP fiber," *Cement and Concrete Composites*, vol. 117, Article ID 103908, 2021.

[5] X. Tan, Z. Hu, C. Chen, and M. Zhao, "3D DEM-FDM coupled analysis of the behavior of an isolated geogrid-encased stone column under axial loading," *Journal of Geotechnical and Geoenvironmental Engineering*, vol. 147, no. 6, Article ID 04021028, 2021.

[6] L. Hu and P. Feng, "Prestressed CFRP-reinforced steel columns under axial and eccentric compression," *Composite Structures*, vol. 268, Article ID 113940, 2021.

[7] L. Hu, P. Feng, and X. L. Zhao, "Fatigue design of CFRP strengthened steel members," *Thin-Walled Structures*, vol. 119, pp. 482–498, 2017.

[8] J. Zhang, Y. Sun, G. Li, Y. Wang, J. Sun, and J. Li, "Machine-learning-assisted shear strength prediction of reinforced concrete beams with and without stirrups," *Engineering with Computers*, vol. 36, pp. 1–15, 2020.

[9] W. Yayong, "Fire Resistance Test of RC Beam Retrofitted with Cover of High Strength Steel Mesh and Polymetric Motar," *Building Structure*, vol. 37, no. 1, pp. 112-113, 2007.

[10] Y. Sun, G. Li, and J. Zhang, "Developing hybrid machine learning models for estimating the unconfined compressive strength of jet grouting composite: a comparative study," *Applied Sciences*, vol. 10, no. 5, 2020.

[11] W. Ge, W. Song, A. F. Ashour, W. Lu, and D. Cao, "Flexural performance of FRP/steel hybrid reinforced engineered cementitious composite beams," *Journal of Building Engineering*, vol. 31, Article ID 101329, 2020.

[12] Y. Sun, G. Li, and J. Zhang, "Investigation on jet grouting support strategy for controlling time-dependent deformation in the roadway," *Energy Science & Engineering*, vol. 8, no. 6, pp. 2151–2158, 2020.

[13] Y. Sun, R. Bi, Q. Chang et al., "Stability analysis of roadway groups under multi-mining disturbances," *Applied Sciences*, vol. 11, no. 17, 2021.

[14] Y. Yong, L. Hui, and C. Wei, "Experimental study on seismic behavior of reinforced concrete frame structure retrofitted by prestressed steel strips," *Engineering Mechanics*, vol. 34, no. 10, pp. 53–60, 2017.

[15] Y. Sun, L. Guichen, Z. Junfei, S. Junbo, and X. Jiahui, "Development of an ensemble intelligent model for assessing the strength of cemented paste backfill," *Advances in Civil Engineering*, vol. 2020, Article ID 1643529, 6 pages, 2020.

[16] C. X. C. C. Yun-peng, "On reliable analysis of section-enlarging reinforcing method in strengthening frame structure," *Shanxi Architecture*, vol. 2, 2010.

[17] J. Sun, Y. Huang, F. Aslani, and G. Ma, "Electromagnetic wave absorbing performance of 3D printed wave-shape copper solid cementitious element," *Cement and Concrete Composites*, vol. 114, Article ID 103789, 2020.

[18] C. J. X. Jin, "Ultimate strength of reinforced concrete columns strengthened by circular steel jacketing," *Journal of South China University of Technology*, vol. 35, no. 10, pp. 78–83, 2007.

[19] Y. Sun, G. Li, J. Zhang, J. Sun, J. Huang, and R. Taherdangkoo, "New insights of grouting in coal mass: from small-scale experiments to microstructures," *Sustainability*, vol. 13, no. 16, 2021.

[20] L. Hu, Y. Wang, P. Feng, H. Wang, and H. Qiang, "Debonding development in cracked steel plates strengthened by CFRP laminates under fatigue loading: experimental and boundary element method analysis," *Thin-Walled Structures*, vol. 166, Article ID 108038, 2021.

[21] L. L. Hu, X. L. Zhao, and P. Feng, "Fatigue behavior of cracked high-strength steel plates strengthened by CFRP sheets," *Journal of Composites for Construction*, vol. 20, no. 6, Article ID 04016043, 2016.

[22] G. Ma, J. Sun, F. Aslani, Y. Huang, and F. Jiao, "Review on electromagnetic wave absorbing capacity improvement of cementitious material," *Construction and Building Materials*, vol. 262, Article ID 120907, 2020.

[23] J. Sun, Y. Huang, F. Aslani, X. Wang, and G. Ma, "Mechanical enhancement for EMW-absorbing cementitious material using 3D concrete printing," *Journal of Building Engineering*, vol. 41, Article ID 102763, 2021.

[24] J. Sun, "Fresh and mechanical behaviour of developed fibre-reinforced lightweight engineered cementitious composites for 3D concrete printing containing hollow glass microspheres," *Ceramics International*, vol. 47, no. 19, pp. 27107–27121, 2021.

[25] *Standard for Test Method of Mechanical Properties on Ordinary concrete*, Ministry of Construction of the People's Republic of China, Beijing, China, 2002.

[26] W. Ge, Y. Wang, A. Ashour, W. Lu, and D. Cao, "Flexural performance of concrete beams reinforced with steel–FRP composite bars," *Archives of Civil and Mechanical Engineering*, vol. 20, pp. 1–17, 2020.

[27] W. Ge, K. Chen, Z. Guan, A. Ashour, W. Lu, and D. Cao, "Eccentric compression behaviour of concrete columns reinforced with steel-FRP composite bars," *Engineering Structures*, vol. 238, Article ID 112240, 2021.

[28] J. Sun, F. Aslani, J. Wei, and X. Wang, "Electromagnetic absorption of copper fiber oriented composite using 3D printing," *Construction and Building Materials*, vol. 300, Article ID 124026, 2021.

[29] "Standard test methods for concrete structures, ," 2012.

[30] J. Li, Q. Qin, J. Sun, Y. Ma, and L. Qia, "Mechanical and conductive performance of electrically conductive cementitious composite using graphite, steel slag, and ggbs," *Structural Concrete*, Wiley, NJ, USA, 2020.

[31] J. Sun, Y. Wang, S. Liu et al., "Mechanical, chemical and hydrothermal activation for waste glass reinforced cement," *Construction and Building Materials*, vol. 301, Article ID 124361, 2021.

[32] W. Liu, *Research on Mechanism of concrete-filled Steel Tubes Subjected to Local Compression*, pp. 64-65, Fuzhou University, Fuzhou, China, 2005.

[33] J. Si, L. Wu, and W. Guo, "Axial compression of reinforced concrete columns strengthened by composite of prestressed plastic-steel strip and angle steel: an experimental study," *Structural Concrete*, Wiley, NJ, USA, 2021.

[34] W. Ma, X. Wang, J. Wang, J. Sun, and X. Xiang, "Generative design in building information modelling (BIM): approaches and requirements," *Sensors*, vol. 21, no. 16, 2021.

[35] J. Sun, Y. Wang, X. Yao et al., "Machine-Learning-Aided prediction of flexural strength and ASR expansion for waste glass cementitious composite," *Applied Sciences*, vol. 11, no. 15, p. 6686, 2021.

[36] J. Sun, Y. Ma, J. Li, J. Zhang, Z. Ren, and X. Wang, "Machine learning-aided design and prediction of cementitious composites containing graphite and slag powder," *Journal of Building Engineering*, vol. 43, Article ID 102544, 2021.

Hindawi
Advances in Civil Engineering
Volume 2021, Article ID 4373486, 11 pages
https://doi.org/10.1155/2021/4373486

Research Article

Experimental Study on Static Performance of Deployable Bridge Based on Cable-Strengthened Scissor Structures

Xiaoming Yu,[1,2] **Yinghua Yang**,[1] **Yanxia Ji**,[3] **and Lin Li**[2]

[1]*Department of Civil Engineering, Xi'an University of Architecture and Technology, Xi'an 710055, China*
[2]*School of Civil Engineering and Architecture, Suqian University, Suqian 223800, China*
[3]*School of Arts and Sciences, Suqian University, Suqian 223800, China*

Correspondence should be addressed to Xiaoming Yu; yuxiaoming2020@foxmail.com

Received 1 October 2021; Accepted 29 October 2021; Published 17 November 2021

Academic Editor: Wenjie Ge

The deployable bridge based on scissor structures is one of the effective methods to quickly restore traffic after natural and man-made disasters. Scissor structures have the advantages of high storage rate, lightweight, and convenient storage and transportation. However, when scissor structures are used as load-bearing structures, their stiffness and bearing capacity are low. In this study, a three-dimensional deployable bridge based on the cable-strengthened scissor structures was proposed. In addition to rapid expansion, steel cables were used to strengthen scissor structures to improve the stiffness and bearing capacity. Besides, the static loading comparative tests on cable-strengthened scissor structures and traditional scissor structures (cable-free scissor structures) were performed. The results show that the stiffness of the cable-free scissor structure is small, the bending moment of members is large, and the stress distribution is uneven. The stiffness of cable-strengthened scissor structure is significantly improved; the bending moment of members is significantly reduced; and the stress distribution in the member section is more uniform. It is proved that cables can be used to improve the stiffness and load-bearing capacity of scissor structures without affecting the deployability.

1. Introduction and Background

The deployable bridge system is an ideal solution for rapid traffic recovery after natural and man-made disasters. This bridge should have the characteristics of fast transportation, convenient installation, and rapid dismantling to meet the requirement of rapid erection and multiarea reuse in the assigned areas, and scissor structures can realize this goal. Scissor structures are composed of several scissor units, and each scissor unit is composed of two members connected through the rotary joints (pivots). The units are interconnected through hinges at their end nodes. In this way, scissor structures have a certain degree of freedom, which can be expanded from a compact packaged state to a large deployed state. This kind of structure is an ideal solution for deployable bridges.

Scissor structures have been widely used, and the geometric and kinematic structures have been mainly studied in the past few years. As a subclass of deployable structures, scissor structures have the advantages of high storage rate, easy conversion, and lightweight. Scissor structures are widely used in small structures such as mobile tents and antennas and slightly large structures such as mobile theatres [1], domes [2], and shelters [3]. Since low requirements of the stiffness and bearing capacity are required for scissor structures in most applications, the research mainly focuses on the geometric and kinematic of the structures. Pinero was the first to introduce the concept of the scissor unit [1]. Using simple scissor units, he designed a mobile theatre and won an architectural competition in London in 1961. Following Pinero, Escrig and Valcarcel developed new spatial grids and patterns composed of two- and three-way scissors for deployable arches, domes, and large-scale umbrellas [4, 5]. Hoberman proposed a novel concept composed of angulated elements that led to the design of radially deploying closed-loop structures [6, 7]. Pellegrino and You

took Hoberman's concept a step further and discovered generalized angulated elements to be used as a building block [8]. Feray Maden and Kelvin Roovers et al. gave the design methods of planar open-loop scissor structures and space lattice scissor structures, respectively [9, 10]. Decan Mao, Yaozhi Luo, and Zhong You discussed the movability of planar closed-loop scissor structures [11]. Jianguo Cai and Yao Chen et al. studied the motion trajectory and motion singularity of plane closed-loop scissor structures [12, 13]. Yenal Akgün and Charis J. Gantes proposed a modified scissor-like element (M-SLE), which can change the geometry of the whole system without changing the size of the bars or the span [14, 15].

Scissor structures are rarely used as a load-bearing structure of the bridge or building in engineering, and the corresponding mechanical properties are studied insufficiently. Igor Raskin and John Roorda conducted a series of studies on the mechanical performance of scissors columns. First, the compressive and flexural stiffness of linearly arranged scissors columns were derived under the assumption of geometric linearity [16]. Second, the scissors column was equivalent to a segmented column connected by a bar with infinite bending stiffness and a spring between the bars; then the calculation method of the compressive buckling capacity of the segmented column was given [17]. Finally, the geometric nonlinear analysis of the compressive deformation of the scissors column was carried out. Bo Li and San-Min Wang et al. studied the compressive buckling capacity of scissors columns with the consideration of self-weight [18]. Raskin and Roorda compared the stiffness of six scissor structures with different unit geometry [19]. Yu et al. proved theoretically that the steel cables can improve the stiffness and bearing capacity of scissor structures [20]. In recent years, Yuki Chikahiro and Ichiro Ario et al. have been engaged in the research and development of deployable bridges based on scissor structures and conducted a series of theoretical research, numerical simulation, and light vehicle load tests of full-scale bridges. According to the previous research, additional reinforcement members have been proposed to improve the load-bearing capacity of the bridge under static and dynamic loads [21–25].

In this study, a three-dimensional deployable bridge based on a cable-strengthened scissor structure was proposed. Compared to traditional scissor structures (i.e., cable-free scissor structures), the load-bearing capacity and stiffness of the proposed cable-strengthened scissor structure were greatly improved. Previous studies have confirmed that when scissor structures are used as load-bearing structures, the bending moment of members is large, the stress distribution in the member section is uneven, and load-bearing capacity of structures is reduced. In this study, the use of steel cables to the strengthen scissor structure was proposed to improve its bearing capacity and stiffness. Different from reference [20], our scissor unit has only upper and lower steel cables instead of many continuous cables, which can reduce the friction and avoid the complex design of the structure. To study the role of steel cables and pretension in scissor structures, the static loading tests of a cable-free scissor structure and a cable-strengthened scissor structure were performed, and the static performance of the two structures was analyzed and compared through the experimental data. The experimental results show that the stiffness of cable-free scissor structure is small, resulting in a large displacement of the structure, large bending moment of the member, and uneven stress distribution. The stiffness of the cable-strengthened scissor structure is significantly improved; the bending moment of the members is significantly reduced; and the stress distribution is more uniform. As a result, the load-bearing capacity of the cable-strengthened scissor structure is greatly improved.

2. Description of the Structural System

Figure 1 shows the schematic diagram of the deployable bridge proposed in this study. The bridge adopts a deck structure; the upper part is a modular deck system; and the cable-strengthened scissor structure is used as the lower bearing structure. The bridge deck system consists of the bridge deck and the lower longitudinal beam. During installation, the end of the longitudinal beam is connected with the buckle at the node of the substructure so as to form the whole deployable bridge system.

The lower bearing structure of the bridge is composed of the cable-strengthened scissor structure based on the modular design. Two steel cables are used to connect the upper and lower nodes of the cable-free scissor unit (Figure 2) to form a planar element (Figure 3). The steel cables in the element do not affect the expansion and contraction of the scissor structure, and the expansion angle can be accurately controlled. When the scissor structure is expanded to the design angle with the help of a deployable controller, the expected expansion shape of the structure is obtained, and the application of pretension is completed simultaneously. The four planar elements can be connected to form a three-dimensional element, that is, a module (Figure 4). Similar to the planar element, the module can expand and contract freely without being affected by the steel cables. When the module is tightened, it can shrink tightly into a bundle, contributing to a high storage rate (Figure 5). To prevent the relative shear deformation between planar elements, two crossed steel cables are added to the upper and lower surfaces of the module to form a geometrically invariant system. The modules are overlapped along the direction of the steel cables to form the bearing structure of the cable-strengthened scissor structure at the lower part of the bridge, as shown in Figure 1.

3. Test Procedures

According to the deployable bridge system proposed in this study, a self-made scale model of the lower bearing structure (Figure 5) was used (i.e., cable-strengthened scissor structures) to test its static performance. The relevant conditions of the test are described as follows.

3.1. Introduction of Model-Related Data. The test model: the test model was composed of three three-dimensional elements, and planar elements of the overlapping part were

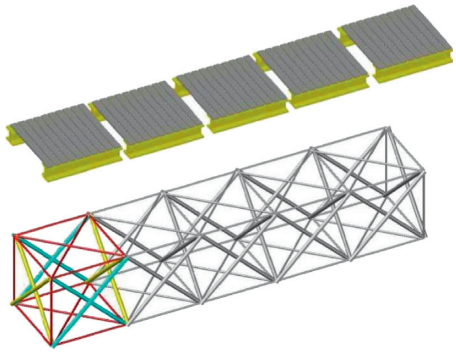

Figure 1: Deployable bridge model.

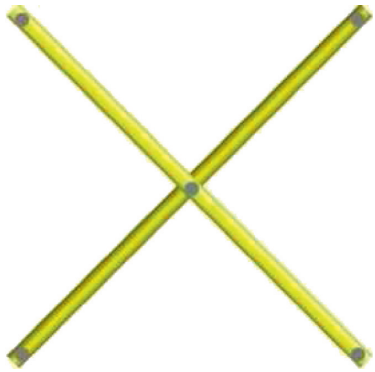

Figure 2: Scissor unit.

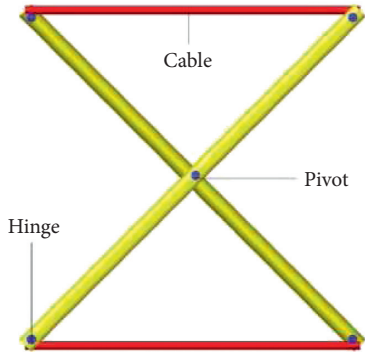

Figure 3: Planar element.

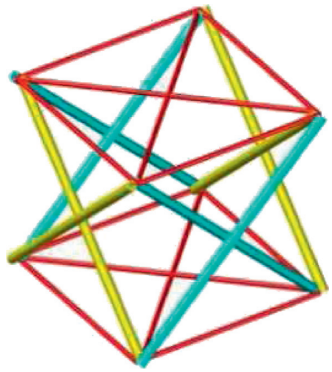

Figure 4: Three-dimensional element.

removed. The size of each three-dimensional element in three directions after the expansion was 0.5 m. The length, width, and height of the combined test model were 1.5 m, 0.5 m, and 0.5 m, respectively, as shown in Figure 6. The included angle between scissor members in each element was about 45°. In this way, the lengths of all members were equal, and the lengths of all steel cables connecting the scissor structure were equal in the longitudinal, transverse, and vertical directions. In this test, the influence of steel cables and pretension on stiffness and bearing capacity, the axial force, and the bending moment of members were mainly observed. Therefore, a planar structure along the length direction can be tested to achieve the purpose of the test. The opposite structure and scissor units in the width direction only played a supporting role. During the test, the steel cables of the opposite plane structure and the units in the width direction were completely released. As a result, when the tested structure was displaced, restraining effects can be avoided. Since the relative movement of two planar structures in the length direction would not occur, the cross steel cables were not set to prevent relative movement in this test.

3.1.1. Scissor Elements in the Model. The bars of the scissor elements in the model were Q345 B steel commonly used in construction engineering, with the specification of 30×3 mm steel pipe with an elastic modulus of 2.06×10^5 MPa. The length of each bar was 730 mm; the holes of 10 mm diameter for connection were set at both ends and the middle of the bar; the distance between the center of the hole diameter at both ends was 707 mm; and the bars were connected by bolts.

The cables in the model consisted of three parts: steel wire rope, cable force measuring device, and wire tightener (Figure 7). The 7×19 steel wire rope with a diameter of 4.2 mm was used as the steel wire rope, and its elastic modulus was calibrated by an electronic universal testing machine. Finally, the value of its elastic modulus was determined to be 1.88×10^5 MPa. To adjust the tension of the steel cables during the test, tighteners that can adjust the length were added to the steel cables. A section of 304 stainless steel bar with a length of 5 cm and a diameter of 10 mm was connected to the steel cable, and its elastic modulus was 1.92×10^5 MPa. Strain gauges were pasted on the surface of the steel bar to control the pretension of the steel cable.

3.2. Introduction to Loading Methods. In this test, the loading of the cable-strengthened and cable-free scissor structure models were conducted to compare the relevant data of the two models.

3.2.1. Loading of the Cable-Strengthened Scissor Structure Model. The four corners of the model were placed on the smooth steel plate, and a 5 cm thick steel plate was installed at the two points of the upper middle part of the scissor structure along the length direction, and the jack was set in

Figure 5: Physical model.

(a) (b)

Figure 6: Test models: (a) cable-strengthened structure and (b) cable-free structure.

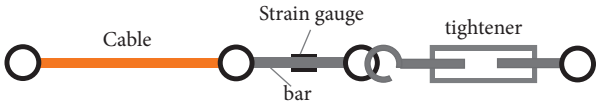

Figure 7: Details of steel cable composition.

the middle of the two points for loading, as shown in Figure 6(a). Before the test, the same pretension was applied to all the cables, and the structure was loaded and unloaded repeatedly so as to eliminate the nonlinear effect caused by the cables. In the data measurement, the designed pretension was first applied to the model by adjusting the tightener, and the magnitude of the pretension was obtained by the strain of the cable force measuring device. Second, the strain gauge was zeroed to remove the influence of gravity and pretension on the test data of the model and steel plate. Finally, under each kind of pretension, the structure was loaded step-by-step with no less than five levels, and the data were collected simultaneously.

3.2.2. Loading of Cable-Free Scissor Structure Model. In the model of cable-free scissor structure, all the steel cables were released in the cable-strengthened scissor structure model, and steel pipes were added on both sides of the model; the diameter of the steel pipes was the same as that of the scissor members, as shown in Figure 6(b). The loading conditions were the same as that of the cable-strengthened scissor structure. The structure was loaded three times, and the structure was loaded step by step with at least five levels, and the data were collected simultaneously.

3.3. Data Determination Method. This test aimed to obtain the influence of the steel cable and pretension values on the structural stiffness and bearing capacity, the variation of the axial force, and the bending moment of members with the external load. Because this symmetrical structure bore the symmetrical load, strain gauges were arranged at the designed position in the plane, as shown in Figure 8. Two strain gauges were symmetrically arranged at position C of bar 1 to measure the surface strain caused by the bending moment (hereinafter referred to as bending strain) on the surface of bar 1 at this point. Two strain gauges were symmetrically arranged at positions A and L of bar 1 to measure the strain caused by the axial force (hereinafter referred to as axial strain) on the surface of bar 1 at these points. Two strain gauges were symmetrically arranged at position D of bar 2 to measure the bending strain of bar 2 at this point, and two strain gauges were symmetrically arranged at positions A and F of bar 2 to measure the axial strain of bar 2 at these points. Two strain gauges were symmetrically arranged at position D of bar 3 to measure the bending strain of bar 3 here, and two strain gauges were symmetrically arranged at positions B and E of bar 3 to measure the axial strain of bar 3 here. A strain gauge was set on the preset steel bar in each section of the steel cable of the

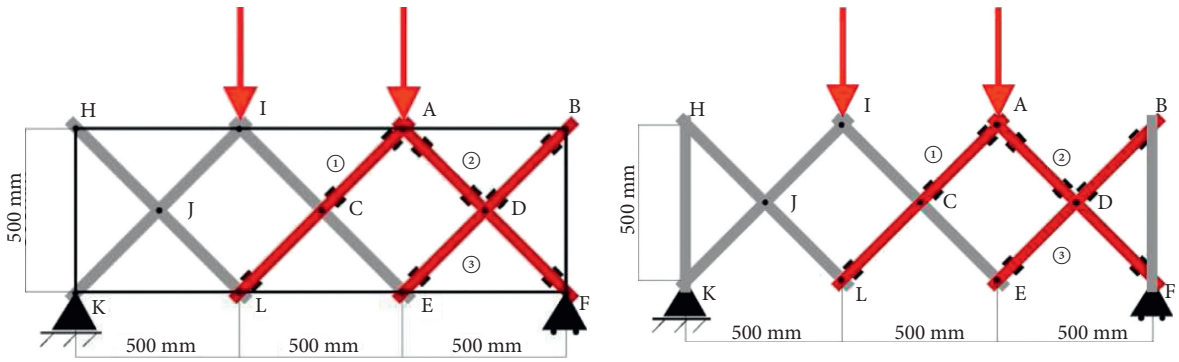

Figure 8: Layout of measuring points in the test model: (a) cable-strengthened structure model and (b) cable-free structure model.

model to control the pretension applied to the steel cable. Two displacement meters were set at positions L and E to measure the vertical displacement of the model during loading.

4. Analysis of Test Results

According to the above test scheme, the relationship between node displacement and the load of the two structures are obtained, as well as the relationship between surface strain at measuring points and load. The detailed test results are analyzed as follows.

4.1. Analysis on Static Performance of the Cable-Strengthened Scissor Structure. In the static test of the cable-strengthened scissor structure, four different pretensions are applied to the structure. The value of pretension is controlled by the strain gauges of the cable force measuring device. The control value of strain and corresponding tension are listed in Table 1. The influence of pretension on structural stiffness, internal force, and stress distribution is analyzed by using the collected data. The conclusions are obtained as follows: if the steel cables are in service, the pretension value of the steel cables basically has no effect on the stiffness. If the cables are out of service, the stiffness will be significantly reduced. The pretension value rarely affects the internal force of the structure with the change of load, and the stress distribution in the cross section is relatively uniform. The detailed analyses of the test results are as follows.

4.1.1. Effect of Cable Pretension on Stiffness. The load-displacement curves of Nodes L and E are shown in Figure 9. The slope of the load-displacement curve reflects the stiffness of the structure. As shown in Figure 9, each curve can be roughly divided into two obvious sections. The lower part of the curve describes the working state of the upper cables and the lower cables, while the upper part of the curve describes that of the lower cables. First, the slopes of the lower part of the curves are approximately equal. This shows that when the upper and lower cables are all in service, the stiffness of the structure is not affected by the pretension value. Second, the upper part of the curve approximates a straight line with

Table 1: Control strain of cable pretension.

Case	Case 1	Case 2	Case 3	Case 4
Strain ($\mu\varepsilon$)	300	400	500	600
Pretension (N)	452	603	754	905

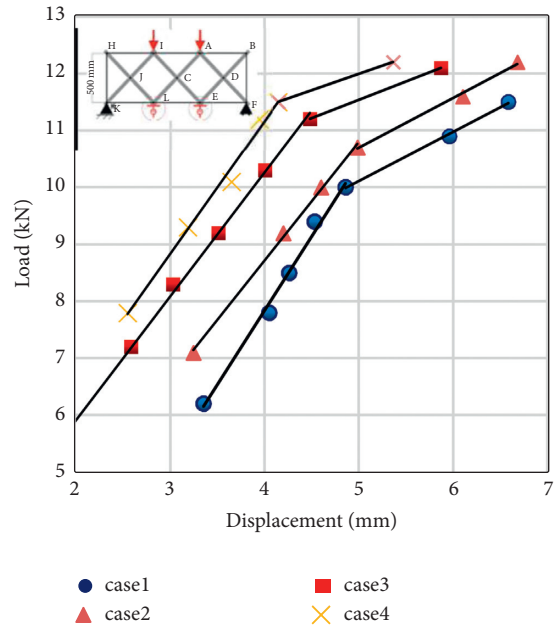

Figure 9: Load-displacement curve of the cable-strengthened structure.

a very close slope. This shows that when the upper cables are out of service, the stiffness of the structure is still not affected by the pretension value, but whether the steel cables are in service has a great impact on the stiffness. The turning point of the curve indicates that the upper cables start to quit work at this time.

4.1.2. Effect of Pretension of Steel Cables on Internal Force. To clearly explain the influence of pretension on the internal force of the structure, bar 1 is taken as an example, and its load-bending strain curves and load-axial strain curves

under different pretensions are obtained, as shown in Figure 10. The longitudinal axis in the figure represents the external load, and the horizontal axis represents the bending strain or axial strain.

4.1.3. Effect of Pretension on Bending Moment. Although the positions of each curve in Figure 10(a) are different, the overall shape of the curve is basically the same as the above load-displacement curve. Each curve can be divided into two distinct sections, corresponding to the working state of the upper cables and the lower cables and that of the single lower cables. The slope of the lower part of the curve is approximately the same. It shows that when the upper and lower cables are all in service, the variation law of the bending moment of the member with the load is hardly affected by the pretension value. The slope of the upper part of the curves is also close, indicating that when the upper cables are out of service, the variation law of the bending moment of the member with the load is still not affected by the pretension value. However, it can be found that the bending moment increases rapidly after the upper cables are out of the service.

4.1.4. Effect of Pretension on the Axial Force. Figure 10(b) shows the influence of pretension on the axial force. These curves show a straight-line rising, and the slope is the same, which shows that the value of pretension has no influence on the change of axial force and has nothing to do with whether the steel cables are in service or not.

4.1.5. Effect of Cable Pretension on Stress Distribution. The value and type of the internal force borne by the member directly determine the design of the cross section. To study the member stress in the cable-strengthened scissor structure, the bending strain at the pivot (position C) and the axial strain of bar 1 are compared. Figure 11 shows ratio curves of bending strain to axial strain of bar 1 with the change of load. The horizontal axis presents the ratio of the bending strain to axial strain, and the longitudinal axis presents the external load. As shown in Figure 11, the ratio is between 1 and 2, indicating that the bending strain is greater than the axial strain. In the design of this structure, the effect of bending moment cannot be ignored. The ratio curve of bending strain to axial strain can be divided into two sections, corresponding to the working state of the upper and lower cables and the single working state of the lower cables. In the lower part of the curve, the ratio decreases with the increase of load, which shows that the growth rate of bending moment is less than that of axial force. In the upper part curve, when the upper cables are not in service, the ratio begins to increase rapidly with the increase of load, which also indicates that the bending moment is accelerating. Through the comparison of the curves, it can be concluded that the joint working of the upper and lower cables is important, while this is dependent on specific conditions.

4.2. Static Performance Analysis of the Cable-Free Scissor Structure. After the static test of the cable-strengthened scissor structure, all the steel cables in the structure are released, and vertical bars are added at both ends of the scissor structure; then a stable symmetrical structure is obtained, as shown in Figure 6(b). The same test equipment is used to load the structure three times, and the structure is loaded step by step for no less than five levels. The data of displacement, bending strain, and axial strain of the structure are collected simultaneously. The test results show that the stiffness of the cable-free scissor structure is relatively small, and the overall deformation of the model under load is clear. The bending strain at the pivot of the member is very large, and the bending moment is an important reference index for the design of the cable-free scissor structure.

4.2.1. Stiffness of the Cable-Free Scissor Structure. Figure 12 shows the displacement-load curve of the cable-free scissor structure. Through observation, it can be seen that the displacement-load relationship is linear in general. When the load is large, the relationship between them shows a nonlinear trend. When the load reaches 9 kN, the displacement of the structure has exceeded 8 mm, and the overall displacement is extremely large. The above situation is shown in the test: with the increase of load, the middle element moves downward, and the displacement increases gradually. When the load is large, the elements on both sides begin to rotate inward and drive the vertical bars at both ends to rotate inward obviously. The large deformation of the structure makes the structure show a certain nonlinearity. The above data and phenomena show that the stiffness of the cable-free scissor structure is relatively small.

4.2.2. Internal Force of the Cable-Free Scissor Structure. Figure 13 shows the load-bending and load-axial strain curves of bars 1, 2, and 3. In the elastic range, the relationship between load and strain can directly reflect the relationship between load and internal force.

The curves in Figure 13 show obvious linearity. However, when the load is large, individual points deviating from the straight line can be observed. This is caused by the structural geometric nonlinearity due to the large deformation of the structure under the large load. As shown in Figure 13(a), the bending strains of bars 1 and 3 are relatively large. Under the same load, the bending strains of bars 1 and 3 are several times the axial strain in Figure 13(b). It indicates that the bending moment of some members of the cable-free scissor structure is very large, which is unfavorable to the load-bearing capacity of the structure.

4.2.3. Stress Distribution in the Member Section of the Cable-Free Scissor Structure. From the above data, it can be seen that bar 2 is located at the support, and the support reaction is large, resulting in a large axial force but a small bending moment. bar 3 is located at the edge of the structure, with small axial force and large bending moment. Therefore, the internal forces of bars 2 and 3 are special. And the

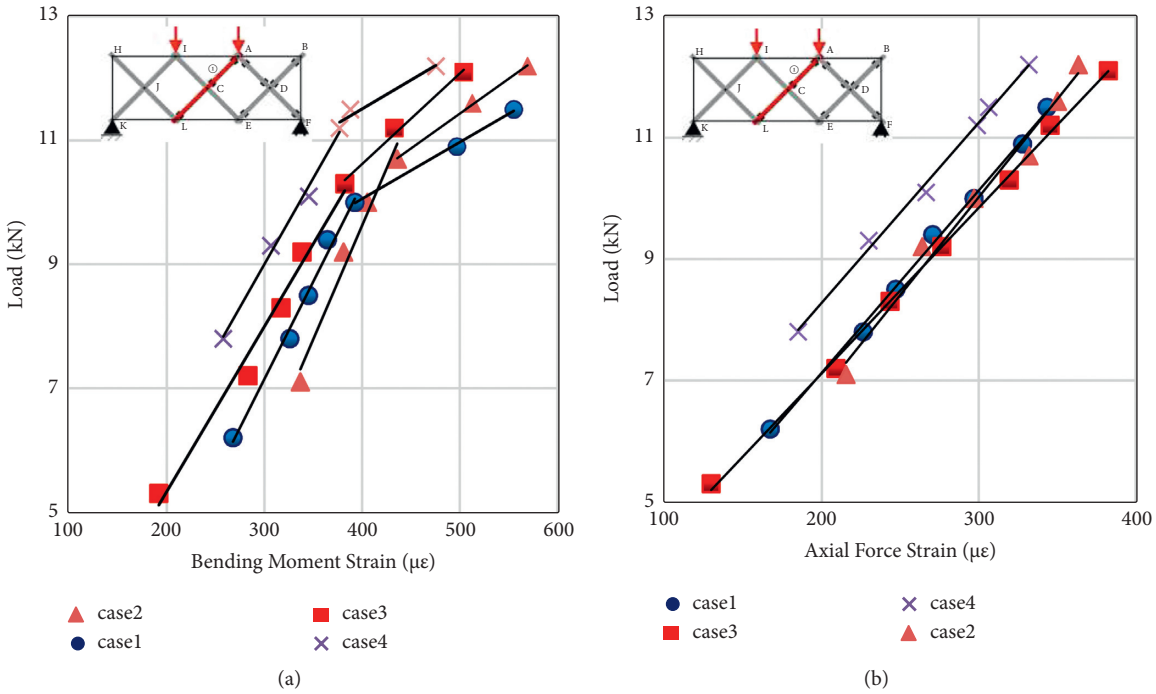

Figure 10: Load-internal force strain curve of bar 1 in the cable-strengthened structure: (a) load-bending strain curves and (b) load-axial strain curves.

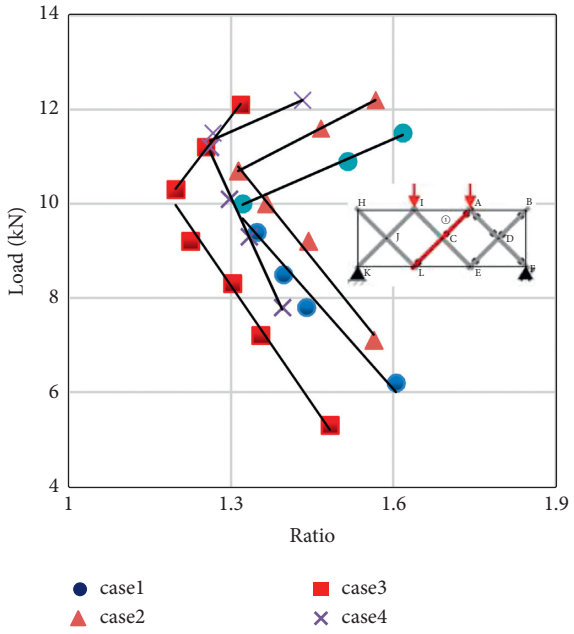

Figure 11: Ratio curves of the bending strain and axial strain of bar 1 in cable-strengthened structure.

characteristics of stress distribution in the member section of the cable-free scissor structure are discussed by using bar 1. Table 2 lists the bending strain, axial strain, and their ratio at the pivot of bar 1 under the load. Through the analysis of data, the bending strain under load is much larger than the axial strain. Although the ratio decreases with the increase of load, the bending strain is still several times the axial strain.

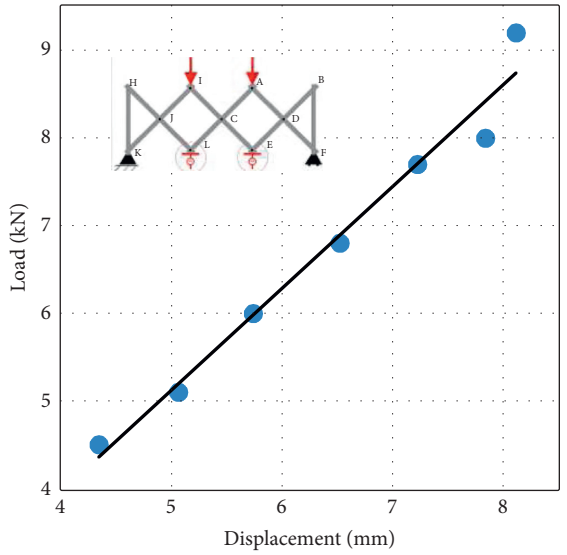

Figure 12: Load-displacement curves of the cable-free structure.

As a result, the uneven distribution of stress is caused; the section size of the member is too large; and the strength of the material cannot be fully used, which is not conducive to reducing the weight of the structure.

4.3. Comparison of Static Performance between the Cable-Free Scissor Structure and the Cable-Strengthened Scissor Structure. The data obtained from the two tests are used for the subsequent analysis. When the strain of the cable force measuring device is 300 $\mu\varepsilon$, the relevant data of the cable-free

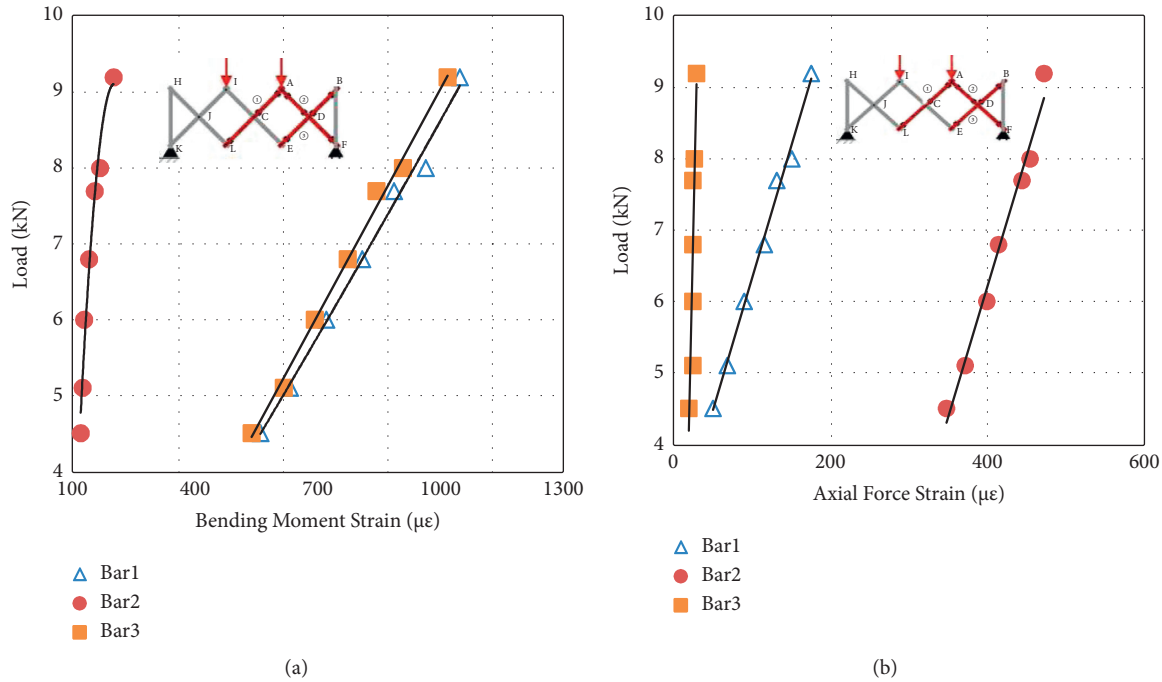

Figure 13: Load-strain curve of bar 1 of the cable-strengthened structure: (a) load-bending strain curves and (b) load-axial strain curves.

Table 2: Comparison of bending strain and axial strain of bar 1 of the cable-free scissor structure.

Load (kN)	4.5	5.1	6	6.8	7.7	8	9.2
Bending strain (με)	635	720	824	927	1,019	1,109	1,208
Axial strain (με)	49	67	89	115	131	150	175
Ratio	13	10.7	9.3	8.1	7.8	7.4	6.9

and cable-strengthened scissor structures are compared. The analysis results show that the existence of steel cables increases the stiffness of scissor structures, the internal force is relatively reduced, and the stress distribution in the cross section is more uniform. Therefore, steel cables play a very intentional role in the load-bearing of the structure. The specific analysis is as follows.

4.3.1. Comparison of Stiffness. Figure 14 shows the load-displacement curves of the cable-free and cable-strengthened scissor structures. Through comparison, it can be found that the slope of the two curves of the cable-strengthened scissor structure is greater than that of the cable-free scissor structure. It indicates that steel cables can significantly improve the stiffness of scissor structures. This conclusion can be proved by comparing displacements under the same load. For example, when the load is 7 kN, the displacement of the cable-strengthened scissor structure is about 3 mm, while that of the cable-free scissor structure has reached about 7 mm, and the displacement of the latter is more than twice that of the former.

4.3.2. Comparison of Internal Force. Figure 15 shows the load-bending strain curves of bar 1 of the cable-free and cable-strengthened scissor structures. It is found that the slope of the two straight lines of the cable-strengthened scissor structure is greater than that of the curve of the cable-free scissor structure, which shows that the bending moment of the member of the cable-free scissor structure increases faster with the increasing external load. Under the same load, the strain of the cable-free scissor structure is much larger than that of the cable-strengthened scissor structure, which indicates that steel cables can reduce the bending moment of the members of scissor structures. Figure 16 shows the load-axial strain curves of the two, the slope of the curve is basically the same, and the axial force of the cable-strengthened scissor structure is slightly higher than that of the cable-free scissor structure. To comprehensively compare the stress conditions of the two structures, the sum of bending strain and axial strain is taken for comparison, as shown in Figure 17. It can be seen that the comprehensive strain of the cable-free scissor structure is significantly higher than that of the cable-strengthened scissor structure. The above analysis shows that the application of steel cables can greatly reduce the internal force of scissor structures.

4.3.3. Comparison of Stress Distribution. As shown in Figure 11 and Table 2, the ratio of bending strain to axial strain of the cable-strengthened scissor structure is basically maintained at 1~2 times, while the bending strain of bar 1 in

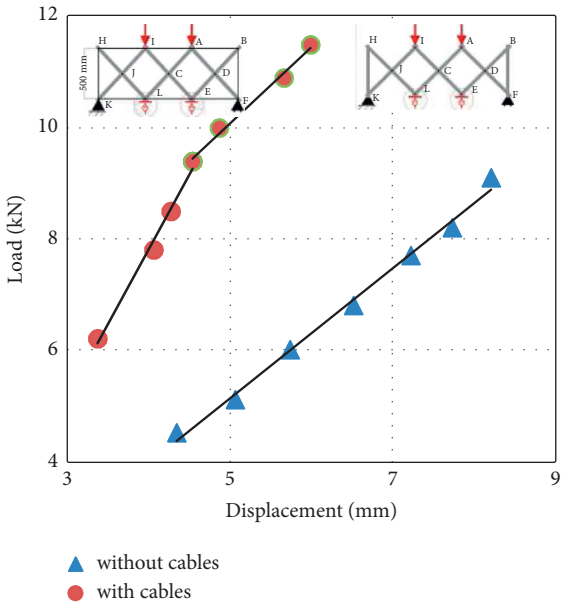

Figure 14: Load-displacement comparison curves of structures with and without steel cables.

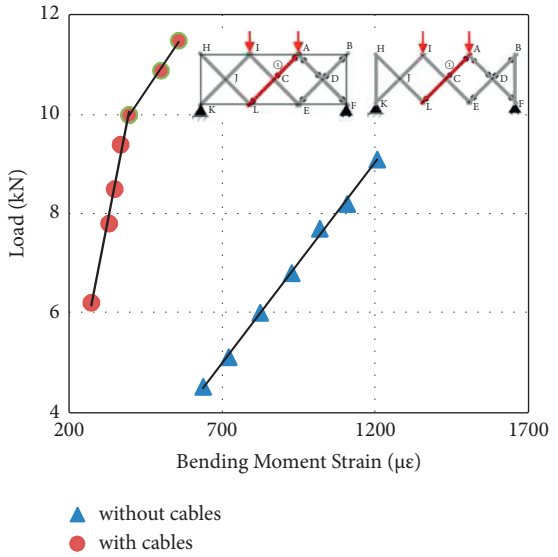

Figure 15: Load-bending strain comparison curves of structures with and without steel cables.

the cable-free scissor structure is several times of the axial strain. It shows that compared with the cable-free scissor structure, the addition of steel cables makes the stress distribution in the member section more uniform, which is conducive to improving the load-bearing capacity of the structure.

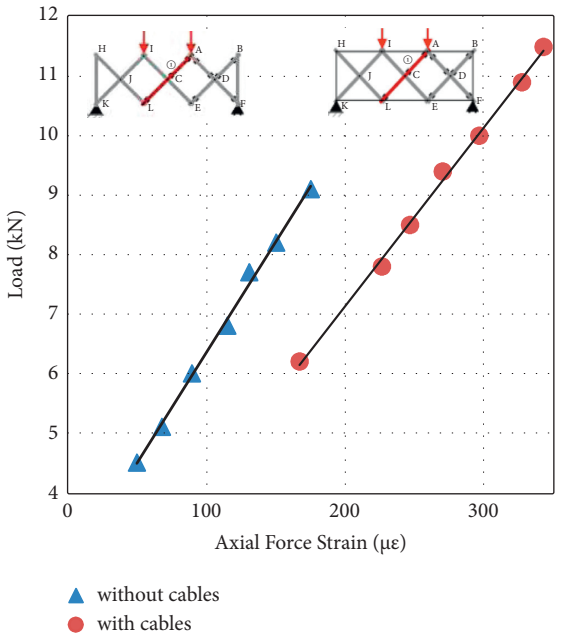

Figure 16: Comparison of the load-axial strain of structures with and without steel cables.

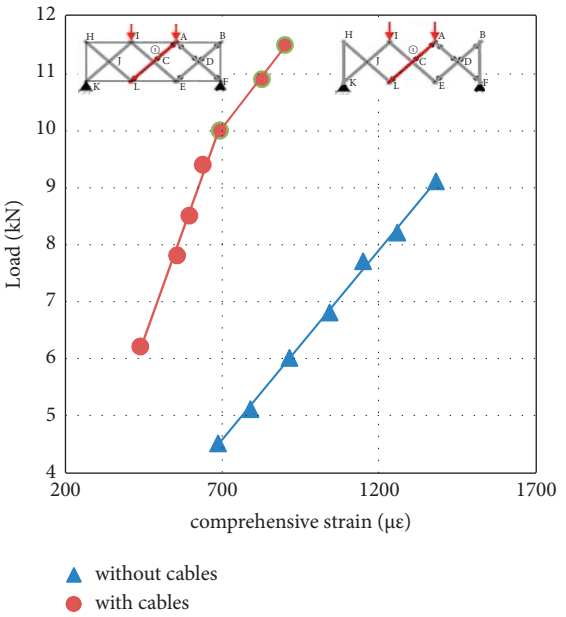

Figure 17: Comparison of the comprehensive strain of structures with and without steel cables.

5. Conclusion

In this paper, a three-dimensional deployable bridge based on a cable-strengthened scissor structure was proposed. In addition to rapid expansion, steel cables were used to strengthen the scissor structure to improve the stiffness and bearing capacity. The static loading comparative tests on the cable-strengthened and cable-free scissor structures were performed. The conclusions are obtained as follows:

(1) The stiffness of the cable-free scissor structure is relatively small, resulting in a large displacement of the structure, large bending moment of the member section, and uneven stress distribution.

(2) The stiffness of the cable-strengthened scissor structures is significantly improved; the bending moment of the members is significantly reduced; and the stress distribution is more uniform. As a result, the load-bearing capacity of the cable-strengthened scissor structure is greatly improved.

(3) The static loading comparative tests show that the addition of steel cables significantly improves the stiffness of scissor structures, greatly reduces the

internal force, and the stress distribution in the member section is more uniform so as to improve the load-bearing capacity of scissor structures.

Data Availability

The data used to support the findings of this study are included within the article.

Conflicts of Interest

The authors declare that they have no conflicts of interest.

Acknowledgments

This research was supported by the scientific research support project of "333 High Level Talent Training Project" of Jiangsu Province, China (Grant no. BRA2020241), and Suqian Sci and Tech Program of Jiangsu Province, China (Grant nos. Z2019112, 2021TD04, and K202012), which are gratefully acknowledged.

References

[1] E. P. Pinero, "Project for a mobile theatre," *Architectural Design*, vol. 12, pp. 154-155, 1961.

[2] J. B. Valcarcel, F. Escrig, and E. Martin, "Expandable domes with incorporated roofing elements," in *Proceedings of the Fourth International Conference on Space Structures*, Space Structures, Thomas Telford, London, UK, 1993.

[3] L. A. Mira, A. P. Thrall, and N. D. Temmerman, "Deployable scissor arch for transitional shelters," *Automation in Construction*, vol. 43, no. 7, pp. 123–131, 2014.

[4] F. Escrig and J. P. Valcarcel, "Geometry of expandable space structures," *International Journal of Space Structures*, vol. 8, no. 1-2, pp. 71–84, 1993.

[5] F. Escrig, "General survey of deployability in architecture," *Mobile and Rapidly Assembled Structures II*, vol. 24, pp. 3–22, 1996.

[6] C. Hoberman, "Reversibly expandable doubly-curved truss structure," U.S. Patent and Trademark Office, Washington, DC, USA, U.S. Patent 4,942,700[P], 1990.

[7] C. Hoberman, "Radial expansion/retraction truss structures," U.S. Patent and Trademark Office, Washington, DC, USA, U.S. Patent 5,024,031, 1991.

[8] Z. You and S. Pellegrino, "Foldable bar structures," *International Journal of Solids and Structures*, vol. 34, no. 15, pp. 1825–1847, 1997.

[9] F. Maden, K. Korkmaz, and Y. Akgün, "A review of planar scissor structural mechanisms: geometric principles and design methods," *Architectural Science Review*, vol. 54, no. 3, pp. 246–257, 2011.

[10] K. Roovers and N. De Temmerman, "Deployable scissor grids consisting of translational units," *International Journal of Solids and Structures*, vol. 121, pp. 45–61, 2017.

[11] D. Mao, Y. Luo, and Y. Zhong, "Planar closed loop double chain linkages," *Mechanism and Machine Theory*, vol. 44, no. 4, pp. 850–859, 2009.

[12] J. Cai, Y. Zhou, Y. Zhu, J. Feng, Y. Xu, and J. Zhang, "Geometry and mechanical behaviour of radially retractable roof structures during the movement process," *International Journal of Steel Structures*, vol. 16, no. 3, pp. 755–764, 2016.

[13] Y. Chen, L. Fan, and J. Feng, "Kinematic of symmetric deployable scissor-hinge structures with integral mechanism mode," *Computers & Structures*, vol. 191, pp. 140–152, 2017.

[14] Y. Akgün, C. J. Gantes, K. E. Kalochairetis, and G. Kiper, "A novel concept of convertible roofs with high transformability consisting of planar scissor-hinge structures," *Engineering Structures*, vol. 32, no. 9, pp. 2873–2883, 2010.

[15] Y. Akgün, C. J. Gantes, W. Sobek, K. Korkmaz, and K. Kalochairetis, "A novel adaptive spatial scissor-hinge structural mechanism for convertible roofs," *Engineering Structures*, vol. 33, no. 4, pp. 1365–1376, 2011.

[16] I. Raskin and J. Roorda, "Linear behaviour of a uniform pantographic column in bending and compression," *International Journal of Space Structures*, vol. 13, no. 4, pp. 187–195, 1998.

[17] I. Raskin and J. Roorda, "Buckling force for deployable pantographic columns," *WIT Transactions on The Built Environment*, vol. 24, 1996.

[18] B. Li, S. M. Wang, C. J. Zhi, X.-X. Xue, and V. Makis, "Analytical and numerical study of the buckling of planar linear array deployable structures based on scissor-like element under its own weight," *Mechanical Systems and Signal Processing*, vol. 83, pp. 474–488, 2017.

[19] I. Raskin and J. Roorda, "Nonlinear analysis of uniform pantographic columns in compression," *Journal of Engineering Mechanics*, vol. 125, no. 12, pp. 1344–1348, 1999.

[20] F. Yu, X. Xu, and Y.-z. Luo, "Research on mechanical properties of cable-strengthened scissor-Hinge mechanism," *Engineering Mechanics*, vol. 38, no. 5, pp. 151–160, 2021.

[21] Y. Chikahiro, I. Ario, and M. Nakazawa, "An experimental study on the design method of a real-sized Mobile Bridge for a moving vehicle," *Mobile and Rapidly Assembled Structures IV*, vol. 136, pp. 140–152, 2014.

[22] Y. Chikahiro, I. Ario, and M. Nakazawa, "Theory and design study of a full-scale scissors-type bridge," *Journal of Bridge Engineering*, vol. 21, no. 9, Article ID 04016051, 2016.

[23] Y. Chikahiro, I. Ario, M. Nakazawa et al., "Experimental and numerical study of full-scale scissor type bridge," *Automation in Construction*, vol. 71, pp. 171–180, 2016.

[24] Y. Chikahiro, I. Ario, P Pawlowski et al., "Dynamics of the scissors-type mobile bridge," *Procedia Engineering*, vol. 199, pp. 2919–2924, 2017.

[25] K. Chanthamanivong, I. Ario, and Y. Chikahiro, "Smart design of coupling scissors-type bridge," *Structures*, vol. 30, no. 1, pp. 206–216, 2021.

Hindawi
Advances in Civil Engineering
Volume 2021, Article ID 1690168, 11 pages
https://doi.org/10.1155/2021/1690168

Research Article

Structural Analysis of Backfill Highway Subgrade on the Lower Bearing Capacity Foundation Using the Finite Element Method

Wenjuan Xu,[1,2] Xin Huang,[1] Jiandong Huang,[3] and Zhengjun Yang[1,4]

[1]*College of Civil Engineering, Nanjing Forestry University, Nanjing 210037, China*
[2]*Jiangsu Agricultural and Forestry Technical College, Zhenjiang 212400, China*
[3]*School of Mines, China University of Mining and Technology, Xuzhou 221116, China*
[4]*Jurong Traffic and Transport Bureau, Zhenjiang 212400, China*

Correspondence should be addressed to Jiandong Huang; huang@cumt.edu.cn

Received 10 September 2021; Revised 22 October 2021; Accepted 25 October 2021; Published 8 November 2021

Academic Editor: Wenjie Ge

The present study is to investigate the stability of the backfill subgrade on the lower bearing capacity foundation. A finite element (FE) model was constructed to simulate the high-filled road subjected to the actual self-weight load. The strength reduction method was adopted to establish an analysis model of slope stability. At the same time, the sensitivity analysis of the factors affecting the slope stability was carried out through parametric studies, including the elastic modulus, cohesion, internal friction angle, and slope rate. The results showed that the slope stability analysis model established by the strength reduction method can characterize the stability of the slope by calculating the slope safety coefficient. The mutation point of the relationship curve between the displacement generated in the slope and the reduction coefficient can be used as the criterion. Under the condition of a given strength reduction coefficient, the calculated results obtained through FE modeling can show the development of the equivalent plastic zone in the form of cloud diagrams.

1. Introduction

Road slope refers to the infrastructure constructed or modified to meet the needs of road construction [1–5]. The slope formed under certain conditions (topography and geology) will break the previous mechanical balance into an unstable body due to changes in external factors. Under the action of its own weight or other loads, it will follow a certain relatively weak surface [4, 6, 7]. A landslide is a kind of bad geological phenomenon such as sliding downwards as a whole, intermittently slowly, and sometimes even suddenly. The factors that cause landslides include excavation of side slopes, rapid embankment filling, earthquakes, river erosion, sudden drops in reservoir water levels, and heavy rains [6, 8–10]. The slope is not only a special geological environment but also an important part of engineering construction. Due to the construction demand for a large number of highway projects in recent years, the stability of the slope during the construction process is a link that cannot be ignored [11–14].

In the past, there were various approximate methods and specialized methods, which can be used to calculate the global safety factor that depends on the slope height, the steepness, and the constitutive properties of the soil constituting the slope. Nash [15] conducted a comprehensive review of many classic slope stability analysis methods. The limitation of many of these classical methods is that Mohr–Coulomb shear strength behavior with a fixed friction angle is usually assumed because of the inherent application of simple statistical methods to the soil. Approximately, the calculation of stress and related shear strength is a continuous mechanical problem with static uncertainties [16–18]. To reduce manual trials and errors associated with these technologies, such as slicing methods, many engineering software packages have been developed, but most software packages still use simple static methods to approximate soil stress and strength [19–22].

In the FE analysis, the method of increasing the external load or reducing the material strength of the rock-

soil mass is the earlier method adopted [23, 24]. The stability analysis of these slopes mainly includes the judgment basis of slope instability, the stability of the excavated slope, the comparative analysis of the selection of different software, and the analysis of the internal force of the slope with the supporting structure [25, 26]. In recent years, the FE method has been increasingly used to predict the displacement and stress in statically indeterminate slopes, dams, and embankments [5, 13, 14, 27–45]. The potential attractiveness of calculating slope stability in a continuum/finite element framework lies in many previous studies [7]. The equilibrium stress, strain, and related shear strength in the soil have been calculated accurately in the studies conducted by Aryal and Duncan [41, 44]. The general material models of soil (including Mohr–Coulomb and many other models) have been employed in the studies conducted by Ardah et al. [46]. The FEM method has been applied in 2D or 3D with complex slope combinations and soil sediments to model almost all types of mechanisms [47]. The FEM method has also been extended to address the damage caused by leakage, brittle soil behavior, random "yield soil" properties, and interventions such as engineering geotextiles, soil nails, drainage ditches, and retaining walls [5, 38, 40, 42–45]. To fully understand the stability condition of the backfill soil on the high-filled road with lower foundation bearing capacity, this article adopts the classic slope stability analysis method. In this method, the inclined soil is subjected to the actual self-weight load, and the purpose is to find a continuous surface through the soil that has the smallest safety coefficient against the slip or shear failure. The safety coefficient is defined as the degree to which the shear strength of the soil is reduced so that the slope has just reached the critical failure state.

2. Research Objective and Overview

The present study is to investigate the stability condition of the backfill soil on the high-filled road with lower foundation bearing capacity, as shown in Figure 1. A FE model was constructed to simulate the high-filled road subjected to the actual self-weight load. The strength reduction method was adopted to establish an analysis model of slope stability. At the same time, the sensitivity analysis of the factors affecting the slope stability was carried out through parametric studies, including the elastic modulus, cohesion, internal friction angle, and slope rate. Under the condition of a given strength reduction coefficient, the simulation results obtained by ABAQUS software show the development of the equivalent plastic zone in the way of cloud maps. The slope is stable under the reduction factor when the failure of transfixion or local yield failure occurs. If the reduction coefficient continues to increase, the slope is in a critical failure state when the plastic strain between adjacent iterative steps increases too much or the equivalent plastic strain reaches the yield limit at some nodes, and the strength reduction coefficient is positioned as the minimum safety factor of the overall stability of the slope.

3. Model Construction

In the present study, the FE method was adopted. In this method, a structure is regarded as a whole composed of a finite number of elements through nodes [5, 14, 30]. Except for the nodes which are fixed on the boundary, the displacement of each node that can produce displacement can be calculated by using equilibrium conditions, and then the internal forces of each element can be calculated by the node displacement [33–35].

In the finite element analysis of the strength reduction of the slope, the stability of the slope usually adopts the nonconvergence of the solution as the failure criterion [48]. Within the maximum number of iterations, if the calculation fails to converge, it means that no stress distribution that can satisfy both the failure criterion and the overall balance is found, which means that the soil has been damaged. Specifically, the actual strength parameters c' and φ' of the backfilled roadbed are divided by a reduction factor F_{trial} at the same time to obtain a set of new values of c'' and φ'' after reduction, i.e.,

$$\begin{cases} c'' = \dfrac{c'}{F_{\text{trial}}}, \\ \varphi'' = \arctan\left|\dfrac{1}{F_{\text{trial}}}\tan\varphi'\right|. \end{cases} \tag{1}$$

Then, the reduced values of c'' and φ'' are taken into the trial calculation of finite elements as new material parameters [49, 50]. When the finite element calculation converges, the value of F_{trial} is slightly larger, and then the trial calculation is carried out until the finite element no longer converges, which indicates that the soil reaches the critical limit state and the slope shear failure occurs. At this time, the critical slip surface and safety factors are obtained.

The gravity load is determined by the following method [51, 52]. On each one of the finite elements, the gravitational load generated by the weight of the soil can be obtained by the following equation:

$$p^{(e)} = \Upsilon \int S^{eN^T} \mathrm{d}S, \tag{2}$$

in which S is the area of the element; e is the element number. The result of this integration is to take the product of the area of each element and the weight of the soil as the element's gravity load and then distribute it to each node. Various complex constitutive models can be considered in the FE analysis, but the most common in engineering analysis is the ideal elastoplastic model because the results of the ideal elastoplastic model are the most comparable to the results of the limit equilibrium method. For general road slopes, the shear failure of the soil is mainly controlled, and the calculation accuracy of the distribution and size of the plastic zone is relatively high, and the requirements for the displacement are relatively low.

In the present study, the Mohr–Coulomb plastic model was employed to characterize the constitutive property of the soil. The yield criterion of the Mohr–Coulomb model is assumed as follows. When the shear stress acting on a certain point is equal to the shear strength of that point, the point

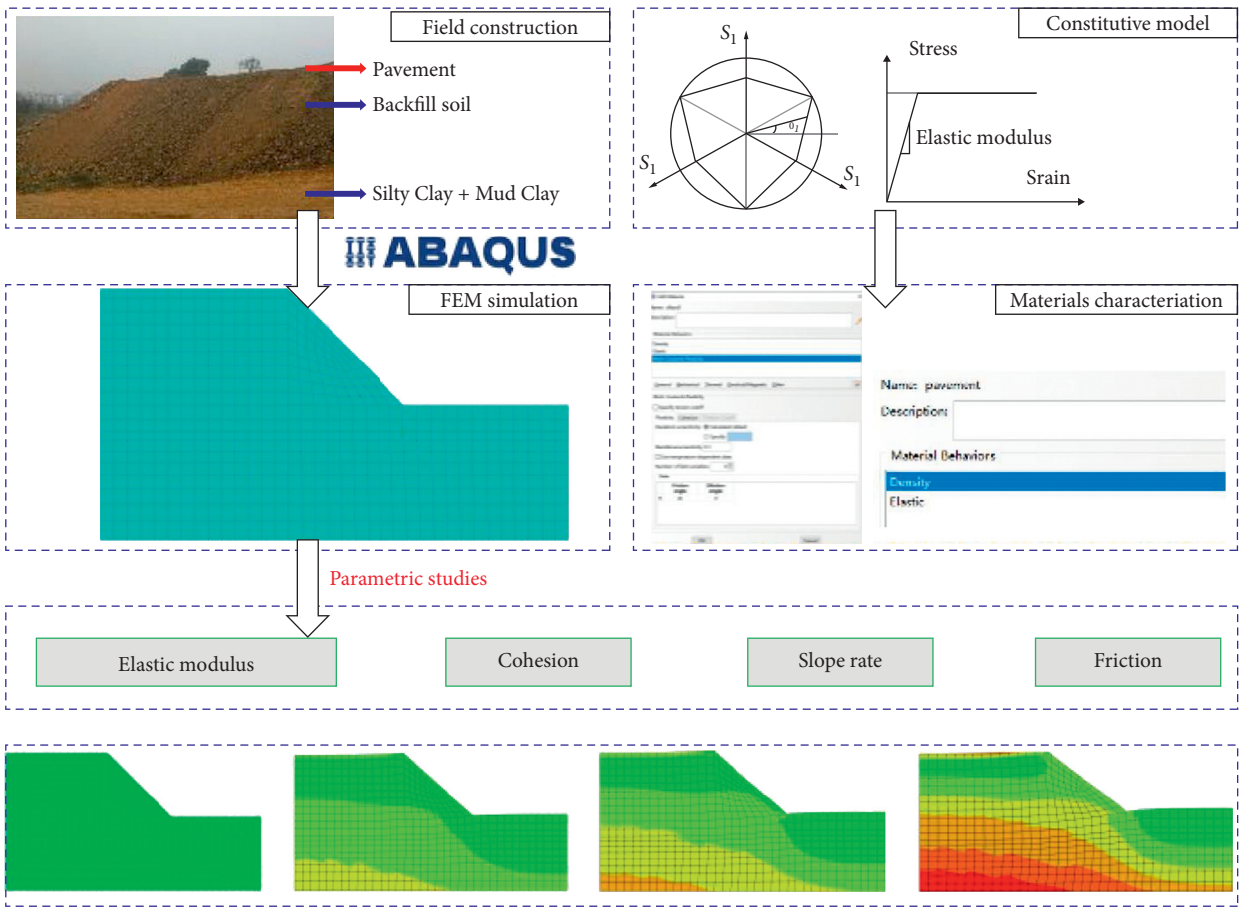

Figure 1: Research objective and overview.

will be broken, and the shear strength has a linear relationship with the normal stress acting on the surface. The yield surface equation of the Mohr–Coulomb model [53, 54] can be presented as follows:

$$F = R_{mc}q - p\tan\varphi - c = 0, \tag{3}$$

in which $\varphi(\theta, f^{\alpha})$ is the friction angle on the meridian plane; $c(\varepsilon^{-pl}, \theta, f^{\alpha})$ represents the changing process of the cohesive force of the material according to the isotropic hardening model. p is the equivalent compressive stress. q is the Mises equivalent stress. R_{mc} is the deviatoric stress coefficient of the Mohr–Coulomb model [55, 56], which can be defined as

$$R_{mc}(\theta, \varphi) = \frac{1}{\sqrt{3}\cos\varphi}\sin\left(\theta + \frac{\pi}{3}\right) + \frac{1}{3}\cos\left(\theta + \frac{\pi}{3}\right)\tan\phi, \tag{4}$$

in which φ is the bevel angle of the yield surface of the Mohr–Coulomb model on the P-RMCQ plane, and it generally refers to the internal friction angle of the material. θ is the direction angle of the generalized shear stress.

3.1. Material Properties. Four types of civil engineering materials were adopted in the present simulation [48]. Table 1 gives the material properties.

The bounding and unbound pavement materials (including the surface layer, base layer, and subbase layer) were simplified to one type of material property [57]. Elastic behavior without plastic deformation characterized by Young's modulus and Poisson's ratio was adopted for the pavement materials. The density of the backfill soil was determined as 1800 kg/m^3. Regarding the Mohr–Coulomb parameters of the backfill soil, the cohesion was determined as 15, 20, and 25 kPa, respectively. The internal friction angle was selected as 25° and 30°, and two elastic moduli of 50 MPa and 100 MPa were determined. The foundation with the lower bearing capacity was characterized by silty clay and mud clay [48]. The corresponding Mohr–Coulomb parameters are shown in Table 1 as well.

3.2. Physical Size of the Whole Model. Figure 2 gives the physical size of the whole model, including the pavement, subgraded by the backfill soil, and the foundation with lower bearing capacity [48].

These physical sizes were determined according to earlier studies [36–42]. The slope angle α is an important parameter considered in the present study, and it varied for different values ($\tan\alpha = 1:1$; $1:1.25$; $1:1.5$; $1:1.75$; $1:2$) to evaluate the effects on the slope stability. To reduce computations, only half of the high-filled subgrade FEM model (symmetric model) was constructed. The width of the pavement was

Table 1: Material properties.

Materials	Density, ρ (kg/m^3)	Cohesion, c (kPa)	Internal friction angle, φ (°)	Elastic modulus, E (MPa)	Poisson's ratio, μ
Pavement materials	2100	—	—	1200	0.35
Backfill soil	1800	15, 20, and 25	25 and 30	40, 60, 80, and 100	0.35
Silty clay	1750	14	22	45	0.4
Mud clay	1700	12	20	40	0.45

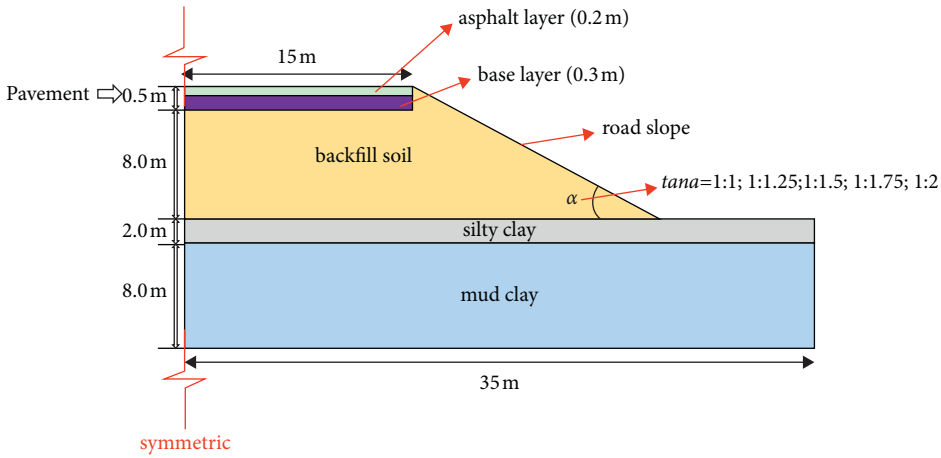

Figure 2: High-filled road with the backfill soil.

selected as 15 m according to the design of the conventional highway. The length of the foundation was determined as 35 m to support the subgrade by the backfill soil. The dimension of the FE model in the longitudinal direction can be regarded as infinite since only the 2D model was employed in this study. Under such conditions, the cross section of the road structure was regarded as the research object of the study, and the longitudinal length of the road structure was considered infinite [48].

3.3. Meshing and Element Selection. Figure 3 gives the FE meshing for different slopes used in the present study.

Element selection is the foundation for the FE analysis. For the same FE model, different calculation results can be obtained by using different elements. Regarding the FE model in the present study, the solid element was the optimized one to simulate one part of the whole model. Since a solid element can be connected to other elements through any of its surfaces, it can construct almost any shape and bear any load in the FE model.

To reduce the computations and improve the calculating accuracy, the 8-node plane-strain-reduced (CPE8R) element was adopted in the present FE simulation. It is a general plane strain element, in fact, a special plane stress element, which can be used to simulate a section of a very long structure, such as a dam. It is understood that the plate or shell element may be more efficient to solve the plane strain problem considering the high efficiency during the application. However, it should be noted that the research objective in the present study is about the subgrade and road pavement, which are not satisfying the premise of plate or shell theory. Therefore, the solid element, CPE8R, was employed in the present study. Also, it should be noted that the structure containing the plane strain element should be defined in the global X-Y plane, that is, for all nodes $z = 0$.

4. Parametric Studies

4.1. Effects of Slope Angle. The soil was defined by the Mohr–Coulomb model, which is the so-called rigid plastic model or Saint-Venant model. Regarding the Mohr–Coulomb model, when the stress of the soil is less than the yield stress, the soil will not deform, just like a rigid body. When the stress reaches the soil yield stress, the plastic deformation will increase until the soil failure occurs. Therefore, the equivalent plastic strain (PEEQ) should be evaluated first, considering the proposed models. Figure 4 gives the results of PEEQ when the slopes are 1 : 1, 1 : 1.25, 1 : 1.5, 1 : 1.75, and 1 : 2, respectively.

As shown in Figure 4, under the conditions of a given strength reduction coefficient, the calculation results obtained through the FE simulation can show the development of the equivalent plastic zone in the form of cloud diagrams. When the slopes were 1 : 5, 1 : 1.75, and 1 : 2, respectively, failure to achieve penetration or local yield failure indicates that the slope is stable under this reduction factor, while when the slopes equal 1 : 1.25 and 1 : 1, the plastic deformation between adjacent iteration steps at some nodes increases too much or the equivalent plastic strain reaches the yield limit. From the displayed results (Figure 4), the plastic zone has penetrated the top of the slope, and the equivalent plastic strain and displacement have an infinite development trend, with obvious sudden changes, indicating that the slope is already in a critical failure state at this time.

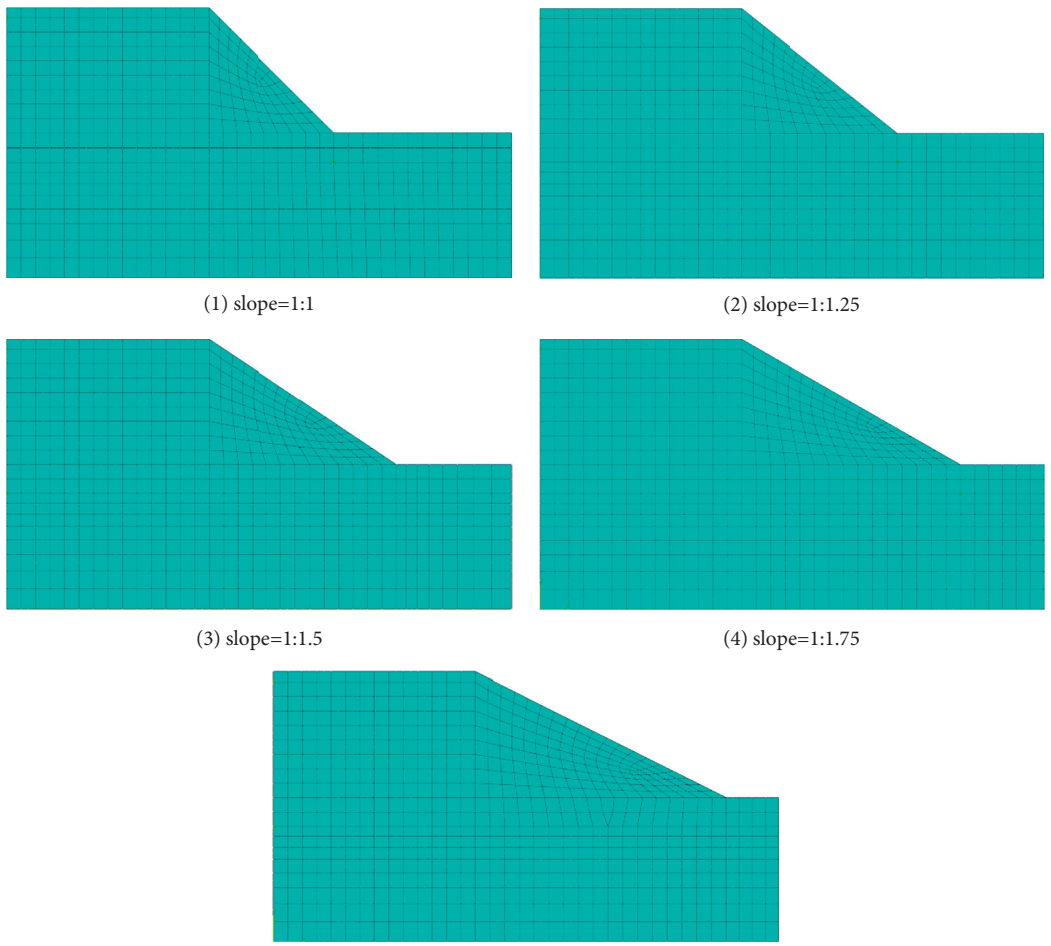

Figure 3: FEM meshes for the five types of slopes. (a) Slope = 1 : 1. (b) Slope = 1 : 1.25. (c) Slope = 1 : 1.5. (d) Slope = 1 : 1.75. (e) Slope = 1 : 2.

Also, it can be observed that when the slopes are 1 : 1, 1 : 1.25, 1 : 1.5, 1 : 1.75, and 1 : 2, the maximum PEEQ are 1.058*e*-2, 9.026*e*-3, 8.999*e*-3, 6.556*e*-3, and 6.807*e*-3. Basically, as the slope decreases, the maximum PEEQ decreases, as shown in Figure 4. It can be indicated that reducing the slope can improve the stability of the road slope. Also, it can be observed that when the slope is lower than 1 : 1.75, the maximum PEEQ tends to converge.

4.2. Effects of Cohesion and Internal Friction Angle. It can be observed that, as the cohesion equals 15 kPa, the maximum PEEQ for internal friction angles 25° and 30° are 1.058×10^{-2} and 1.022×10^{-2}, respectively. A higher internal friction angle can increase the value of maximum PEEQ. As the cohesion equals 20 kPa, the maximum PEEQ when the internal friction angles equal 25° and 30° are 1.019×10^{-2} and 1.023×10^{-2}, respectively. However, as the cohesion increases to 30 kPa, the maximum PEEQ when the internal friction angles equal 25° and 30° are still 1.019×10^{-2} and 1.023×10^{-2}, respectively. This means that, as the internal friction angles equal 25° and 30°, even the cohesion increases, and the maximum PEEQ will remain the same.

Also, it can be observed that when the internal friction angle equals 25°, the maximum PEEQ when the cohesions equal 15 kPa, 20 kPa, and 30 kPa are $1.058e^{-2}$, $1.019e^{-2}$, and $1.019e^{-2}$, respectively. The result proves that 20 kPa is the split point of the maximum PEEQ. When the internal friction angle equals 30°, the maximum PEEQ when the cohesions equal 15 kPa, 20 kPa, and 30 kPa are 1.022*e*-2, 1.023*e*-2, and 1.023*e*-2, respectively. This result can also prove that 20 kPa is the split point of the maximum PEEQ. It can further be observed that the increase rate of the maximum PEEQ between 15 kPa and 20 kPa is very small (about 0.1%). Therefore, it can conclude that higher cohesion and internal friction angle can decrease the maximum PEEQ, but when the cohesion or internal friction angle is higher than one constant value, the maximum PEEQ will remain the same.

The cohesive force of the backfill has a great influence on the overall stability of the slope. With the increase of the cohesion of the backfill, the safety and stability factor also greatly increases, indicating that when the cohesive force of the subgrade soil is high, the stability of the roadbed slope is also high. It can be seen from Figure 5 that the cohesion is increased by 5 kPa, and the stability coefficient can be

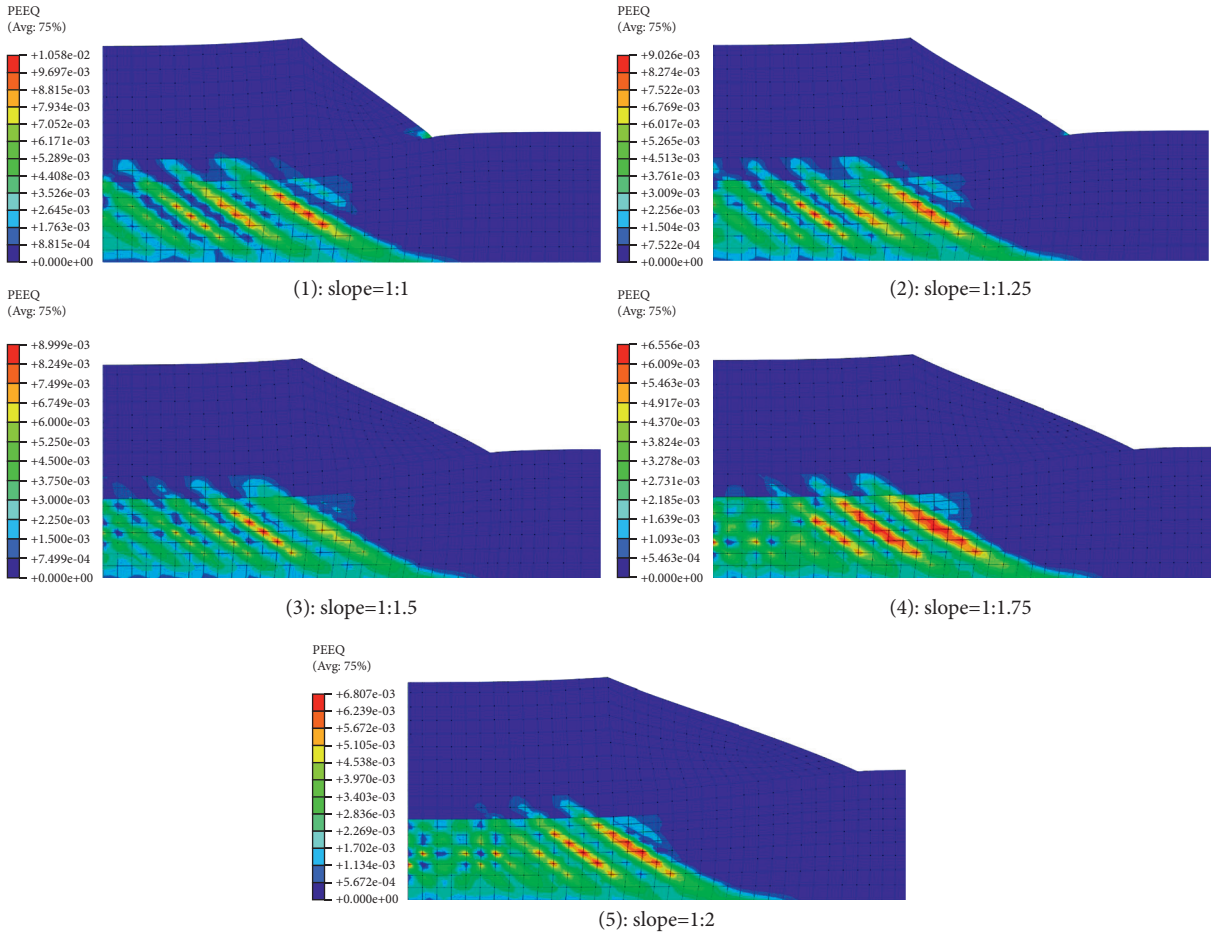

Figure 4: Effects of road slopes on PEEQ. (a) Slope = 1 : 1. (b) Slope = 1 : 1.25. (c) Slope = 1 : 1.5. (d) Slope = 1 : 1.75. (e) Slope = 1 : 2.

increased by about 10%. When the cohesion is large, the contribution to the safety and stability coefficient gradually decreases. It can also be seen that if the backfill material with greater cohesion is selected, the stability of the roadbed slope can be significantly improved. The safety and stability factor remains unchanged as the cohesive force of the weak foundation changes. The main reason may be related to the high fill height of the roadbed. Because when the height of the roadbed is large, the additional stress generated by the external load has a limited range, that is, the working area of the roadbed does not penetrate deep into the soil foundation, the influence of the change of the soil foundation material parameters on the results can be almost ignored. Through the above analysis, we can know the importance of subgrade soil cohesion in highway engineering, and foundation cohesion has little effect on stability.

4.3. Effects of Elastic Modulus. According to the strength reduction theory, when the finite element calculation does not converge due to the reduction of strength parameters, the slope shear failure occurs. Therefore, the reduction coefficient of the strength parameter corresponding to the last convergence calculation can be defined as the safety coefficient of the slope. Based on this determination criterion, Figure 6 gives the relationship between the elastic modulus and safety coefficient when the cohesion and internal friction angle equal 15 kPa and 25°, respectively.

It can be found from Figure 6 that the elastic modulus of the backfill soil has little effect on the safety and stability coefficient of the slope. In the case of a lower modulus of elasticity, the safety and stability coefficient of the slope is higher than that of the high modulus of elasticity. The possible reason is that the plastic expansion zone is generated, and when the elastic modulus of the subgrade that occupies most of the entire embankment is small, the overall settlement displacement of the structure increases, which causes the center of gravity of the plastic zone to decrease, which will reduce the sliding force. On the contrary, the safety and stability coefficient of the slope is increased, and this kind of situation cannot be attributed to the improvement of the safety and stability of the slope.

Figure 7 gives the safety coefficients of the road slope for varying cohesion and internal friction angle.

The slight effect of the elastic modulus on the safety coefficient of the road slope can also be found since the slope safety coefficients were almost the same for different elastic moduli. However, it should be noted that the slope safety coefficient was obviously improved when the internal friction angle increased from 25° to 30°. The internal friction angle is the representative of the internal friction of the soil,

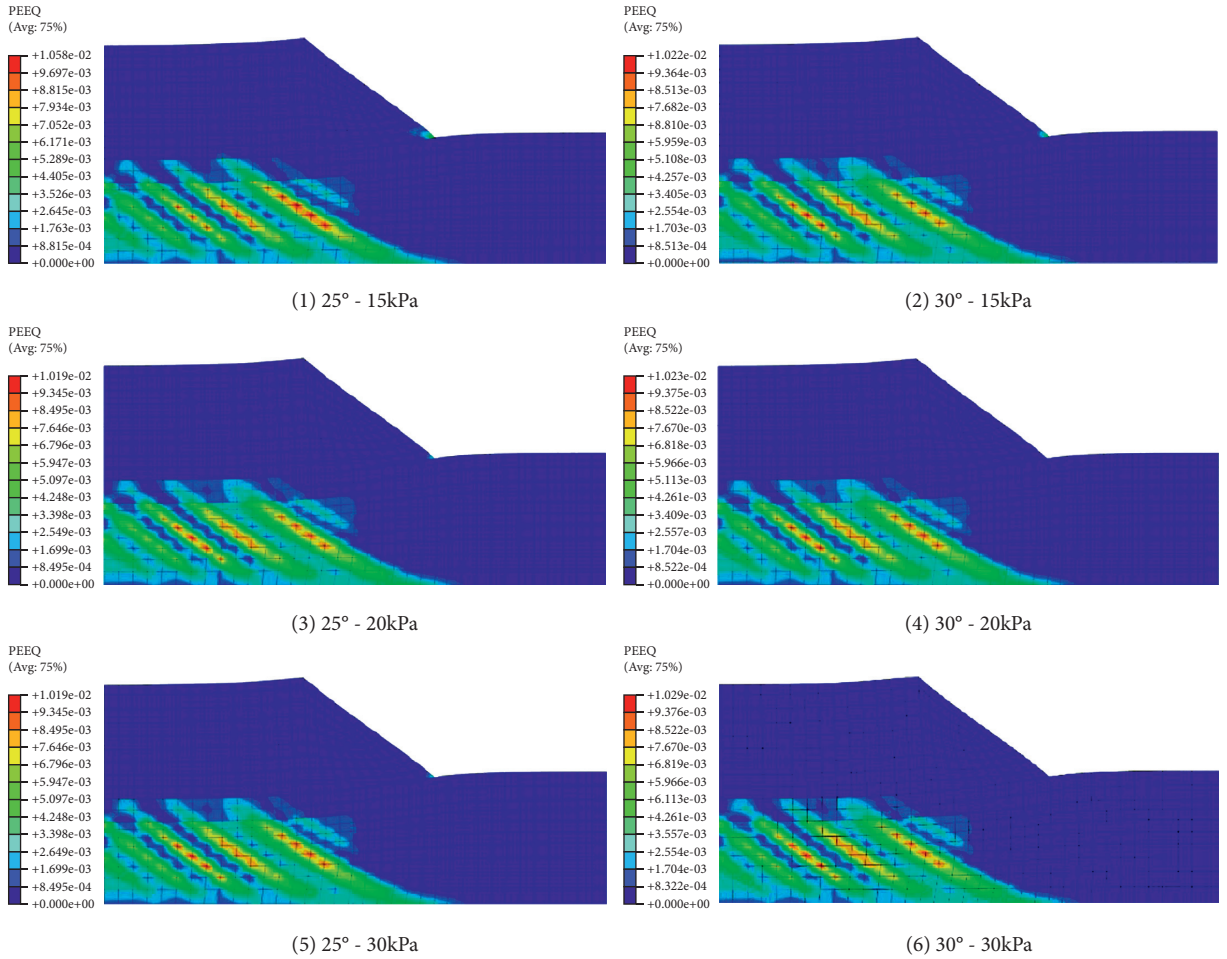

Figure 5: Effects of cohesion and internal friction angle. (a) 25°-15 kPa. (b) 30°-15 kPa. (c) 25°-20 kPa. (d) 30°-20 kPa. (e) 25°-30 kPa. (f) 30°-30 kPa.

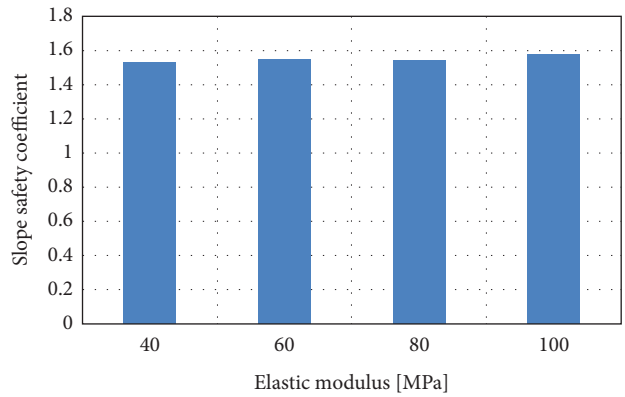

Figure 6: Relationship between the elastic modulus and safety coefficient ($c = 15$ kPa; $\varphi = 25°$).

which specifically includes the surface friction between the soil particles and the bite force generated by the interlocking action between the soil particles. The larger the internal friction angle, the greater the internal friction force, so as the internal friction angle increases, the maximum equivalent plastic strain value becomes smaller, resulting in a higher value of the slope safety factor.

Figure 8 gives the safety coefficients of the road slope when the cohesion was 15 kPa and 20 kPa, respectively.

A slight effect of the elastic modulus on the safety coefficient of the road slope can also be found because of the similar values of slope coefficients. Besides, the cohesion increased the values of the slope safety coefficient. Various physical and chemical forces between soil particles

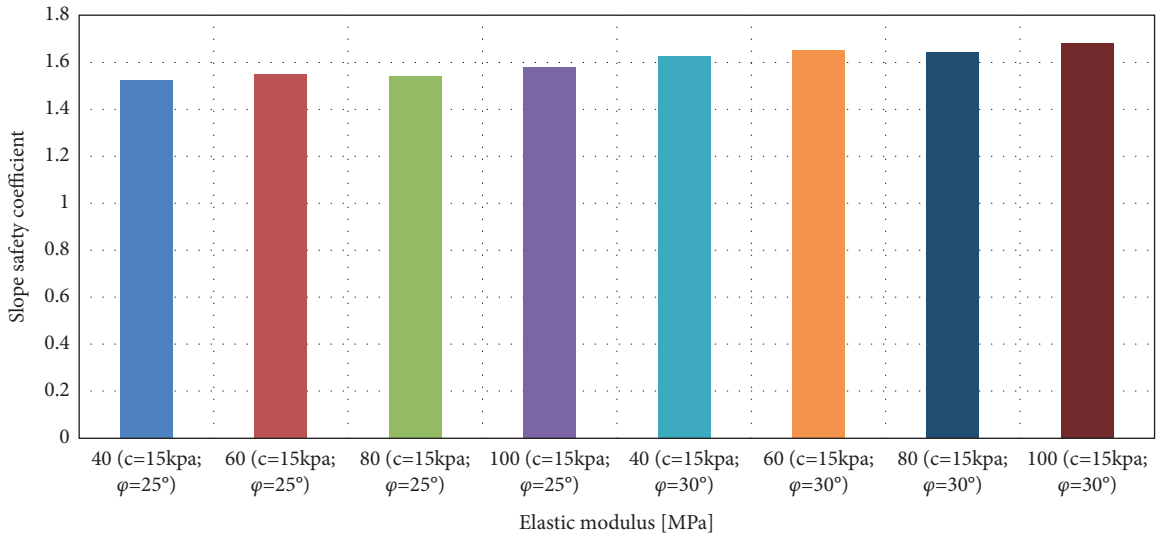

Figure 7: Safety coefficients of the road slope for varying cohesion and internal friction angle.

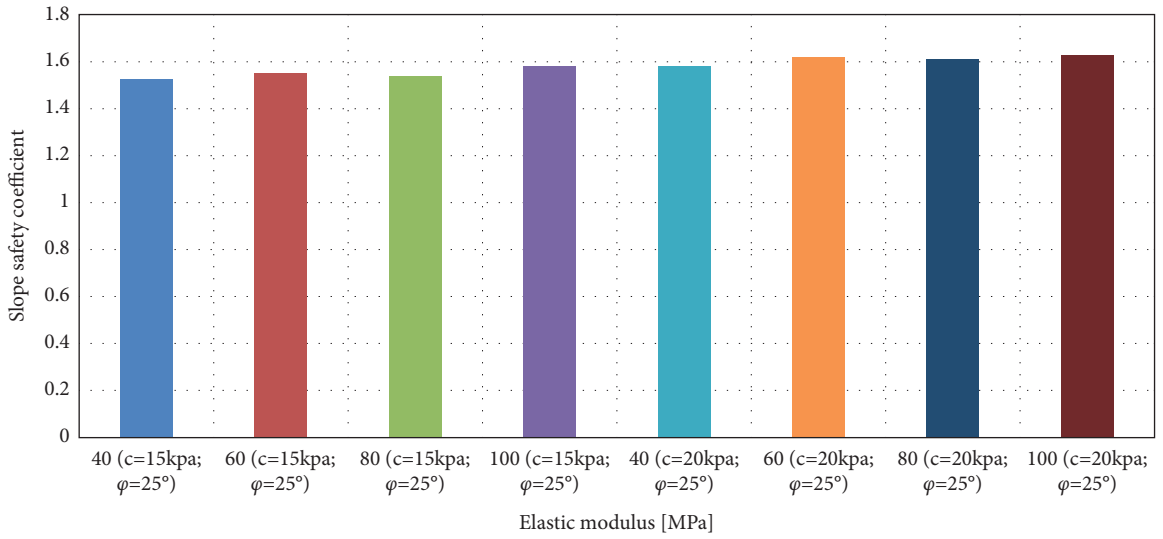

Figure 8: Safety coefficients of the road slope when the cohesion was 15 kPa and 20 kPa.

determine the value of soil cohesion, including Coulomb force, static force, van der Waals force, and cementation. The greater the cohesive force, the greater the suction force between the particles so that only when the external force is given greater pulling force can plastic strain occur, and the corresponding antisliding force is greater.

5. Conclusions

According to the current construction requirements of the process of backfilling the subgrade on the weak foundation, this paper conducted a FE analysis on the slope of this special engineering condition based on the commonly used strength reduction method in the stability analysis of the road slope. To accurately investigate the influence of slope and the mechanical properties of the soil on the stability of the backfill subgrade during the construction process, the slope stability model based on the strength reduction method is established in this study. At the same time, the influence analysis of the slope, cohesion, and internal friction angle on the slope stability was carried out. The research process can highlight the following conclusions:

(1) The slope stability analysis model established by the strength reduction method can characterize the stability of the slope by calculating the slope safety coefficient. In the analysis process, the mutation point of the relationship curve between the displacement generated in the slope and the reduction coefficient is used as the criterion.

(2) As the slopes were lower than 1 : 1.5, failure to achieve penetration or local yield failure indicates that the slope is stable under this reduction factor, while as the slopes were higher than 1 : 1.5, the plastic

zone has penetrated the top of the slope, and the equivalent plastic strain and displacement have an infinite development trend, indicating a critical failure state. As the slope decreases, the maximum PEEQ decreases; reducing the slope can improve the stability of the road slope. When the slope is lower than 1 : 1.75, the maximum PEEQ tends to converge. Higher values of internal friction angle and cohesion can increase the value of maximum PEEQ, but when the cohesion or internal friction angle is higher than one constant value, the maximum PEEQ will remain the same. The effects of the elastic modulus of the backfill soil on the safety and stability coefficient of the slope are slight.

Regarding future development, a more precise 3D FEM model should be proposed by considering the dimensional sizes in the longitudinal direction. The reasonable physical sizes of the FEM model should also be optimized and determined in the future. Comparison results between the 2D and 3D models should also be included to evaluate the accuracy and efficiency.

Data Availability

The data used to support the findings of this study are available from the corresponding author upon request.

Conflicts of Interest

The authors declare that they have no conflicts of interest to report regarding the present study.

Acknowledgments

This research was funded by the Faculty Start-up Grant of China University of Mining and Technology (Grant no. 102520282) and the Natural Science Foundation of Jiangsu Province (Grant no. BK20210513).

References

[1] A. W. Bishop, "The use of the slip circle in the stability analysis of slopes," *Géotechnique*, vol. 5, no. 1, pp. 7–17, 1955.

[2] Y. Sebsadji, S. Glaser, S. Mammar, and J. Dakhlallah, "Road slope and vehicle dynamics estimation," in *Proceedings of the 2008 American Control Conference*, June 2008.

[3] P. Lingman and B. Schmidtbauer, "Road slope and vehicle mass estimation using Kalman filtering," *Vehicle System Dynamics*, vol. 37, no. sup1, pp. 12–23, 2002.

[4] H. Ohnishi, J. Ishii, M. Kayano, and H. Katayama, "A study on road slope estimation for automatic transmission control," *JSAE Review*, vol. 21, no. 2, pp. 235–240, 2000.

[5] J. Huang, T. Duan, Y. Lei, and M. Hasanipanah, "Finite element modeling for the antivibration pavement used to improve the slope stability of the open-pit mine," *Shock and Vibration*, vol. 2020, Article ID 6650780, 11 pages, 2020.

[6] W. Shan, C. C. Zhang, and Y. Guo, "Mechanism of shallow slide on soil road cutting slope during spring in seasonal frozen region," *Applied Mechanics and Materials*, Trans Tech Publication, Bäch SZ, Switzerland, 2012.

[7] J. Huang, Y. Sun, and J. Zhang, "Reduction of computational error by optimizing SVR kernel coefficients to simulate concrete compressive strength through the use of a human learning optimization algorithm," *Engineering with Computers*, vol. 37, 2021.

[8] F. J. Swanson and C. T. Dyrness, "Impact of clear-cutting and road construction on soil erosion by landslides in the western Cascade Range, Oregon," *Geology*, vol. 3, no. 7, pp. 393–396, 1975.

[9] D. Tarchi, G. Antonello, N. Casagli, and P. Farina, *On the Use of Ground-Based SAR Interferometry for Slope Failure Early Warning: The Cortenova Rock Slide (Italy)*, pp. 337–342, Springer, New York USA, 2005.

[10] J. Huang, J. Zhang, J. Ren, and H. Chen, "Anti-rutting performance of the damping asphalt mixtures (DAMs) made with a high content of asphalt rubber (AR)," *Construction and Building Materials*, vol. 271, Article ID 121878, 2021.

[11] H. Luo, T. Zhao, M. Dong et al., "Field studies on the effects of three geotextiles on runoff and erosion of road slope in Beijing, China," *Catena*, vol. 109, pp. 150–156, 2013.

[12] J. L. Clayton, *Evaluating Slope Stability Prior To Road Construction*, Vol. 307, US Department of Agriculture, Forest Service, Intermountain Forest and Range, , Ogden, UT, USA, 1983.

[13] J. Huang, M. Losa, P. Leandri, S. G. Kumar, J. Zhang, and Y. Sun, "Potential anti-vibration pavements with damping layer: finite element (FE) modeling, validation, and parametrical studies," *Construction and Building Materials*, vol. 281, Article ID 122550, 2021.

[14] Z. Cai and X. Zheng, "A private and efficient mechanism for data uploading in smart cyber-physical systems," *IEEE Transactions on Network Science and Engineering*, vol. 7, no. 2, pp. 766–775, 2018.

[15] D. Nash, "A comparative review of limit equilibrium methods of stability analysis," *Slope stability*, pp. 11–75, 1987.

[16] W. Verhaeghe, W. Desmet, D. Vandepitte, and D. Moens, "Interval fields to represent uncertainty on the output side of a static FE analysis," *Computer Methods in Applied Mechanics and Engineering*, vol. 260, pp. 50–62, 2013.

[17] R. Ibrahim and C. Pettit, "Uncertainties and dynamic problems of bolted joints and other fasteners," *Journal of Sound and Vibration*, vol. 279, no. 3-5, pp. 857–936, 2005.

[18] G. S. Kumar and S. Suresha, "Evaluation of workability and mechanical properties of nonfoaming warm mix asphalt mixtures," *Advances in Civil Engineering Materials*, vol. 7, no. 1, pp. 132–157, 2018.

[19] P. W. Mayne, "Stress-strain-strength-flow parameters from enhanced in-situ tests," in *Proceedings of the International Conference On in Situ Measurement of Soil Properties and Case Histories*, Bali, Indonesia, May 2001.

[20] K. Senneset and N. Janbu, "Shear strength parameters obtained from static cone penetration tests," *Strength Testing of Marine Sediments: Laboratory and In-Situ Measurements*, ASTM International, West Conshohocken, PA, USA, 1985.

[21] S. M. Olson and T. D. Stark, "Yield strength ratio and liquefaction analysis of slopes and embankments," *Journal of Geotechnical and Geoenvironmental Engineering*, vol. 129, no. 8, pp. 727–737, 2003.

[22] J. Huang, T. Duan, Y. Zhang, J. Liu, J. Zhang, and Y. Lei, "Predicting the permeability of pervious concrete based on the beetle antennae search algorithm and random forest model," *Advances in Civil Engineering*, vol. 2020, Article ID 8863181, 11 pages, 2020.

[23] W. Wei, Y. M. Cheng, and L. Li, "Three-dimensional slope failure analysis by the strength reduction and limit equilibrium methods," *Computers and Geotechnics*, vol. 36, no. 1-2, pp. 70–80, 2009.

[24] M. Prokurov, A. Indykin, and A. Alekseytsev, "Increasing the reliability of the soil slopes design using evolutionary modelling," *MATEC Web of Conferences*, vol. 251, no. 3, Article ID 04017, 2018.

[25] J. T. Christian, C. C. Ladd, and G. B. Baecher, "Reliability applied to slope stability analysis," *Journal of Geotechnical Engineering*, vol. 120, no. 12, pp. 2180–2207, 1994.

[26] C. H. Juang, Y.-Y. Jhi, and D.-H. Lee, "Stability analysis of existing slopes considering uncertainty," *Engineering Geology*, vol. 49, no. 2, pp. 111–122, 1998.

[27] B. Yang, X. Li, Y. Hou et al., "Non-invasive (non-contact) measurements of human thermal physiology signals and thermal comfort/discomfort poses-a review," *Energy and Buildings*, vol. 224, Article ID 110261, 2020.

[28] S. Xie, Z. Yu, and Z. Lv, "Multi-disease prediction based on deep learning: a survey," *Computer Modeling in Engineering and Sciences*, vol. 127, no. 3, pp. 1–34, 2021.

[29] Z. Wan, Y. Dong, Z. Yu, H. Lv, and Z. Lv, "Semi-supervised support vector machine for digital twins based brain image fusion," *Frontiers in Neuroscience*, vol. 15, p. 802, 2021.

[30] Z. Lv, S. Zhang, and W. Xiu, "Solving the security problem of intelligent transportation system with deep learning," *IEEE Transactions on Intelligent Transportation Systems*, vol. 22, no. 7, pp. 1–10, 2020.

[31] Z. Lv, L. Qiao, K. Cai, and Q. Wang, "Big data analysis technology for electric vehicle networks in smart cities," *IEEE Transactions on Intelligent Transportation Systems*, vol. 22, no. 3, pp. 1–10, 2020.

[32] M. Jahanbakht, W. Xiang, L. Hanzo, and M. R. Azghadi, "Internet of underwater Things and big marine data analytics—a comprehensive survey," *IEEE Communications Surveys & Tutorials*, vol. 23, pp. 904–956, 2021.

[33] X. Cheng, B. Yang, A. Hedman, T. Olofsson, H. Li, and L. G. Van, "NIDL: a pilot study of contactless measurement of skin temperature for intelligent building," *Energy and Buildings*, vol. 198, pp. 340–352, 2019.

[34] Z. Cai and Z. He, "Trading private range counting over big IoT data," in *Proceedings of the 2019 IEEE 39th International Conference on Distributed Computing Systems (ICDCS)*, July 2019.

[35] M. Hudson, I. Idriss, and M. Beikae, *User's Manual for QUAD4M: A Computer Program to Evaluate the Seismic Response of Soil Structures Using Finite Element Procedures and Incorporating a Compliant Base*, University of California, Los Angeles, CA, USA, 1994.

[36] J. Huang, X. Li, J. Zhang, Y. Sun, and J. Ren, "Determining the Rayleigh damping parameters of flexible pavements for finite element modeling," *Journal of Vibration and Control*, vol. 27, 2021.

[37] J. Huang, T. Duan, Y. Sun, L. Wang, and Y. Lei, "Finite element (FE) modeling of indirect tension to cylindrical (ITCY) specimen test for damping asphalt mixtures (DAMs)," *Advances in Civil Engineering*, vol. 2020, Article ID 6694180, 11 pages, 2020.

[38] A. Hamim, N. I. M. Yusoff, H. Ceylan, S. A. P. Rosyidi, and A. El-Shafie, "Comparative study on using static and dynamic finite element models to develop FWD measurement on flexible pavement structures," *Construction and Building Materials*, vol. 176, pp. 583–592, 2018.

[39] O. E. Gungor, I. L. Al-Qadi, A. Gamez, and J. A. Hernandez, "In-situ validation of three-dimensional pavement finite element models," *The Roles of Accelerated Pavement Testing in Pavement Sustainability*, Springer, Berlin, Germany, pp. 145–159, 2016.

[40] J. Fu, J. Liu, X. Zhang, L. Lei, X. Ma, and Z. Liu, "Mesoscale experimental procedure and finite element analysis for an indirect tensile test of asphalt concrete," *Road Materials and Pavement Design*, vol. 19, no. 8, pp. 1904–1925, 2018.

[41] J. M. Duncan, "State of the art: limit equilibrium and finite-element analysis of slopes," *Journal of Geotechnical engineering*, vol. 122, no. 7, pp. 577–596, 1996.

[42] D. Deb and K. C. Das, "A new doubly enriched finite element for modelling grouted bolt crossed by rock joint," *International Journal of Rock Mechanics and Mining Sciences*, vol. 70, pp. 47–58, 2014.

[43] K.-J. Bathe, *Finite Element Procedures*, Klaus-Jurgen Bathe, Berlin, Germany, 2006.

[44] K. P. Aryal, "Slope stability evaluations by limit equilibrium and finite element methods," Norwegian University of Science and Technology, Trondheim, Norway, 2006.

[45] M. Ameri, M. Malakouti, and P. Malekzadeh, "Quasi-static analysis of multilayered domains with viscoelastic layer using incremental-layerwise finite element method," *Mechanics of Time-Dependent Materials*, vol. 18, no. 1, pp. 275–291, 2014.

[46] A. Ardah, M. Abu-Farsakh, and G. Voyiadjis, "Numerical evaluation of the performance of a geosynthetic reinforced soil-integrated bridge system (GRS-IBS) under different loading conditions," *Geotextiles and Geomembranes*, vol. 45, no. 6, pp. 558–569, 2017.

[47] G. You, M. A. Mandalawi, A. Soliman, and K. Dowling, "Finite element analysis of rock slope stability using shear strength reduction method," in *Proceedings of the International Congress and Exhibition Sustainable Civil Infrastructures: Innovative Infrastructure Geotechnology*, July 2017.

[48] H. L. Gongyun, *Application of Finite Element Software ABAQUS on Road Engineering*, Southeast University Press, Nanjing, China, 2008.

[49] Z. Yingren and Z. Shangyi, "Application of strength reduction FEM in soil and rock slope," *Chinese Journal of Rock Mechanics and Engineering*, vol. 19, p. 37, 2004.

[50] S. Y. Zhao, Y. R. Zheng, and Y. F. Zhang, "Study on slope failure criterion in strength reduction finite element method," *Rock and Soil Mechanics*, vol. 2, pp. 332–336, 2005.

[51] A. S. Genikomsou and M. A. Polak, "Finite element analysis of punching shear of concrete slabs using damaged plasticity model in ABAQUS," *Engineering Structures*, vol. 98, pp. 38–48, 2015.

[52] E. Duni, G. Monfrino, R. Saponaro et al., "Numerical simulation of full vehicle dynamic behaviour based on the interaction between ABAQUS/standard and explicit codes," in *Proceedings of the Abaqus Users' Conference*, Munich, Germany, June 2003.

[53] D. J. Robert, "A modified Mohr-Coulomb model to simulate the behavior of pipelines in unsaturated soils," *Computers and Geotechnics*, vol. 91, pp. 146–160, 2017.

[54] J. Clausen, L. Damkilde, and L. V. Andersen, "Robust and efficient handling of yield surface discontinuities in elasto-plastic finite element calculations," *Engineering Computations*, vol. 32, no. 6, 2015.

[55] D. A. Lockner and S. A. Stanchits, "Undrained poroelastic response of sandstones to deviatoric stress change," *Journal of Geophysical Research: Solid Earth*, vol. 107, no. B12, 2002.

[56] N. Changizi and G. P. Warn, "Stochastic stress-based topology optimization of structural frames based upon the second deviatoric stress invariant," *Engineering Structures*, vol. 224, Article ID 111186, 2020.

[57] J. Huang, P. Leandri, G. Cuciniello, and M. Losa, "Mix design and laboratory characterisation of rubberised mixture used as damping layer in pavements," *International Journal of Pavement Engineering*, vol. 22, pp. 1–15, 2021.

Hindawi
Advances in Civil Engineering
Volume 2021, Article ID 5432746, 18 pages
https://doi.org/10.1155/2021/5432746

Review Article

A Review of the Structural Fire Performance Testing Methods for Beam-to-Column Connections

Noor Azim Mohd. Radzi, Roszilah Hamid, Azrul A. Mutalib, and A. B. M. Amrul Kaish

Department of Civil Engineering, Faculty of Engineering and Built Environment, Universiti Kebangsaan Malaysia, 43600 UKM Bangi, Selangor D. E., Malaysia

Correspondence should be addressed to Roszilah Hamid; roszilah@ukm.edu.my

Received 12 August 2021; Revised 4 October 2021; Accepted 8 October 2021; Published 3 November 2021

Academic Editor: Wenjie Ge

The structural fire performance tests for beam-to-column connections are critical in determining their fire performance at high temperatures. The current standard fire testing methods provide the procedures for establishing the fire resistance of each construction element exposed to a standard fire. However, these methods cannot verify the fire behaviour of the connections between building elements. Researchers have performed numerous fire tests on beam-to-column connections despite the lack of structural fire performance testing methods. This paper presents a comprehensive literature review of the structural fire performance testing methods for beam-to-column connections. The major areas in this review are travelling fires, development of travelling fires on beam-to-column connections, fire testing considerations, fire testing criteria, recent fire testing, and loading applications. This paper identifies the key issues and challenges of the structural fire performance testing methods for beam-to-column connections. Finally, this paper provides recommendations and discusses the way forward for structural fire performance tests on beam-to-column connections.

1. Introduction and Objectives

Structural fires occur primarily in residential, commercial, or community-based buildings. Fire exposures could significantly reduce the strength, insulation, and integrity of a building's main structural elements [1, 2]. The beam-to-column connections are critical elements of any building structure [3, 4]. The collapse of the World Trade Centre and the results of the Cardington full-scale building fire tests in the United Kingdom demonstrate that beam-to-column connections are vulnerable during the heating and cooling phases of fire [5, 6]. Therefore, it is critical to ensure the connections fulfil the requirements for fire safety and durability [3, 7, 8].

Researchers are conducting structural fire performance tests on beam-to-column connections to determine their fire performance at high temperatures. The fire tests provide the critical thermal parameters for beam-to-column connections, including failure patterns, crack developments, moment-rotation-temperature curves, load-deflection curves, stress-strain curves, internal temperature distributions, residual strength, and physical damages [9]. The most widely used fire test specifications are ASTM E119 [10] and ISO 834 [11]. ASTM E119 specifies the test method for evaluating the duration building elements can contain a fire, retain the building's structural integrity, or exhibit both properties during a predetermined test exposure. ISO 834 specifies the test for determining the fire resistance of construction elements when exposed to standard fire conditions. However, the standard fire testing methods do not have the procedures for verifying the fire behaviour of connections between building elements [10, 11]. Instead, the fire tests focus on vertical building elements, such as walls, partitions and columns, and horizontal building elements, such as floors, roofs, beams, and girders. In addition, the fire tests do not consider the effects of horizontal and vertical travelling fires and only use the standard fire curves with uniform burning and homogenous temperature conditions.

Despite the lack of structural fire performance testing methods for beam-to-column connections, researchers have conducted numerous fire tests on rigid, semirigid and

pinned beam-to-column connections [12, 13]. Most large-scale fire tests involved steel and composite beam-to-column connections because of the greater fire risk of these connections than concrete materials. The large-scale tests demonstrated the performance on a realistic scale when subject to the actual conditions of applied thermal and static loadings to comply with the regulatory requirements [14]. However, there has been a shift to focus on large-scale nonstandard fire testing using real fire rather than the standard fire [15, 16]. The standard fire testing furnace is unrealistic for most real structures and fundamentally incapable of rationally simulating several essential and interrelated anticipated behaviours observed in actual building fires. The design of structural fire protection methods based on the standard fire tests of a single element does not account for the connection behaviour or the entire structure [17].

With the increasing conflicts in the standard fire testing methods for beam-to-column connections, researchers need to understand the critical elements in the fire tests. This paper presents a comprehensive literature review of the structural fire performance testing methods for beam-to-column connections. Figure 1 illustrates the framework of this review paper. In stage one of the literature review, the authors searched and screened the Web of Science and Scopus databases for the literature concerning building fires and fire testing of beam-to-column connections and defined the critical concept in building fires, including travelling fires and standard fires. The review includes the consideration in fire testing, namely, the time–temperature fire curves, testing methods, and cooling phase. In stage two, the authors reviewed and extracted the fire testing methods and data from previous studies and summarised the main criteria for fire testing of beam-to-column connections. In stage three, the authors identified the key issues and challenges in the structural fire performance testing methods for beam-to-column connections and analysed and synthesised the fire testing data. Finally, this paper provides the recommendations and presents the way forward for the structural fire performance tests of beam-to-column connections to help steer future research in structural fire engineering, particularly large-scale experimental research.

2. Fire Testing of Beam-to-Column Connections

2.1. Travelling Fires. In buildings with large, open compartments, the fire does not burn simultaneously throughout the entire floor plate of the structure. Instead, the fire tends to travel horizontally and vertically as the flames spread by igniting the fuel in their path and burning a limited area at any one time [18, 19]. This condition, known as travelling fires, is different from the commonly used fire scenarios for the structural design of modern buildings. The traditional methods assume uniform burning and homogenous temperature conditions throughout a compartment, regardless of its size [20, 21]. In addition, the methods for validating the parameters and standard fires using small fire compartments, better known as "black boxes," reduce the accuracy of the predicted structural fire behaviour [22].

Stern-Gottfried et al. [20] introduced the pioneering method for estimating the temperature of compartment travelling fires. The large firecell method (LFM) [23] developed in 1996 employs specific fire models to determine the temperature–time relationships for travelling fires through a firecell. However, LFM is primarily a research tool used for single element checks in a design. The travelling fires methodology (TFM) [24, 25], developed in 2012, calculates the fire-induced thermal field such that it is physically based, is compatible with the subsequent structural analysis, and accounts for the fire dynamics. This method uses two temperature fields to represent the gas temperature in a compartment. The near field (T_{nf}) is the high temperature in the flaming region of the fire that is exposed directly to the flames. The far field (T_{ff}) is the cooler temperature for the smoke in the rest of the compartment, which is exposed to hot combustion gases but experiences less intense heating than from the flames. TFM is effective in providing a flexible technique with an extensive range of possible fires in any compartment. In 2015, Rackauskaite et al. [21] developed the improved TFM (iTFM) for studying the effect of nonuniform heating associated with the travelling fires by investigating the peak temperature location along the fire path. They found that the peak temperature in the compartment occurs primarily towards the end of the fire path. However, Dai et al. [19] stated that, despite the experimental and theoretical works carried out during the past twenty years, more practical large-scale travelling fires experiments are required to expand the knowledge on travelling fires.

The structural response of travelling fires has a significant impact on structural performance. Bailey et al. [26] found that progressive horizontal spreading fire enhanced some of the distortions caused by the fire compared with simultaneous burning across the same compartment range. Ellobody and Bailey [27] found that horizontally travelling fires influence time-deflection behaviour. Law et al. [18] observed that the most severe structural response caused by horizontal travelling fires is approximately 25% of the floor plate in size. Roben et al. [28] found that the interfloor time delay influenced the structural behaviour in the vertical travelling fires that involve large and multiple floors. They recommended considering several rates of spread and ensuring the structural integrity for each rate to identify a worst-case rate of vertical fire spread. Behnam [29] found that structures exposed to nonuniform fires are more susceptible to failure than those exposed to uniform fires. The fire resistance of structures towards travelling fires is 91 minutes compared with the 140-minute resistance towards uniform temperature. Behnam and Ronagh [30] recommended implementing more provisions in the codes for postfire structure and the appropriate rate of vertical spread of fire between floors. Further, Jiang et al. [31] demonstrated that slow fires could cause partial collapse, whereas fast travelling fires could cause global collapse. The travelling speed has a considerable impact on the failure sequence of columns, damage range, and collapse mode of the structures.

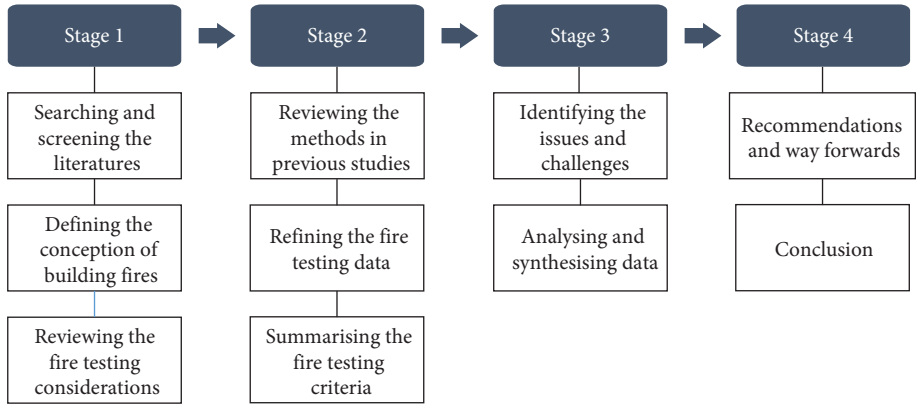

Figure 1: Framework of the review paper.

2.2. Development of Travelling Fires on Beam-to-Column Connections. Figure 2 shows the temperature development due to localised horizontal and vertical travelling fires for pinned concrete beam-to-column connections. Figure 2(a) shows the flame spread by igniting the fuel and burning the middle of the lower floor. Point A is the near field with the highest temperature, while point B is the far field with a cooler temperature. Once the local fuel is completely burnt, the near field travels horizontally to a new area from point A to B. Figure 2(b) shows the near field for the beam-to-column connection (point B) exposed to the highest temperature. The fire continues to burn at the same rate until all the fuel is burnt. At this time, the local fuel at point A is completely burnt and the structure begins to cool, and the fire damage sustained by the structure, such as deflection, crack, and spalling, becomes apparent. The fire travels vertically to the upper floor from point B to C through a damaged structural joint, unprotected service ducts, combustible façade materials, and unprotected openings, such as non-fire-rated windows. The flame movement increases the temperature at the top, creating the far field. Figure 2(c) shows a similar process, where point C is the near field exposed to the highest temperature. The near field travels horizontally to the middle of the upper floor. The local fuel at point B burns out, and the structure begins to cool.

Figure 2(d) shows the temperature-time curves for points A, B, and C during the fire. Vertical travelling fires spread for a longer duration than horizontal travelling fires due to structural constraints. According to Law et al. [18], the maximum temperature in the near field region is between 800 and 1000°C for a small fire and 1200°C for larger enclosure fires. They chose the 1200°C maximum value to represent the worst-case scenario of the fire. The maximum temperature of the near field region was calculated using the simple ceiling jet correlation developed by Alpert [32]:

$$T_{\max} - T_{\infty} = \frac{5.38\,(\dot{Q}/r)^{2/3}}{H}, \tag{1}$$

where $T_{\max}$ is the maximum temperature within the ceiling jet (°C), T∞ is the ambient temperature (°C), $\dot{Q}$ is the heat release rate (kW), r is the distance from the centre of the fire (m), and H is the floor to ceiling height (m). Clifton [23] stated that the temperatures for the preheating and delayed cooling (after the burnout) periods, which is exposed to hot combustion gases but experiences less intense heating than from the flames, was taken to be between 200 and 675°C. Subsequently, the preheating and delayed cooling periods changed to the temperature between 400 and 800°C. The far field temperature was calculated using the following:

$$T_{ff} = \frac{\left[\int_{r_{nf}}^{r_{ff}} (T_{\max})^4 \mathrm{d}r\right]^{1/4}}{\left(r_{ff} - r_{nf}\right)^{1/4}}, \tag{2}$$

where T_{ff} is the far field temperature (°C), r_{nf} is the distance between the end of the near field (m), r_{ff} is the distance between the end of the far field (m), and r is the distance from the centre of the fire (m). The temperature fields calculated at points A, B, and C are applied to both concrete and steel structures through heat transfer analyses. These analyses consider the temperature of steel rebar within concrete or steel beams to determine structural performance.

2.3. Fire Testing Considerations. Even though building fires are horizontal and vertical travelling fires, most fire tests on beam-to-column connections employed the standard time-temperature fire curves as a reference. Figure 3 shows a comparison of the real fire time-temperature curves and the standard time-temperature fire curves. The real fire time-temperature curves have three phases, growth, burning (flashover and fully developed), and decay (cooling) [34, 35]. The most widely employed time-temperature curve for real fire exposure is the "Swedish" fire curve representing different natural fire environments [34, 36]. Real fires begin with the burning of one item, and the fire gradually spreads to other nearby objects and grows in size and intensity [36]. The standard time-temperature fire curves (Figure 3) are developed in growth and burning stages continuously over time. The ASTM E119 and ISO 834 practices are similar for building fires. Both fire curves are dependent on the burning rate of the materials present in the building materials and contents. They represent a severe fire expected in a typical building environment but does not represent all potential fire scenarios. Even though there are many studies on the

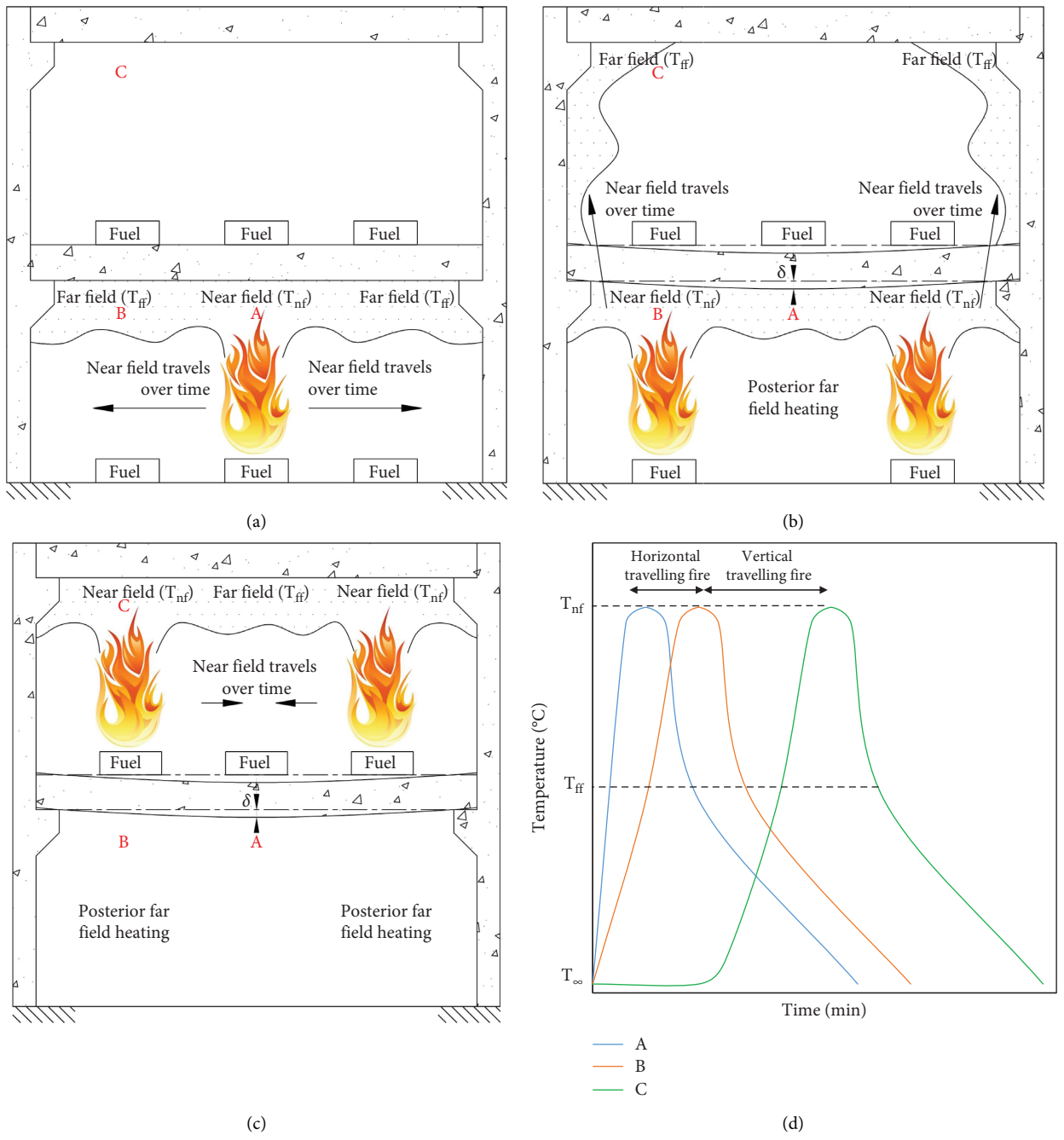

FIGURE 2: Temperature development due to localised travelling fire: (a) horizontal, (b) vertical, (c) horizontal, and (d) temperature-time curves at A, B, and C.

heating phase of a building fire, the effects of the cooling phase on structures are not well-understood [33]. Structural vulnerability increases during the cooling phase [37].

In addition to selecting the appropriate fire curve, researchers considered several factors to address the lack of structural fire performance testing methods for beam-to-column connections. Researchers need to understand the purpose of connection testing. The connection testing performed at ambient temperature sought to determine the joint bending moment-rotation characteristics since the bending moment is the primary action acting on the joints. During fire exposure, the connection testing sought to determine the combination of axial force, shear force, and bending moment that vary throughout the fire exposure. The researchers then selected the time-temperature fire curves for the fire tests and the load condition based on the specified fire exposure period. Finally, they compared the postfire results against the required performance criteria for the beam and column elements. In all assessments of structural fire resistance, the temperature developments in a structure should be determined, followed by evaluating the structural behaviour at elevated temperatures [38].

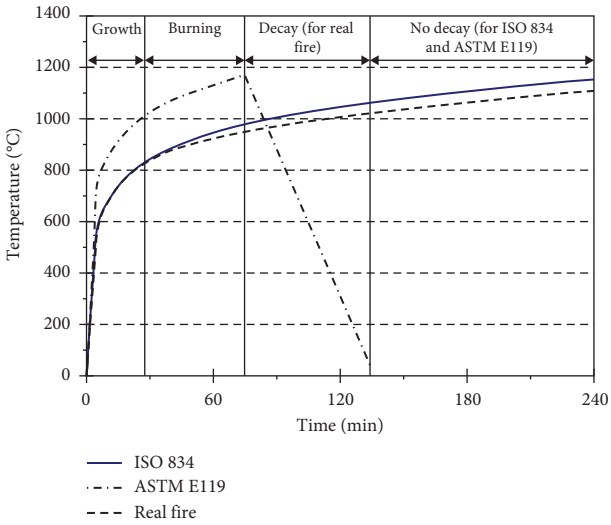

Figure 3: A comparison of real fire time-temperature curve with standard time-temperature fire curve (ASTM E119 and ISO 834) [34].

2.4. Fire Testing Criteria. Figure 4 summarises the fire testing criteria for beam-to-column connections from the test objective and performance criteria adopted in previous studies. Criteria 1 to 7 are the materials, type of connection, method of connection, boundary condition (constraints), fire source, type of analysis, and load application. The beam and column specimens are concrete, steel, composite, or timber. The beam-to-column connections are rigid, semirigid, or pinned, depending on the connection stiffness. The beam and column elements were assembled using either a wet, dry, or semidry method, and the boundary condition (constraints) for support is a roller, pin, or fixed end. The fire source for producing the heat is an electrical furnace, gas burner, and flexible ceramic pad. Most previous research analysed fire exposure together with static or cyclic load. The load applied in the different stages are preloading, concurrent loading (during the fire tests), and postfire loading.

2.5. Recent Fire Tests. Table 1 summarises the outcomes of the fire tests on beam-to-column connections conducted from 2007 to the present using the seven fire test criteria listed in Figure 4. More than 50% of the articles on the beam-to-column connections fire tests were published in the last five years, suggesting that researchers focused on this area of research.

Concerning Criteria 1, researchers have performed many fire tests on the beam-to-column connections fabricated from steel and composite materials due to the greater fire risk of these connections than those from concrete materials (Table 1). Steel and composite materials experience catenary action that may fracture the connections and exert additional forces on the columns at very high temperatures [47]. Among the mode of failure observed in the fire tests on steel and composite materials is the yielding of the endplate, yielding of the column flange, bolt (thread) stripping, bolt fracture, fracture of the endplate and slab cracking, and pulling out of the shear studs for composite connections. However, the literature showed that concrete connections also have a high fire risk [12]. The researchers observed that the concrete connections in the structures damaged in the fire tests could resist significant moments even at large deformations. Besides, the growing use of engineered timber structures in the design of high-rise buildings (more than five-storey high) presents fundamental challenges for structural fire-safe design [48, 49]. The fire behaviour of the connections often limits the fire performance of heavy timber structural systems. The improved fire performance of dowelled timber connections could significantly improve the fire performance of whole timber structures [50, 51].

Criteria 2 classifies the connections with low stiffness as pinned, and those with high stiffness are fixed or rigid connections (Table 1). The connections with partial strength and have a certain degree of rotational stiffness are classified as semirigid. The columns are stronger than the beams and the connections and act as elastic restraints during the fire tests, where the failures are dependent on the beams or connections [38–40]. For the concrete connections, the tension reinforcement at the support is carried through to the connections and effectively overlapped [42]. Precast concrete connections, such as corbel and hybrid, are semirigid connections [46].

Concerning Criteria 3, most steel connections were assembled using the dry method, and the composite and concrete connections were assembled using the wet method (Table 1). For precast concretes, a combination of dry and wet methods is considered a semidry method. Wet-assembled partially precast structures were designed to emulate cast-in-situ concrete structures with rigid connections through the cast-in-place concrete pouring of the joints. In addition, the use of mechanical devices such as bolts and welds to connect the dry-assembled structures avoids the need for in-situ concrete pouring.

Regarding Criteria 4, the thermal behaviour of the connection is influenced by the boundary conditions (constraints) of the beam and column (Table 1). The fire is treated as a thermal boundary condition when focusing on structural performance [52]. The structural model of a fire test can be assigned as a partial element, single element, subframe assembly, transiently simulated restrained assembly, and full-scale structure [53]. The simply supported and cantilever setups are most often adopted boundary conditions for the beam constraints. In the simply supported setup, the beam midsection was fixed in the axial direction, which effectively prevents rotation about the two principal axes of the beam cross section but allows the beam to twist about its longitudinal axis [43]. However, the members in a framed structure behave differently from the isolated members simply supported at both ends because the structural continuity imposes a finite amount of restraint to the end of any connected member [39]. In the cantilever setup, also known as subassemblies, the ends of the beam are free. According to Raouffard and Nishiyama [1], the degree of structural indeterminacy of the test specimens is reduced by removing the midsection of the beam and turning it into

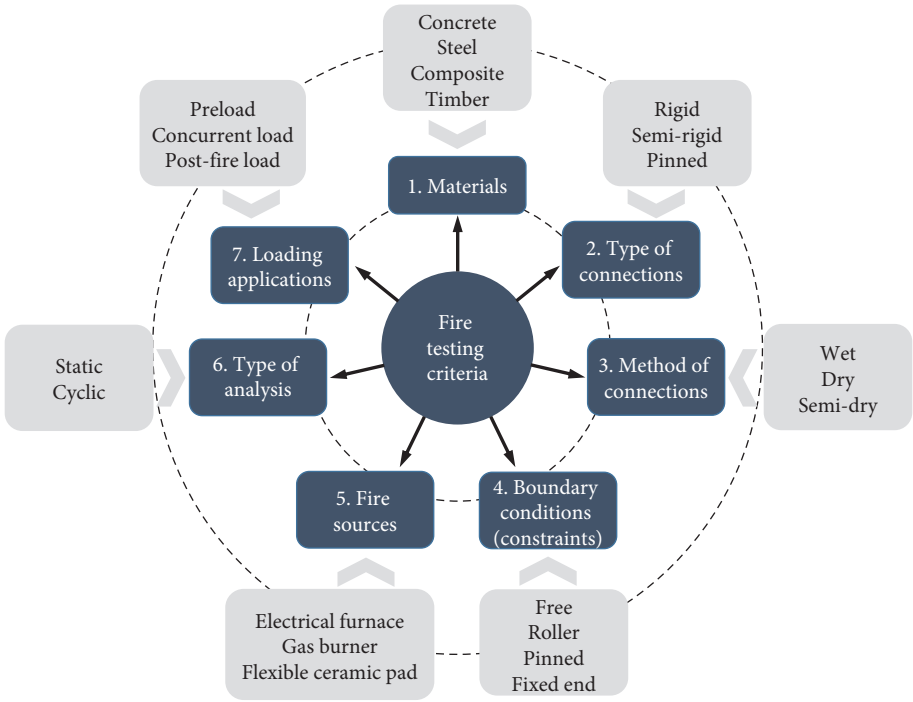

Figure 4: The fire testing criteria for beam-to-column connections.

two separate cantilever beams. For the column constraints, most of the top and bottom ends are restrained from lateral movement to ensure a good distribution of the axial column load and provide axial restraint to the beam [38]. As a result, the end of the column is free to move in the longitudinal direction. Another boundary condition is where both ends of the column are hinged, with an axial compressive load applied on the top [54].

For Criteria 5, most fire tests use a standard furnace to simulate the fire exposure (Table 1). Most research adopted the ISO 834 and ASTM E119 fire curves using a furnace. The loading points are outside the furnace. The items installed in the furnace such as the steel bar (to prevent the loading jacks from sliding towards each other) [38, 41], the top flange of the steel beam [38, 40], the sides and top of the reinforced concrete (RC) slab, and the upper part of the square concrete-filled steel tube (CFST) column were wrapped with a layer of ceramic fibre blanket before igniting the furnace.

Table 1 shows that, for Criteria 6, most analyses of the structural fire performance tests for beam-to-column connections used static load instead of cyclic load. Researchers have performed many static loading tests to investigate the progressive collapse resistance of RC moment frames during a fire [55]. Researchers also analysed reverse cyclic loadings to evaluate seismic behaviours with fire effects.

It is worth noting that Table 1 shows significant inconsistencies for Criteria 7. The load was applied either in the preloading (structural response at ambient conditions), concurrent loading (thermo-mechanical response during fire exposure), or postfire loading (residual response after cooling down) stage, or a combination of these stages. The following section will describe the loading application criteria in detail.

2.6. Load Applications. Two types of loading were used to simulate the maximum load condition following ASTM E119 and ISO 834 [10, 11]. ASTM E119 uses the superimposed load, while ISO 834 uses the service load. The loads are defined differently. Service load is the maximum load intensity expected during the life span of the structure. It is a combination of unfactored dead load and unfactored live load. Superimposed load, also known as superimposed dead load, considers the weight of the nonstructural and semipermanent members, including the facade members, floor cover, suspended ceiling, and ductwork. It does not take into account the live load and thus is less than the service load. However, ASTM E119 states that superimposed loads can consider the maximum load condition allowed under each nationally recognised structural design criteria.

Figure 5 presents a summary of the load application and performance criteria during the beam-to-column connections fire tests. The figure shows the ambient, growth and burning, and decay phases. In the ambient phase, the specimens were preloaded with a load equal to the initial crack load or loaded based on the load ratio before carrying out the fire tests. In the growth and burning phase, the load was applied to the specimens either constantly or gradually. The constant load is the superimposed or service load stated in the ASTM E119 and ISO 834, while the gradual load is the incremental load applied to the specimens until they fail. The load application criteria were based on the research objectives. Table 2 shows that investigation of thermal behaviour, thermal interaction and strength reduction requires applying a constant load to the specimens and terminating the test at the performance criteria limit. Table 3 shows that determination of failure load and maximum deformation (deflection, expansion, or contraction) requires applying

Table 1: Previous tests on beam-to-column connections at high temperatures following the fire testing criteria.

Authors, year, and ref. no.	1. Materials	2. Type of connection	3. Methods of connection	4. Boundary conditions		5. Fire sources		6. Type of analysis	7. Loading applications		
				Beam	Column	Method	Fire curve		Preload	Concurrent load	Postfire load
Ding and Wang (2007) [38]	Steel	Semirigid	Dry	Pinned[a]	Lateral movement restrained	Furnace	ISO 834	Static	✓	✓	—
Han et al. (2010) [39]	Composite	Rigid	Wet	Pinned[a]	Top = pinned, bottom = fixed end	Furnace	ISO 834	Static	✓	✓	—
Ding and Wang (2009) [40]	Steel	Semirigid	Dry	Pinned[a]	Lateral movement restrained	Furnace	ISO 834	Static	✓	✓	—
Wang et al. (2011) [41]	Steel	Pinned	Dry	Pinned[a]	Lateral movement restrained	Furnace	ISO 834	Static	—	✓	—
Song et al. (2015) [42]	Composite	Rigid	Wet	Free[b]	Top = rotation and horizontal restrained, bottom = fixed end	Furnace	ISO 834	Static	✓	✓	✓
Yahyai and Rezaeian (2016) [43]	Steel	Semi-rigid	Dry	Fixed end[a]	Fixed end	Furnace	ISO 834	Static	✓	✓	—
Heiza et al. (2016) [45]	Concrete	Rigid	Wet	Free[b]	Fixed end	Furnace	ASTM E119	Cyclic	✓	✓	✓
Raouffard and Nishiyama (2017) [1]	Concrete	Rigid	Wet	Free[b]	Fixed end	Furnace	ISO 834	Static	✓	✓	—
Yang and Fu (2019) [56]	Composite	Rigid	Wet	Free[b]	Top = lateral movement restrained; bottom = pinned	Furnace	ISO 834	Static	—	✓	—
Teja et al. (2019) [46]	Concrete	Semirigid	Semidry	Free[b]	Fixed end	Gas burner	400 °C	Static	—	✓	—

[a]Simply supported setup. [b]Cantilever setup.

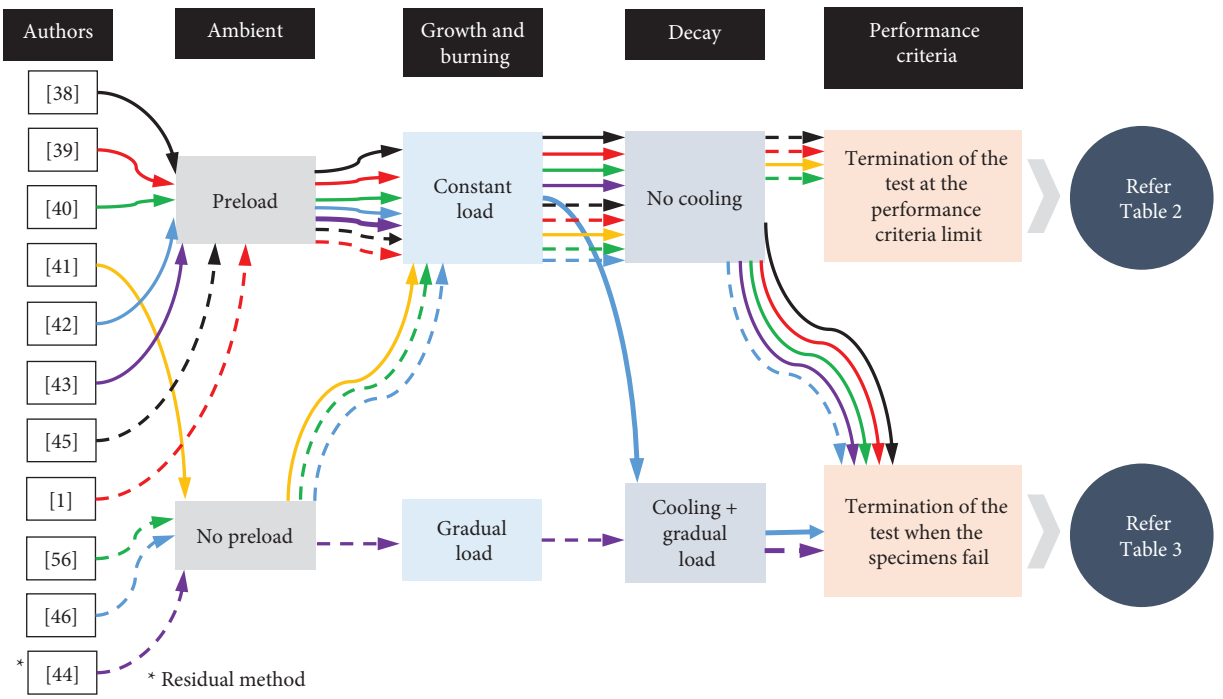

Figure 5: The load application and performance criteria for fire tests on beam-to-column connections.

Table 2: Studies that terminated the fire tests at performance criteria limit.

Author, year, and ref. no.	Objectives	Beam span/length (mm)	Load applications	Performance criteria
Wang et al. (2011) [41]	Investigate the relative behaviour and robustness of different types of steel connection in steel-framed structures in fire	1980	A constant load 40 kN was applied to the steel in each hydraulic loading Jack, which corresponds to a load ratio of 0.5 in the beam	Specimens sustained the applied load during fire classification period. The test beams were able to experience very large deflections (span/8~span/6) without fracture
Heiza et al. (2016) [44]	Investigate the structural behaviour and strength reduction of RC beam-to-column connections exposed to fire under cyclic loading	1050	Preloaded with 15 cycle of load (less than initial crack load) fire tests under loading equal to initial crack load for 1 or 2 hours	Specimens sustained the applied load during fire classification period with concrete spalling and cracking
Raouffard and Nishiyama (2017) [1]	Investigate the mechanical and thermal interactions structural response of RC beam-to-column subassemblies under no lateral thermally induced thrust and no moment redistribution influence	1000	Preloaded until first crack vertical load (17.3 kN) constant	The fire tests terminated after 74 min as soon as the tensile longitudinal steel bars of the upward-loaded cantilever beam attained the predefined critical temperature 530°C
Yang and Fu (2019) [45]	Investigate the experimental and numerical simulation of steel beam to CFST column composite connections with RC slabs	2650	Load ratio (0.1 to 0.35) and constant	The tests ceased when the connection specimens achieved fire resistance when the deformation or deformation rate of the square CFST column or steel beam meet the ultimate conditions specified in the ISO 834. The failure patterns of the connection include tube buckling, flange buckling, and separation

Table 3: Studies that terminated the fire tests when the specimens failed.

Author, year, and ref. no.	Objectives	Beam span/length (mm)	Load applications	Performance criteria
Ding and Wang (2007) [38]	Present the experimental results of structural fire behaviour of CFT column, including failure modes, development of forces, and deflections in the beams	2000	Preloaded with nominal load ratio (0.25 to 0.5 or 30 to 60 kN) and constant	The heating continued until structural failure and termination of the tests; the heating stopped when the beam reach catenary action and forced cooling to the ambient temperature
Han et al. (2010) [39]	Presented the behaviour of RC beam to CFST column planar frames, including the deformations and failures of the test specimens	2325	Preloaded (19.5 to 39 kN) and constant	The fire tests were stopped immediately when the tested specimens could not withstand the loads applied on the CFST columns and RC beam
Ding and Wang (2009) [40]	Investigate structural behaviour under cooling phase	2000	Fire exposure for self-weight load for 30 min	The heating and loading continue until the connection fail; the test assemblies were heated to temperatures close to the failure temperatures and then cooled down while still maintaining the applied loads on the beams
Song et al. (2015) [42]	Present the test results on the mechanical behaviour of SRC joints during the heating and cooling phases	3700	Preloaded and constant during heating and cooling phase	In postfire loading phase, the column load was kept constant, and the beam loads increased gradually until the connection failure
Yahyai and Rezaeian (2016) [43]	Investigate the behaviour of beam and splice connections in column-tree MRF at elevated temperatures	3980	Preloaded (load ratio 0.7 or 20.6 kN) and constant	The heating and loading continue until the connection fail
Teja et al. (2019) [46]	Study the performance of the three different beam column connections in precast structures exposed to fire and axial load	670	Vertical load (7 to 17 kN) constant	The heating and loading continues until specimens fail

gradual load to the specimens and terminating the test after specimen failure. The residual method simulates the typical idealised column removal scenarios (with and without the cooling effect). The specimens were exposed to fire and then subjected to gradual loading until failure [44].

Table 2 lists the studies that terminated the fire tests at the performance criteria limit. Wang et al. [41] investigated the relative behaviour and robustness of different steel connections in steel-framed structures exposed to fire. They applied a constant load of 40 kN to the steel specimens in each hydraulic loading Jack, corresponding to a load ratio of 0.5 in the beam. The steel connection specimens sustained the applied load during the fire classification period without experiencing a fracture. Heiza et al. [45] studied the structural behaviour and strength reduction of RC beam-to-column connections exposed to fire under cyclic loading. They preloaded the concrete specimens with 15 load cycles (less than the initial crack load) before conducting the fire tests at a constant load equal to the initial crack load. The specimens sustained the applied load during the fire classification period and showed concrete spalling and cracking. Raouffard and Nishiyama [1] investigated the mechanical and thermal interactions structural response of RC beam-to-column subassemblies under no lateral thermally induced thrust and no moment redistribution influence. They preloaded the concrete specimens until the first crack load before applying a constant vertical load (17.3 kN). The fire tests were terminated after 74 minutes as soon as the tensile longitudinal steel bars of the upward-loaded cantilever beam achieved the predefined critical temperature of 530°C. Yang and Fu [56] performed the experimental and numerical simulation of steel beam to CFST column composite connections with RC slabs by applying a constant load ratio of 0.1 to 0.35 to the composite specimens. They terminated the tests when the connection specimens achieved fire resistance (deformation and deformation rate).

Table 3 lists the studies that terminated the fire tests when the specimens failed. Ding and Wang [38] investigated the structural fire behaviour of concrete-filled tubular (CFT) columns, including the failure modes, force development, and beam deflections. They applied a constant load ratio (0.25 to 0.5 or 30 to 60 kN) to the beam and exposed the structural assembly to the standard fire condition in a furnace while maintaining the applied loads. They continued the heating until the structure failed. Han et al. [39] investigated the behaviour of RC beam to CFST column planar frames, including the deformations and failures of the test specimens. They preloaded the composite specimens to eliminate possible equipment malfunction before applying a constant load of between 19.5 and 39 kN. They immediately terminated the fire tests when the CFST columns and RC beam could not withstand the applied loads. Ding and Wang [40] investigated the structural behaviour in the cooling phase. They tested right of the ten test specimens to failure

during heating; in the other two tests, the test assemblies were heated to temperatures close to the failure temperatures of the axially unrestrained steel beams and then cooled while still maintaining the applied loads on the beams. Song et al. [42] investigated the mechanical behaviour of steel-reinforced concrete (SRC) joints during the heating and cooling phases. They preloaded the composite specimens using three jacks before conducting the fire tests under a constant load. In the postfire loading phase, the column load was kept constant, and the beam loads were increased gradually until the connection failed. Yahyai and Rezaeian [43] investigated the behaviour of beam and splice connections in column-tree moment resisting frames (MRF) at elevated temperatures. They preloaded the steel specimens with a constant load ratio of 0.7 or 20.6 kN and applied the heating and loading until the connection failed. Teja et al. [46] studied the thermal performance of three different beam-to-column connections in precast structures subjected to a constant load (7 to 17 kN) during heating until the connections failed.

Figure 5 shows the load applications after the fire tests (residual method), where Li et al. [44] simulated the typical idealised column removal scenario under fire. In this study, the RC beam-to-column connection specimens with varying reinforcement development lengths were exposed to fire, with and without cooling effects, and then subjected to pushdown loads. A vertical load of 20 to 90 kN was applied until the bottom reinforcements fractured or pulled out.

Table 2 shows that Heiza et al. [45] and Raouffard and Nishiyama [1] did not apply the superimposed and service load required by ASTM E119 and ISO 834. Instead, they used the first crack load, P_f, as a reference value for the load. Mindess et al. [57] and Hamad and Sldozian [58] defined the first crack load as the point on the load-deflection curve at which the curve first become nonlinear. The first crack strength represents the RC behaviour to the inception and beginning of a crack in the matrix. There are two methods for determining the first crack value. The first method is visual observation during the load test. However, concrete contains microcracks that grow as soon as the concrete is loaded. Thus, it is hard to achieve the first crack deflection because it is minor due to various extraneous deflections that may occur due to machine deformations and placing them on the supports. The second method is calculating the first crack deflections, δ [57] using the following formula:

$$\delta = \underbrace{\frac{23Pl^3/1296EI}{\text{flexural component}}}_{} \times \underbrace{\frac{\left[1 + 216d^2\,(a+\mu)/115l^3\right]}{\text{shear component}}}_{}, \quad (3)$$

where d is the midspan deflection, P is the load at first crack, l is the span length, E is the modulus of elasticity, μ is Poisson's ration, I is the moment of inertia, and d is the beam depth.

2.7. Conclusion on the Fire Testing of Beam-to-Column Connections. The following conclusions are drawn based on the discussion in Sections 2.1–2.6. In buildings with large, open compartments, the fire tends to travel horizontally and vertically as the flames spread by igniting the fuel in their path and burning it in a limited area at any one time. The localised horizontal and vertical travelling fires induce the temperature development of the beam-to-column connections through two temperature fields, the near and far fields. Researchers considered several factors to address the lack of structural fire performance testing methods for the beam-to-column connections. Based on the test objective and performance criteria adopted in previous studies, this review paper has summarised seven fire testing criteria. Of these, there is significant inconsistencies in Criteria 7 (loading applications), where the load was applied either in the preloading (structural response at ambient conditions), concurrent (thermomechanical response during fire exposure), or postfire (residual response after cooling down) phase, or a combination these phases. The loads were applied to the specimens constantly or gradually. The fire tests were terminated at the performance criteria limit when investigating the thermal behaviour, thermal interaction, and strength reduction. When determining the failure load and maximum deformation (deflection, expansion or contraction), the fire tests were terminated at specimens' failure. Besides the superimposed and service load stated in ASTM E119 and ISO 834, the researchers also employed the first crack load as the reference value for the load.

3. Issues and Challenges

3.1. Selection of the Structural Assembly. The literature shows that researchers faced a conflict when selecting a fire test method, whether standard fire testing or nonstandard structural fire testing. Regardless of the fire test method, the beam-to-column connection structural assembly must represent the actual structural behaviour [10]. Several factors are taken into account before assembling the specimens. Figure 6 demonstrates the relationship performance of the fire test based on different structural assemblies and fire curves.

The specimens for the beam-to-column connections can be assembled as a partial element, single element, subframe assembly, restrained assembly, or full-scale structure [53]. According to the ASTM E119 and ISO 834 guidelines, the specimens can only be assembled as a partial element and single element (vertical and horizontal building elements) subject to the standard time-temperature fire curves conditions, as shown in Figure 6. The fire testing of beam-to-column connections in previous research did not follow ASTM E119 and ISO 834 guidelines. The specimens were assembled as subframe assemblies subjected to elevated temperature (steady-state and transient) [46] and restraint assemblies subjected to standard time-temperature fire curves [1, 38, 43, 45, 56]. According to Gales et al. [53], the objective of the large-scale nonstandard structural fire tests that employed the full-scale structures and real fire curves is to understand the real structural performance of buildings subjected to construction and real fires. It is not possible to achieve this understanding through the standard fire testing furnace.

Based on Figure 6, it is apparent that a more complex structural assembly gives more accurate test results. The full-scale structures with complex structural assembly represent the building's actual structural behaviour. However, setting

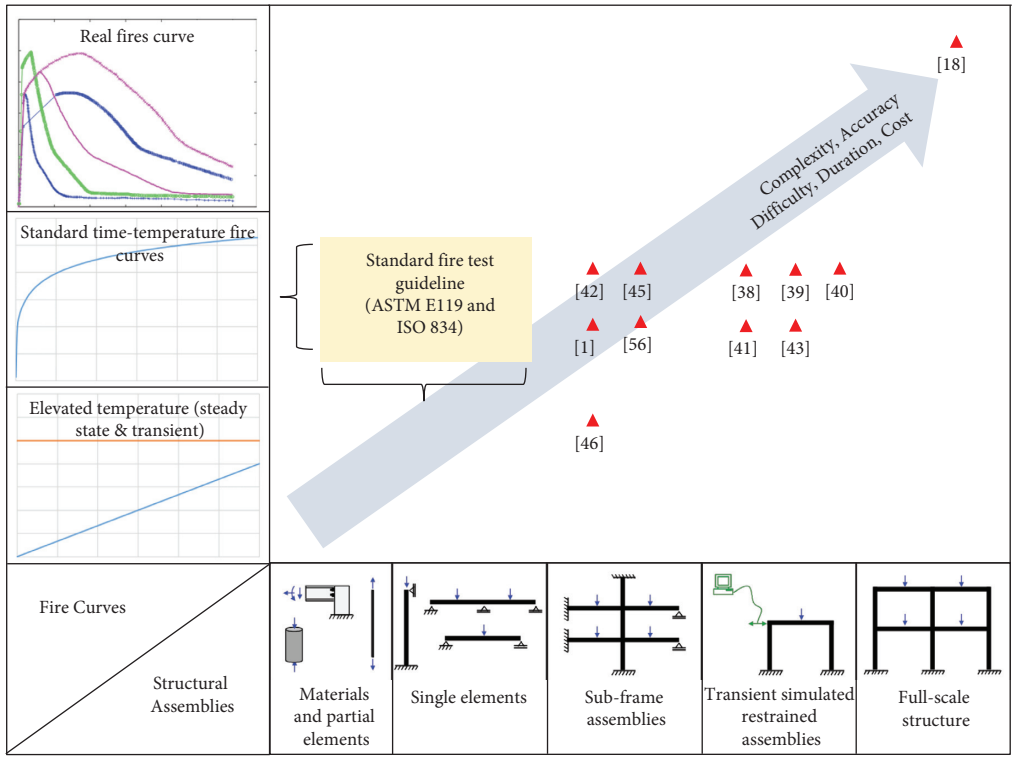

Figure 6: The relationship performance of fire tests based on different fire curves and structural assemblies.

up a complex structural assembly, including the specimen and testing procedures, are complicated and time-consuming. For example, the Cardington full-scale building fire tests in the United Kingdom for an eight-storey office building specimens involved six fire tests on the composite frame, namely, the restrained beam test, plane frame test, first corner test, second corner test, large compartment test, and demonstration test [59]. In addition, a nonstandard structural fire test is expensive and requires a real fire in actual scale framed buildings. The test also requires sufficient instrumentation to understand the fire and the structural response. Because of the high cost of physical fire tests, the finite element methods based on well-validated models are viable alternatives.

3.2. Real Fire Time-Temperature Curves vs. Standard Time-Temperature Fire Curves. In recent years, researchers and regulators have dealt with the use of standard time-temperature fire curves in simplified single element tests and isolated structural members subjected to unrealistic temperature-time curves [15, 16, 60, 61]. The standard time-temperature fire curves have little resemblance to the real fire temperature-time history. They do not have a decay phase and represent any real fire. They were designed to typify the temperatures experienced during the post-flashover phase of most fires [53]. The mock-up assembly's fire-resistance rating (hours) cannot represent the actual construction and real fire. It only tests the survival components of the fire exposure and can be compared as a relative index system to the design. As a result, nonstandard structural fire testings that employed real fire curves are a more rational approach that might present the full suite of interactions expected in actual building fires.

Even though the standard time-temperature fire curves do not have a decay stage at the end and appear more severe than a real fire, they are suitable for all three phases (growth, burning, and decay) of the fire tests. ISO 834 specifies that, even after termination, the fire tests can be continued after they have achieved the selected performance criteria to gather additional data, including the data on failure patterns and ultimate failure load. ASTM E119 evaluates the ability of the assemblies to remain intact in the decay phase by applying a specified standard fire hose stream to the structure.

Kodur and Agrawal [62] presented the postfire residual response of structural elements after cooling. Figure 7 shows that the heating scenario was subjected to the fire classification period (1, 1.5, and 2 hours) specified in ISO 834. The fire classification period is the performance resistance to the standard exposure elapsing before observing the first critical point in behaviour is observed. The fire classification period does not refer to the survival times or any explicit attempt to quantify the structural damage of the real structure in a real fire but to the expected fire resistance period for the structural components subjected to a standard temperature-time curve in standard furnace fire tests [2]. The decay stage is simulated through a linear decrease in air temperature following the fire exposure.

3.3. Structural Response of the RC Beam-to-Column Connections in the Cooling Phase. Many studies have been conducted on the cooling phase of steel and composite beam-to-column connections, but there is a dearth of study

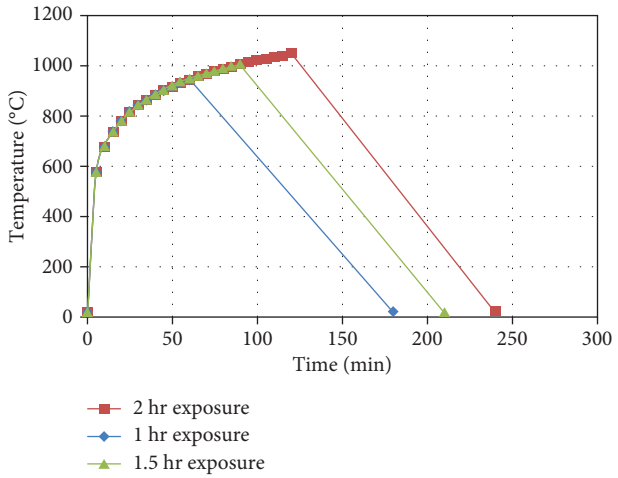

Figure 7: Fire exposure using the ISO 834 fire curve with a decay phase [62].

on the structural response of RC beam-to-column connections in the cooling phase. There is a significant difference in the thermal properties of concrete and steel materials. The thermal conductivity of steel (between 27 and 53 W/mK) is higher than concrete (between 0.5 and 1.3 W/mK) [63, 64]. This significant difference enhances the ability of a material to transfer heat in the cooling phase of connections. The literature shows that the temperature of the CFST column and steel beam in the joint zone is lower than those in the nonjoint zones during the heating phase but higher during the cooling phase [65]. Besides the thermal properties, the SRC column and beam showed significant deformation in the cooling phase than the heating phase, leading to the potential failure of SRC joints in the cooling phase [42, 66]. The relative increase in the beam-to-column rotation angle in the cooling phase is approximately 1.5 times higher than the increase in the heating phase. The duration of the heating phase that causes failure of the composite column during or after the cooling phase is always shorter than the fire resistance of structures exposed only to heating [67].

Heiza et al. [45] investigated the structural response of RC beam-to-column connections during the cooling phase. Their study focused on the structural behaviour and strength reduction of RC beam-to-column connections exposed to fire under cyclic loading. They removed the front part of the furnace at the end of the heating phase and begun the loading cycles while recording the deflection, strain, and cracks at each load increment until they reached the failure load. However, they did not explain the cooling phase effect and comparison of the heating and cooling phases.

Kodur and Agrawal [62] studied the structural response of RC structure in the cooling phase and found that the single RC beam element retained 60 to 70% of the ultimate room temperature capacity for a range of parametric fire exposure scenarios with a distinct cooling phase. Dwaikat and Kodur [68] found that the cooling phase reduces the fire-induced spalling in concrete. They observed that the pore pressure decreased with fire exposure because of the lower temperature and did not anticipate further concrete spalling. Gernay [69] addressed that the fire safety analysis of RC structure should consider until the complete burnout of a fire, cooling phase, and beyond to assess the safety during fire brigades intervention, building inspection, and possibly building rehabilitation.

3.4. Test Load Value. There are three issues when applying the test load on the beams. First, not all fire tests are conducted with preloading under ambient conditions, as shown in Figure 5. ASTM E119 stated that the test specimens should truly represent the construction, for which classification is desired, as to materials, workmanship, and details, such as dimensions of parts. The test specimens should be constructed under conditions representative of building construction and operation. The absence of preload before the fire tests will not provide an initial load to the beam, equal to the initial crack load or based on load ratio, and eliminate possible equipment malfunction. In real building conditions, the fire starts when a service load is applied to the structure.

Second, because the test load applied to the beam is lower than the required value, the test could not simulate the maximum superimposed and service load condition throughout the fire tests. The test load value is dependent on several factors, including the beam span. A short beam span produces a lower test load value. Given the current standard fire testing methods, the standards specify that the beam span exposed to the fire should not be less than 3.7 m (ASTM E119) and 4.0 m (ISO 834). However, Tables 2 and 3 show that the beam span for the specimens with the simply supported setup is between 1980 mm and 3980 mm, and the length of the cantilever beam is between 670 mm and 1050 mm. Assuming a cantilever beam is half the actual beam span (subassembly's concept), the beam length is between 1340 mm and 2100 mm. The beam span of specimens is less than the length required in the standards, and the shorter beam span provides a lower superimposed load or service load than the required load, and the beam will not react accordingly to the lower applied load.

Finally, another significant issue is the application of the first crack load as the reference test load. The theoretical first crack load is low compared with the observed experimental first crack loads. Kankam and Odum-Ewuakye [70] investigated the flexural strength and deformation of two-way RC slabs and found that the experimental failure loads are approximately 170% of the predicted values. Audu and Oseni [71] investigated the cracks and crack patterns on RC slabs and found that the difference between the experimental first crack load and the theoretical first crack load is between 14.2% and 59.7%. As the load increases, the crack formation is followed by multiplication and further cracking. The complete development of yield lines gave a lower theoretical yield load than the experimental values. This behaviour could be due to the adopted safety factor in the design.

3.5. Constraints in the Data Collection. The beam-to-column connections elements are exposed to high temperatures in the furnace, making it difficult to determine some of the

required study parameters. It is essential to address several factors when comparing the test result from the ambient temperature with the high temperature. In some cases, the instruments have to be protected with fire-resistive material to prevent damage.

Researchers could not record the crack development and failure mode during the heating and loading of the RC specimens and only obtain the result after the furnace cooled down. Similarly, the failures of steel connections, such as buckling, shear fracture of the bolt, and bearing deformation of the bolt holes, are only visible after the fire test. This situation is different from the normal load test, where researchers can monitor the outcomes of load applications. The strain gauge used at ambient temperature is very sensitive to high temperatures. Researchers need to use temperature resistive strain gauges for the reinforcing bars, steel structure, and concrete structure. However, the strain gauges did not perform well at high temperatures and failed to capture significant data [1].

The inclinometer for measuring the inclination and rotation of the beam cannot be used in a fire test. Figure 8 shows the inclinometer being used at ambient temperature [73]. Nonetheless, researchers can use the results from the linear variable differential transformer (LVDT) from the column and beam to calculate the rotation (milirad) [73]. The calculation is given by

$$\theta = \left\{ \left[\tan^{-1} \frac{b}{d} \right] - \left[\tan^{-1} \frac{a}{c} \right] \right\} \frac{100\pi}{18}, \quad (4)$$

where a is the displacement at column; b is the displacement at beam; c is the distance from LVDT to centre of rotation for column; d is the distance from LVDT to centre of rotation for beam.

The structural deformation during the fire test influences the consistency of the constant load applied to the beam. Whether the load is applied hydraulically, mechanically or by weights, there will be changes in the dimension or shape of an element of construction due to structural and thermal actions as the load increase. These changes include deflection, expansion, and contraction of the structural elements. It is difficult to control and monitor the loading consistency throughout the fire duration. The application of permanent load blocks to the designated position of the specimens [1, 43] requires a bigger space and more supporting equipment. The limited space makes it hard to install the load blocks and protect them with a ceramic fibre blanket in the furnace, as shown in Figure 9. Some electric furnaces are not designed for the load-bearing function. The rapid deflection of the beams during the fire test could bring down the loading blocks and damage the furnace [1]. In addition, the large load blocks and narrow space could prevent the heating in the furnace from achieving the required time-temperature fire curves.

3.6. Boundary Conditions for the Column. The restrained lateral movement and fixed end at the top and bottom column support in previous studies did not simulate the actual bending moment diagram of the column structure. By considering the length of the column is half from the actual storey of the building, the representative and definable manner bending moment diagram of the column will be shown as Figure 10. On this basis, the top and bottom of column support located at A and B (centre of column) will behave as a pin with zero moments. At the connection, there will be a significant value of moment for the column.

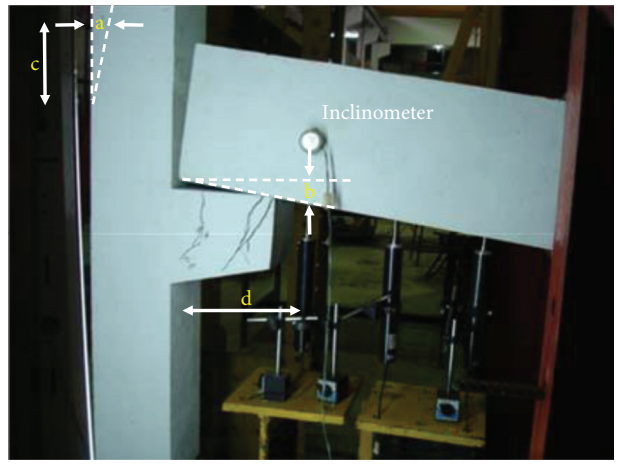

Figure 8: The installed inclinometer and measurement of the displacement of the beam and column [73].

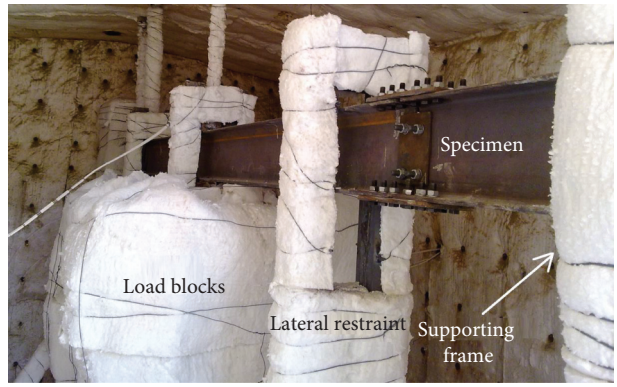

Figure 9: The load blocks in fire tests [43].

However, a different reaction was observed when applying the restrained lateral movement and fixed end conditions, and there will a significant value of bending moment diagram at column support located at A and B. The columns were restrained from lateral movement (to provide axial restraint to the beam) at the ends and were free to move in the longitudinal direction [38].

3.7. Fire Intensity at the Connections. The estimation of the maximum temperature in building fires is made at the location of the local fuel and flaming region. Considering a similar fire development with horizontal and vertical travelling fires shown in Figure 2, the maximum temperature is at the midspan of the beam instead of the connection region. However, the literature review revealed that previous fire testing provided direct heating to the connection, which did not accurately simulate the intensity of a real fire. After

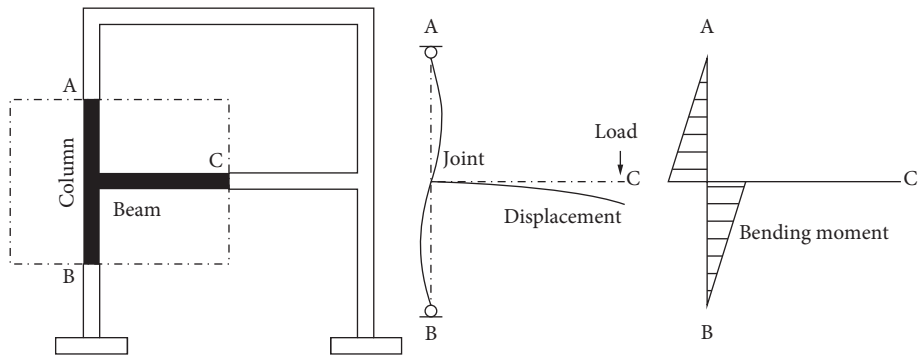

Figure 10: Bending moment diagram for the column member.

ignition occurs in a building, the fire spreads upward to the top structural member because the flame spreads on the burning object before moving to the adjacent connections [36]. The fire plume provides a buoyant convective transport of the combustion products up to the ceiling. The critical factor influencing the flame spread is the heating rate of the fire sources ahead of the flame. The thickness and temperature of the hot layer increase as the fire grows. According to Merci and Van Maele [72], the total heat release rate determines the average temperature rise of the hot smoke layer. However, the fire source area and roof opening have less influence on the average temperature rise.

Wroblewski et al. [74] described real fire incidents involving the concept of fire spread. The centre of the RC girders exhibited significant fire damage and pushed-out joining parts; the posttensioned roof girders, RC slabs, and columns sustained considerable damage, as shown in Figure 11. These thermal reactions reduced the moment capacity, rotational capacity, and rotational stiffness of the beam-to-column connections. Han et al. [39] found that the connection zone of the frame has a significantly lower temperature than the beam and column sections. The connection zone behaved as a rigid connection and did not show signs of failure in the fire tests.

3.8. Conclusion of the Issues and Challenges. The following conclusions are drawn based on the discussions in Sections 3.1–3.7. The selected beam-to-column connection structural assembly must represent the actual structural behaviour. A more complex structural assembly will produce a more accurate result even though the fire test is more time-consuming and expensive and involves complicated procedures. Even though the standard time-temperature fire curves do not have a decay phase at the end and appear more severe than the real fire, they are suitable for conducting fire tests for the growth, burning, and decay phases. There are many studies on the cooling phase of steel and composite beam-to-column connections, but there is a dearth of studies on the structural response of the RC beam-to-column connections in the cooling phase. The literature review revealed that there are three issues with the test load applied to the beam. (1) Not all fire tests are conducted with preloading at ambient conditions, (2) the test load applied to the beam is lower than the required load, and (3) the theoretical

Figure 11: Deformation of the centre of the RC girders in a real fire incident [74].

first crack load is lower than the observed experimental first crack loads. There is also difficulty in determining some of the required study parameters because the beam-to-column connections elements are in the furnace and exposed to high temperatures. The restrained lateral movement and fixed end conditions at the top and bottom of the column support in previous studies did not simulate the actual bending moment diagram of the column structure. The maximum temperature in building fires is estimated at the flaming region, depending on the location of the local fuel. The literature review revealed that previous fire testings provided direct heating to the connection, which did not accurately simulate the intensity of a real fire.

4. Recommendations and the Way Forward

There is a need for researchers and regulators to provide a standard method for determining the fire resistance of beam-to-connection connections exposed to fire. This need arises due to the increasing conflicts in the current fire testing methods and disagreement on the standard fire tests adopted in simplified single element tests and isolated structural members subjected to unrealistic temperature-time curves. The fire tests of the beam-to-connection connection elements may consider all phases of the fire, including the growth, flashover, fully developed, and decay or cooling phases, to obtain a complete result. In some cases,

the buildings collapse in the decay phase of the fire. The concept of equivalent fire severity relates the severity of an expected real fire to the standard fire tests. This concept is essential when comparing published fire-resistance ratings from standard tests with the severity estimates of a real fire.

The test load applied to the beam has to simulate the maximum load condition in the fire tests. The maximum load condition is a superimposed load, service load, actual material properties, characteristic material properties, or the first crack load representing the worst-case structure scenario. The testing laboratory should indicate the basis for determining the test load and the condition allowed under each nationally recognised structural design criteria. The maximum load condition will facilitate the primary goal of load testing to demonstrate the safety of a structure against failure.

The structural fire safety design must consider the severe condition of the midspan and structural member's connection during the fire. Even though the fire spread concept states that the maximum temperature is often recorded at the midspan of the member instead of the connection, the literature review showed that the connection elements of any building structure are critical and vulnerable during the heating and cooling phases of the building fire. The moment-rotation-temperature characteristics of the connections at elevated temperatures are influenced by the fire effects on the RC structure, including deflection, cracking, spalling, loss of stiffness, and strength and loss of reinforcement strength.

Finally, the adoption of performance-based structural fire design (PBSFD) in beam-to-column connections could explicitly define the levels of structural fire safety performance and produce more efficient and economical building designs [75, 76]. PBSFD uses analytical tools and experimental findings to design structures for fire safety. It does not rely on the current prescriptive code of requirements for structural fire protection, known as standard fire resistance design (SFRD), that does not explicitly evaluate structural fire performance. It is essential to understand and quantify the behaviour of the connections for a range of fire scenarios to ensure a resilient structure for extreme fire events.

5. Conclusions

This paper has reviewed the structural fire performance testing methods of beam-to-column connections of the fire testings conducted from 2007 to the present. The structural fire performance tests of beam-to-column connections provided significant results on the connections' fire performance and fire resistance. The required fire performances were assessed according to standardised test procedures with strict performance criteria. Based on the literature review, the following conclusions are drawn.

(i) The fire in a building with large, open compartments tends to travel horizontally and vertically as flames spread by igniting and burning the fuel in their path in a limited area at any one time.

(ii) A real fire develops in four phases, growth, flashover, fully developed, and decay or cooling. However, the standard temperature–time fire curves have little resemblance to the real fire temperature-time history.

(iii) ASTM E119 and ISO 834 provide the method for determining the fire resistance of the construction elements exposed to the standard fire conditions. However, these standards do not provide the methods for verifying the fire behaviour of the connections between building elements. They focus on separate vertical and horizontal building elements.

(iv) Despite the lack of fire performance test guidelines for the beam-to-column connections, researchers have conducted numerous fire tests on rigid, semirigid, and pinned beam-to-column connections.

(v) The seven fire testing criteria for the beam-to-column connections summarised from previous studies are the materials, type of connections, method of connections, boundary conditions (constraints), fire sources, type of analysis, and load applications.

(vi) There are significant inconsistencies in the loading applications (Criteria 7), where the load is applied in the preloading, concurrent, and postfire phases, or a combination of these phases.

(vii) The issues and challenges faced by researchers are the selection of structural assembly, arguments of real fire time-temperature curves against standard time-temperature fire curves, structural response of the RC beam-to-column connections in the cooling phase, test load value, constraints in data collection, boundary conditions of the column, and fire intensity at the connections.

(viii) There is a need for researchers and regulators to provide a standard method for determining the fire resistance of the beam-to-connection connections exposed to fire. The test load applied to the beam has to simulate a maximum load condition during the fire tests. The structural fire safety design should consider the severe conditions of the midspan and structural member's connection during the fire. The adoption of PBSFD in beam-to-column connections has explicitly defined the levels of structural fire safety performance and produces more efficient and economical building designs [77].

Data Availability

No data were used to support this study.

Conflicts of Interest

The authors declare that they have no known conflicts of financial interests or personal relationships that could have appeared to influence the work reported in this paper.

Acknowledgments

The authors acknowledge the financial support from Universiti Kebangsaan Malaysia through Research University Grant (grant no. GUP-2018-027) and laboratory facilities provided by the Department of Civil Engineering, Faculty of Engineering and Built Environment, Universiti Kebangsaan Malaysia.

References

[1] M. M. Raouffard and M. Nishiyama, "Fire response of exterior reinforced concrete beam-column subassemblages," *Fire Safety Journal*, vol. 91, pp. 498–505, 2017.

[2] V. Dao, J. Torero, C. Maluk, and L. A. Bisby, "Fire performance of concrete using novel fire testing," *Concr. Aust.*vol. 42, no. 1, pp. 58-59, 2016.

[3] I. Hollý and I. Harvan, "Connections in precast concrete elements," *Key Engineering Materials*, vol. 691, pp. 376–387, 2016.

[4] H. H. Ghayeb, H. A. Razak, and N. H. R. Sulong, "Seismic performance of innovative hybrid precast reinforced concrete beam-to-column connections," *Engineering Structures*, vol. 202, Article ID 109886, 2020.

[5] S. Elsawaf and Y. C. Wang, "Behaviour of restrained structural subassemblies of steel beam to CFT column in fire during cooling stage," *Engineering Structures*, vol. 46, pp. 471–492, 2013.

[6] J. Beitel and N. Iwankiw, *Analysis Of Needs And Existing Capabilities For Full-Scale Fire Resistance Testing, Nist Gcr 02-843-1*NIST, Gaithersburg, MD, USA, 2008, http://www.bfrl.nist.gov/866/pubs/NISTGCR02-843.pdf.

[7] Building and Construction Authority (Bca), *Connections for Advanced Precast Concrete System*, Building and Construction Authority (BCA), Singapore, 2018.

[8] R. Mokhtar, Z. Ibrahim, M. Z. Jumaat, Z. A. Hamid, A. H. A. Rahim, and A. Rahim, "Behaviour of semi-rigid precast beam-to-column connection determined using static and reversible load tests," *Measurement*, vol. 164, Article ID 108007, 2020.

[9] N. A. M. Radzi, R. Hamid, and A. A. Mutalib, "A review of methods, issues and challenges of small-scale fire testing of Tunnel lining concrete," *Journal of Applied Sciences*, vol. 16, no. 7, pp. 293–301, 2016.

[10] American Society of Testing Materials, *ASTM E119-07: Standard Methods of Fire Test of Building Construction and Materials*, ASTM International, PA, USA, 2007.

[11] International Organization for Standardization, *ISO 834-1, Fire Resistance Test - Elements of Building Construction, Part 1: General Requirements*, International Organization for Standardization, Geneva, Switzerland, 1999.

[12] N. A. M. Radzi, R. Hamid, A. A. Mutalib, and A. B. M. Kaish, "A review of precast concrete beam-to-column connections subjected to severe fire conditions," *Advances in Civil Engineering*, vol. 2020, Article ID 8831120, 23 pages, 2020.

[13] Y. Li and J. Zhao, "Research review on the behavior of steel beam to column endplate connections in fire," *Progress in Steel Building Structures*, vol. 22, no. 1, 2020.

[14] T. Lennon, *Structural Fire Engineering*, ICE Publication, London, UK, 2011.

[15] J. Gales, L. A. Bisby, and M. Gillie, "Unbonded post tensioned concrete in fire: a review of data from furnace tests and real fires," *Fire Safety Journal*, vol. 46, no. 4, pp. 151–163, 2011.

[16] L. Bisby, J. Gales, and C. Maluk, "A contemporary review of large-scale non-standard structural fire testing," *Fire Science Reviews*, vol. 2, no. 1, p. 1, 2013.

[17] K. H. Almand, *NET-SFPE workshop for development of a national R&D roadmap for structural fire safety design and retrofit of structures: Proceedings*, NlSTlR 7133, National Institute of Standards and Technology, Gaithersburg, MD, USA, 2004.

[18] A. Law, J. S. Gottfried, M. Gillie, and G. Rein, "The influence of travelling fires on a concrete frame," *Engineering Structures*, vol. 33, no. 5, pp. 1635–1642, 2011.

[19] X. Dai, S. Welch, and A. Usmani, "A critical review of "travelling fire" scenarios for performance-based structural engineering," *Fire Safety Journal*, vol. 91, pp. 568–578, 2017.

[20] J. Stern-Gottfried and G. Rein, "Travelling fires for structural design-Part I: literature review," *Fire Safety Journal*, vol. 54, pp. 74–85, 2012.

[21] E. Rackauskaite, C. Hamel, A. Law, and G. Rein, "Improved formulation of travelling fires and application to concrete and steel structures," *Structures*, vol. 3, pp. 250–260, 2015.

[22] A. Buchanan, "The challenges of predicting structural performance in fires," *Fire Safety Science*, vol. 9, pp. 79–90, 2008.

[23] G. C. Clifton, "Fire models for large firecells," HERA, Report R4-83, HERA, Manukau City, 1996.

[24] J. Stern-Gottfried and G. Rein, "Travelling fires for structural design-Part II: design methodology," *Fire Safety Journal*, vol. 54, pp. 96–112, 2012.

[25] J. S. Gottfried, *Travelling Fires for Structural Design*The University of Edinburgh, King's Buildings campus, Edinburgh, Scotland, 2011.

[26] C. G. Bailey, I. W. Burgess, and R. J. Plank, "Analyses of the effects of cooling and fire spread on steel-framed buildings," *Fire Safety Journal*, vol. 26, pp. 273–293, 1996.

[27] E. Ellobody and C. G. Bailey, "Structural performance of a post-tensioned concrete floor during horizontally travelling fires," *Engineering Structures*, vol. 33, no. 6, pp. 1908–1917, 2011.

[28] C. Röben, M. Gillie, and J. Torero, "Structural behaviour during a vertically travelling fire," *Journal of Constructional Steel Research*, vol. 66, no. 2, pp. 191–197, 2010.

[29] B. Behnam, "On the effect of travelling fire on the stability of seismic-damaged large reinforced concrete structures," *International Journal of Civil Engineering*, vol. 14, no. 8, pp. 535–545, 2016.

[30] B. Behnam and H. R. Ronagh, "Behavior of moment-resisting tall steel structures exposed to a vertically traveling post-earthquake fire," *The Structural Design of Tall and Special Buildings*, vol. 24, pp. 421–439, 2014.

[31] J. Jiang, Y. Lu, X. Dai, G.-Q. Li, W. Chen, and J. Ye, "Disproportionate collapse of steel-framed gravity buildings under travelling fires," *Engineering Structures*, vol. 245, Article ID 112799, 2021.

[32] R. L. Alpert, "Calculation of response time of ceiling-mounted fire detectors," *Fire Technology*, vol. 8, no. 3, pp. 181–195, 1972.

[33] K. L. Friquin, *Charring Rates of Heavy Timber Structures for Fire Safety Design A Study of the Charring Rates under Various Fire Exposures and the Influencing Factors*, Norwegian University of Science and Technology, Trondheim, Norway, 2010.

[34] T. Gernay and J.-M. Franssen, "The introduction and the influence of semi-rigid connections in framed structures subjected to fire," *Fire Safety Journal*, vol. 114, Article ID 103007, 2020.

[35] M. F. Green, N. Benichou, V. Kodur, and L. A. Bisby, "Design guidelines for fire resistance of FRP-Strengthened concrete

structures," in *Proceedings of the 8th International Symposium on Fiber Reinforced Polymer Reinforcement for Concrete Structure (FRPRCS-8)*, pp. 1–10, Patras, Greece, July 2007.

[36] A. H. Buchanan and A. K. Abu, *Structural Design for Fire Safety*, John Wiley & Sons, Hoboken, N J, US, 2017.

[37] B. Behnam, "Failure sensitivity analysis of tall moment-resisting structures under natural fires," *International Journal of Civil Engineering*, vol. 16, no. 12, pp. 1771–1780, 2018.

[38] J. Ding and Y. C. Wang, "Experimental study of structural fire behaviour of steel beam to concrete filled tubular column assemblies with different types of joints," *Engineering Structures*, vol. 29, no. 12, pp. 3485–3502, 2007.

[39] L. H. Han, Y. Q. Zheng, Z. Tao, and W. H. Wang, "Experimental behaviour of reinforced concrete (RC) beam to concrete-filled steel tubular (CFST) column frames subjected to ISO-834 standard fire," *Engineering Structures*, vol. 32, pp. 3130–3144, 2010.

[40] J. Ding and Y. C. Wang, "Temperatures in unprotected joints between steel beams and concrete-filled tubular columns in fire," *Fire Safety Journal*, vol. 44, no. 1, pp. 16–32, 2009.

[41] Y. C. Wang, X. H. Dai, and C. G. Bailey, "An experimental study of relative structural fire behaviour and robustness of different types of steel joint in restrained steel frames," *Journal of Constructional Steel Research*, vol. 67, pp. 1149–1163, 2011.

[42] T. Y. Song, L. H. Han, and Z. Tao, "Structural behavior of SRC beam-to-column joints subjected to simulated fire including cooling phase," *Journal of Structural Engineering*, vol. 141, no. 9, pp. 1–12, 2015.

[43] M. Yahyai and A. Rezaeian, "Behavior of beams in bolted column-tree frames at elevated temperature," *Fire and Materials*, vol. 40, no. 3, 2016.

[44] Z. Li, Y. Liu, J. Huo, H. Rong, J. Chen, and A. Y. Elghazouli, "Experimental assessment of fire-exposed RC beam-column connections with varying reinforcement development lengths subjected to column removal," *Fire Safety Journal*, vol. 99, pp. 38–48, 2018.

[45] K. Heiza, M. Taha, and M. Soliman, "Performance of reinforced concrete beam column connections exposed to fire under cyclic loading," in *Proceedings of the 2016 International Conference on Civil, Architecture and Environmental Engineering (ICCAE 2016)*, pp. 1–23, Taipei, Taiwan, July 2016.

[46] C. S. Teja, T. S. Moturu, G. Y. Kumar, H. A. Khan, G. Y. Kumar, and H. A. Khan, "Effect of fire on prefabricated concrete beam column connections," *International Journal of Recent Technology and Engineering*, vol. 8, no. 2, pp. 1433–1436, 2019.

[47] L. Chen and Y. C. Wang, "Methods of improving survivability of steel beam/column connections in fire," *Journal of Constructional Steel Research*, vol. 79, pp. 127–139, 2012.

[48] R. Aseeva, B. Serkov, and A. Sivenkov, *Fire Behavior and Fire Protection in Timber Buildings*, Springer Series in Wood Science, New York, NY, USA, 2014.

[49] P. Palma and A. Frangi, "Modelling the fire resistance of steel-to-timber dowelled connections loaded perpendicularly to the grain," *Fire Safety Journal*, vol. 107, pp. 54–74, 2019.

[50] D. Brandon, C. Maluk, M. P. Ansell et al., "Fire performance of metal-free timber connections," *Construction Material*, vol. 168, pp. 173–186, 2015.

[51] D. Brandon, M. Ansell, J. Bregulla, R. Harris, and P. Walker, "Behaviour of non-metallic shear connections in fire," in *Proceedings of the WCTE 2014 - World Conference on Timber Engineering*, Quebec City, Canada, August 2014.

[52] J. L. Torero, A. Law, and C. Maluk, "Defining the thermal boundary condition for protective structures in fire," *Engineering Structures*, vol. 149, pp. 104–112, 2017.

[53] J. Gales, C. Maluk, and L. Bisby, "Large-scale Structural Fire Testing-How did we get here, where are we, and where are we going?" in *Proceedings of the 15th International conference on experimental mechanics: Fire symposium*, Porto, Portugal, July 2012, http://hdl.handle.net/1842/6176.

[54] T. Y. Song, L. H. Han, and Z. Tao, "Performance of steel-reinforced concrete beam-to-column joints after exposure to fire," *Journal of Structural Engineering*, vol. 14210 pages, 2016.

[55] F. F. Feng, H. J. Hwang, and W. J. Yi, "Static and dynamic loading tests for precast concrete moment frames under progressive collapse," *Engineering Structures*, vol. 213, no. 4, Article ID 110612, 2020.

[56] Y. F. Yang and F. Fu, "Fire resistance of steel beam to square CFST column composite joints using RC slabs: experiments and numerical studies," *Fire Safety Journal*, vol. 104, pp. 90–108, 2019.

[57] S. Mindess, L. Chen, and D. R. Morgan, "Determination of the first-crack strength and flexural toughness of steel fiber-reinforced concrete," *Advanced Cement Based Materials*, vol. 1, no. 5, pp. 201–208, 1994.

[58] A. J. Hamad and R. J. A. Sldozian, "Flexural and flexural toughness of fiber reinforced concrete-American standard specifications review," *GRD Journals- Global Research and Development Journal for Engineering*, vol. 4, no. 3, pp. 5–13, 2019.

[59] K. S. Al-Jabri, I. W. Burgess, T. Lennon, and R. J. Plank, "Moment-rotation-temperature curves for semi-rigid joints," *Journal of Constructional Steel Research*, vol. 61, no. 3, pp. 281–303, 2005.

[60] R. K. Qureshi, N. Elhami-Khorasani, and T. Gernay, "Adaption of active boundary conditions in structural fire testing," *Journal of Structure Fire Engineering*, vol. 10, no. 4, pp. 504–528, 2019.

[61] C. Maluk, L. Bisby, G. Terrasi, M. Krajcovic, and J. L. Torero, "Novel fire testing methodology: Why, how and what now?" in *Proceedings of the Mini Symposium on Performance-based Fire Safety Engineering of Structures as part of the 1st International Conference on Performance*, Hong Kong, December 2012.

[62] V. K. R. Kodur and A. Agrawal, "An approach for evaluating residual capacity of reinforced concrete beams exposed to fire," *Engineering Structures*, vol. 110, pp. 293–306, 2016.

[63] European Committee For Standardization, *Eurocode 2: Design of concrete Structures - Part 1-2: General Rules - Structural Fire Design*, European Committee For Standardization, Brussels, Belgium, 2011.

[64] European Committee For Standardization, *Eurocode 3: Design of Steel Structures - Part 1-2: General Rules - Structural Fire Design*, European Committee For Standardization, Brussels, Belgium, 2011.

[65] T. Y. Song, L. H. Han, and B. Uy, "Performance of CFST column to steel beam joints subjected to simulated fire including the cooling phase," *Journal of Constructional Steel Research*, vol. 66, pp. 591–604, 2010.

[66] T. Y. Song, L. H. Han, and H. X. Yu, "Temperature field analysis of SRC-column to SRC-beam joints subjected to simulated fire including cooling phase," *Advances in Structural Engineering*, vol. 14, no. 3, pp. 353–366, 2011.

[67] T. B. Chu and Q. V. Truong, "Numerical studies of composite steel-concrete columns under fire conditions including cooling phase," in *Proceedings of the Congrès International de*

Géotechnique Ouvrages Structures, Springer, Ho Chi Minh City, Vietnam, pp. 213–223, October 2017.

[68] M. B. Dwaikat and V. K. R. Kodur, "Hydrothermal model for predicting fire-induced spalling in concrete structural systems," *Fire Safety Journal*, vol. 44, pp. 425–434, 2009.

[69] T. Gernay and J. M. Franssen, "A performance indicator for structures under natural fire," *Engineering Structures*, vol. 100, pp. 94–103, 2015.

[70] C. K. Kankam and B. Odum-Ewuakye, "Babadua reinforced concrete two-way slabs subjected to concentrated loading," *Construction Building Materials*, vol. 20, no. 5, pp. 279–285, 2006.

[71] M. T. Audu and O. W. Oseni, "First crack and yield load of Fanpalm reinforced concrete slabs," *International Journal of Science and Research*, vol. 4, no. 11, pp. 1979–1981, 2015.

[72] B. Merci and P. Vandevelde, "Experimental study of natural roof ventilation in full-scale enclosure fire tests in a small compartment," *Fire Safety Journal*, vol. 42, pp. 523–535, 2007.

[73] A. B. Abd Rahman, C. D. P. Leong, A. Saim, and M. H. Osman, "Hybrid beam-to-column connections for precast concrete frames," in *Proceedings of the 6th Asia-Pacific Struct. Eng. Constr. Conf. (APSEC 2006)*, pp. A281–A290, Kuala Lumpur, Malaysia, September 2006.

[74] R. Wróblewski, J. Gierczak, P. Smardz, and A. Kmita, "Fire and collapse modelling of a precast concrete hall," *Structure and Infrastructure Engineering*, vol. 12, no. 6, pp. 714–729, 2016.

[75] M. Smith and J. Gales, "Connection behaviour in contemporary canadian buildings subjected to real fires," in *Proceedings of the SFPE performance based design conference*, p. 6p. 6, 2018.

[76] American Society of Civil Engineers, *Performance-Based Structural Fire Design: Exemplar Designs of Four Regionally Diverse Buildings Using ASCE 7-16*, Appendix E. American Society of Civil Engineers, Honolulu, HI, USA, April 2018.

[77] K. S. Al-Jabri, J. B. Davison, and I. W. Burgess, "Performance of beam-to-column joints in fire-A review," *Fire Safety Journal*, vol. 43, no. 1, pp. 50–62, 2008.